Differential Top-Quark-Pair Cross Sections in pp Collisions at $\sqrt{s} = 7$ TeV with CMS and Charge Multiplication in Highly-Irradiated Silicon Sensors

Dissertation

zur Erlangung des Doktorgrades

des Department Physik

der Universität Hamburg

vorgelegt von

Jörn Lange

aus Münster

Hamburg

2013

Abstract

Modern particle-physics experiments like the ones at the Large Hadron Collider (LHC) are global and interdisciplinary endeavours comprising a variety of different fields. In this work, two different aspects are dealt with: on the one hand a top-quark physics analysis and on the other hand research and development towards radiation-hard silicon tracking detectors.

The high centre-of-mass energy and luminosity at the LHC allow for a detailed investigation of top-quark-pair ($t\bar{t}$) production properties. Normalised differential $t\bar{t}$ cross sections $\frac{1}{\sigma}\frac{d\sigma_{t\bar{t}}}{dX}$ are measured as a function of nine different kinematic variables X of the $t\bar{t}$ system, the top quarks and their decay products (b jets and leptons). The analysis is performed using data of proton-proton collisions at $\sqrt{s} = 7\,\mathrm{TeV}$ recorded by the CMS experiment in 2011, corresponding to an integrated luminosity of $5\,\mathrm{fb}^{-1}$. A high-purity sample of $t\bar{t}$ events is selected according to the topology of the lepton+jets decay channel. Lepton-selection and trigger efficiencies are determined with data-driven methods. The top-quark four-vectors are reconstructed using a constrained kinematic fit. The reconstructed distributions are corrected for background and detector effects using a regularised unfolding technique. By normalising the differential cross sections with the in-situ measured total cross section, correlated systematic uncertainties are reduced, achieving a precision of typically 4–11%. The results are compared to standard-model predictions from Monte-Carlo event generators and approximate next-to-next-to-leading-order (NNLO) perturbative QCD calculations. A good agreement is observed.

A high-luminosity upgrade of the LHC (HL-LHC) is envisaged for 2022, which implies increased radiation levels for the silicon tracking detectors. The innermost pixel layer is expected to be exposed to a 1-MeV-neutron-equivalent fluence in the order of $10^{16}\,\mathrm{cm}^{-2}$. The novel effect of radiation-induced charge multiplication (CM) is studied as an option to overcome the expected signal-to-noise degradation due to radiation damage (mainly due to charge-carrier trapping). Epitaxial silicon pad diodes of 75–150 μm thickness and of standard and oxygen-enriched materials are investigated after irradiation with 24 GeV protons up to equivalent fluences of $10^{16}\,\mathrm{cm}^{-2}$. Charge collection in response to different radiation (670, 830, 1060 nm laser light, α and β particles) is studied with the transient-current technique and a ^{90}Sr β setup. The different penetration properties of the radiation types are used to localise the CM region. The dependence of CM on voltage, fluence, thickness, material, temperature and annealing time is studied, as well as its proportionality, spatial uniformity and long-term stability. The absolute amount of charge in response to β particles is measured, and the impact of CM on noise, signal-to-noise and the charge-spectrum width is investigated. Implications for realistic segmented devices at the HL-LHC are discussed.

Zusammenfassung

Moderne Teilchenphysikexperimente, wie die am Large Hadron Collider (LHC), stellen globale und interdisziplinäre Projekte dar, die eine Vielzahl unterschiedlicher Bereiche umfassen. In dieser Arbeit werden zwei Aspekte davon behandelt: einerseits eine Top-Quark-Physik-Analyse und andererseits Forschung und Entwicklung von strahlenharten Siliziumspurdetektoren.

Die hohe Schwerpunktsenergie und Luminosität des LHCs erlauben eine detaillierte Untersuchung der Eigenschaften der Top-Quark-Paar-Produktion ($t\bar{t}$). Normierte differentielle $t\bar{t}$-Wirkungsquerschnitte werden als Funktion von kinematischen Variablen des $t\bar{t}$-Systems, der Top-Quarks und ihrer Zerfallsprodukte (b-Jets und Leptonen) gemessen. Die Analyse basiert auf Daten von Proton-Proton-Kollisionen mit $\sqrt{s} = 7\,\text{TeV}$ und einer integrierten Luminosität von $5\,\text{fb}^{-1}$, die vom CMS-Experiment 2011 aufgezeichnet wurden. Ein Datensatz von $t\bar{t}$-Ereignissen hoher Reinheit wird gemäß der Topologie des Lepton+Jets-Kanals selektiert. Die Leptonselektions- und Triggereffizienzen werden datenbasiert bestimmt. Die Top-Quark-Vierervektoren werden mit einem kinematischen Fit unter Verwendung von Zwangsbedingungen rekonstruiert. Die rekonstruierten Verteilungen werden mit einer regularisierten Entfaltungsmethode in Bezug auf Detektoreffekte korrigiert. Indem die differentiellen Verteilungen mit Hilfe des in-situ gemessenen Gesamtwirkungsquerschnitts normiert werden, verringern sich korrelierte systematische Unsicherheiten, so dass eine Genauigkeit von typischerweise 4–11% erreicht wird. Die Ergebnisse werden mit Standardmodellvorhersagen von Monte-Carlo-Ereignisgeneratoren und approximativen Rechnungen in drittführender Ordnung (NNLO) QCD verglichen. Es ist eine gute Übereinstimmung zu erkennen.

Ein Umbau des LHCs auf eine höhere Luminosität (HL-LHC) ist für das Jahr 2022 geplant. Dies wird zu einer höheren Strahlenbelastung für die Siliziumspurdetektoren führen. Die innerste Pixellage wird voraussichtlich einer 1-MeV-Neutronenäquivalenten Fluenz von ca. $10^{16}\,\text{cm}^{-2}$ ausgesetzt sein. Der neuartige Effekt der strahlungsinduzierten Ladungsverstärkung (LV) wird als vielversprechende Option untersucht, um die erwartete Verschlechterung des Signal-zu-Rausch-Verhältnisses auf Grund von Strahlenschäden (insbesondere durch Ladungsträgereinfang) auszugleichen. Dazu werden epitaktische Siliziumflächendioden zwischen 75 und 150 μm Dicke aus Standard- und sauerstoffangereichertem Material untersucht, die mit 24 GeV-Protonen bis zu einer Äquivalentfluenz von $10^{16}\,\text{cm}^{-2}$ bestrahlt wurden. Die gesammelte Ladung für unterschiedliche Strahlungsarten (670, 830, 1060 nm Laserlicht, α- und β-Teilchen) wird mit der Transient-Current-Technik und einem ^{90}Sr-β-Aufbau gemessen. Die unterschiedlichen Eindringtiefen der Strahlungsarten werden genutzt, um die LV-Region zu lokalisieren. Die Abhängigkeit der LV von der angelegten Spannung, Fluenz, Dicke, Material, Temperatur und Ausheilzeit wird untersucht, ebenso wie die Proportionalität, Flächenhomogenität und Langzeitstabilität der LV. Der absolute Wert der gesammelten Ladung für β-Teilchen wird gemessen, und der Einfluss von LV auf das Rauschen, Signal-zu-Rausch-Verhältnis und die Breite des Ladungsspektrums wird untersucht. Die Auswirkungen auf realistische segmentierte Sensoren für den HL-LHC werden diskutiert.

Contents

Chapter 1

Introduction

The quest to understand nature has been a driving force of human mind ever since. Modern fundamental physics addresses both the largest and the smallest scales in the universe.

For the experimental investigation of the microscopic properties of matter, particle accelerators are employed, such as the world's most powerful Large Hadron Collider (LHC) at the European Laboratory for Particle Physics (CERN) in Geneva. The LHC is mainly designed to collide protons (pp) at a centre-of-mass energy of 14 TeV. In 2010/2011, a centre-of-mass energy of 7 TeV was achieved, and 8 TeV in 2012. From the energy released in such collisions, new (potentially unknown) particles are created, which can be measured in large particle detector systems surrounding the interaction points. The careful design, research and development (R&D), building, commissioning, calibration and running of both accelerator and detectors constitute a prerequisite of each particle-physics analysis. It has been a tremendous, decades-long effort of international and interdisciplinary collaborations of thousands of scientists and engineers. In order to reflect at least a small part of this extraordinarily diverse and complex field, the work in this thesis is devoted to two different parts: on the one hand a particle-physics analysis of differential top-quark-pair production and on the other hand research and development towards radiation-hard tracking detectors for a future high-luminosity upgrade of the LHC.

1.1 Differential Top-Quark-Pair Production

With a mass of $173\,\mathrm{GeV}$[1], the top quark is the heaviest known elementary particle to date. It therefore plays a special role in the standard model of particle physics (SM). For example, the Higgs boson, endowing particles with mass, couples preferentially to the top quark. Another consequence is a fast decay before hadronising to bound states, unlike lighter quarks. This enables a unique opportunity to study the properties

---

[1]In this thesis, natural units $c = \hbar = \epsilon_0 = 1$ are employed. Thus, energy, momentum and mass all have the dimensions of energy and are expressed in units of electron-volts (eV). Electric charge is given in units of elementary charge e.

of a basically bare quark. Moreover, top quarks play an important role in searches for physics beyond the standard model.

The top quark was discovered in 1995 at the proton-antiproton collider Tevatron and first basic properties were measured there. At the LHC, the production rate is much higher due to both larger cross sections at higher centre-of-mass energies and larger luminosities. Already in 2011, 800,000 top-antitop-quark pairs ($t\bar{t}$) were produced, and even 5 m. in 2012. Consequently, the LHC is considered a *Top Factory*, which opens up a new era of precision and properties measurements in the top-quark sector.

This offers the possibility of measuring $t\bar{t}$ cross sections differentially as a function of kinematic variables of the $t\bar{t}$ system, the top quarks and their decay products. Such distributions offer much more information on the production mechanism than the single quantity of the inclusive cross section. Thus, they constitute a detailed test of the SM, in particular of perturbative Quantum Chromodynamics (pQCD), which describes the strong interaction at high energies. They are also sensitive to QCD parameters such as parton distribution functions (PDF) and the strong coupling constant α_s, as well as to potential new physics effects.

Before the LHC era, differential $t\bar{t}$ cross sections have been measured only as a function of the transverse momentum p_T of the top quarks [1, 2] and the invariant mass of the $t\bar{t}$ system [3] with large, dominantly statistical uncertainties of about 20%. During the startup phase of the LHC in 2010, first pioneering differential measurements were done as a function of the p_T and pseudorapidity η of the muon into which the top quark decays [4, 5] using data recorded by the CMS experiment with integrated luminosities of 3 to 36 pb^{-1}.

That work is carried on in this thesis, which is based on data recorded by the CMS experiment in 2011 corresponding to 5 fb^{-1} of pp collisions at 7 TeV. The much higher integrated luminosity in combination with an improved understanding of the detector allows to measure those quantities much more precisely and in more measurement intervals than before. A major achievement is the extension to a total of 9 different kinematic variables of different objects in a $t\bar{t}$ event as summarised in Tab. 1.1, many of them measured for the first time: the p_T and rapidity y of both the individual top quarks and the $t\bar{t}$ system as a whole; the invariant mass of the $t\bar{t}$ system $m^{t\bar{t}}$; and the p_T and η of the decay products (b jets and muons or electrons). This allows for the first time to gain a global picture of dynamics and kinematics of $t\bar{t}$ production and decay. Each variable reflects a different aspect. $m^{t\bar{t}}$ corresponds to the centre-of-mass energy of the colliding partons at leading order and is sensitive to potential new heavy resonances. $y^{t\bar{t}}$ reflects the boost of the $t\bar{t}$ system along the beam direction due to different proton-momentum fractions x of the colliding partons, which makes it especially sensitive to PDFs (in particular to gluon PDFs at high x). $p_T^{t\bar{t}}$ is sensitive to higher-order effects as it balances the p_T of additionally radiated partons. p_T^t and y^t represent the dynamics of $t\bar{t}$ production in the $t\bar{t}$ rest frame, convoluted with the respective distributions of the $t\bar{t}$ system. The variables of the decay products are furthermore also sensitive to the properties of the decay vertices.

The measurement in this thesis is performed in the lepton+jets decay channel with

Object	Measured Quantities			Reconstruction and Correction Level
t$\bar{\text{t}}$ System	$p_\text{T}^{\text{t}\bar{\text{t}}}$	$y^{\text{t}\bar{\text{t}}}$	$m^{\text{t}\bar{\text{t}}}$	kinematic reco. needed
Top Quarks	p_T^{t}	y^{t}		$\rightarrow$ parton level
b Jets	p_T^{b}	η^{b}		directly measurable
Leptons (e/μ)	p_T^{ℓ}	η^{ℓ}		$\rightarrow$ stable particle level

Table 1.1: Overview on measured kinematic quantities.

one muon or electron, one corresponding neutrino and four jets (two out of which originate from b quarks) in the final state at leading order. It is complemented by a similar analysis in the dilepton decay channel presented in [6, 7].

The structure and strategy of the analysis part of this thesis is as follows: An introduction to the SM with emphasis on top-quark physics is given in Sec. 2, followed by a description of the experimental setup of colliders and detectors in Sec. 3 and of the simulation tools in Sec. 4. The strategy of this analysis relies on the selection of a high-purity t$\bar{\text{t}}$ sample as detailed in Sec. 5. Subsequently, a data-driven determination of efficiencies is described in Sec. 6. The kinematic variables of the top quarks and the t$\bar{\text{t}}$ system need to be reconstructed with the help of a constrained kinematic fit (see Sec. 7). The event yields are corrected for background, as well as for detector effects using a regularised unfolding technique (see Sec. 8). Top-quark and t$\bar{\text{t}}$ quantities are corrected to parton level, the ones of the decay products to stable particle level as indicated in Tab. 1.1. Finally, the distributions are normalised by the in-situ measured inclusive cross section. Thereby, many systematic uncertainties, which are discussed in Sec. 9, cancel at least partly. The results are presented and compared to simulations from different Monte-Carlo event generators and calculations at fixed perturbative order, as well as to results from other channels and experiments in Sec. 10. Final conclusions are drawn and an outlook is given in Sec. 15.

1.2 Charge Multiplication in Highly-Irradiated Silicon Detectors

The LHC has already now almost reached its design luminosity of $10^{34}\,\text{cm}^{-2}\text{s}^{-1}$. Over the next 10 years, it is expected to deliver about 300–500 fb^{-1} of data. However, for the study of rare processes much higher luminosities are desirable. Thus, a luminosity upgrade to $5 \times 10^{34}\,\text{cm}^{-2}\text{s}^{-1}$ and techniques such as luminosity-levelling are envisaged for about 2022 (high-luminosity LHC (HL-LHC), formerly also called Super-LHC) [8]. It is expected to deliver a total of 3000 fb^{-1}. However, this implies severe consequences for the detectors as the hit occupancy, number of pile-up interactions and the radiation level will rise significantly.

The tracking system, in particular the innermost pixel layers, will be affected most, where particle fluences of up to $(1–2)\cdot10^{16}$ cm^{-2} are expected over the HL-LHC lifetime.

This will lead to an unprecedented level of radiation damage in the silicon tracking sensors, manifesting itself in an increase of leakage current, charge-carrier trapping and a change in the depletion voltage and electric-field distribution in the sensor. A significant degradation of the signal-to-noise ratio and hence of the detection efficiency and resolution is expected, ultimately rendering the detectors inoperable. Thus, the development of radiation-hard silicon detectors is of utmost importance. With this aim, new materials, devices and operation concepts are studied in the framework of the CERN-RD50 collaboration and within the tracker collaborations of the LHC experiments.

The most limiting factor at HL-LHC fluences is expected to originate from the trapping of charge carriers at radiation-induced defects. This will result in a decrease of the charge-collection efficiency (CCE). However, in a previous work [9], a different behaviour was observed for highly-irradiated thin (75–150 μm) epitaxial pad sensors (i.e. unsegmented large-area diodes) operated at high voltages. The CCE was seen to increase steeply with voltage and eventually exceeded unity, i.e. that more charge was collected than deposited inside the sensor. This clearly indicates the onset of internal charge multiplication, which (over)compensates trapping. This effect has also been observed in highly-irradiated planar strip sensors [10–13] and 3D detectors [14, 15], which suggests that this is a general radiation-induced effect.

Charge multiplication is a well-known phenomenon at high electric fields, which accelerates charge carriers so much that they in turn can create further free charge carriers - a process called avalanche or impact ionisation. It is widely exploited in gaseous radiation detectors and silicon photo detectors such as avalanche photo diodes (APD) or silicon photomultipliers (SiPM). However, radiation-induced multiplication in silicon tracking sensors is a novel effect. It is very intriguing to think of it as a self-healing radiation effect, which counteracts the degradation of the signal-to-noise ratio due to other radiation effects such as trapping. However, before it can be considered as the long-sought solution towards radiation-hard detectors, it must be assured that the effect is well-understood and can be controlled such that no detrimental side effects occur, which might spoil the beneficial aspects. In particular, it needs to be studied why and under which conditions this effect sets in and where the charge-multiplication region is located with respect to the sensor depth. Moreover, one needs to know whether the multiplication is proportional to the deposited charge, uniform over the sensor area and stable in time during operation. Equally important is the study of the impact on the noise, which is expected to increase due to multiplied leakage current and possible statistical fluctuations in the multiplication process. Also the signal-charge spectrum might broaden. These questions are addressed in this thesis by charge-collection studies in 75–150 μm thick epitaxial pad sensors in response to different types of radiation.

The structure of the second part of this thesis dealing with radiation-induced charge multiplication is as follows: the basics of silicon detectors and corresponding radiation damage are reviewed in Secs. 11 and 12. The devices under test and the experimental techniques for charge-collection studies are described in Sec. 13. The results are presented in Sec. 14. Final conclusions are drawn and an outlook is given in Sec. 15.

Chapter 2

The Standard Model of Particle Physics and the Top Quark

The idea that all matter in the universe is composed of fundamental, indivisible building blocks dates back several thousand years to ancient Indian and Greek philosophers. In modern physics, this principle is still valid and is described by the *Standard Model* (SM) of elementary particle physics. A detailed introduction of the SM can be found e.g. in [16–20]. In the following, a short overview based thereon is given.

The SM is based on a small number of fundamental, point-like constituents of matter, namely twelve fermions with spin 1/2, and three interactions between them, which are the electromagnetic, weak and strong interaction. These interactions in turn are also described by the exchange of another class of elementary, point-like particles, namely bosons with spin 1. The strengths of the interactions are determined by coupling constants, which are related to quantum numbers of the particles called *charges*. Gravity, the fourth fundamental interaction known in nature, cannot be included in the SM within the current theoretical framework, but can be safely neglected in present particle-physics experiments due to the small masses and hence minimal gravitational couplings of the particles at the currently achievable energy scales.

The theoretical and mathematical framework of the SM is based on quantum-field theories combining special relativity and quantum mechanics. A system of particles (or even vacuum) is determined by its Lagrangian density, which is a function of the fields and from which the equations of motions can be derived. The attractiveness of the SM from a theoretical point of view is, among others, based on the fact that the description of the interactions arises naturally from symmetry principles, namely by demanding the Lagrangian to be invariant under certain local unitary transformations. The symmetry group of the SM related to these so-called *gauge* transformations is composed of $SU(3)_C \times SU(2)_L \times U(1)_Y$. From an experimental point of view, the SM is extremely successful in describing and predicting almost every particle-physics measurement over the last decades. However, the SM also has shortcomings such as a number of arbitrary, unpredictable input parameters and its incompleteness due to the inability to incorporate gravity and observations such as dark matter and energy or the excess of matter over antimatter in the universe.

In the following, a summary of the particles and their interactions is given, with special emphasis on the top quark, which is the particle under study in this thesis.

2.1 Particles and Interactions

		Fermions (Spin 1/2) Generations			Gauge Bosons (Spin 1) Interactions		
		I	II	III	Weak	EM	Strong
Leptons	Neutral ($Q=0$)	ν_e	ν_μ	ν_τ	Z^0		
	Mass	<2 eV	<0.19 MeV	<18.2 MeV	$Q=0$		
	Charged ($Q=-1$)	e	μ	τ	91.2 GeV		
	Mass	511 keV	106 MeV	1.8 GeV		Photon	
Quarks	Up-Type ($Q=+\frac{2}{3}$)	u	c	t	$W^\pm$	$Q=0$	
	Mass	2.3 MeV	1.3 GeV	173 GeV	$Q=\pm1$	$<10^{-18}$	Gluon
	Down-Type ($Q=-\frac{1}{3}$)	d	s	b	80.4 GeV	eV	$Q=0$
	Mass	4.8 MeV	95 MeV	4.2 GeV			0 eV

Higgs Boson (Spin 0)
$Q = 0$
$126\,\text{GeV}$

Table 2.1: Overview on the elementary particles of the SM including their electric charges and measured masses [19, 21, 22]. The limits of the neutrino masses are from direct measurements. Neutrino-oscillation experiments and constraints from cosmological observations imply much more stringent limits [23]. The mass of the Higgs boson refers to the one of the recently discovered Higgs-like boson [24, 25]. The mass of the gluon is a theoretical value. The curly brackets denote to which particles the gauge and Higgs bosons couple.

The particle[1] content of the SM is summarised in Tab. 2.1.

2.1.1 Fermions

The twelve fundamental fermions with spin 1/2 are grouped into different types, namely leptons with either electrical charge 0 (neutrinos) or -1, and quarks with electrical charge +2/3 (up-type) or -1/3 (down-type). Each fermion type appears in three different generations with the same properties but different masses. The first generation, consisting of up and down quark, electron and its corresponding neutrino, comprises

---

[1]Unless denoted otherwise, *antiparticles*, which have the same properties as particles, but with opposite additive quantum numbers, are implicitly included when referring to *particles*. Antiparticles are denoted with a bar, e.g. $\bar{t}$ for an antitop quark.

the fermions with the lowest masses of each type, respectively[2]. Thus, the first three are the constituents of ordinary stable matter as the higher-mass particles of higher generations eventually decay into their first-generation counterparts. The up-type quark of the third generation, the top quark, acquires a special role in the SM, being its heaviest particle. This is discussed in detail later.

2.1.2 Gauge Bosons and Interactions

The gauge bosons with spin 1 ($W^{\pm}$, Z^0, photon γ and gluons g) act as mediators of the interactions. The curly brackets in Tab. 2.1 denote to which fermions they couple. This is determined by their charges g, which are directly related to the coupling constants α of the interaction via $\alpha \propto g^2$. Note that in addition, the gauge bosons can partly also couple to each other, depending on the respective group structure. The magnitudes of the coupling constants play a decisive role, both for understanding the fundamental principles of the interactions as well as for the calculation of physical observables like cross sections. Such calculations rely on perturbation theories, i.e. the expansion of the solution in orders of the coupling constants, which can only converge if $\alpha \ll 1$. The expansion terms can be illustrated using *Feynman diagrams*. They are exemplified in Fig. 2.1 for leading order (LO) and next-to-leading order (NLO) top-quark production, which is explained in Sec. 2.2.1 in more detail. An interesting effect is the running of the coupling constants due to *renormalisation* of divergences occurring in loop calculations (see e.g. Fig. 2.1 *bottom right*). This introduces a dependence of the coupling on the so-called *renormalisation scale* μ_R, which is usually identified with the typical energy or momentum[3] scale of the process, such as its momentum transfer Q or the invariant mass m^X of a produced particle or particle system X.

The electromagnetic (EM) interaction is mediated by the exchange of virtual photons, which couple to particles with electric charge. Photons themselves are electrically neutral and therefore do not interact with each other. Furthermore, they are massless. The coupling constant α_{EM} increases from $\alpha_{EM} \approx 1/137$ at low energy scales to $1/129$ at the Z-boson mass scale of $91\,\text{GeV}$, but remains $\ll 1$ up to very high energy scales. The underlying theory is called Quantum Electrodynamics (QED), which is based on the $U(1)_{EM}$ symmetry group. Although QED is a very successful and precise theory on its own, it turns out that for a fundamental description, the electromagnetic interaction needs to be unified with the weak interaction as described below.

The weak interaction is mediated by the exchange of $W^{\pm}$ and Z^0 bosons[4], which couple to particles with weak charge g_w. This is the case for all fermions as well as the W and Z bosons themselves due to the non-Abelian nature of the underlying $SU(2)$ symmetry (note that in addition, the $W^{\pm}$ bosons also couple to the photon due to their electric charge). However, it turns out that the properties of the weak interactions and its gauge bosons can only be understood in unification with the electromagnetic inter-

---

[2]Except for the neutrinos, where due to the larger flavour mixing this assignment is not meaningful.

[3]If the energy of a particle is much larger than its mass, the energy also equals the momentum magnitude, such that both can be used interchangeably.

[4]In the following, the charge superscripts are omitted if possible.

action, called electroweak theory with the corresponding $SU(2)_L \times U(1)_Y$ symmetry group. Y refers to a new quantum number called hypercharge, whereas L denotes the special role of left-handed particles, to which e.g. the W bosons couple exclusively, violating parity. The unification implies that the weak and the electric charges are related to each other via a weak mixing angle and the bare weak charge is of the same order as the electric charge. However, the W and Z bosons are observed to be very massive (see Tab. 2.1), which leads to a suppression of the coupling strength at low energies. Another special property of the weak interaction is the coupling of the W bosons to different fermion types (*flavour*) at the same interaction vertex, namely either to a neutrino and a charged lepton or to an up-type and a down-type quark. Usually, this occurs within the same generation, but for the quarks, also inter-generational flavour-changing couplings are observed. They are accommodated by the introduction of the unitary Cabibbo-Kobayashi-Maskawa (CKM) matrix, which describes the probability of the flavour mixing. The magnitudes of its elements are given by [19]:

$$\mathbf{V}_{CKM} = \begin{pmatrix} V_{ud} & V_{us} & V_{ub} \\ V_{cd} & V_{cs} & V_{cb} \\ V_{td} & V_{ts} & V_{tb} \end{pmatrix} = \begin{pmatrix} 0.974 & 0.225 & 0.004 \\ 0.225 & 0.973 & 0.041 \\ 0.009 & 0.040 & 0.999 \end{pmatrix} \tag{2.1}$$

As can be seen, the off-diagonal elements are non-zero, but small, in particular those between the third and the other two generations.

The mediators of the strong interactions are the massless gluons. They couple to a charge denoted as *colour* (C), which appears in three states: blue, red and green (plus their respective antistates). This is why the underlying theory is called Quantum Chromodynamics (QCD) with its symmetry group $SU(3)_C$. Of the fermions, only quarks carry colour, but similarly to the weak interaction, the gluons carry colour themselves, enabling self-interactions. This, in combination with the number of colour states, leads to the opposite behaviour of the running strong coupling constant α_s compared to the other interactions, namely an increase with decreasing energy or, alternatively, increasing distance scale. Thus, for two separating coloured particles, it becomes energetically more beneficial to create new quark-antiquark pairs until all particles are bound into colour-neutral hadrons than to exist individually. Such hadrons comprise baryons of three quarks (one of each colour) or mesons of two quarks with colour-anticolour. This process is called *hadronisation* and the principle that no free coloured particles exist *confinement*. In fact, a quark or gluon from high-energy collisions usually leads to a bunch of hadrons called *jet* with similar direction and momentum as the original quark. Turning the argument around, α_s decreases for increasing energy or decreasing distance, enabling the perturbative description of QCD at scales much larger than the characteristic QCD scale $\Lambda_{QCD} \approx 200\,\text{MeV}$. This phenomenon is called *asymptotic freedom*. At the Z-boson mass scale, the coupling strength amounts to $\alpha_s(M_Z) = 0.12$, still significantly larger than for the other interactions.
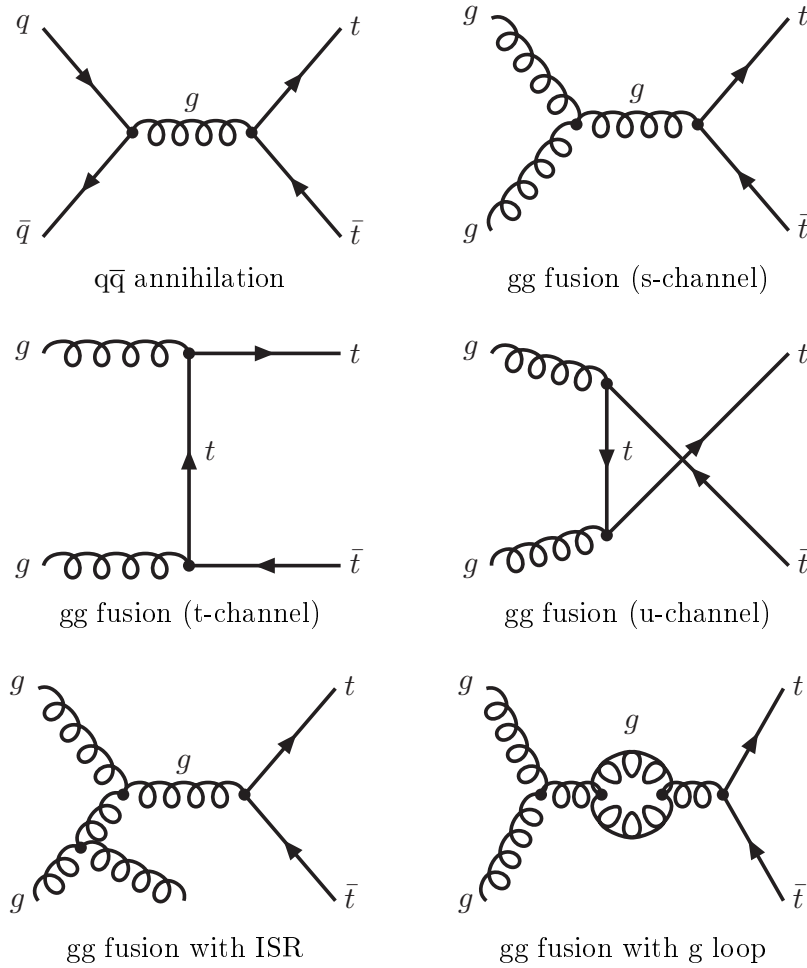
Figure 2.1: Feynman diagrams for $t\bar{t}$ production at leading-order (*top* and *middle row*) and selected ones at next-to-leading order (*bottom row*).

2.1.3 Electroweak Symmetry Breaking

The principle of gauge invariance, on which the SM is based, turns out to forbid explicit mass terms in the Lagrangian of the gauge bosons in general and of the fermions in the left-handed formulation of the electroweak interaction. This seems to contradict the actual observation of weak gauge-boson and fermion masses in nature. Thus, a mechanism is needed to accommodate them in the SM under preservation of the electroweak gauge symmetry. Whereas in general different solutions are conceivable, it is accomplished in the SM by the *Higgs mechanism* [26–28], which introduces a doublet of complex scalar fields (the *Higgs fields*) with a potential. While the Lagrangian itself including the potential and its set of minima preserve the symmetry, the actual minimum that happens to be chosen by nature, corresponding to the vacuum state, does not. This is referred to as *spontaneous electroweak symmetry breaking*. By the choice of the minimum, the masses of the W and Z bosons are created, while retaining the photon massless. The vacuum expectation value of the field is related to the W-

boson mass and the weak coupling constant and amounts to 246 GeV. This mechanism is accompanied by the prediction of a new particle, namely a massive *Higgs boson* with spin 0, which corresponds to excitations of the field in its potential. This particle is predicted to couple both to the W and Z bosons and to itself. Moreover, the concept can be extended to also incorporate the mass generation of the fermions via Yukawa couplings between a fermion-antifermion pair and the Higgs boson with the coupling constant proportional to the respective fermion mass.

Recent observations of a new boson by the ATLAS and CMS experiments at the LHC with a measured mass of 126.0 ± 0.6 GeV [24] and 125.3 ± 0.6 GeV [25], respectively, are compatible with such a SM Higgs boson. However, further investigations are ongoing to test precisely if all its properties such as spin, parity and couplings are consistent with the SM predictions or rather hint to alternative models.

2.2   The Top Quark

The top quark is a special particle in the SM with a number of unique properties, many of which are connected to its large mass of about $m_t = 173$ GeV. Extensive overviews on top-quark physics are given e.g. in [29–31]. This section gives a short summary, with special emphasis on the production at hadron colliders as differential top-quark-pair cross sections are studied in this thesis.

Its prediction in the framework of the SM dates back to the postulation of a third generation of quarks as a mechanism to explain CP violation in 1973 [32]. However, as a consequence of its large mass, which necessitates a high centre-of-mass energy $\sqrt{s}$ in particle collisions for its production, it was not directly discovered before 1995, when it was observed by the experiments CDF [33] and D0 [34] at the proton-antiproton ($p\bar{p}$) collider Tevatron at $\sqrt{s} = 1.8$ TeV[5]. Since 2010, top quarks are also produced abundantly in proton-proton (pp) collisions at the Large Hadron Collider (LHC) at $\sqrt{s} = 7$ TeV (2010-2011) or 8 TeV (2012). As this analysis is performed with data of pp collisions at $\sqrt{s} = 7$ TeV recorded in 2011, the following discussion always refers to these conditions, if not stated otherwise. So far, lepton colliders have not yet achieved enough collision energy for top-quark production.

2.2.1   Top-Quark Production at Hadron Colliders

At hadron colliders, top quarks are mainly produced in pairs ($t\bar{t}$) by the strong interaction. Such collisions are complicated by the internal structure of the hadron. This is described by the *Parton*[6] *Distribution Functions* (PDFs) $f_{a|h}(x, \mu_F)$, which represent the number density of a specific parton type a with longitudinal momentum fraction x of the hadron h (see Fig. 2.2) at an energy scale μ_F (for the exact meaning of μ_F see below). In a simplified picture, the proton consists of three valence quarks (uud), which

---

[5]In 2001 the Tevatron upgraded to 1.96 TeV.
[6]*Parton* refers collectively to quarks and gluons.
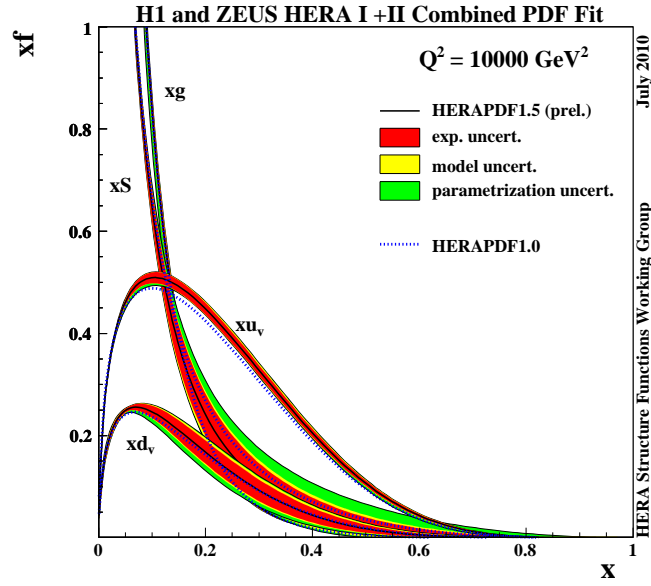
Figure 2.2: Parton Distribution Functions (PDFs) of the proton as a function of the proton momentum fraction x from NLO HERAPDF1.5. The PDFs for the valence (u_v, d_v) and sea (S) quarks as well as for the gluons (g) are shown at a hard-scattering scale (explained below) of $Q = 100\,\text{GeV}$. It is in the order of the scale relevant for top-quark or W- and Z-boson production. Taken from [35], details in [36].

determine its quantum numbers and carry a momentum fraction $x = 1/3$. However, at high collision energies with large energy transfers, corresponding to small distances, increasingly more so-called sea quarks and gluons from QCD interactions inside the proton are resolvable, which dominate at low x. Due to the non-perturbative nature of confinement, PDFs need to be measured experimentally, which is mainly based on deep-inelastic scattering at the electron-proton collider HERA [36] and fixed-target experiments, as well as on jet data at hadron colliders.

In the regime of asymptotic freedom, the cross section $\sigma_{h_1 h_2 \to X}$ for the production of a final state X in hadron-hadron ($h_1 h_2$) collisions with $\sqrt{s}$ can be factorised into the cross section $\hat{\sigma}_{ab \to X}$ of two partons a and b colliding with the reduced centre-of-mass energy of

$$\sqrt{\hat{s}} = \sqrt{x_1 x_2 s},\qquad(2.2)$$

convoluted with their corresponding PDFs:

$$\sigma_{h_1 h_2 \to X} = \sum_{a,b} \int_0^1 dx_1 \int_0^1 dx_2 f_{a|h_1}\left(x_1, \mu_F^2\right) f_{b|h_2}\left(x_2, \mu_F^2\right) \hat{\sigma}_{ab \to X}\left(m_t, \hat{s}, \alpha_s(\mu_R), \mu_R, \mu_F\right)$$

$$(2.3)$$

The cross sections are integrated over all momentum fractions x_i and summed over all relevant parton types a, b. Thus, the partonic cross section represents the actual hard process at small distances, which is calculated perturbatively, whereas the PDFs include the long-distance effects of the partons inside the hadrons. Both energy regimes are separated by the *factorisation scale* μ_F, on which $\hat{\sigma}_{ab \to X}$ and the PDFs depend. In addition, $\hat{\sigma}_{ab \to X}$ also depends on the renormalisation scale μ_R (see Sec. 2.1.2). As both scales are no fundamental parameters of the SM, being basically arbitrary, the final cross section calculated to all perturbative orders is independent of them. However, at finite orders, residual dependencies remain. Both scales are usually set to the physical energy scale of the process (e.g. in case of $t\bar{t}$ production typically the top-quark mass m_t), which will be referred to as *hard-scattering scale* in the following. A variation of this scale by conventionally a factor of $1/2$ and 2 is supposed to indicate the theoretical uncertainty due to the ignorance of higher orders. In addition, theoretical cross sections contain PDF uncertainties arising from their experimental determination.
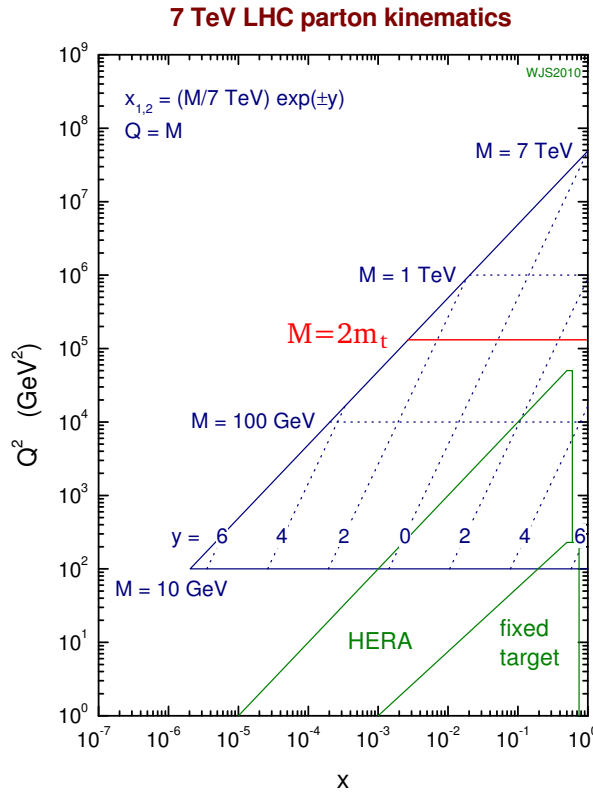
Figure 2.3: The relation between the invariant mass m^X (here denoted M) of a system produced in hadron collisions, its rapidity y and the two parton-momentum fractions x_i (along a constant line of M, there are always two points of the same rapidity magnitude corresponding to x_1 and x_2, respectively). M is here identified with the hard-scattering scale Q of the process. $t\bar{t}$ production at the threshold corresponds to $M = m^{t\bar{t}} = 2m_t = 346\,\text{GeV}$ or $Q^2 = 1.2 \cdot 10^5\,\text{GeV}^2$ as indicated. The kinematic plane (x, Q^2) accessible for the LHC at $\sqrt{s} = 7\,\text{TeV}$ is compared to the one for the ep collider HERA and fixed-target experiments. Taken from [37] and modified.

It is instructive to consider the kinematics of the final state in such collisions. The geometry of colliders implies the decomposition of kinematic vectors into a component longitudinal to the beam direction (z-axis) and transverse to it. The longitudinal momentum p_z is typically expressed by the rapidity y defined as

$$y = \frac{1}{2} \ln \left(\frac{E + p_z}{E - p_z} \right), \tag{2.4}$$

where E is the total energy of the particle (or particle system). Rapidities are preferred as they are additive under Lorentz transformations, so that rapidity differences become Lorentz-invariant. Thus, differential cross sections $\frac{d\sigma}{dy}$ are shape-invariant under Lorentz transformations.

The final-state system X is produced with an invariant mass of $m^X = \sqrt{\hat{s}}$, which is given by Eq. 2.2. Depending on the difference of the momentum fractions of the two colliding partons, x_1 and x_2, the system is boosted longitudinally along the beam direction:

$$y^X = \frac{1}{2} \ln \left(\frac{x_1}{x_2} \right). \tag{2.5}$$

With Eq. 2.2 and Eq. 2.5, the relation between m^X, y^X and the two momentum fractions is given by

$$
\begin{aligned}
x_1 &= \frac{m^X}{\sqrt{s}} e^{+y^X}, \\
x_2 &= \frac{m^X}{\sqrt{s}} e^{-y^X},
\end{aligned}
\tag{2.6}
$$

which is graphically displayed in Fig. 2.3.

Top-quark pairs can be either produced in quark-antiquark ($q\bar{q}$) annihilation or in gluon-gluon (gg) fusion. The corresponding Feynman graphs are shown in Fig. 2.1. The minimum energy for $t\bar{t}$ production is $\sqrt{\hat{s}} = m^{t\bar{t}} = 2m_t \approx 346\,\text{GeV}$ (production threshold). For central production with $y = 0$, both partons have the same $x_1 = x_2 = 2m_t/\sqrt{s}$, which amounts to about 0.2 at the Tevatron and 0.05 at the LHC with 7 TeV. At $x \approx 0.2$, the PDFs of valence quarks dominate as can be seen from Fig. 2.2. In combination with the Tevatron being a $p\bar{p}$ collider, this leads to a $t\bar{t}$ production of 85% via $q\bar{q}$ annihilation and 15% via gg fusion. At the LHC, in contrast, the situation is reversed as the gluon PDFs are clearly dominant at $x \approx 0.05$. The maximum possible rapidity of the $t\bar{t}$ system is reached in very asymmetric collisions with one parton at $x_1 = 1$ and the other one at $x_2 = 0.002$ (at the LHC with 7 TeV) for the production threshold and amounts to $y_{max} = 3$ (see Fig. 2.3). For $t\bar{t}$ production above the threshold, the situation is different. For example, at $m^{t\bar{t}} = 1\,\text{TeV}$, the needed momentum fraction for central production is $x = 0.15$ at the LHC, which is similar to the value for the Tevatron at the threshold. Thus, also the contribution of the

production through $q\bar{q}$ annihilation is larger (but not identical to the Tevatron due to the difference in colliding particles). The maximum rapidity for $m^{t\bar{t}} = 1\,\text{TeV}$ is less with $y_{max} = 2$.
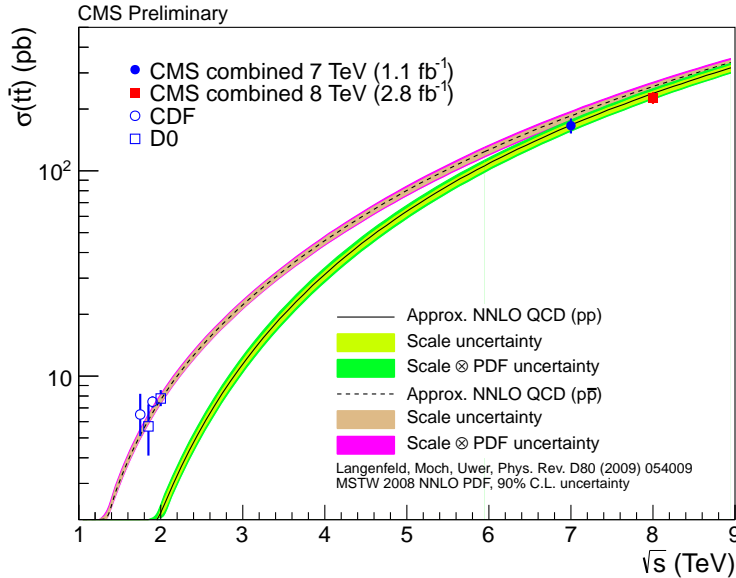
Figure 2.4: The $t\bar{t}$ production cross section in pp and p$\bar{\text{p}}$ collisions as a function of $\sqrt{s}$. Predictions at approximate NNLO are compared to measurements at 7 and 8 TeV by CMS (LHC) and at 1.8 and 1.96 TeV by D0 and CDF (Tevatron). Taken from [38].

The cross sections can be calculated in perturbation theory to different orders in α_s, with increasing precision for higher orders. Very recently, next-to-next-to-leading-order (NNLO) calculations have become available for the inclusive $t\bar{t}$ cross section [39–41]. They include diagrams with the real emission of up to two partons, also referred to as *QCD inital/final state radiation* (ISR/FSR) as shown in Fig. 2.1 *bottom left*, and with up to two virtual loop corrections (Fig. 2.1 *bottom right*). However, in Monte-Carlo event generators (see Sec. 4) only calculations up to next-to-leading order (NLO) are used so far, including diagrams with maximally one emitted parton or loop. For some of the differential cross-section predictions, calculations up to NLO+NNLL (next-to-next-to-leading logarithms) or approximate NNLO are available. They make use of the fact that the dominant higher-order contributions come from soft-gluon radiation, which lead to large logarithmic terms, especially close to the threshold. They can be formally resummed to all orders in perturbation theory up to next-to-next-to-leading logarithms (NNLL). These corrections can be added to fixed-order calculations, giving NLO+NNLL or NNLO+NNLL cross sections [41,42,42]. For approx. NNLO cross sections, the NNLL terms are expanded at fixed order in α_s to NNLO [43,44]. Sometimes, also other subdominant corrections are added.

The inclusive $t\bar{t}$ cross section at the LHC for $\sqrt{s} = 7\,\text{TeV}$ is predicted to $158^{+23}_{-24}\,\text{pb}$ at NLO [45], $163^{+11}_{-10}\,\text{pb}$ at approx. NNLO (using $m_t = 173\,\text{GeV}$ and the MSTW2008 NNLO PDF set [46]) [43] and $172.0^{+6}_{-8}\,\text{pb}$ at NNLO+NNLL (using $m_t = 173.3\,\text{GeV}$ and

MSTW2008 NNLO PDF) [41], including hard-scattering-scale and PDF uncertainties. Fig. 2.4 shows the dependence of the pp and p$\overline{\text{p}}$ cross section on $\sqrt{s}$ as predicted to approximate NNLO precision. This agrees well with measurements at 1.8 and 1.96 TeV by D0 and CDF (Tevatron) and at 7 and 8 TeV by CMS (LHC).
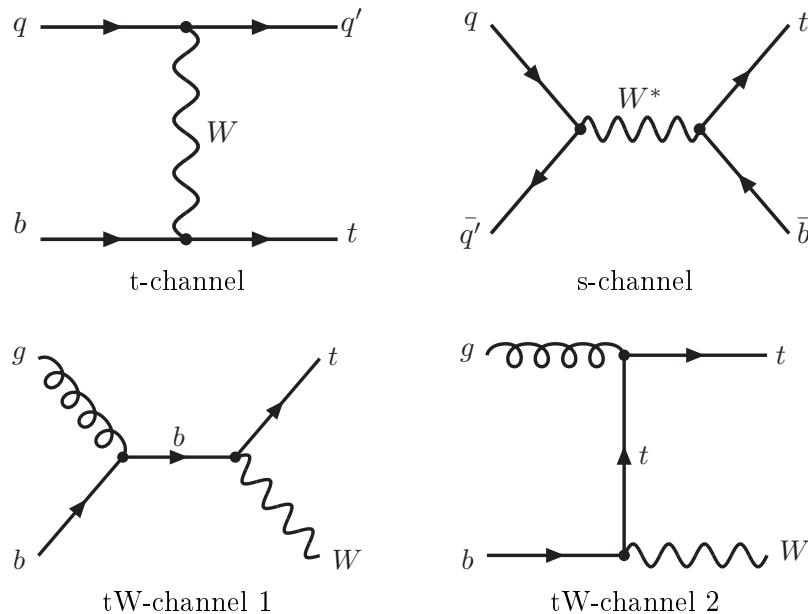
Figure 2.5: Feynman diagrams for single-top-quark production at leading order.

In addition to the production of t$\overline{\text{t}}$ pairs by the strong interaction, single-top quarks can be produced by the electroweak interaction, involving the Wtb vertex (see Fig. 2.5). The dominant production takes place in the t-channel (denoting the virtuality of the W boson), in which the top quark is created by a fusion of a W boson and a b quark. As the u quarks dominate the valence PDFs at a pp collider, the production in this channel is charge-asymmetric with the predicted cross section of top-quark production (41.9 pb) being about twice the one of antitop quarks (22.7 pb) [47]. The situation is similar in the s-channel, in which a W boson creates either a top and an antibottom quark (3.2 pb) or their charge-conjugates (1.4 pb) [48]. The associated production of a top (antitop) quark and a W boson (tW-channel), however, involves a gluon and a b-flavour sea (anti)quark in the initial state and is therefore charge-symmetric with a predicted cross section of 7.9 pb [49] for each charge.

2.2.2 Mass and Decay

Many interesting properties of the top quark derive from the fact that it is the heaviest known particle. Different mass concepts exist such as the pole mass or the $\overline{\text{MS}}$ mass scheme. Typically, the first is quoted, which is theoretically defined by the real part of the complex top-quark propagator. Measurements based on the kinematics of the top-quark decay products are usually identified with the pole mass (although

the exact identity is not completely clear) and constitute the most precise quark mass determinations with $m_t = 173.2 \pm 0.9\,\text{GeV}$ (Tevatron [21]) or $m_t = 173.4 \pm 1.0\,\text{GeV}$ (CMS [22]).

The top quark almost exclusively decays via the electroweak interaction into a W boson and a b quark due to the CKM matrix element $V_{tb} \approx 1$ (see Eq. 2.1). Its large mass has dramatic consequences as it is the only particle that decays into a real W boson, and its decay width is related to the mass via $\Gamma_t \propto m_t^3$. Thus, a very large decay width of $\Gamma_t = 1.3\,\text{GeV}$ is expected, yielding a lifetime $\tau_t \propto 1/\Gamma_t$ of only $5 \cdot 10^{-25}\,\text{s}$. This is about one order of magnitude smaller than the hadronisation time scale of $\tau_{had} \propto 1/\Lambda_{QCD} \approx 3 \cdot 10^{-24}\,\text{s}$. As a result, the top quark decays before it can form bound states with other quarks. This unique feature enables to treat them as bare quarks, whose properties can be calculated almost completely perturbatively. Also, important kinematic and dynamic information of the top quarks is transferred to its decay products without being diluted by hadronisation effects, e.g. spin correlation between the two top quarks in $t\bar{t}$ production.

$t\bar{t}$ Decay Channels
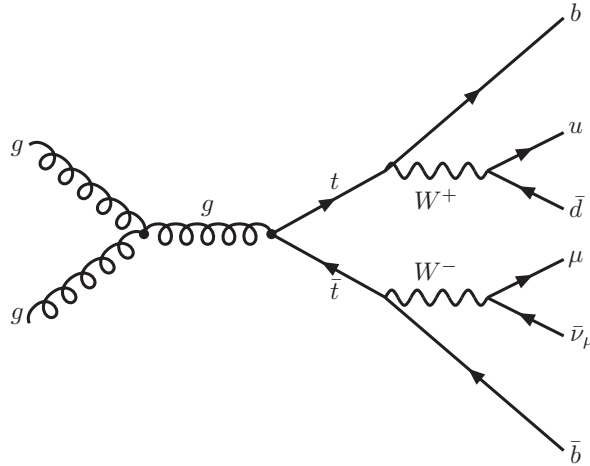
Figure 2.6: Feynman diagram at leading order for $t\bar{t}$ production with subsequent decay into one muon, one neutrino and four quarks (muon+jets channel).

As the top quark decays so fast, its experimental signature is completely determined by its decay products. Strictly speaking, also predictions should include both top-quark production and decay simultaneously. However, despite the large absolute value of the decay width, its relative size Γ_t/m_t is small due to the large mass, which allows factorisation into on-shell top-quark production and subsequent decay (*narrow width approximation*).

Due to the almost exclusive $t \to Wb$ decay, a $t\bar{t}$ event contains two b quarks and two W bosons, which decay further as exemplified in Fig. 2.6. A W boson can decay either into a charged lepton and the corresponding neutrino of one of the three generations

or into a pair of light quarks ($u\bar{d}$, $c\bar{s}$). The decay into quarks of the third generation is kinematically forbidden as their masses are together larger than the W-boson mass. As the quarks have three colour states, there are effectively nine lepton or quark types as possible W-boson decay modes. They are all equally probable (1/9) if the masses of the decay products are neglected as the W boson is much heavier than them. The possible decay modes of a $t\bar{t}$ event, which are characterised by the combination of two W-boson decays, are shown in Tab. 2.2. Three main categories can be distinguished: Events with both W bosons decaying into quarks, which subsequently hadronise into jets (*all-hadronic channel*), with both W bosons decaying into leptons (*dilepton channel*) or with one of them decaying into jets and the other one into leptons (*lepton+jets channel*).

		W^+ boson			
		$u\bar{d}, c\bar{s}$ ($\approx \frac{6}{9}$)	$e^+\nu_e$ ($\approx \frac{1}{9}$)	$\mu^+\nu_\mu$ ($\approx \frac{1}{9}$)	$\tau^+\nu_\tau$ ($\approx \frac{1}{9}$)
W^- boson	$\bar{u}d, \bar{c}s$ ($\approx \frac{6}{9}$)	45.7 %	7.3 %	7.3 %	7.3 %
	$e^-\bar{\nu}_e$ ($\approx \frac{1}{9}$)	7.3 %	1.2 %	1.2 %	1.2 %
	$\mu^-\bar{\nu}_\mu$ ($\approx \frac{1}{9}$)	7.3 %	1.2 %	1.2 %	1.2 %
	$\tau^-\bar{\nu}_\tau$ ($\approx \frac{1}{9}$)	7.3 %	1.2 %	1.2 %	1.2 %

Table 2.2: Overview on $t\bar{t}$-pair decay channels and their branching ratios as characterised by the decay of the two W bosons according to the measured values in [19], assuming lepton universality.

The all-hadronic channel has the largest branching ratio (BR) of 45.7 %, but its signature at hadron colliders suffers from an overwhelming background from QCD multijet events, whose cross section is orders of magnitude higher than the one for $t\bar{t}$ production.

On the contrary, the dilepton channel has the lowest BR of 10.8 % (4.8 % excluding decays into tau-leptons), but also the cleanest signature due to the presence of two leptons, which are easily distinguishable from multijet events. However, the reconstruction of the $t\bar{t}$-event topology, which is vital for differential cross-section measurements as a function of kinematic quantities of the top quark, is complicated by the presence of two neutrinos. These are not measurable in the detector themselves and can be only deduced from a transverse-momentum imbalance of the other particles in the event ($E_\mathrm{T}^\mathrm{miss}$, see Sec. 5.1.7), but it is difficult to disentangle the contributions of each of the neutrinos.

Finally, the lepton+jets (ℓ+jets) channel is a good compromise between a reasonable BR, manageable background and reconstructable $t\bar{t}$-event topology. Therefore, it is the channel of choice in this analysis. In fact, the total BR of 43.8 % is almost as large as the all-hadronic one, adding up the three lepton generations. However, according to common practise, in the following the ℓ + jets channel is restricted to a muon or an electron in the final state, which reduces the BR to 29.2 %. The reason is that τ leptons decay further into neutrinos and either hadrons ($\approx 2/3$ BR) or muons or electrons ($\approx 1/6$ BR each) before reaching the detector, thereby complicating their identification.

As can be seen from Fig. 2.6, the final state at leading order is characterised by one lepton and neutrino from one of the W-boson decays and four jets. Two of these arise from b quarks from the top-quark decay and the other two from light quarks from the W-boson decay. If the $E_{\mathrm{T}}^{\mathrm{miss}}$ is identified with the neutrino transverse momentum, only its longitudinal component is unmeasured. With the help of kinematic constraints, it is possible to reconstruct the $t\bar{t}$-event topology, e.g. using a kinematic fit as described in Sec. 7. Main background processes with similar signatures include W and Z bosons in association with additional jets (W/Z+jets, also referred to as V+jets), single top quarks, QCD multijets and dibosons (WW, WZ, ZZ, also referred to as VV). How the $t\bar{t}$ event is selected and background suppressed is described in detail in Sec. 5.

2.2.3 The Top Quark in the Standard Model and Beyond

The Top Quark in the SM

Every measurement of the properties of the top quark, including its mass, spin, production and decay mechanisms, is a test of the SM. As $t\bar{t}$ pairs are produced in the strong and decay via the electroweak interaction, both can be probed.

On the one hand, $t\bar{t}$-production cross-section measurements, in particular differential ones, are a precise test of QCD at an unprecedented energy scale at the LHC. They offer the unique possibility to study the production of an effectively bare quark in the perturbative regime and to verify the developed calculational methods (see above and also Sec. 4). Also, subtle higher-order effects such as charge asymmetries can be studied. This effect emerges in interferences of different diagrams of the $q\bar{q}$ annihilation at NLO and leads to a correlation in the direction between the incoming quarks and outgoing top quarks. At the $p\bar{p}$ collider Tevatron, it manifests itself as a forward-backward asymmetry, whereas it only leads to a broader rapidity distribution of top quarks compared to antitop quarks at the pp collider LHC, which is further diluted due to the dominant gg production mechanism. In contrast to experiments at the LHC, which observes agreement between measurements and predictions [50, 51], the asymmetry is seen to be significantly larger at the Tevatron than predicted by NLO SM calculations, especially at large $m^{t\bar{t}}$ [52, 53]. This deviation fuels the development of models interpreting this as indications of new physics (see below). In addition, differential and inclusive cross-section measurements are sensitive to QCD parameters such as α_s and PDFs and allow to constrain them in regions so far badly explored, such as gluon PDFs at high x.

On the other hand, the top quark also plays a dominant role in the electroweak sector. Its mass is intriguingly close to the scale of electroweak symmetry breaking with top-quark Yukawa couplings in the order of 1. This means that the SM Higgs boson couples preferentially to top quarks. The main Higgs-boson production mechanism at the LHC is the gluon-gluon fusion via a top-quark loop. Another one involves the associated production of a Higgs boson and a $t\bar{t}$ pair. Moreover, higher-order corrections of SM-parameter calculations are very sensitive to the large top-quark mass. For instance, corrections of the W-boson mass depend quadratically on the top-quark mass

and logarithmically on the Higgs-boson mass, thereby linking these three important SM parameters. Until the recent discovery of the Higgs-like boson, this was used as a way to predict the Higgs-boson mass. Now, the argument is turned around and assuming a Higgs-boson mass of 126 GeV from the recent measurements, the electroweak sector of the SM can be tested for its consistency. For example, Fig. 2.7 shows the predictions of the W-boson and top-quark masses using a fit with all other measured SM parameters as input (with and without assuming the Higgs-boson mass). This prediction and the actual measurements are in good agreement, indicating the consistency of the SM.
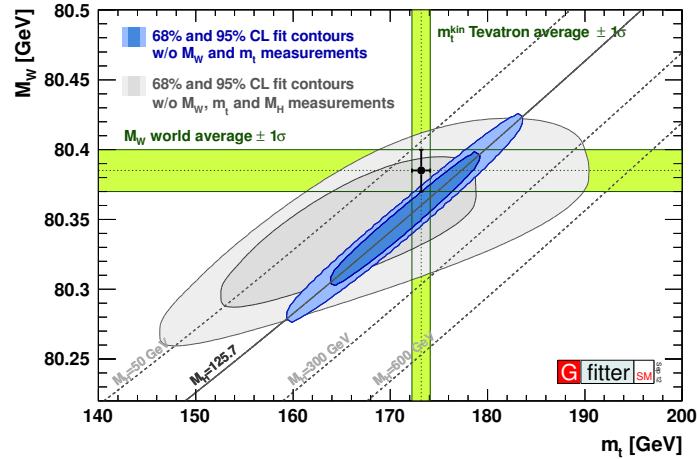
Figure 2.7: The masses of the top quark and the W boson from a SM fit to precision data with (*blue ellipsis*) and without (*grey ellipsis*) assuming the Higgs-boson mass compared to direct measurements (*green bands*). Taken from [54].

The Top Quark Beyond the SM

The SM is a very successful theory but has some limitations as already mentioned. They are addressed by a variety of new theories beyond the SM (BSM), which mostly incorporate the SM as effective low-energy approximation, but predict new phenomena such as heavy unknown particles or interaction mechanisms at higher energies. In the corresponding searches, the top quark often plays an important role. On the one hand, the signatures of new physics can resemble the ones of $t\bar{t}$ events with high-energetic leptons, jets and $E_{\mathrm{T}}^{\mathrm{miss}}$, which therefore become an important background. Differential $t\bar{t}$ cross-section measurements of kinematic distributions can help to constrain it. On the other hand, new physics could manifest itself directly both in the production and the decay of top quarks.

Also in many BSM theories, the top quark plays a special role in electroweak symmetry breaking, either by a large coupling to a BSM Higgs or even by being partly responsible itself for the electroweak symmetry breaking. The latter is proposed e.g. in top-colour [55] or top-colour-assisted technicolour [56] models involving a $t\bar{t}$ condensate or Little Higgs [57] models.

In a variety of theories, new heavy resonances are predicted, which are phenomeno-logically similar to the Z boson. Besides a sequential-SM Z$'$ boson [58], which has the same couplings as the SM Z boson, some models predict a preferred decay into $t\bar{t}$ pairs. Examples include a leptophobic Z$'$ boson predicted by the afore-mentioned top-colour-assisted technicolour model [59,60], axigluons [61] as well as Kaluza-Klein excitations of the graviton [62] and of weak [63] and strong [64] gauge bosons occurring in extra-dimensional models [65,66]. Such neutral bosons could manifest themselves prominently in the $t\bar{t}$-invariant-mass distribution as a narrow resonance, which would also alter other distributions such as top-quark p_{T}. However, some models rather predict a modification of the $t\bar{t}$-invariant-mass and other distributions in a broader range, such as high-scale new physics described by effective field theories [67]. Many of these models also provide a possible explanation for the observed Tevatron $t\bar{t}$ charge asymmetry mentioned above [68,69].

Also in supersymmetric extensions of the SM (SUSY) [70], the top quark and its supersymmetric scalar partner (stop) might play an important role. In many scenarios, the supersymmetric partners of the third-generation quarks are lighter than those of the first generations and thus might be the only ones accessible at the LHC. If the stop quark is not much heavier than the top quark, it could mitigate quadratically divergent contributions to the Higgs-boson mass dominated by virtual top-quark loops. A stop quark could decay into a top quark and a neutral lightest supersymmetric particle, such that the signature of a pair-produced stop-antistop quark would resemble $t\bar{t} + E_{\mathrm{T}}^{\mathrm{miss}}$. However, in some scenarios, the stop-quark mass is very similar to the one of the top quark and would manifest itself only in deviations of kinematic distributions sensitive to the spin [71]. Another feature of SUSY is the prediction of a charged Higgs boson, into which the top quark could decay instead of a W boson.

Chapter 3

Experimental Setup - Collider and Detector

Besides the study of naturally occurring particle interactions from sources such as cosmic rays and radioactive decays, the controlled collision of particles at research laboratories constitutes the main experimental technique in elementary particle physics. Typically electrons or protons, but also heavy ions are accelerated to high energies and brought to collision at a defined interaction point. Large and sophisticated particle-detector systems measure the properties of the collision products. This analysis is based on proton-proton collision data recorded by the Compact Muon Solenoid (CMS) [72,73] experiment at the Large Hadron Collider (LHC) [74] in 2011, which are described in the following.

3.1   The Large Hadron Collider

The LHC is a circular collider for protons and heavy ions with a circumference of 26.7 km operated by the European Organisation for Nuclear Research (CERN[1]). With centre-of-mass energies for proton-proton collisions of 7 TeV in 2010 and 2011, 8 TeV in 2012 and an envisaged design energy of 14 TeV, it is the world's most powerful accelerator. The particle beams counter-rotate in two evacuated beam pipes. They are guided and focused by superconducting dipole and quadrupole magnets with fields as high as 8 T. The acceleration is performed using superconducting radio-frequency cavities. The superconductivity necessitates a cooling down to 1.9 K with liquid helium.

Before being injected into the LHC, the particles are pre-accelerated in several steps; first in different linear accelerators (LINAC), then in the Proton Synchrotron (PS) to 25 GeV and finally in the Super Proton Synchrotron (SPS) to 450 GeV (see Fig. 3.1). The pre-accelerators are also used for different purposes such as other particle-physics experiments, test beams or irradiation of detector material for radiation-hardness studies as explained in Sec. 13.2. Finally, the protons or heavy ions are brought to collision

---

[1]Formerly called Conseil Européen pour la Recherche Nucléaire.
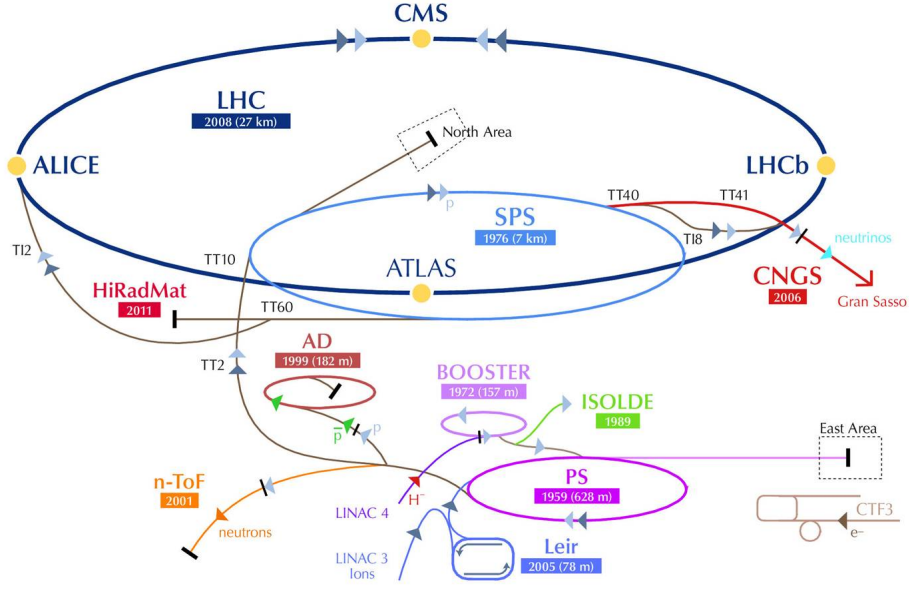
Figure 3.1: The CERN accelerator complex including the four major experiments at the LHC. Taken from [75].

at four interaction points surrounded by particle detectors. These include the two multi-purpose detectors ATLAS [76] and CMS, which are designed for a variety of SM physics measurements as well as searches for the Higgs boson and physics beyond the SM, LHCb [77] optimised for the study of hadrons from b quarks and ALICE [78] specialised on heavy-ion collisions and the study of quark-gluon plasma. LHCf [79] and TOTEM [80] are smaller-size experiments dedicated to forward physics and measuring the total inelastic cross section. CMS is explained in more detail below.

The rate dN/dt of produced events depends on the process-specific cross section σ as well as on the *instantaneous luminosity* $\mathcal{L}$, which depends on collider conditions:

$$\frac{dN}{dt} = \mathcal{L} \cdot \sigma. \tag{3.1}$$

To obtain the total number of events N, this equation needs to be integrated over time, motivating the definition of the *integrated luminosity* $L = \int \mathcal{L} dt$.

The instantaneous luminosity is related to the beam and collision parameters via

$$\mathcal{L} = \frac{N_b N_p^2 f}{A}, \tag{3.2}$$

where N_b is the number of bunches in a beam, N_p the number of protons in a bunch, f the revolution frequency and A the effective width of the beam transverse to the beam direction. The latter depends on the beam focus, the bunch size and the beam crossing angle.

The revolution frequency amounts to about 11 kHz. The other parameters are

tunable. The LHC is designed to run at $\mathcal{L} = 10^{34} \mathrm{cm}^{-2}\mathrm{s}^{-1}$ with $1.15 \cdot 10^{11}$ protons per bunch and 2808 bunches per beam, separated by 25 ns (40 MHz bunch crossing rate). In 2011, a maximum of $4 \cdot 10^{33} \mathrm{cm}^{-2}\mathrm{s}^{-1}$ was reached with $1.5 \cdot 10^{11}$ protons per bunch (larger than design) and 1380 bunches per beam with a separation of 50 ns [81]. Fig. 3.2 shows the evolution of the instantaneous and integrated luminosity during 2011. $\mathcal{L}$ increased significantly by more than one order of magnitude from March to the end of the run in October. In total, an integrated luminosity of 6.1 fb^{-1} was delivered to CMS, out of which 5.6 fb^{-1} were recorded. In 2012, 23.3 fb^{-1} (21.8 fb^{-1}) were delivered to (recorded by) CMS with a maximum instantaneous luminosity of $7.7 \cdot 10^{33}$ cm^{-2}s^{-1} [82].
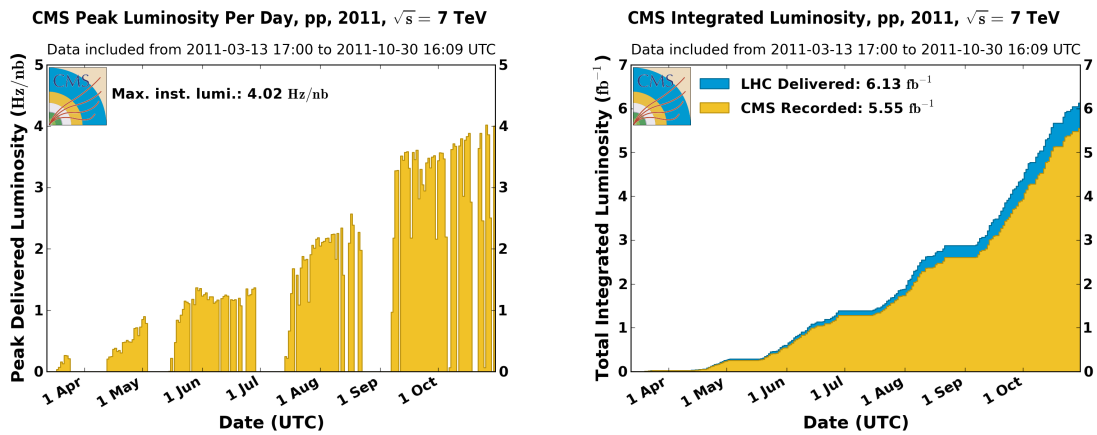
Figure 3.2: The evolution of the instantaneous luminosity (*left*) and the integrated luminosity (*right*) delivered by the LHC (*blue*) and recorded by CMS (*orange*) in 2011. 1 Hz/nb corresponds to 10^{33} cm^{-2}s^{-1}. Taken from [82].

3.2   The Compact Muon Solenoid Detector

The CMS experiment [72, 73] is one of the two multipurpose experiments at the LHC located in a cavern about 100 m underground around one of the interaction points. An overview is shown in Fig. 3.3, exhibiting the typical cylindrical onion-like structure of most particle detectors at colliders with a tracking system in the centre, surrounded by calorimeters and muon detectors, all in a magnetic field. Its specific design is driven by the operation conditions and physics goals mentioned above, which require a good electron, muon and photon identification, a good momentum, photon-energy and vertex resolution as well as a large geometrical coverage for a good $E_{\mathrm{T}}^{\mathrm{miss}}$ resolution. The main features of CMS include an all-silicon inner-tracking system in combination with a superconducting solenoidal magnet providing a high field of 3.8 T parallel to the beam line, as well as a high-resolution electromagnetic calorimeter of scintillating crystals. As the coil of a strong magnet implies a lot of absorbing material, it is beneficial to place both the inner tracker and the main parts of the calorimeters inside the coil. Thus, although CMS has a large weight of 12,500 t, it is relatively "compact"

(compared to e.g. ATLAS) with a length of 21.6 m and a diameter of 14.6 m. A more detailed description of the individual subdetectors is given below.
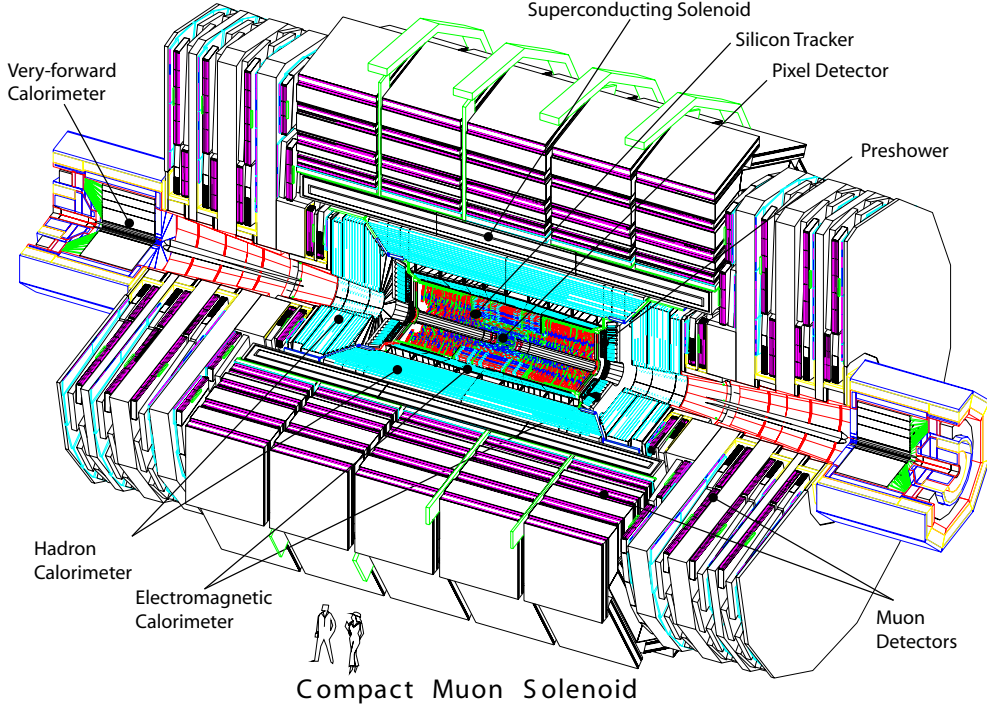
Figure 3.3: Perspective view of the CMS detector with its subsystems. Taken from [73].

CMS uses a right-handed coordinate system with its origin at the nominal interaction point in the centre of the detector. The x axis points towards the centre of the LHC ring, the y axis upwards and the z axis along the anti-clockwise beam direction. The symmetry of the detector and the collisions suggest the introduction of spherical coordinates with an azimuthal angle Φ defined with respect to the x axis in the x-y plane and a polar angle θ with respect to the z axis. Instead of θ, the pseudorapidity $\eta = -\ln\left(\tan\frac{\theta}{2}\right)$ is preferentially used as it is equal to the rapidity y (see Eq. 2.4 in Sec. 2.2.1) in the massless limit. The angular distance between two particles is usually expressed in η-Φ space as $\Delta R = \sqrt{\Delta\Phi^2 + \Delta\eta^2}$.

3.2.1 Inner Tracking System

For the direction, momentum and charge-sign measurement of charged particles as well as vertex reconstruction, a precise tracking system is needed that samples a number of detector hits along the trajectory of the particle. Usually, gas or semiconductors are used as sensitive material, in which a traversing ionising particle generates a current signal that is readout electronically.

The transverse momentum p_T is extracted from the bending of the trajectory in a magnetic field with a relative resolution of
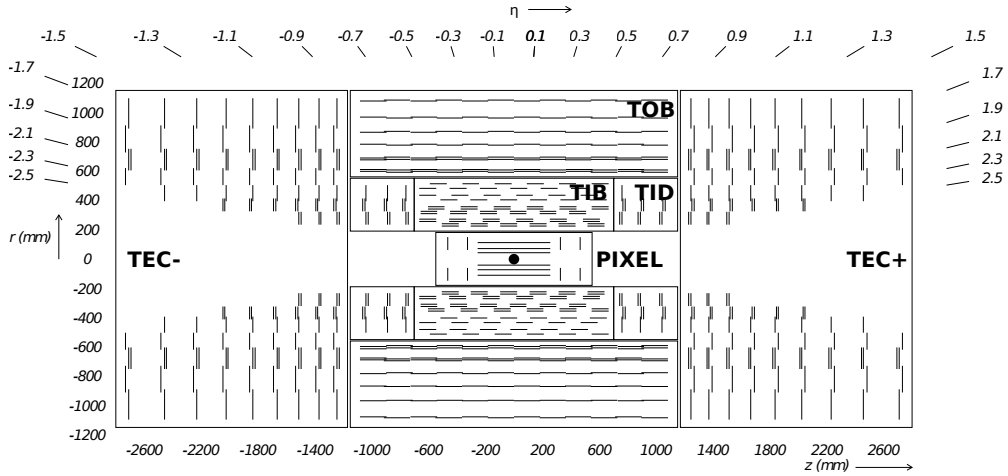
Figure 3.4: Sketch of the CMS silicon tracking system with its subsystems as described in the text. The lines represent the individual pixel- and strip-sensor modules. Stereo modules are indicated with a double line. Taken from [73].

$$\frac{\sigma(p_{\mathrm{T}})}{p_{\mathrm{T}}} = \frac{\sigma_x p_{\mathrm{T}}}{0.3 QBL^2} \sqrt{\frac{720}{N+4}} \oplus \sigma_{MS,rel}, \tag{3.3}$$

where $\oplus$ refers to addition in quadrature and Q is the particle charge (p_{T} in [GeV], otherwise SI units) [19, 83]. From the first term, which is linear in p_{T}, it can be seen that it is beneficial to have a good spatial hit resolution σ_x, a large magnetic field B, a large tracker length L and a large number of hits N (assumed to be equidistant here, valid for about $N \geq 10$). The second term $\sigma_{MS,rel}$ derives from multiple scattering, which depends on the amount of material in units of radiation length[2] x/X_0. $\sigma_{MS,rel}$ is independent of p_{T} and hence the dominating term at low p_{T} ($\lesssim 10\,\mathrm{GeV}$ at CMS). For a good impact-parameter and vertex resolution, it is additionally required to measure as close as possible to the interaction point.

Other aspects that need to be taken into account for the design of the tracker are a high track multiplicity of about 1000 particles per bunch crossing at the design luminosity and energy, the high bunch-crossing rate and a high radiation level due to the large particle flux traversing the detector, especially close to the interaction point. As a result, the semiconductor silicon was chosen as detector material for the inner tracking system because it can be used to build finely-segmented sensors with high resolution, fast response and readout and sufficient radiation hardness. The latter aspect is discussed and studied in detail in the second part of this thesis (Sec. 11ff.), where also more information on the principles of silicon detectors is given. A system for cooling down to $-10°\mathrm{C}$ is needed to limit noise due to radiation-induced leakage

---

[2]The radiation length X_0 is defined as the mean distance inside a material after which the energy of an electron is reduced to $1/e$ of its original energy due to bremsstrahlung. It also corresponds to $7/9$ of the mean free path of a photon for e^+e^--pair production.

current.

The CMS detector has the largest silicon tracker of all particle physics experiments to date with a sensitive area of about $200\,\mathrm{m}^2$. It has a length of $5.8\,\mathrm{m}$ with a radius of $1.1\,\mathrm{m}$ and covers the range up to $|\eta| = 2.5$ An overview is given in Fig. 3.4. The tracker is divided into different parts, taking the decrease of particle flux from the interaction point outwards into account.

Pixel Tracker

The region closest to the interaction point is subject to the largest track density. To keep the sensor-cell occupancy at a level of 10^{-4} and obtain an unambiguous space-point measurement, pixel detectors are chosen with a cell size of $100 \times 150\ \mu\mathrm{m}^2$. In total, there are 1,440 modules with 66 million pixels. They are arranged in three cylindrical barrel layers with radial distances of 4.4, 7.3 and $10.2\,\mathrm{cm}$ to the beam line and two endcap discs at each side of the barrel. With a high hit efficiency well above 99%, the pixel detector typically measures three hits for $|\eta| < 2.2$ and two hits for $2.2 < |\eta| < 2.5$. The spatial hit resolution is measured to be about $10\ \mu\mathrm{m}$ along the short pixel edge ($r\Phi$ in the barrel) and 20 to $45\ \mu\mathrm{m}$ along the long pixel edge (z in the barrel), depending on the incidence angle [84].

Strip Tracker

To reduce the number of readout channels and hence the amount of material, power consumption, cost and data volume, silicon strip detectors are employed at larger radii of 20 to $116\,\mathrm{cm}$, where the smaller track density permits a larger cell size. The strip tracker consists of 15,148 strip modules with about 10 million readout channels and is further subdivided into different parts. The Tracker Inner Barrel and Discs (TIB/TID) are composed of four barrel layers with strips parallel to the beam line and three endcap discs at each side with radial strips. The strips have a pitch of 80 to $141\ \mu\mathrm{m}$, a length of $10\,\mathrm{cm}$ and a sensor thickness of $320\ \mu\mathrm{m}$, resulting in an occupancy of 2 to 3% and an $r\Phi$ resolution of 16 to $27\ \mu\mathrm{m}$ in the barrel [84]. The Tracker Outer Barrel (TOB) with six layers and the Tracker Endcaps (TEC) with nine discs at each side use strips with 97 to $184\ \mu\mathrm{m}$ pitch, $25\,\mathrm{cm}$ length and 320 to $500\ \mu\mathrm{m}$ sensor thickness. This leads to an occupancy at the percent level and an $r\Phi$ resolution of 25 to $41\ \mu\mathrm{m}$ in the barrel [85]. Some of the inner layers of all strip tracker subdivisions have an additional module mounted back-to-back on the first one under a stereo angle of $100\,\mathrm{mrad}$, thereby providing also a position measurement in the direction along the strips (z in the barrel, r in the endcaps). The resulting z resolution is $230\ \mu\mathrm{m}$ in TIB and $530\ \mu\mathrm{m}$ in TOB [73].

The design and performance of the tracker provide a p_T resolution at the percent level for tracks up to $100\,\mathrm{GeV}$ [73], a transverse impact parameter resolution of better than $30\ \mu\mathrm{m}$ for central tracks with $p_\mathrm{T} > 5\,\mathrm{GeV}$ and a primary vertex resolution of better than $30\ \mu\mathrm{m}$ for vertices with at least 30 tracks [86].

3.2.2 Electromagnetic Calorimeter

The electromagnetic calorimeter (ECAL) surrounds the tracker and is intended to measure the energy and position of mainly electrons and photons, which induce electromagnetic showers in the material. Also here the design is driven by the requirements of a fast, radiation-hard and high-resolution detector, which is vital for the measurement of the Higgs boson decaying into two photons. In addition, a high-density material is needed to fit into the limited space within the solenoid. As a result, the ECAL is made of lead tungstate ($PbWO_4$) crystals, which act both as absorbers with a short radiation length ($X_0 = 0.89$ cm) and as scintillators with a fast decay (80% of the light is emitted within 25 ns). The scintillation light with wavelengths around 420 nm is detected by avalanche photodiodes (APD) in the barrel and vacuum phototriodes in the endcaps.

The ECAL barrel (EB) is located at a distance of 1.3 m from the beam pipe and covers the region up to $|\eta| < 1.479$. It is equipped with 61,200 crystals with a high granularity of 0.0174×0.0174 in η-Φ corresponding to 22×22 mm^2 at the front face. The length of 230 mm corresponds to $25.8\,X_0$. They are slightly tilted by 3° with respect to the direction towards the interaction point to avoid particles passing through the cracks of the crystals.

The ECAL endcaps (EE), one at each side of the barrel, extend the geometrical coverage to $|\eta| < 3.0$. The 7324 crystals have a front-face cross section of 28.6×28.6 mm^2 and a length of 220 mm corresponding to $24.7\,X_0$ and are also slightly tilted. In front of each EE disc, a preshower detector covers the region $1.653 < |\eta| < 2.6$. It is a two-layer sampling calorimeter consisting of lead as absorber with a total of $3\,X_0$ and silicon strip sensors. Its high spatial resolution improves the discrimination between a neutral pion decaying into two photons and a single photon.

The performance of the ECAL has been studied in test beams. The relative energy resolution for electrons is measured as

$$\frac{\sigma(E)}{E} = \frac{2.8\%}{\sqrt{E/\text{GeV}}} \oplus \frac{12\%}{E/\text{GeV}} \oplus 0.3\%. \tag{3.4}$$

The first term arises from stochastic effects due to fluctuations in the lateral shower containment, photostatistics and preshower energy deposition, the second term comes from noise and the third constant term from non-uniformity of the longitudinal light collection, intercalibration errors and energy leakage from the back.

Thus, the relative resolution is found to be better than 0.5% for electrons with $p_\text{T} > 50$ GeV.

3.2.3 Hadronic Calorimeter

The hadronic calorimeter (HCAL) is a sampling calorimeter intended to measure the energy and position of charged and neutral hadrons. Its design is driven by space restrictions between the ECAL and the solenoid.

The barrel (HB, $|\eta| < 1.3$) and endcaps (HE, $1.3 < |\eta| < 3.0$) are mainly composed of non-magnetic brass with an interaction length[3] of $\Lambda_I = 16.4\,\mathrm{cm}$ (the first and last layer is made of steel), interspersed with plastic scintillator tiles. They are readout via wavelength-shifting fibres connected to hybrid photodiodes (HPD). The calorimeter is segmented and arranged in towers of 0.087×0.087 in η-Φ (0.17×0.17 for $|\eta| \geq 1.6$), whose axes point to the interaction point. One tower matches to 5×5 ECAL crystals. Whereas the HE has a sufficient depth of about $10\,\Lambda_I$, the HB is restricted by available space to only $5.8\,\Lambda_I$ for $|\eta| = 0$ (plus a contribution of about $1\,\Lambda_I$ from the ECAL). Thus, the barrel is complemented by the outer calorimeter (HO) outside the solenoid, which extends the depth to at least $11.8\,\Lambda_I$. It uses the solenoid itself and partly additional steel as absorber in combination with additional scintillator layers.

The forward calorimeter (HF) is placed at $z = \pm 11.2\,\mathrm{m}$ and extends the coverage up to $|\eta| = 5.2$. The high particle flux in this region requires radiation-hard materials. Thus, Cherenkov-light-emitting quartz fibres are chosen as active material. Together with steel as absorber, they are arranged in towers of 0.175×0.175 in η-Φ. To compensate the missing ECAL in this region, quartz fibres of different lengths are used to identify early-showering electrons and photons.

The performance of the HCAL has been studied in test-beam data. For a $50\,\mathrm{GeV}$ jet, a relative energy resolution from the combined ECAL and HCAL system of 15 to 20% is obtained. However, the particle-flow object-reconstruction framework employed at CMS greatly improves the resolution to a few percent for large parts of the phase space by combining the information from all CMS subdetector systems (see Sec. 5).

3.2.4 Muon System

Muons are typically considered as minimum-ionising particles (except at high energies) and traverse the tracker and calorimeters without significant energy loss in contrast to other particle types. Thus, they can be efficiently identified by dedicated muon detectors outside the calorimeters, which also provide an additional momentum measurement. Their signature often provides a good signal-to-background discrimination and is hence heavily used in many analyses and for triggering (see below).

The muon system is shown in Fig. 3.5. It is embedded into the return yoke of the solenoid. Due to the needed large area coverage at radii from 4 to 7 m, gaseous detectors are chosen. Different technologies are used as the conditions vary with pseudorapidity.

In the barrel region with a low particle flux and a homogeneous magnetic field, four layers (called stations) of drift tube chambers (DT) are installed, which extend up to $|\eta| = 1.2$. Each station has tubes aligned along the beam line, measuring in $r\Phi$, and the first three also perform a measurement in the perpendicular z direction. The endcap discs ranging from $|\eta| = 0.9$ to 2.4 are equipped with four stations of cathode-strip chambers (CSC), which can cope better with the higher particle flux and the stronger and less homogeneous magnetic field in this region. CSCs work as

---

[3]The interaction length Λ_I is defined as the mean free path of a hadron before undergoing an inelastic nuclear interaction.
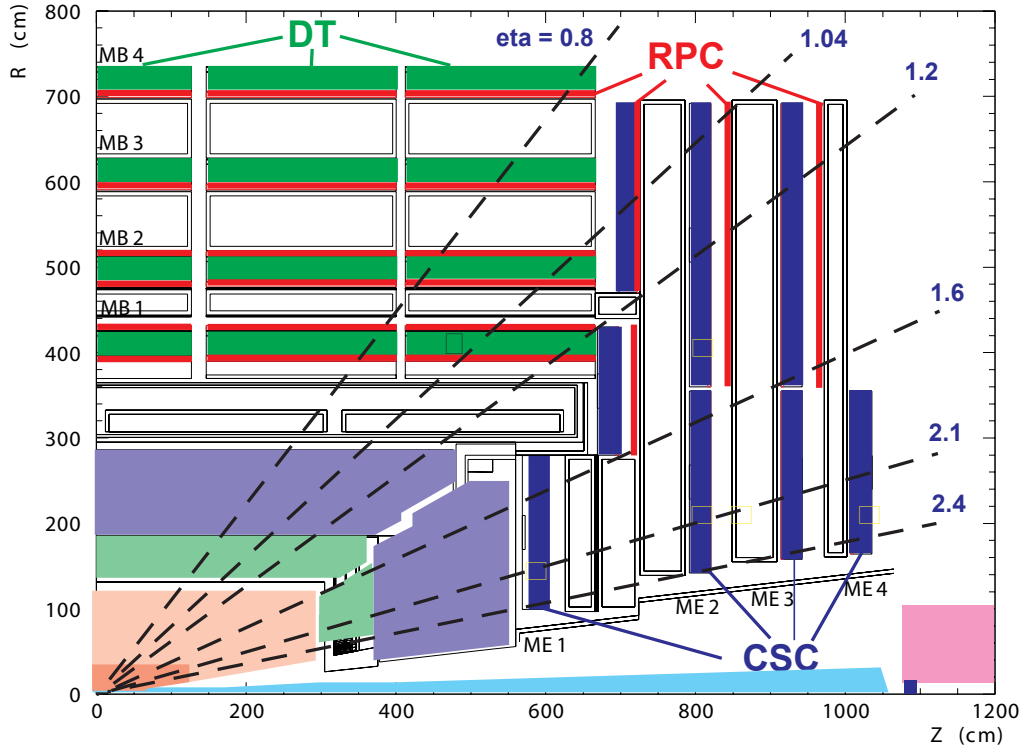
Figure 3.5: Sketch of the muon system subdetectors for a quarter of the CMS detector in an r-z view. Taken from [73].

multi-wire proportional chambers. Cathode strips running radially with respect to the beam line and wires perpendicular to these strips provide measurements in $r\Phi$ and η, respectively. Both the DTs in the barrel and the CSCs in the endcaps up to $|\eta| = 1.6$ are complemented by resistive plate chambers (RPC), which consist of a gas-filled gap between two plates with high resistivity and are operated in avalanche mode. They provide good timing information, but a less precise position determination than the other systems. Thus, they are mainly used to improve the bunch-crossing assignment and for trigger purposes.

The relative p_T resolution of the muon system alone is about 10 to 20% in the central part up to about 1 TeV. For a precise momentum determination, a combined track is formed from hits in the inner tracking detector and muon system (see Sec. 5.1.3), resulting in a p_T resolution of about 1 to 2% in the barrel [87] between 20 and 100 GeV. At high p_T, the muon system significantly contributes with its large lever arm, keeping the resolution below 10%.

3.2.5 Trigger System and Data Acquisition

Due to the high granularity and large numbers of readout channels of the CMS detector, the data size of one event is about 1 MB. In combination with the large bunch-crossing

rate of nominally 40 MHz (20 MHz to date), the amount of produced data exceeds the one that can be stored and analysed in detail by far. A rate suppression by more than five orders of magnitude to 100 to 300 Hz is needed and achieved by the *trigger* system. Its task is the fast and efficient online selection of potentially interesting events that are intended to be analysed offline. It works in two steps. For certain objects used in this analysis, a more detailed description of the online reconstruction is also given in Sec. 5.

First, the rate is reduced to about 100 kHz by the hardware-based *level-1 (L1) trigger* step. The time for a decision is limited to 3 μs per event, during which the data is stored temporarily in data pipelines. Only information from the calorimeters and the muon system with a reduced granularity can be processed fast enough. Track reconstruction in the inner tracking system is too time-consuming. From this, primitive particle candidates and global energy sums are reconstructed with simplified algorithms. This is done first locally and regionally in the individual detector systems (global calorimeter and global muon trigger) and subsequently merged in the global trigger. Finally, an event is selected for further processing if certain thresholds are passed, e.g. related to p_T, η or object-identification criteria.

In a next step, the selected data is processed by the *high-level trigger (HLT)*. As it is software based and information from all subsystems can be analysed with more sophisticated algorithms, it is already similar to the offline reconstruction and selection. However, also here the time is limited to 50 ms per event, so that time-consuming algorithms such as track reconstruction are only performed in interesting regions. The event is finally recorded for offline analysis if the requirements of at least one trigger path are met.

As shown in Fig. 3.2, the instantaneous luminosity increased significantly during 2011, and along with it the event rate. To keep the total trigger rate constant, different techniques are possible. Ideal would be to find improved trigger algorithms with a higher background suppression at a constant efficiency. Alternatively, the trigger thresholds can be raised or additional identification criteria can be introduced, which mostly leads to a reduced signal acceptance or efficiency. Also, completely new trigger paths can be created by combining e.g. single-lepton and jet trigger paths. If triggers with certain thresholds but too high rates are wished to be kept for dedicated purposes, they can be recorded with a *prescale n* such that only every *n*-th event fulfilling the trigger requirement is stored.

3.2.6   Luminosity Measurement

According to Eq. 3.1, the instantaneous luminosity can be obtained by measuring the rate of a process with a precisely known cross section or other parameters that are correlated with the luminosity.

For online luminosity monitoring at CMS, the HF calorimeter is used [88]. Either the *zero-counting* method is applied, which measures the average fraction of empty HF towers, or the average transverse energy per tower is measured.

Also for offline luminosity determination, different methods are available, which are based on rate measurements in the HF or tracker. The luminosity used for this analysis was obtained with the *pixel-cluster-counting* method, which measures the number of clusters in the pixel system per bunch crossing [89].

In all cases, the absolute luminosity calibration is performed with *Van-der-Meer* separation scans [90]. The rate corresponding to the methods above is measured as a function of transverse beam separation, which allows to determine the effective beam profile. Together with measurements of the beam currents giving the number of protons per bunch, this is used to calculate the absolute luminosity according to Eq. 3.2.

Chapter 4

Event Simulation

The prediction of the outcome of experiments is an important task in developing, validating or falsifying theoretical models. In Sec. 2.2.1 the theoretical framework for the calculation of cross sections at hadron colliders using PDFs and partonic cross sections was introduced. However, between the production of particles in a hard-scattering collision described at limited perturbative orders and the actual measurement of signals in a detector, the particle objects evolve through parton showering, hadronisation, decay and interaction with the detector material, as illustrated in Fig. 4.1. The single steps are explained in detail below. This complete chain of evolution of a collision event is simulated numerically with the help of Monte-Carlo (MC) event generators, utilising random numbers. The resulting output has the same format as recorded events in real data, so that the whole data analysis can be performed equally on simulated events. In fact, the simulation is often used to design and optimise the analysis strategy such as the event selection. After a thorough validation that the simulation gives reliable results, e.g. by data-to-simulation comparisons of control distributions, the simulation can be also used to correct the data to one of the intermediate levels in Fig. 4.1. For example, it is used to estimate reconstruction and selection efficiencies. Also, the background contamination of a selected sample can be estimated from the simulation.

4.1 Simulation Chain and Event Generators

An overview on the different simulation steps is given in the following. Some event generators cover the whole chain up to the hadronisation step, e.g. PYTHIA [93] and HERWIG [94], whereas others are specialised to only parts of it.

4.1.1 Hard Scattering

As first step, the hard scattering is simulated based on the factorisation into PDFs and the partonic matrix element (ME), which is calculated perturbatively. The multi-purpose event generators PYTHIA and HERWIG can only calculate $2 \rightarrow 2$ matrix elements at LO, i.e. with two initial- and two final-state partons. In contrast, the gen-
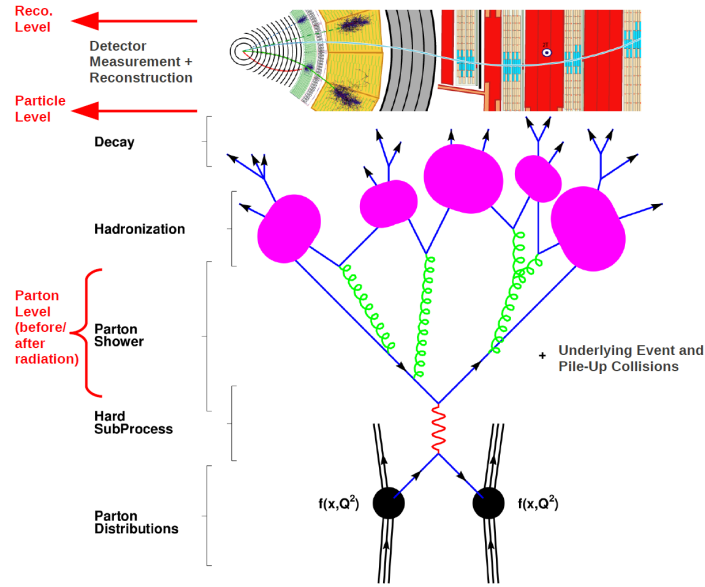
Figure 4.1: Object-evolution levels, corresponding to the different steps of event simulation. Taken from [91, 92] and modified.

erators MC@NLO [95] and POWHEG [96,97] calculate $2 \rightarrow 2$ matrix elements at NLO, i.e. they take Feynman diagrams with one loop (virtual radiation) or one additionally emitted parton (real initial- or final-state radiation (ISR/FSR)) into account. Moreover, so-called *multi-leg* generators can simulate processes at tree-level including real emission of further partons (but without the inclusion of virtual radiation in loops). For example, MADGRAPH [98,99] can simulate $2 \rightarrow n$ processes, with n up to 9. This technique is beneficial for processes, for which a large amount of hard ISR/FSR is expected, such as for $t\bar{t}$ production or its dominant backgrounds W/Z+jets.

The object-evolution level after this step is referred to as *ME* or *parton level before radiation*.

4.1.2 Parton Showering and Matching

As explained above, the simulation of the hard scattering results in a limited number of partons in the final state due to the limited order of perturbation theory applied. Higher-order corrections including additional ISR/FSR from the branching of the partons are approximated by the *parton-shower* (PS) concept, which is assumed to be universal and hence can be applied to all QCD processes. It involves the evolution of the partons created at the high energy scale of the hard scattering down to lower scales, until finally $\alpha_s \approx 1$ at about $1\,\text{GeV}$, where the non-perturbative hadronisation starts (see below). The evolution is mathematically described by the *DGLAP* equations [100–102]. Parton-showering algorithms are included in the multi-purpose event generators PYTHIA and HERWIG with different implementations, e.g. different ordering of the evolution scale (transverse-momentum-ordered and angular-ordered,

respectively). Via an interface, they can be also used in case the hard scattering is simulated by the other specialised generators mentioned above. If the hard-scattering generators themselves are used to simulate, at least partly, hard additional radiation, special care needs to be applied. A matching between the hard-scattering generator and the parton shower has to be performed such that double counting of parton emission in the same phase-space region is avoided. To achieve this, MADGRAPH uses the k_T MLM algorithm [103], which vetoes the emission of partons via showering above a user-defined matching threshold. On the contrary, POWHEG and MC@NLO use two different subtraction schemes.

The object-evolution level after this step is referred to as *parton level after radiation*.

4.1.3   Hadronisation

Having evolved to an energy scale of about 1 GeV, hadronisation into colourless baryons or mesons begins. The corresponding models are phenomenological and have to be tuned to measurements. The same generators used for parton showering are also utilised for hadronisation, i.e. either PYTHIA or HERWIG, which employ completely different models.

In PYTHIA, the *Lund string model* is applied to describe the fragmentation of the partons after showering. It is based on the assumption that the colour potential between two partons increases linearly with their separation for distances larger than about 1 fm, leading to colour-field strings between them. At a certain distance threshold, it becomes energetically beneficial to create a q$\bar{\text{q}}$ pair from the string energy, which breaks the string into two separate colour-singlet parts. After possibly several iterations, on-shell hadrons form from the remaining groups of colour-connected partons.

In contrast, in the *cluster model*, which is used in HERWIG, all gluons are first split into q$\bar{\text{q}}$ pairs, before quarks that are close to each other in phase space are grouped to colourless clusters. After potentially splitting heavy clusters to lighter ones, the remaining light clusters finally decay isotropically in their rest frames into pairs of hadrons.

In addition, the decay of short-lived particle resonances is simulated by the generators.

The object-evolution level after this step is referred to as *hadron* or *particle level*.

4.1.4   Underlying Event and Pile-Up

The partons initiating the hard interaction are accompanied by the other constituents of the colliding hadrons, which form so-called beam remnants. These are coloured and therefore hadronise as well, providing additional particles in the final state. Furthermore, the partons of the beam remnants might also interact with each other, leading to multiple-parton-interactions. All these effects not deriving from the primary hard interaction are collectively referred to as *underlying event* (UE) and need to be described

by phenomenological models in HERWIG and PYTHIA tuned to data. In this analysis, the PYTHIA Z2 tune is used [104]. Moreover, at high luminosities, multiple-hadron interactions called *pile-up* (PU) occur. They can be described completely independently from each other and are simulated with PYTHIA.

4.1.5 Detector Simulation

After the simulation of the collision and its subsequent evolution, it is of paramount interest how such an event is actually measured by the detector. Only a detailed simulation of the geometry of the detector including its magnetic field, the interaction of the particles with this material (both dead and active sensor components) and the complete electronic readout chain allows a direct comparison between events from the simulation and real data. A full simulation of the CMS detector is implemented using the GEANT4 software package (v. 9.4) [105,106]. A good agreement between simulation and data is observed and residual deviations are corrected.

The object-evolution level after this step is referred to as *reconstruction level*.

4.2 Simulated Samples

The simulated MC samples used in this analysis are generated in the course of the *Fall11* CMS MC production. An overview is given in Tab. 4.1. Some more details, in particular concerning the used generator setups, can be found in [107].

At hard-scattering level, events with top-quark pairs with up to three additional partons as well as the production of W and Z bosons[1] with up to four additional partons are simulated with MADGRAPH (v. 5.1.1). For the determination of certain systematic uncertainties and for comparison to the final results, $t\bar{t}$ events are additionally simulated with POWHEG (v. 1.0) and MC@NLO (v. 3.41). POWHEG is also used to generate single-top and single-antitop-quark events in the s, t and tW channels. Events with two vector bosons (WW, WZ, ZZ) are simulated[2] with PYTHIA (v. 6.424), as well as QCD-multijet production. For the muon channel, multijet events with $\hat{p}_T > 20$ GeV and a preselection of at least one muon with $p_T^\mu > 15$ GeV are simulated[3]. For the electron channel, one filter enriches the QCD-multijet sample with events including electrons from the decay of hadrons with b or c quarks (*BCtoE*). Another one preselects events in which final-state particles might be misreconstructed as electrons (*EM enriched*). In both cases, there are three different samples for $\hat{p}_T$ from 20 to 30, 30 to 80 and 80 to 170 GeV.

The LO hard-scattering generators MADGRAPH and PYTHIA use the CTEQ6L1 LO PDF set, whereas the NLO generators POWHEG and MC@NLO apply the CTEQ6M

---

[1]Here, *Z-boson production* refers to all Z/γ^* processes, i.e. it includes production via a virtual photon. An invariant dilepton mass of $m^{\ell\ell} > 50$ GeV is required.

[2]For the WZ and ZZ simulation, an invariant mass of $m^{\ell\ell} > 40$ GeV is required.

[3]$\hat{p}_T$ refers to the p_T of the outgoing partons of the hard 2→2 process simulated by PYTHIA before parton showering in their rest frame.

NLO PDF set [108]. MADGRAPH, POWHEG and PYTHIA use PYTHIA for parton showering, hadronisation and UE simulation, whereas MC@NLO is interfaced to HERWIG (v. 6.520).

The renormalisation and factorisation scale are subsumed under the (squared) hard-scattering scale Q^2. For $t\bar{t}$ and single-(anti)top production with POWHEG or MC@NLO, the scale is set to $Q^2 = m_t^2$. For $t\bar{t}$ and W/Z+jets production with MADGRAPH, it is set to $Q^2 = m_X^2 + \sum_i p_{\mathrm{T},i}^2$, where m_X refers to the mass of the top quark, W or Z boson, respectively. The sum runs over the transverse momenta of the additional partons from the ME. The MADGRAPH matching threshold is set to 20 GeV for $t\bar{t}$ and 10 GeV for W/Z+jets production. The initial parton-shower evolution scale is coupled to the Q value, but can differ by a tuned factor between 1 and 2.

In addition, specific samples are produced with systematic variations of the Q^2 scale, matching threshold and top-quark mass (see Sec. 9). For an unfolding closure test, a Z′ boson of 750 GeV mass is simulated with MADGRAPH (see Sec. 8.2.5).

4.3   Normalisation and Correction of Simulation using Event Weights

The simulated events need to be corrected for various reasons. These corrections are performed using event weights. Each simulated event is assigned a statistical weight w that can be either the same for all simulated events or might depend on specific properties of an event or its objects.

4.3.1   Normalisation to Integrated Luminosity and Higher Order Cross Sections

Ideally, more events than expected from the integrated data luminosity are generated in order to enhance the statistical precision of the simulated sample. Moreover, inclusive cross-section calculations are typically available at higher perturbative orders than implemented in the matrix-element calculation of the event generators. Thus, the simulated event number N_{gen} is normalised to match the expected number of events for the integrated data luminosity of this analysis using the higher-order cross section. The following event weight is applied:

$$w = \frac{\sigma \cdot L}{N_{gen}}. \tag{4.1}$$

The values for σ and N_{gen} are given in Tab. 4.1. For $t\bar{t}$ production, an NNLO+NNLL cross-section calculation is taken (using $m_t = 173.3$ GeV and MSTW2008 NNLO PDF) [41]. For single-top processes, the cross sections are provided by approximate NNLO calculations [47–49]. NNLO cross sections for W-boson production in the leptonic decay channels ($W \to l\nu$) as well as Z-boson production decaying into two leptons

Sample	Generators (ME + PS)	N_{gen}	σ [pb]
Central Samples			
$t\bar{t} \to X$ Main Sample	MADGRAPH + PYTHIA	3,701,947	172.0
$W \to \ell\nu$	MADGRAPH + PYTHIA	81,345,381	31,314
$Z/\gamma^* \to \ell^+\ell^-$ ($m^{\ell\ell} > 50\,\text{GeV}$)	MADGRAPH + PYTHIA	36,209,629	3,048
t (s-ch.)	POWHEG + PYTHIA	259,971	2.7
t (t-ch.)	POWHEG + PYTHIA	3,900,171	41.9
t (tW-ch.)	POWHEG + PYTHIA	814,390	7.9
$\bar{t}$ (s-ch.)	POWHEG + PYTHIA	137,980	1.4
$\bar{t}$ (t-ch.)	POWHEG + PYTHIA	1,944,826	22.7
$\bar{t}$ (tW-ch.)	POWHEG + PYTHIA	809,984	7.9
QCD μ enr.	PYTHIA	25,080,241	84,679
QCD EM enr., $\hat{p}_T$ 20-30	PYTHIA	35,721,883	2,502,660
QCD EM enr., $\hat{p}_T$ 30-80	PYTHIA	70,392,060	3,625,840
QCD EM enr., $\hat{p}_T$ 80-170	PYTHIA	8,150,672	142,813
QCD BCtoE, $\hat{p}_T$ 20-30	PYTHIA	2,071,133	139,299
QCD BCtoE, $\hat{p}_T$ 30-80	PYTHIA	2,030,033	143,845
QCD BCtoE, $\hat{p}_T$ 80-170	PYTHIA	1,082,691	9,431
WW	PYTHIA	4,225,916	43
WZ ($m^{\ell\ell} > 40\,\text{GeV}$)	PYTHIA	4,265,243	18.2
ZZ ($m^{\ell\ell} > 40\,\text{GeV}$)	PYTHIA	4,191,045	5.9
Samples for Systematic Variations and Other Studies			
$t\bar{t} \to X$ Additional Central Sample	POWHEG + PYTHIA	16,439,970	172.0
$t\bar{t} \to X$ Additional Central Sample	MC@NLO + HERWIG	16,810,548	172.0
$t\bar{t} \to X$ Q^2 Scale Up	MADGRAPH + PYTHIA	3,696,269	172.0
$t\bar{t} \to X$ Q^2 Scale Down	MADGRAPH + PYTHIA	4,004,587	172.0
$t\bar{t} \to X$ Matching Scale Up	MADGRAPH + PYTHIA	4,029,823	172.0
$t\bar{t} \to X$ Matching Scale Down	MADGRAPH + PYTHIA	1,545,688	172.0
$t\bar{t} \to X$ Mass Up (184.5 GeV)	MADGRAPH + PYTHIA	1,671,859	172.0
$t\bar{t} \to X$ Mass Down (161.5 GeV)	MADGRAPH + PYTHIA	1,620,072	172.0
$W \to \ell\nu$ Q^2 Scale Up	MADGRAPH + PYTHIA	9,784,907	31,314
$W \to \ell\nu$ Q^2 Scale Down	MADGRAPH + PYTHIA	10,092,532	31,314
$W \to \ell\nu$ Matching Scale Up	MADGRAPH + PYTHIA	10,461,655	31,314
$W \to \ell\nu$ Matching Scale Down	MADGRAPH + PYTHIA	9,956,679	31,314
$Z/\gamma^* \to \ell^+\ell^-$ Q^2 Scale Up	MADGRAPH + PYTHIA	1,593,052	3,048
$Z/\gamma^* \to \ell^+\ell^-$ Q^2 Scale Down	MADGRAPH + PYTHIA	1,658,995	3,048
$Z/\gamma^* \to \ell^+\ell^-$ Matching Scale Up	MADGRAPH + PYTHIA	1,641,367	3,048
$Z/\gamma^* \to \ell^+\ell^-$ Matching Scale Down	MADGRAPH + PYTHIA	1,615,032	3,048
t (s-ch.) Q^2 Scale Up	POWHEG + PYTHIA	285,972	2.7
t (s-ch.) Q^2 Scale Down	POWHEG + PYTHIA	285,602	2.7
t (t-ch.) Q^2 Scale Up	POWHEG + PYTHIA	1,032,197	41.9
t (t-ch.) Q^2 Scale Down	POWHEG + PYTHIA	1,039,406	41.9
t (tW-ch.) Q^2 Scale Up	POWHEG + PYTHIA	437,736	7.9
t (tW-ch.) Q^2 Scale Down	POWHEG + PYTHIA	437,819	7.9
$\bar{t}$ (s-ch.) Q^2 Scale Up	POWHEG + PYTHIA	153,981	1.4
$\bar{t}$ (s-ch.) Q^2 Scale Down	POWHEG + PYTHIA	153,971	1.4
$\bar{t}$ (t-ch.) Q^2 Scale Up	POWHEG + PYTHIA	565,520	22.7
$\bar{t}$ (t-ch.) Q^2 Scale Down	POWHEG + PYTHIA	565,454	22.7
$\bar{t}$ (tW-ch.) Q^2 Scale Up	POWHEG + PYTHIA	437,798	7.9
$\bar{t}$ (tW-ch.) Q^2 Scale Down	POWHEG + PYTHIA	437,863	7.9
Z' 750 GeV	MADGRAPH + PYTHIA	206,525	3.2

Table 4.1: Overview on the simulated samples: MC event generators used for the hard scattering + parton shower, number of simulated events N_{gen} and cross section σ used for normalisation (see text).

with an invariant dilepton mass larger than $50\,\mathrm{GeV}$ ($Z/\gamma^* \to \ell^+\ell^-$) are calculated with FEWZ [109]. For diboson production, the parton-level integrator MCFM [45] is used to compute NLO cross sections. For QCD-multijet production, only a LO cross-section calculation from PYTHIA is available. The Z' cross section is taken from [60]. The cross-section values given in Tab. 4.1 always refer to the exact simulated process, i.e. they include the appropriate branching ratios and efficiencies of the applied filters.

4.3.2   Pile-Up Reweighting

PU interactions as introduced above have a large influence on the analysis (e.g. jet energy, lepton isolation etc.) as will become apparent from Sec. 5. Although efforts are made to mitigate their effects (see Secs. 5.1.2, 5.1.5), it is vital that the simulated PU-multiplicity distribution agrees with the one in data. Both are compared in Fig. 4.2. The simulated distribution is known by construction from the simulation setup, whereas the one in data is estimated from the instantaneous luminosities of all colliding bunch pairs and the total inelastic cross section for proton-proton interactions of $73.5\pm1.6\,\mathrm{mb}$ as determined by the TOTEM collaboration [110]. A mean PU multiplicity of 9.5 for the full 2011 dataset is obtained. Although both distributions have a maximum at about 6 PU interactions, especially the tails at high PU multiplicities differ. Thus, event weights as a function of the number of PU events are calculated from the ratio of the data to the simulated distribution and are applied to the simulated events [111]. The weights are normalised such that their mean is 1, thereby leaving the total number of simulated events unaffected. This procedure is referred to as PU reweighting and is the recommended standard approach at CMS [112].
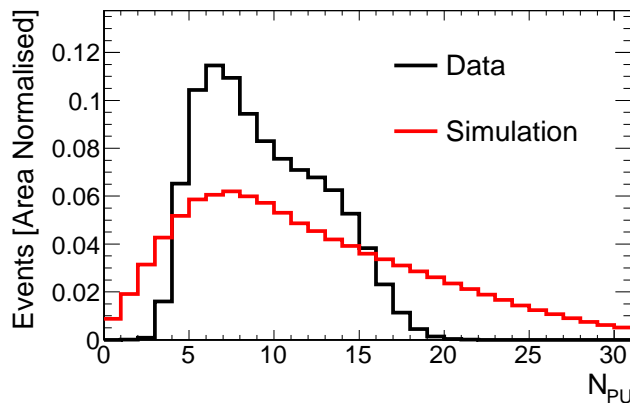
Figure 4.2: Comparison of pile-up distributions for data and the simulated samples before reweighting.

In order to verify the correctness of the PU reweighting, the distributions for the number of reconstructed primary vertices N_{PV} are compared for simulation and data (more details on their reconstruction is given in Sec. 5.1.2). This distribution corresponds to the number of PU events folded with the probability of about 70% that such
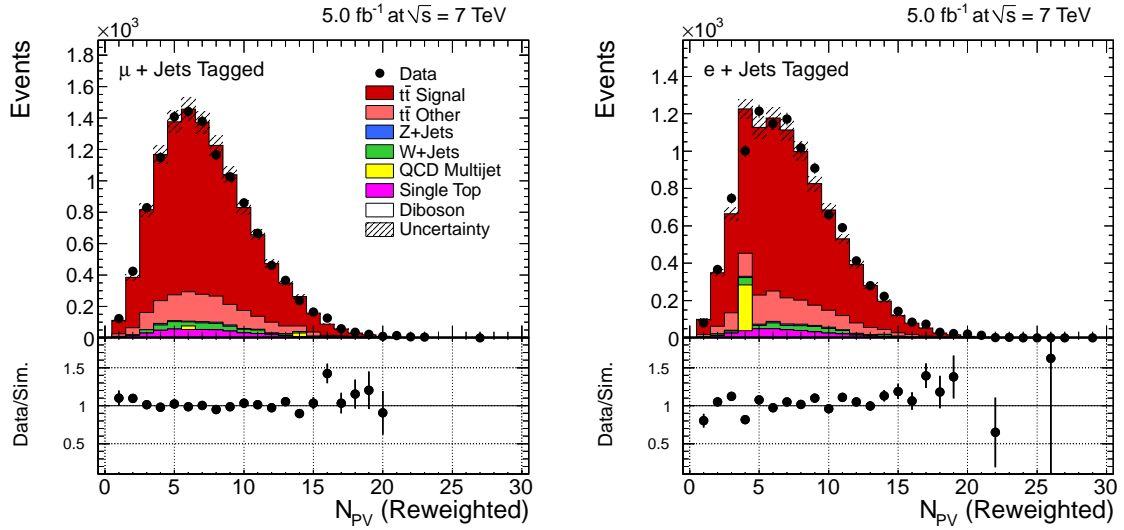
Figure 4.3: Distribution of reconstructed primary vertices N_{PV} after PU reweighting for the muon+jets *(left)* and the electron+jets *(right)* channel after the full event selection. For more details on the event selection and the presentation of such monitoring distributions, see Sec. 5.

an event yields a reconstructed vertex [113], plus the vertex from the hard primary interaction. As illustrated in Figure 4.3, the distributions agree well for both decay channels after the full event selection.

4.3.3   Data-Driven Efficiency Corrections

The performance of the CMS detector simulation is validated and corrected for using measurements in data. Data-to-simulation scale factors (SF) for the trigger, lepton selection and b-tagging efficiencies are applied to the simulation as event weights. This is explained in detail in Sec. 6.

Chapter 5

Object Reconstruction and Event Selection

Before events of a certain particle-physics process can be analysed, they need to be reconstructed from the detector raw data and discriminated against events from background processes. In a first step, basic objects like tracks, vertices and calorimeter clusters are reconstructed, followed by the reconstruction of single particles in a particle-flow approach (see below). From this particle collection, higher-level physics objects like jets are derived. Subsequently, further identification (ID) and selection steps to reduce background contamination are applied in order to obtain a clean sample of events from the process of interest.

This analysis is performed on $t\bar{t}$ events in the ℓ+jets channel (see Sec. 2.2.2). Thus, the final state comprises one isolated lepton[1] from a W-boson decay, a corresponding neutrino resulting in missing transverse energy ($E_{\mathrm{T}}^{\mathrm{miss}}$), and four quarks (two light and two b quarks) hadronising into jets. QCD higher-order contributions can result in additional jets.

The reconstruction and selection is based on the common reference selection recommended by the CMS Top-Quark-Physics Analysis Group, similar to the documentation in [114]. In addition, it is optimised for high signal purity, which is mandatory for differential cross sections that rely on the correct reconstruction of the kinematic top-quark quantities. This is achieved by the use of b-jet identification.

5.1 Object Reconstruction and Selection in the Particle-Flow Framework

The whole object reconstruction is based on the particle-flow (PF) technique [115], which attempts to reconstruct every stable particle individually, thereby distinguish-

---

[1]Phenomenologically, a lepton (here: muon or electron) is referred to as *isolated* if it is produced by a real W or Z boson, i.e. not by a hadron decay inside a jet. Experimentally, isolation refers to the amount of energy deposited in a cone around the leptons (see below).

ing muons, electrons, photons and charged and neutral hadrons. Such a global and consistent reconstruction approach is made possible by using complementary information from all detector subsystems. Due to its well-performing tracker, the separation power of the high magnetic field, the high-granularity ECAL and the hermeticity of ECAL and HCAL, the CMS detector is especially well-suited for the application of PF reconstruction. In particular, the performance of the reconstruction of collective objects such as jets and $E_\mathrm{T}^\mathrm{miss}$ benefits from this, as well as the one of charged-lepton isolation.

Single particles are reconstructed from blocks of linked elementary signatures like charged-particle tracks, vertices and calorimeter clusters, and identified by applying certain quality criteria. As this procedure is performed successively and already associated elementary signatures are removed, ambiguities are avoided.

5.1.1   Track Reconstruction

Track reconstruction at CMS is performed in the challenging environment of a large track and hit density and of a large amount of detector material leading to substantial multiple scattering, energy loss and interactions. The standard track-reconstruction algorithm capable of coping with these conditions is the combinatorial track finder [116] based on a Kalman Filter (KF) [117]. The first step consists of seed finding in the inner tracker layers, which are identified either as hit triplets or as doublets with additional beam-spot constraint. From this, a starting trajectory is determined and extrapolated to the next detector layer, which is scanned for compatible hits around the predicted point. In case a hit is found, it is added to the trajectory, which is updated by using the KF fit. This procedure is repeated as long as compatible hits are found, maximally up to the last layer. Finally, the complete collection of identified hits is refit with the KF method both inside-out and outside-in. The combination gives the best estimate of the fit parameters. This procedure is performed in an iterative manner. In the first step, stringent fit criteria are applied, which are subsequently loosened in further iterations after removing the hits associated to the tracks from earlier iterations.

For non-Gaussian distributions like in the case of electron bremsstrahlung, optimised adaptations of the KF like the Gaussian Sum Filter (GSF) are used as detailed in Sec. 5.1.4.

5.1.2   Primary-Vertex Reconstruction and Charged-Hadron Subtraction

The position of the primary vertex (PV) corresponding to the pp-interaction point varies due to the spread of the protons in the colliding bunches. Thus, it needs to be determined for each event. Moreover, due to pile-up more than one PV can be present in the event.

A PV is reconstructed from tracks fulfilling certain quality criteria on the number of associated hits in the inner tracking system, the normalised χ^2 of the trajectory fit

and the impact parameter with respect to the nominal beam spot [86]. A group of good tracks is considered as a vertex candidate if they are closer than 1 cm in longitudinal direction at their point of closest approach to the beam line. These candidates are used as input to an adaptive vertex-fitting procedure [118]. Each track is assigned a weight according to its compatibility to the fitted vertex, with the sum of these weights being denoted as the degrees of freedom (ndof) of the vertex.

A PV is considered well-reconstructed if ndof > 4 and if it lies within a longitudinal distance of $|z| < 24$ cm and a transverse distance of $\rho < 2$ cm to the nominal interaction point.

Finally, the vertex corresponding to the hard pp interaction of interest is determined as the one with the highest p_T^2 sum over all tracks associated with the vertex. Other primary vertices are considered as coming from pile-up interactions. In the framework of PF, the impact of pile-up effects can be mitigated by removing all charged hadrons originating from these identified pile-up vertices from the event. Thus, they are neither taken into account for jet clustering nor for the calculation of lepton-isolation variables as explained in the following.

5.1.3   Muons

Basic Reconstruction

Muons are reconstructed from a track in the muon system and/or a track in the inner tracker. There are three main reconstruction methods used in CMS [87]:

Standalone muons are based on hits in the muon system only, which are fit with the KF algorithm starting from track segments in the innermost muon chambers. This method is mainly used for the reconstruction of cosmic muons as the volume of the muon system is much larger than the one of the tracker. For pp interactions, however, the addition of tracker information increases the precision largely.

Thus, for the *global-muon* reconstruction method, each standalone track is matched to a tracker track (outside-in approach) and a combined KF fit of corresponding hits from both the muon system and the tracker is performed. The combination of the superior tracker momentum resolution with the large lever arm of the muon system guarantees an optimum performance over a wide p_T range (see Sec. 3.2.4). Especially above 200 GeV, the resolution is improved over the tracker-only fit, which is the third muon-reconstruction method.

In the *tracker-muon* reconstruction method (inside-out approach), tracks from the inner tracker are considered as potential muon candidates. If the track extrapolation to the muon system (taking expected energy loss and multiple-scattering effects into account) matches at least one muon segment, the candidate is selected as tracker muon. As only one muon segment is required, the efficiency of strongly bent tracks at low p_T is improved compared to global muons that need more segments.

Muons used within the PF framework are based on global muons [119]. Also non-isolated muons inside jets are intended to be reconstructed. As it is very important for

the reconstruction of neutral hadrons in jets that charged hadrons are not misidentified as muons, non-isolated PF muons undergo a loose pre-identification step. It is based on a loose requirement on a minimum number of hits of the muon track and the compatibility of associated calorimeter deposits and muon segments with the muon expectation.

Selection: Identification and Isolation

For the $t\bar{t}$-event selection, further identification and isolation requirements are applied to the basic PF muons in order to suppress background from misreconstructed or real leptons from other processes.

Tight Muon

A tight muon is required to be reconstructed as a *tracker muon* in addition to the *global-muon* requirement, which is already part of the PF muon definition. For a good identification and a precise determination of the momentum, certain track-quality requirements are applied. The global track fit is required to have a $\chi^2/\mathrm{ndof} < 10$ and to include at least one valid hit in the muon system. Its corresponding tracker track should have at least 11 tracker hits including one hit in the pixel detector and be matched to the outer track segments of at least two stations of the muon system. To assure that the muon originates from the initial pp collision, the two-dimensional impact parameter d_B with respect to the beam spot is required to be smaller than 0.02 cm and the distance between the z position of the origin of the muon track and the z component of the primary vertex, Δz, is required to be smaller than 0.5 cm. With this selection, cosmic muons and muons from the in-flight decay of light hadrons are significantly suppressed.

In order to exclude non-prompt muons from semileptonic decays of hadrons within a jet as well as misidentified charged hadrons from a jet punching through to the muon system, the muon is demanded to be isolated. A relative PF isolation variable (I_{rel}) is defined as the summed p_T of PF charged and neutral hadrons (*ch.h.*, *n.h.*) and PF photons (γ) within an opening cone of $\Delta R < 0.4$ around the selected muon, divided by its p_T:

$$I_{rel} = \frac{\sum p_T^{ch.h.} + \sum p_T^{n.h.} + \sum p_T^{\gamma}}{p_T^{\mu}} \tag{5.1}$$

In order to remove noise and pile-up effects, only photons and neutral hadrons with $p_T > 500\,\mathrm{MeV}$ and charged hadrons from the main primary vertex are taken into account. A muon is considered to be isolated if $I_{rel} < 0.125$.

Loose Muon

For a veto on additional loose muons in the event (see Sec. 5.2.4), PF muons without further identification and a relaxed isolation requirement of $I_{rel} < 0.2$ are used.

Trigger Reconstruction and Selection

Muon trigger reconstruction at L1 is based on local trigger primitives that are combined to muon-track candidates using regional track finders separately in all muon subsystems. Subsequently, DT muon candidates in the barrel (or CSC candidates in the endcaps) are matched to RPC candidates in the Global-Muon-Trigger (GMT) system and are finally merged. Based on a p_T and quality ranking, four final candidates are chosen for further processing. The muon HLT is subdivided into level 2 and 3 (L2/3). At L2, a standalone trigger-muon object is reconstructed, on which a loose p_T filter is applied. At L3, inner-tracker information[2] is added and a global fit with a more precise p_T determination is performed, which is used for final HLT p_T filtering. Optionally, simple identification and isolation requirements can be applied. At L2, a calorimeter-based absolute isolation variable (i.e. not relative to the muon p_T as in the offline case) is derived from energy deposits around the projected track. It is required to be less than 2 to 4 GeV depending on $|\eta|$. At L3, track-based absolute isolation is defined by the summed p_T of surrounding tracks and demanded to be less than about 1 GeV.

5.1.4   Electrons

Basic Reconstruction

The signature of electrons is characterised by energy deposition in the ECAL associated with a track. However, due to the large amount of material in the tracker of up to two radiation lengths, emission of bremsstrahlung photons is frequent. Thus, potential additional ECAL clusters from bremsstrahlung photons are grouped together with the seed cluster associated to the primary electron into one electron supercluster (SC). A SC is characterised by a narrow width in η typical of electromagnetic showering and a large spread in Φ as bremsstrahlung photons can be radiated along the whole electron trajectory bent in the magnetic field. Moreover, bremsstrahlung emission leads to kinks in the electron trajectory, resulting in a failure or bad quality of the standard KF fit that assumes a minimum-ionising particle only undergoing multiple scattering. Thus, the track needs to be refit with a Gaussian Sum Filter (GSF) algorithm [120] taking the highly non-Gaussian bremsstrahlung energy loss into account. However, a GSF fit is computationally expensive and can be performed only on a limited number of seeds. Two different seeding strategies are used: An ECAL- (outside-in) and tracker-driven (inside-out) approach.

---

[2]Due to CPU constraints at HLT, only tracks in a narrow region compatible with the L2 muon are reconstructed.

The classical ECAL-driven seeding is based on the barycentre of the supercluster, which is used to infer the position of the electron track in the pixel and inner strip layers. General track seeds, i.e. pairs or triplets of hits, that match this position are used as input for the GSF fit. This method performs well for high-p_T and isolated electrons as it relies on the supercluster barycentre as the position of the original electron independent of bremsstrahlung, which is only true if all bremsstrahlung clusters are reconstructed and correctly associated to the supercluster. Only superclusters with $E_T > 4\,\text{GeV}$ and $H/E < 0.15$ (the ratio between the HCAL and ECAL energy deposit) are taken into account.

In order to find seeds also for non-isolated and low-p_T electrons, which is vital for PF event reconstruction, a tracker-driven approach based on electron pre-identification complements the ECAL-driven one. In the absence of bremsstrahlung, the standard KF fits are expected to give good results also for electron tracks with adequate momentum determination and a reconstruction of the tracks up to the ECAL surface. Thus, if a KF track can be matched to a nearby ECAL cluster with the ratio between track momentum and matched cluster energy (E/p) close to unity, its innermost hits are selected as electron track seeds. In the case of significant energy loss by bremsstrahlung, an alternative approach is needed, which is based on track properties. In such cases, the electron as reconstructed with a KF fit is typically not reaching the ECAL surface, leading to a small number of hits and a large track χ^2. Tracks selected based on these criteria are refit with a simplified GSF algorithm. A multivariate analysis based on characteristics of this GSF refit, the original KF fit and track-cluster matching is used to pre- identify electron candidates whose seeds are selected.

Seeds from both ECAL- and tracker-driven approaches are merged and fed into a complete GSF refit.

In some cases, bremsstrahlung photons in turn undergo conversion into an electron-positron pair, potentially resulting in multiple reconstructed GSF tracks per electron. Thus, for tracks with similar initial directions, a cleaning based on the radial distance of the first GSF track hit to the beam line is applied. If both tracks have hits close to the beam line, additional cleaning criteria are used.

Combined Reconstruction and Pre-Identificaton

Finally, the track and the clusters need to be joined for a combined electron reconstruction. In the PF approach, instead of using the standard ECAL supercluster, the electron track is linked to the individual ECAL and HCAL clusters from the primary electron and the bremsstrahlung photons. The linking of the bremsstrahlung clusters is performed using tangents to the GSF track for each tracker layer. These are assumed to be potential bremsstrahlung trajectories and therefore tried to be matched to calorimeter clusters. All ECAL and preshower clusters linked to the track are collected into a new PF supercluster. Electron-energy corrections based on the comparison of true and reconstructed energy in simulated events are applied. For the final electron-momentum determination, the tracker momentum is combined with the corrected PF supercluster energy, leading to an improved precision.

In order to distinguish electrons from charged-hadron background already at the level of PF electrons, a first step of loose identification using a multivariate method is performed. One set of electron-identification variables used as input is based on the momentum-energy matching between the tracker and the ECAL, which is dominated by bremsstrahlung effects. Others include shower shape, track quality or kinematic variables. More details concerning these variables are given in the next section. The thus pre-identified PF electrons are used as input for both the $t\bar{t}$-event selection (isolated electrons) and jet clustering (non-isolated electrons).

Selection

Further selection steps are applied to the basic PF electrons in order to obtain well-identified and isolated electrons for the $t\bar{t}$-event selection. Due to cracks in the transition region of the ECAL barrel and end-cap and resulting very low efficiencies, electrons with a supercluster in the η range of 1.4442 to 1.5660 are discarded.

Tight Electron

In order to suppress electrons from light-hadron decays in flight, the same requirements as for a tight muon are applied concerning the two-dimensional impact parameter, $d_B < 0.02$ cm, and the longitudinal distance between the origin of the muon track and the primary vertex, $\Delta z < 0.5$ cm.

Further identification cuts are optimised separately in different categories (*Cut in Categories* (CiC) approach[3]) based on the detector geometry and amount of bremsstrahlung as each category has different measurement characteristics and purity [121, 122]. Thus, the electron collection is subdivided into the barrel and the endcap category, and for each of these into three different bremsstrahlung categories defined in a two-dimensional plane of the variables E/p_{in} and f_{brem}. E/p_{in} measures the consistency between the corrected energy of the supercluster, E, and the original electron-track momentum measured at the vertex, p_{in}. f_{brem} gives the fraction of momentum radiated by bremsstrahlung with respect to p_{in}. Moreover, in each category the cuts are determined in a p_T-dependent way.

The variables used for identification include track-cluster-match variables: E_{seed}/p_{in}, which measures the match between the seed-cluster energy and the original track momentum, as well as $\Delta\Phi_{in}$ and $\Delta\eta_{in}$, which measure the geometrical matching between the supercluster and the track extrapolated from the vertex to the calorimeter. Also the cluster-shape variable $\sigma_{i\eta i\eta}$ is exploited. It gives the supercluster width in η, which should be unaffected by the spread in Φ due to radiation and discriminates broader showers from hadrons against narrower electron showers. Furthermore, the hadronic-leakage variable H/E is used, which gives the ratio between the HCAL energy directly behind the ECAL seed cluster and ECAL energy. It is expected to be small for electron-induced showers and large for hadron-induced showers.

---

[3]In this analysis, only the ID selection is performed in a CiC approach, the isolation and conversion rejection criteria are applied separately as described.

The cut values on these variables are determined such that the signal-to-background ratio (S/B) exceeds a specific value in each category depending on the desired tightness of the selection. The tight electron selection of this analysis uses the *HyperTight1* working point [122]. The constructed constant S/B implies that for categories with more background contamination like the endcaps or mismeasured tracks, the cuts are chosen tighter than in purer categories, resulting in a lower efficiency.

As for the muons, in order to reject non-prompt electrons from the decay of hadrons within a jet, a relative isolation criterion is applied based on the PF isolation variable as defined in Eq. 5.1 (with p_T^e instead of p_T^μ). The electron is considered to be isolated if $I_{rel} < 0.125$.

Another potential background consists of electrons from the conversion of prompt photons in one of the detector layers. This is partly already rejected by the impact parameter (d_B) requirement. In addition, electrons are rejected if at least one expected hit in the tracker layers before the first valid hit of the reconstructed electron track is missing. Furthermore, electrons are only accepted if no conversion partner track is found either close-by with a distance in rΦ less than 0.02 cm or parallel to the electron track, i.e. with an angular difference $\Delta \cot \theta < 0.02$ between the electron and the partner track.

Loose Electron

Loose electrons as used for a veto in the event selection (see Sec. 5.2.4) are also based on PF electrons. In the muon channel, loose electrons do not require any further identification, whereas the requirement of a relaxed ID working point (*Loose*) is imposed in the electron channel. In both cases, a relaxed isolation requirement of $I_{rel} < 0.2$ is applied.

Trigger Reconstruction and Selection

Electron trigger objects at L1 are built from trigger primitives based on local ECAL-energy deposits. L1 trigger objects are accepted and used as a seed for the HLT electron paths if they exceed a configurable E_T threshold. An electron HLT object is based on an ECAL supercluster built similarly to the offline reconstruction. It is required to be matched to the L1 object and to two pixel hits compatible with an electron trajectory coarsely back-propagated from the supercluster. Already at HLT level, coarse identification and isolation requirements can be applied. Track information is inferred from a KF fit with relaxed requirements, which is expected to converge also in case of bremsstrahlung. In this analysis, track-based ID is applied by requiring $\Delta \eta_{in} < 0.008$ and $\Delta \Phi_{in} < 0.07$ (0.05) in the barrel (endcap), corresponding to the *TrkIdT* working point. In addition, calorimeter-based ID at the *CaloIdVT* working point is required: $H/E < 0.05$ and $\sigma_{i\eta i\eta} < 0.011$ (0.031). Optionally, detector-based relative isolation criteria are applied (*CaloIsoT* and *TrkIsoT* working points), defined by the summed E_T of calorimeter clusters and p_T of tracks in a cone around the candidate, divided by the p_T of the electron: *ecalIso*/p_T, *hcalIso*/p_T and *trkIso*/p_T

are each required to be less than 0.125 (0.075) in the barrel (endcap).

5.1.5   Jets

Due to QCD confinement, quarks and gluons are observed as bunches of collimated particles called jets (see Sec. 2).

Jet Types

Different input objects can be used for jet construction. In simulation, it is possible to obtain a complete list of generated stable particles after hadronisation, whose four-momentum vectors can be used for jet clustering (*generated jets*). In data, input objects need to be reconstructed from detector signals. The classical approach is based on clustering calorimeter objects only (*calorimeter jets*). This is still partly used for triggering due to the fast and robust reconstruction. However, for offline analysis, CMS uses the more advanced PF approach [115] as explained above (*PF jets*). Those are clustered from the list of stable PF particles, thereby being conceptually similar to jets on generator level. The advantage is the use of complementary information of other detector systems, especially the tracker, which enhances the resolution, and the consistent description of jet input objects and other objects used for event selection, avoiding ambiguities.

PF Input Objects

The main constituents of jets are charged hadrons (about 65% of the jet energy, mainly charged pions), photons ($\approx 25\%$, mainly from π^0 decays) and neutral hadrons ($\approx 10\%$). These are reconstructed after the removal of the detector signatures of already identified PF leptons. Each remaining track gives rise to a charged hadron. If its track momentum is compatible with the energies of the linked ECAL and HCAL clusters within the resolutions, its momentum is redetermined from a resolution-weighted combination of track momentum and cluster energies. If the cluster energies exceed the track momentum significantly, the charged-hadron momentum is taken from its track and the excess gives rise to a photon or neutral hadron. If the excess can be attributed to energy in the ECAL, it gives rise to a photon. Only if it is larger than the ECAL energy, the remaining excess from the HCAL is assigned to a neutral hadron. Photons are prioritised over hadrons as they leave on average much more energy in the ECAL. ECAL and HCAL clusters not linked to any track give also rise to photons and neutral hadrons, respectively.

Due to semileptonic decays of hadrons, jets may also contain leptons. PF leptons are used as jet input objects if they are not considered as isolated in the event selection. Thus, loose muons and electrons as defined above are removed from the input list (a process called *top projection*) in order to avoid double-counting.

Jet Clustering

The input objects are clustered to jets using the anti-k_T algorithm [123], which belongs to the class of sequential recombination algorithms. First, an effective distance variable d_{ij} is calculated between all possible pairs of objects i, j using their corresponding transverse momenta k_T, their distance in rapidity-azimuth space, $\Delta R_{ij} = \sqrt{(y_i - y_j)^2 + (\Phi_i - \Phi_j)^2}$ and a configurable radius parameter R:

$$d_{ij} = \min(\frac{1}{k_{T,i}^2}, \frac{1}{k_{T,j}^2})\frac{\Delta R_{ij}^2}{R^2}. \tag{5.2}$$

The object pair with the smallest d_{ij} is combined to a pseudo-jet that is fed back to the list of objects. The procedure is iterated until the smallest d_{ij} is larger than $d_i = \frac{1}{k_{T,i}^2}$. In that case, object i is considered a jet and removed from the list of input objects. This procedure is repeated until all objects are clustered.

In contrast to other sequential recombination algorithms, the anti-k_T clustering leads to regularly-shaped jets resembling a cone of radius R. In this analysis, $R = 0.5$ is chosen.

Furthermore, the important jet-algorithm requirement of infrared and collinear (IRC) safety is met, i.e. that the resulting jets are insensitive to the emission of soft particles and collinear splitting. This is on the one hand theoretically important for the cancellation of divergences from IRC processes and loop diagrams in perturbative QCD calculations. It is also convenient from the experimental perspective as otherwise, the result would become dependent on the spatial detector resolution and the reconstruction efficiency of low-energetic particles.

Jet-Energy Calibration and Resolution

The measured jet energy differs from the original energy of the underlying stable particles due to detector effects such as the non-uniform and non-linear response of the calorimeter, energy loss from particles outside the jet area or undetected neutrinos and energy gain due to pile-up. Thus, the jet energy needs to be calibrated.

One needs to distinguish between the jet-energy scale (JES), which is defined by the average response of the measured jet energy with respect to the energy of the underlying particles, and the jet-energy resolution (JER), which gives the spread of the response in the Gaussian core region.

The JES calibration is performed in a factorised approach at CMS [124].

First, an offset correction is applied in order to subtract remaining energy contributions from pile-up (charged hadrons associated with pile-up vertices have been subtracted already before, cf. Sec. 5.1.2) using the jet-area method [125, 126]. The correction is determined for each event and jet separately from the average pile-up energy density ρ_{PU} in the event and the area A_j of the respective jet. The jet area refers to the so-called *catchment area* obtained by reclustering the original jet input

objects together with a large number of artificially added extremely soft particles. ρ_{PU} is determined from a reclustering of the event with the k_T algorithm[4] with radius parameter $R = 0.6$, which is able to cluster the diffuse soft particle background from pile-up and underlying event into jets, covering basically the full y-Φ space. For each such k_T jet, its density ρ_j is determined from its energy and catchment area. From all ρ_j, the median is calculated as it is insensitive to the presence of the few hard jets from the primary interaction. Finally, the median is corrected for the underlying-event contribution to obtain ρ_{PU}.

The next JES calibration step is based entirely on simulation and corrects the energies of the measured jets as a function of p_T and η to match on average the energies of the underlying generated particle-level jets. The correction factors for calorimeter jets are much larger (≈ 2 at $30\,\mathrm{GeV}$, decreasing with energy) compared to PF jets (1.05 to 1.1). The latter ones profit from the excellent tracker resolution and that the individual particles are already precalibrated, thus minimising the effect of non-linear calorimeter response.

Finally, the JES is also measured in data and small residual corrections of typically 1 to 3% in the kinematic region relevant for this analysis (see Sec. 5.2.5) are applied to account for differences with respect to the simulation. These residual corrections are determined from events in which the p_T of one jet can be balanced with another reference object. This reference object is in a first step just another jet (dijet events) in a central reference region ($|\eta| < 1.3$), relative to which the JES can be measured and corrected as a function of η. Subsequently, for the measurement of the absolute JES in the central reference region as a function of p_T, events with a jet-balancing reference object of excellent resolution like a photon or a Z boson are chosen.

The total JES uncertainty for PF jets in the kinematic region of this analysis amounts to 1 to 3% depending on p_T and $|\eta|$.

Also, the jet-energy resolution (JER) is measured exploiting the p_T balance in dijet and photon+jet events [20, 124]. Typical values for PF jets range from $\approx 15\%$ around $30\,\mathrm{GeV}$ to $\approx 5\%$ at several hundred GeV. It is observed that the resolution in data is systematically larger than the predicted one, mostly between 5 and 13% depending on $|\eta|$ (see Tab. 5.1). The jet resolution in simulation is corrected for this difference.

Jet Identification

In order to distinguish real jets from instrumental noise, the jets are required to fulfil certain quality criteria. They should have at least two constituents, out of which at least one is charged. The charged-hadronic-energy fraction is required to be > 0, whereas the neutral-hadronic-energy fraction as well as the charged- and neutral-electromagnetic-energy fraction should be < 0.99.

---

[4]The k_T algorithm can be obtained from the anti-k_T algorithm (Eq. 5.2) by replacing $\frac{1}{k_{T,i}}$ with $k_{T,i}$.

$|\eta|$ range	JER SF
$0.0 < |\eta| < 0.5$	1.05 ± 0.06
$0.5 < |\eta| < 1.1$	1.06 ± 0.06
$1.1 < |\eta| < 1.7$	1.10 ± 0.07
$1.7 < |\eta| < 2.3$	1.13 ± 0.09
$|\eta| > 2.3$	1.29 ± 0.20

Table 5.1: Data-to-simulation scale factors (SF) for the jet-energy resolution for different $|\eta|$ intervals.

Trigger Reconstruction and Selection

Jets at L1 are built from coarse calorimeter clusters and selected if the measured energy exceeds a configurable threshold. At HLT, jets are reconstructed as calorimeter jets during most of 2011 data taking due to their robust and fast algorithms. However, different online and offline jet reconstruction leads to a non-optimal performance, especially for the trigger turn-on curve at the cut threshold as shown in Sec. 6.1.3. Thus, a simplified fast reconstruction of PF jets at HLT has been developed, which is used at a late stage of 2011 data taking. In both cases, the anti-k_T algorithm is used for jet clustering, but JES corrections are applied only to calorimeter HLT jets. The performance is discussed in Sec. 6.1.3.

5.1.6   Identification of b-Jets

The identification of jets arising from the hadronisation of b quarks, commonly referred to as *b tagging*, is an important tool for the selection of events including top quarks. It is explained in more detail in [127]. It is based on several characteristic properties of b jets due to the large mass, high fraction of semileptonic decays and long lifetime of B hadrons ($\tau_B \approx 1.5\,\mathrm{ps}$). The first two properties give rise to muons that are less collimated with the jet axis than in case of light-hadron decays and thus have a significant momentum component transverse to the axis (p_T^{rel}). This is exploited especially for b-tagging-performance measurements (cf. Sec. 6.2). The b-tagging algorithms developed and applied by CMS mainly utilise the long lifetime resulting in a B-hadron flight distance L in the order of typically a mm to cm before decay[5]. Thus, measurable quantities include secondary decay vertices (SV) displaced from the primary collision vertex and large impact parameters (IP) of the tracks of the decay products with respect to the primary vertex as illustrated in Fig. 5.1 (*left*).

Robust algorithms used in early CMS analyses are based on either of those quantities, but this analysis exploits the better performance of the *Combined Secondary Vertex (CSV)* algorithm that combines multiple SV and track-based variables. The efficiency is improved by including also events without a successful SV fit, for which

---

[5]The mean flight distance is given by $< L >= \beta\gamma c\tau$, where β is the velocity in units of the speed of light, $\gamma = 1/\sqrt{1 - \beta^2} = E/m$ the relativistic Lorentz factor and $c\tau_{B^\pm} = 492\ \mu$m [19].
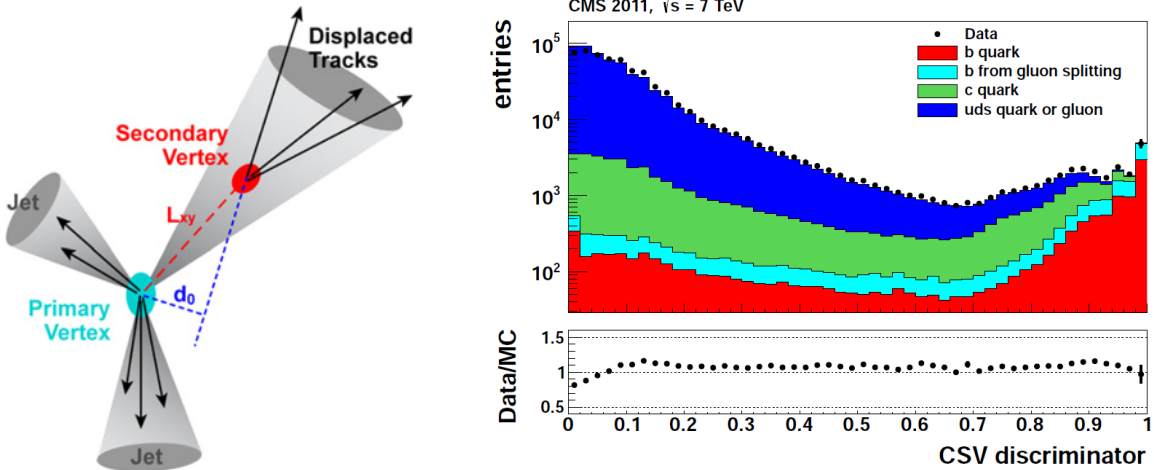
Figure 5.1: *Left:* Illustration of an event with one jet displaying a secondary vertex. L_{xy} denotes the flight distance of the B hadron in the transverse plane from the PV to the SV and d_0 is the impact parameter of one of the tracks with respect to the primary vetex. Taken from [128]. *Right:* The distribution of the CSV discriminator in data and simulation for different jet types in QCD-multijet events. Taken from [127].

either a pseudo vertex from tracks with large IP significance is constructed or, in case also this fails, only the track-based variables are used. This SV category (real, pseudo or none) is also used as one of the discriminating variables. Others, which are related to the SV properties, include the significance of the flight distance in the transverse plane L_{xy}, the SV mass, number of tracks at the SV, ratio of the energy of tracks associated to the SV with respect to all tracks in the jet and the η of the SV tracks with respect to the jet axis. Furthermore, the following track-based-only variables are taken into account: the number of tracks in the jet, the 3D-IP significance for each track in the jet, and the 2D-IP significance of the first track that raises the jet mass above 1.5 GeV (the charm threshold) when summing up tracks starting from the one with the largest 2D-IP significance. Likelihood ratios are formed from these variables to create the discriminator. The distribution in data compared to the one in simulation for QCD-multijet events is shown in Fig. 5.1 (*right*).

In this analysis, a b jet is considered b tagged if its discriminator value exceeds 0.679. This value refers to the medium working point of the algorithm (CSVM), which implies that on average about 67% of the b jets in a $t\bar{t}$ sample are correctly identified, whereas only about 1.5% of light jets are misidentified as b jets. These efficiency values are corrected for in a data-driven way as described in Sec. 6.2.

5.1.7 Missing Transverse Energy

The missing transverse momentum $\vec{E}_T^{\mathrm{miss}}$ is defined as the total-momentum imbalance in the transverse plane, which is computed from the negative vector sum of the p_T of all PF candidates. Its magnitude E_T^{miss} is referred to as missing transverse energy. It

is the signature of particles that do not interact in the detector, such as neutrinos in the case of a $t\bar{t}$ event. Its reconstruction is very sensitive to mismeasurements, noise, detector malfunctions etc., which can be misinterpreted as $E_\mathrm{T}^\mathrm{miss}$. However, this was studied in detail [129] and $E_\mathrm{T}^\mathrm{miss}$ resolutions between 5 and 10% were found.

$E_\mathrm{T}^\mathrm{miss}$ is not used for event selection in this analysis, but as input for the kinematic event reconstruction representing the neutrino momentum (cf. Sec. 7).

5.2   Event Selection

5.2.1   Data Sample

This analysis is based on the full dataset from proton-proton collisions at a centre-of-mass energy of 7 TeV recorded by the CMS detector in 2011. The data declared as good for analysis by the CMS Data-Quality-Monitoring group [130] corresponds to an integrated luminosity of $L = 5.0 \pm 0.1\,\mathrm{fb}^{-1}$. The precise central value used in the electron channel is 4.980 fb^{-1}, the one in the muon channel is slightly reduced to 4.955 fb^{-1} due to trigger prescales (see below).

The same event selection is also performed on the simulated signal and background samples presented in Sec. 4.2.

5.2.2   Online Selection: Trigger

As the instantaneous luminosity and running conditions were changing fast during 2011 data taking, both the triggers themselves and their prescales had to be adapted continuously. The running periods and different trigger menus, which define the deployed triggers and their prescales, are shown in Tab. 5.2.

In the muon channel, single-isolated-muon triggers were used for data taking as shown in Tab. 5.3, which require at least one isolated muon-trigger object as defined in Sec. 5.1.3. The HLT p_T thresholds had to be raised from 17 GeV to 24 GeV from menu 2e33 on. The muon-trigger acceptance ranges up to $|\eta| = 2.4$, but from menu 3e33A on, additional cuts on $|\eta| < 2.1$ were applied at HLT level. Some of the triggers are prescaled to a small extent during a limited number of runs, which reduces the effective luminosity by 0.5% from 4.980 fb^{-1} to 4.955 fb^{-1}. In simulation, the trigger with the cuts on 24 GeV and $|\eta| < 2.1$ (IsoMu24eta2p1) is applied to all events.

In the electron channel, events were selected online with electron-hadron (EleHad) cross triggers, which require at least one electron-trigger object with $p_\mathrm{T} > 25$ GeV and $|\eta| < 2.5$ and at least three central jet-trigger objects with $p_\mathrm{T} > 30$ GeV and $|\eta| < 2.6$ as defined in Secs. 5.1.4 and 5.1.5. The electron-trigger object is required to be isolated from menu 1e33v2 on. During most of the run periods, the jet-trigger objects were based on HLT calorimeter jets, but in the last trigger menu (5e33) they were replaced by HLT PF jets. To simulated events, the cross trigger with an isolated electron and calorimeter jets (IsoEle25TriJet) is applied.

Run Period	Run Range	Trigger Menu	Int. Lumi. [pb^{-1}]
A	$160404 - 163869$	5e32	216
A	$165088 - 165969$	1e33v1	136
A	$165970 - 166967$	1e33v2	542
A	$167039 - 167913$	1.4e33	277
A	$170249 - 173198$	2e33	831
A	$173236 - 173692$	3e33A	265
B	$175860 - 178380$	3e33B	1829
B	$178381 - 180252$	5e33	885

Table 5.2: Running periods and trigger menus during 2011 data taking. The trigger-menu names refer to the maximum target instantaneous luminosity (in cm^{-2}s^{-1}) during its deployment period, including optionally a version or run number. The integrated luminosity corresponds to the recorded data certified as good during the mentioned run range.

Channel	Trigger (Nominal Name)	Trigger (Abbrev.)	Menu
	Analysis Triggers		
μ	HLT_IsoMu17	IsoMu17	5e32 - 1.4e33
	HLT_IsoMu24	IsoMu24	2e33
	HLT_IsoMu24_eta2p1	IsoMu24eta2p1	3e33A - 5e33
e	HLT_Ele25_CaloIdVT_TrkIdT_ CentralTri/TriCentralJet30	Ele25TriJet	5e32, 1e33v1
	HLT_Ele25_CaloIdVT_CaloIsoT_ TrkIdT_TrkIsoT_TriCentralJet30	IsoEle25TriJet	1e33v2 - 3e33B
	HLT_Ele25_CaloIdVT_CaloIsoT_ TrkIdT_TrkIsoT_TriCentralPFJet30	IsoEle25TriPFJet	5e33
	Additional Utility Triggers		
μ	HLT_Mu17_TriCentralJet30	Mu17TriJet	5e32, 1e33v1
	HLT_IsoMu17_TriCentralJet30	IsoMu17TriJet	1e33v2 - 3e33B
	HLT_IsoMu17_TriCentralPFJet30	IsoMu17TriPFJet	5e33
e	HLT_Ele27_CaloIdVT_CaloIsoT_ TrkIdT_TrkIsoT	IsoEle27	5e32
	HLT_Ele32_CaloIdVT_CaloIsoT_ TrkIdT_TrkIsoT	IsoEle32	1e33v2 - 3e33B (prescaled from 1.4e33 on)

Table 5.3: Triggers used to select events for the $t\bar{t}$ analysis (*top*) and for efficiency determination (utility triggers, *bottom*). They are referred to by their abbreviation in the text. The values in the trigger names refer to the p_T [GeV] and optionally $|\eta|$ thresholds of the triggers. The identification and isolation requirements are explained in Sec. 5.1.

For the measurement of trigger and lepton-selection efficiencies (cf. Sec. 6), additional utility triggers are exploited. These include single-isolated-electron triggers with p_T thresholds of 27 and 32 GeV (partly prescaled) and mostly isolated muon-hadron (MuHad) cross triggers with a muon p_T threshold of 17 GeV and jet-trigger objects identical to the cross triggers in the electron channel.

5.2.3   Data Cleaning and Primary-Vertex Selection

In order to remove events from beam-background processes or with instrumental noise, two cleaning filters are applied to data only. One of them filters events with anomalous signals in the HCAL due to instrumental noise in the Hybrid Photo Diodes and Readout Boxes using timing and pulse-shape information (*HB-HE noise filter*) [129]. Another one removes events from beam interactions upstream the detector by requiring the fraction of tracks with high purity to be greater than 25% in events with at least 10 tracks (*beam scraping filter*).

Both in data and simulation, events are required to have one well-reconstructed primary vertex as defined in Sec. 5.1.2.

5.2.4   Lepton Selection

Kinematic Selection

Following the signal topology, events with exactly one tight (i.e. well identified and isolated) lepton (muon or electron) as defined in Secs. 5.1.3 and 5.1.4 are selected. Due to the large mass of the top quark, leptons from $t\bar{t}$ events are expected to have a larger transverse momentum and to be more central in η than leptons from main background processes like W+jets and QCD multijets. This difference is exploited in the event selection for background suppression. However, also external constraints like the trigger thresholds and the uniformity between electron and muon selection, which is necessary for a combination of the channels, need to be taken into account. As a result, the lepton is required to fulfil:

$$p_\mathrm{T}^\ell > 30 \,\mathrm{GeV} \text{ and } |\eta^\ell| < 2.1 \tag{5.3}$$
$$I_{rel} < 0.125$$
$$N^\ell = 1$$

Veto on Additional Loose Leptons

In addition, an event veto against further leptons with looser requirements is applied. This is intended to reject dileptonic events, in particular from other $t\bar{t}$ channels or $Z \to \ell\ell$ processes.

In both decay channels, events with additional loose muons as defined in Sec. 5.1.3 with $p_\mathrm{T} > 10\,\mathrm{GeV}$ and $|\eta| < 2.5$ are rejected. Furthermore, in the muon channel also additional loose electrons as defined in Sec. 5.1.4 with $p_\mathrm{T} > 15\,\mathrm{GeV}$ and $|\eta| < 2.5$ are vetoed. In the electron channel, events are rejected if they contain an additional loose electron with $p_\mathrm{T} > 20\,\mathrm{GeV}$ and $|\eta| < 2.5$ whose invariant mass in combination with the selected tight electron lies within $\pm 15\,\mathrm{GeV}$ around the mass of the Z boson (91 GeV).

5.2.5   Jet Selection and b-Jet Identification

Also jets arising from $t\bar{t}$ events are generally more central and high-energetic than those originating from the background processes. Also for jets, external constraints need to be taken into account, such as a reliable reconstruction and resolution, trigger thresholds and the containment of the jet cones within tracker and ECAL acceptances. Thus, jets are required to fulfil:

$$p_\mathrm{T}^\mathrm{jets} > 30\,\mathrm{GeV} \text{ and } |\eta^\mathrm{jets}| < 2.4 \tag{5.4}$$
$$N^\mathrm{jets} \geq 4$$

According to the $t\bar{t}\,\ell+$jets topology, events with at least four such jets are selected.

Finally, at least two out of these are required to be identified as b jets by the CSVM b-tagger as explained in Sec. 5.1.6 in order to suppress remaining background, mainly from W+jets events, and thereby maximise the signal purity:

$$N^\mathrm{b\ jets} \geq 2 \tag{5.5}$$

5.2.6   Number and Composition of Selected Events

This section gives an overview on the number and composition of selected events, which is summarised in Tab. 5.4. It is given separately for the muon and the electron decay channel as well as combined and is further subdivided into selection steps before and after applying b tagging (pretagged/tagged). In addition, the reconstruction of the $t\bar{t}$-event topology by a kinematic fit, which is explained in detail in Sec. 7, is included in the tables (kin-rec) because it acts like an additional selection step due to inefficiencies in the kinematic event reconstruction. These mainly arise from not enough b or light jets taken into account in the kinematic fit, thereby preventing a successful $t\bar{t}$-event reconstruction (see Sec. 7.2). Note that no additional cuts on the fit quality are made. The predictions from simulation include the application of pile-up reweighting and data-driven corrections of trigger and lepton-selection efficiencies, and after b tagging also of b-tag efficiencies. The derivation of these data-to-simulation scale factors is detailed in Sec. 6.

Before the b-tagging selection step, 48,062 events are selected in data in the muon and 43,091 in the electron channel, which adds up to 91,153 events combined. After

Channel	Muon			Electron		
Selection Step	Pretagged	Tagged	Kin-Rec	Pretagged	Tagged	Kin-Rec
	Event Yield					
N(Data)	48,062	11,986	10,766	43,091	10,224	9,076
N(Simulation)	49,176	11,855	10,584	43,731	9,738	8,673
	Expected Event Composition					
t$\bar{\text{t}}$ (μ/e prompt)	0.48	0.80	0.80	0.44	0.79	0.79
t$\bar{\text{t}}$ other	0.08	0.13	0.13	0.07	0.13	0.13
W+Jets	0.35	0.03	0.03	0.30	0.03	0.03
Z+Jets	0.05	0.01	0.01	0.07	0.01	0.01
QCD	< 0.01	< 0.01	< 0.01	0.08	< 0.01	< 0.01
Single Top	0.03	0.04	0.04	0.03	0.04	0.04
Diboson	0.01	< 0.01	< 0.01	0.01	< 0.01	< 0.01

Channel	Combined		
Selection Step	Pretagged	Tagged	Kin-Rec
	Event Yield		
N(Data)	91,153	22,210	19,842
N(Simulation)	92,907	21,593	19,257
	Expected Event Composition		
t$\bar{\text{t}}$ (ℓ prompt)	0.46	0.79	0.79
t$\bar{\text{t}}$ other	0.08	0.13	0.13
W+Jets	0.33	0.03	0.03
Z+Jets	0.06	0.01	0.01
QCD	0.04	< 0.01	< 0.01
Single Top	0.03	0.04	0.04
Diboson	0.01	< 0.01	< 0.01

Table 5.4: Event yield and expected event composition (i.e. fraction of expected events from one process with respect to all expected events) after the full event selection without b-tag requirement (pretagged), after b-tag requirement (tagged), and after the kinematic event reconstruction (kin-rec) for the separate channels (*top*) and combined (*bottom*). The prediction from simulation includes pile-up reweighting, trigger- and lepton-selection-efficiency scale factors, and after b tagging also b-tag-efficiency scale factors (cf. Sec. 6).

b tagging, the event numbers in data amount to 11,986 in the muon, 10,224 in the electron and 22,210 in the combined channel. The numbers of selected events in simulation agree with those in data at the 1–2% level before b tagging and within 1% (muon), 5% (electron) and 3% (combined) after b tagging. Given an uncertainty on the simulated yields of about 7% before and 9% after b-tagging, the agreement between data and simulation is found to be good. This uncertainty is dominated by the normalisation of the number of simulated events according to Eq. 4.1 due to a 2% luminosity uncertainty and uncertainties on the theoretical cross sections (mainly 5% from $\sigma_{t\bar{t}}$). Furthermore, experimental uncertainties add, mainly a jet-energy-scale uncertainty of 5% and after b-tagging also a b-tag-efficiency uncertainty of 5% (see Sec. 9 for details on the uncertainty determination).

The kinematic $t\bar{t}$-event reconstruction is successful for 10,766 (muon), 9,076 (electron) and 19,842 (combined) events in data, which are the final numbers of events used in this analysis. The $t\bar{t}$-event-reconstruction efficiency of about 90% shows excellent agreement between data and prediction on the one hand and the different channels on the other hand.

The event selection finally results in a high-purity sample of $t\bar{t}$ events. After b tagging, the expected event composition contains about 92% $t\bar{t}$ events, adding ℓ + jets events with prompt decays into one muon or electron ($t\bar{t}$ μ/e prompt, 79%) and $t\bar{t}$ events from other decay channels ($t\bar{t}$ other, 13%) that pass the selection cuts. The latter originate mostly from the τ+jets channel with the τ lepton decaying further to a muon or electron or from the dileptonic decay mode, where one of the leptons is either not measured or consists of a hadronically decaying τ lepton. The largest background consists of single-top-quark events with about 4% (of which 66% stem from the tW channel, 30% from the t channel and 4% from the s channel). All other background events like vector-boson production or QCD-multijet events are expected to sum up to less than 5%. Especially interesting to note is the expected small fraction of W+jets events after b tagging (3%), which in contrast is predicted to be the most relevant background before the b-tag requirement ($\approx 30 - 35\%$). QCD-multijet events are already efficiently suppressed by requiring an isolated, high-energetic lepton. As can be seen, the kinematic event reconstruction has almost no influence on the expected event composition.

Monitoring Distributions after Selection

Figs. 5.2 to 5.11 show monitoring distributions at reconstruction level after the event selection before and after applying the b-tag requirement, but before kinematic event reconstruction for both channels. The measured distribution in data (*black points*) is compared to the SM prediction from the simulation, which is composed of the stacked contributions of the separate processes (*coloured histograms*).

For the data points, the statistical uncertainties according to the Poisson distribution are shown as error bars (often too small to be visible). For the uncertainty band of the simulated yields, the uncertainty of the luminosity measurement and of the theoretical inclusive $t\bar{t}$ cross section used to normalise the simulated signal distribution is

taken into account. The appropriate data-driven corrections mentioned above are applied to the simulation. Below each distribution, the ratio of observed events in data to expected events from simulation indicates their level of agreement. The corresponding error bars refer to the statistical data uncertainty only. In the simulated distributions in the electron channel, unnatural spikes arise occasionally from fluctuations due to the limited number of simulated events in the QCD-multijet sample after selection, combined with large weights.

The presented kinematic variables include the p_T, η and relative isolation of the selected lepton (Figs. 5.2 and 5.3 before b tagging; 5.8 and 5.9 after b tagging), the p_T and η of all jets (*top row* of Figs. 5.4 and 5.5 before b tagging; 5.10 and 5.11 after b tagging), the p_T of the first and second leading jet (same figures, *second row*), the jet multiplicity and the E_T^{miss} distribution (same figures, *bottom row*). In general, a good agreement is observed. The p_T distributions of the jets are observed to be slightly softer in data, i.e. tend to lower values. This shape difference propagates to the final differential cross section results related to the p_T spectrum of the top quarks and b jets (cf. Sec. 10). As discussed there, higher-order effects improve the description.

B-tag-related distributions are shown in Figs. 5.6 and 5.7: the b-tag discriminator of the used CSV algorithm (*left*) and the b-tag multiplicity (*right*). As the b-tag discriminator distribution includes the entries from all selected jets in the event, the $t\bar{t}$ sample peaks both at 0 (tendentially no b jet) and at 1 (tendentially a b jet) due to the two light and two b jets in such an event at leading order. As can be seen, the jets from background processes tend to lower values, so that cutting at the medium working point of 0.679 largely suppresses them. This is also reflected in the b-tag multiplicity distribution, which shows the transition from background-rich 0- and 1-b-tag bins to the background-suppressed region for at least 2 b tags.
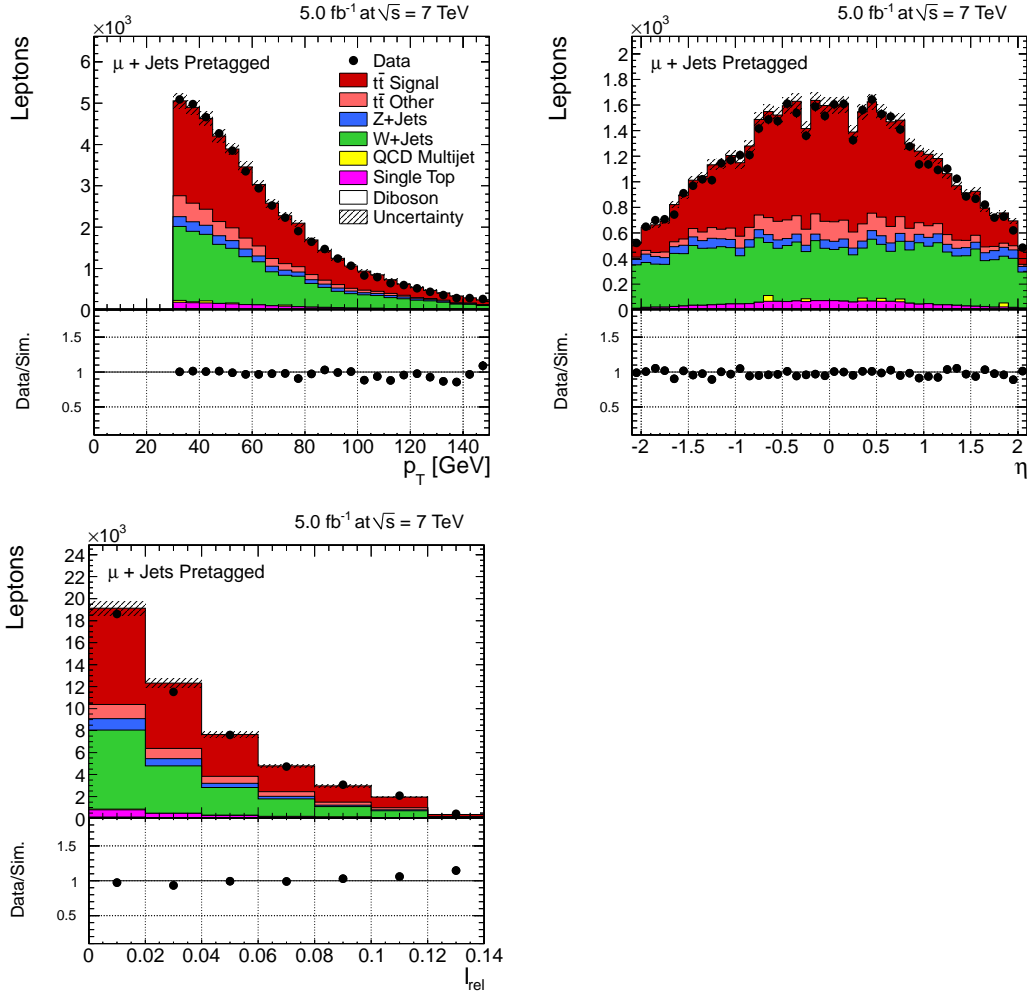
Figure 5.2: Kinematic muon variables (p_T, η, relative isolation I_{rel}) after selection (before b tagging) in the muon channel. The error bars represent the statistical uncertainty of the data. The hatched error band of the simulated distributions corresponds to the uncertainty of the luminosity measurement and of the theoretical inclusive $t\bar{t}$ cross section. Data-driven corrections related to pile-up as well as to lepton-selection and trigger efficiencies are applied to the simulation.
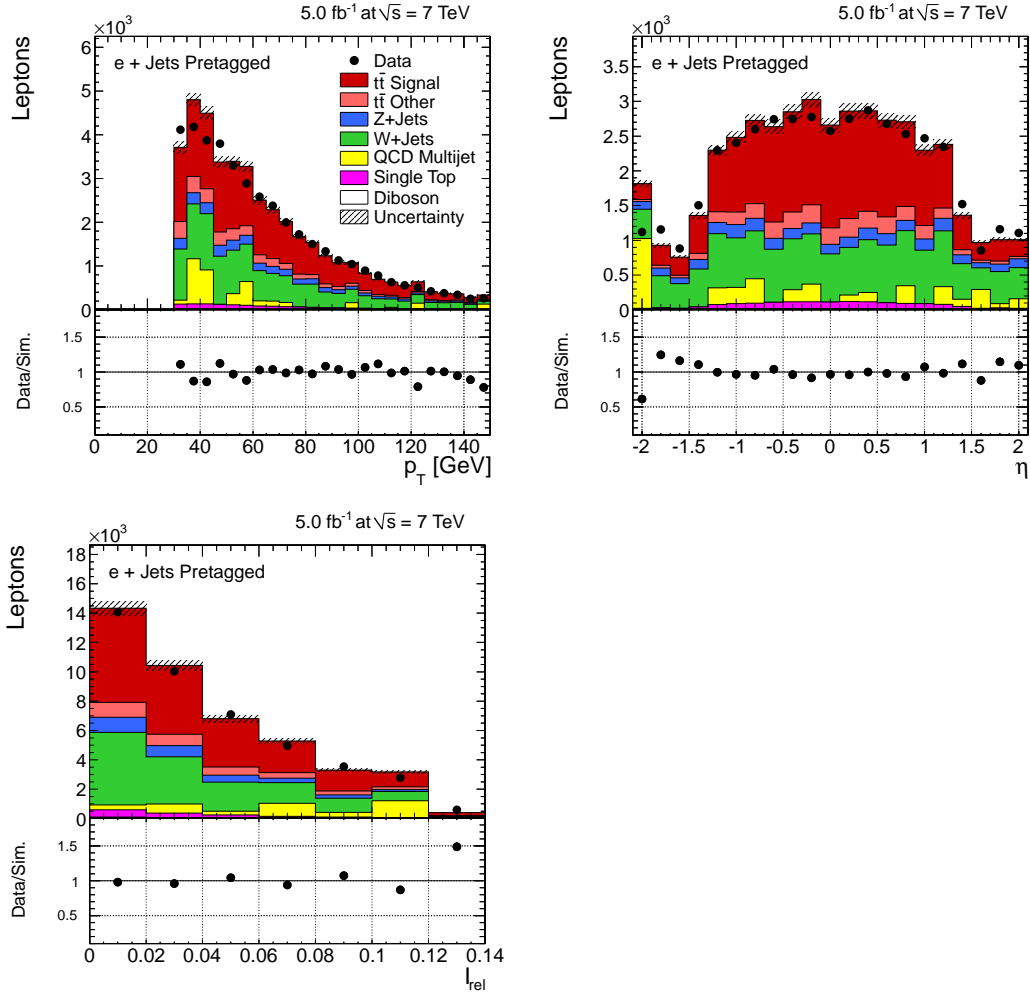
Figure 5.3: Kinematic electron variables (p_T, η, relative isolation I_{rel}) after selection (before b tagging) in the electron channel. The error bars represent the statistical uncertainty of the data. The hatched error band of the simulated distributions corresponds to the uncertainty of the luminosity measurement and of the theoretical inclusive $t\bar{t}$ cross section. Data-driven corrections related to pile-up as well as to lepton-selection and trigger efficiencies are applied to the simulation.

Figure 5.4: Kinematic jet variables and $E_{\mathrm{T}}^{\mathrm{miss}}$ after selection (before b tagging) in the muon channel. The error bars represent the statistical uncertainty of the data. The hatched error band of the simulated distributions corresponds to the uncertainty of the luminosity measurement and of the theoretical inclusive $t\bar{t}$ cross section. Data-driven corrections related to pile-up as well as to lepton-selection and trigger efficiencies are applied to the simulation.
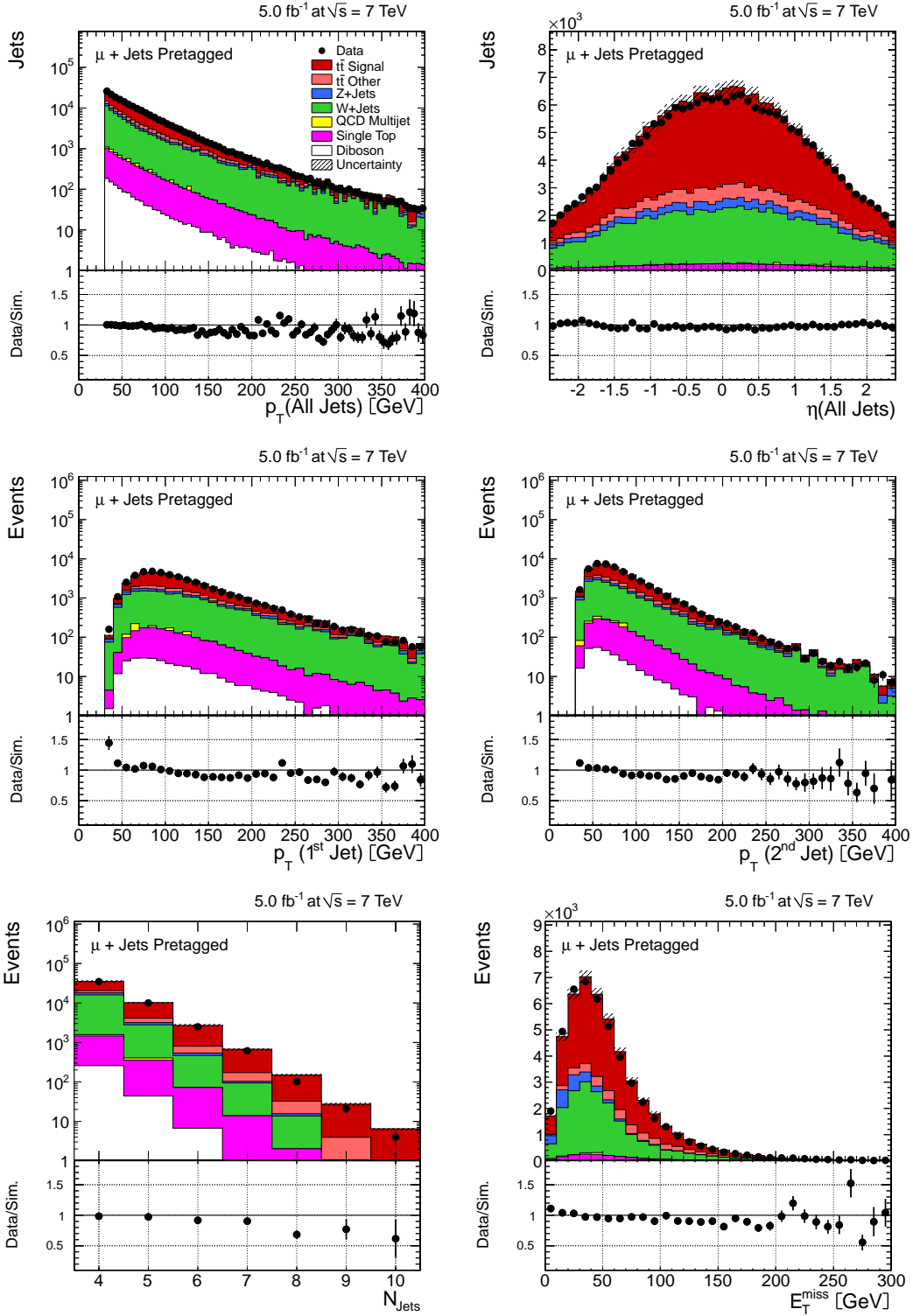
Figure 5.5: Kinematic jet variables and E_T^{miss} after selection (before b tagging) in the electron channel. The error bars represent the statistical uncertainty of the data. The hatched error band of the simulated distributions corresponds to the uncertainty of the luminosity measurement and of the theoretical inclusive $t\bar{t}$ cross section. Data-driven corrections related to pile-up as well as to lepton-selection and trigger efficiencies are applied to the simulation.
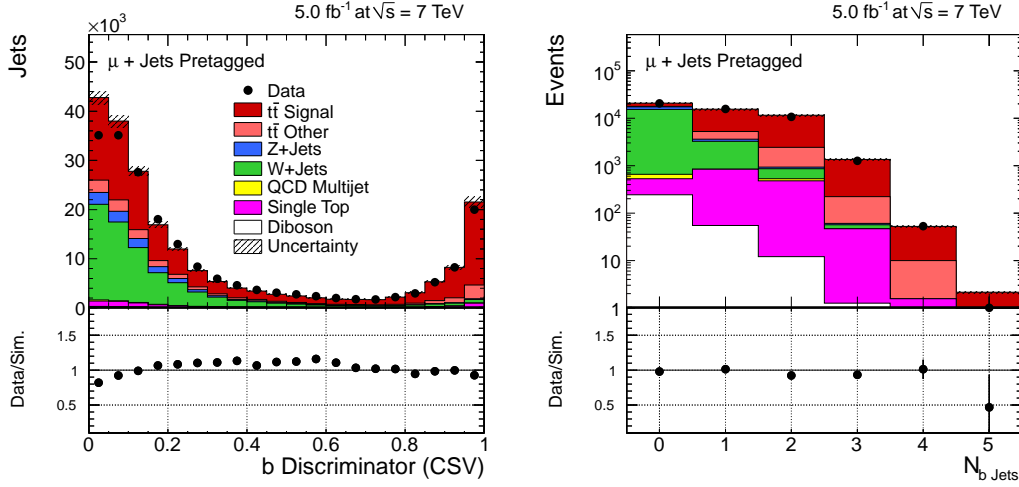
Figure 5.6: Monitoring distributions for b tagging in the muon channel: CSV discriminator and b-jet multiplicity. The error bars represent the statistical uncertainty of the data. The hatched error band of the simulated distributions corresponds to the uncertainty of the luminosity measurement and of the theoretical inclusive $t\bar{t}$ cross section. Data-driven corrections related to pile-up as well as to lepton-selection and trigger efficiencies are applied to the simulation.
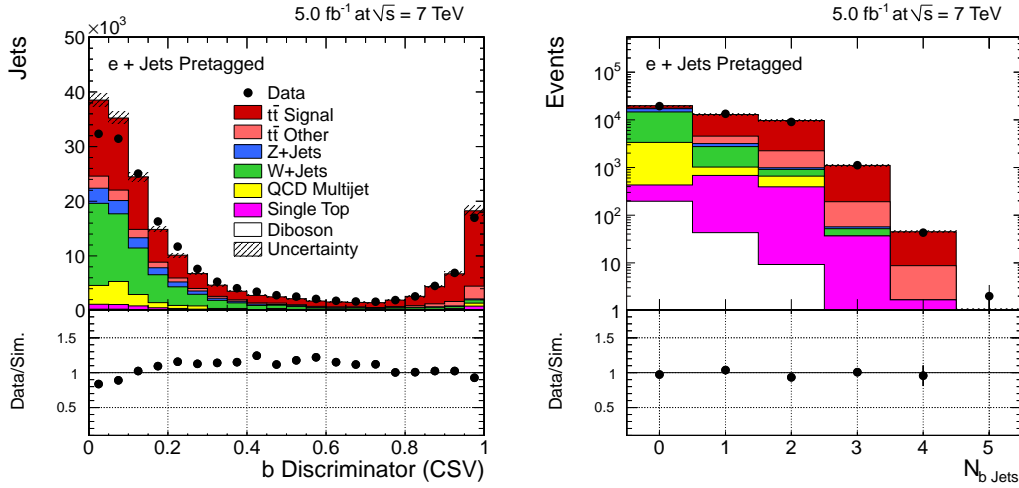

Figure 5.7: Monitoring distributions for b tagging in the electron channel: CSV discriminator and b-jet multiplicity. The error bars represent the statistical uncertainty of the data. The hatched error band of the simulated distributions corresponds to the uncertainty of the luminosity measurement and of the theoretical inclusive $t\bar{t}$ cross section. Data-driven corrections related to pile-up as well as to lepton-selection and trigger efficiencies are applied to the simulation.
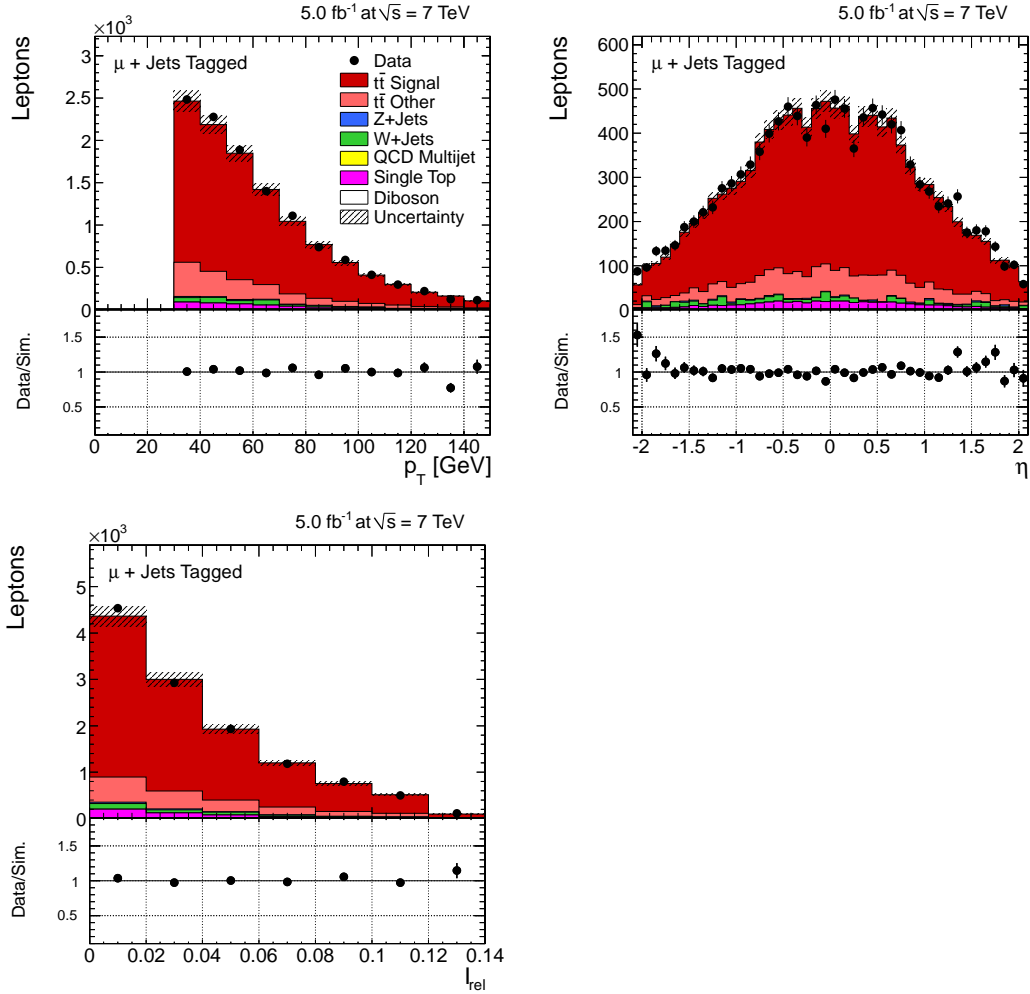
Figure 5.8: Kinematic muon variables (p_T, η, relative isolation I_{rel}) after selection (after b tagging) in the muon channel. The error bars represent the statistical uncertainty of the data. The hatched error band of the simulated distributions corresponds to the uncertainty of the luminosity measurement and of the theoretical inclusive $t\bar{t}$ cross section. Data-driven corrections related to pile-up as well as to lepton-selection, trigger and b-tag efficiencies are applied to the simulation.
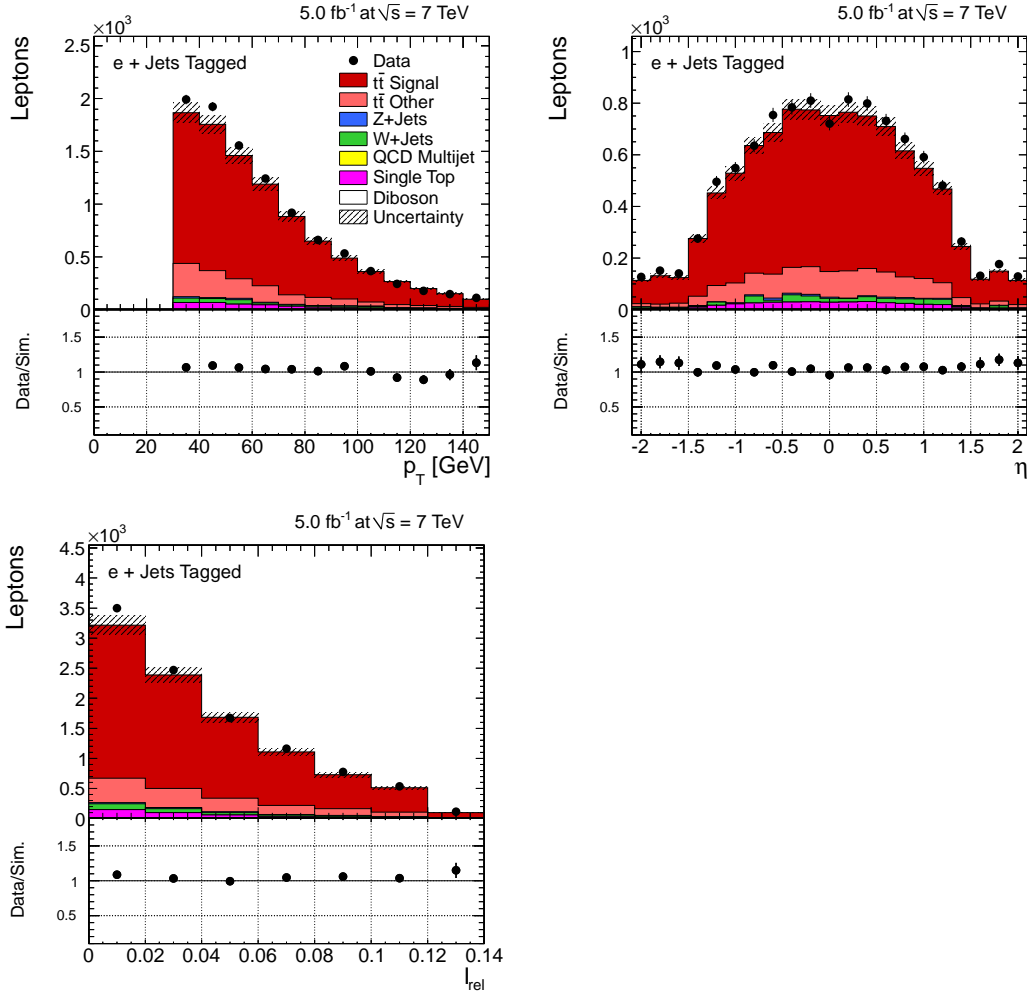
Figure 5.9: Kinematic electron variables (p_{T}, η, relative isolation I_{rel}) after selection (after b tagging) in the electron channel. The error bars represent the statistical uncertainty of the data. The hatched error band of the simulated distributions corresponds to the uncertainty of the luminosity measurement and of the theoretical inclusive $t\bar{t}$ cross section. Data-driven corrections related to pile-up as well as to lepton-selection, trigger and b-tag efficiencies are applied to the simulation.
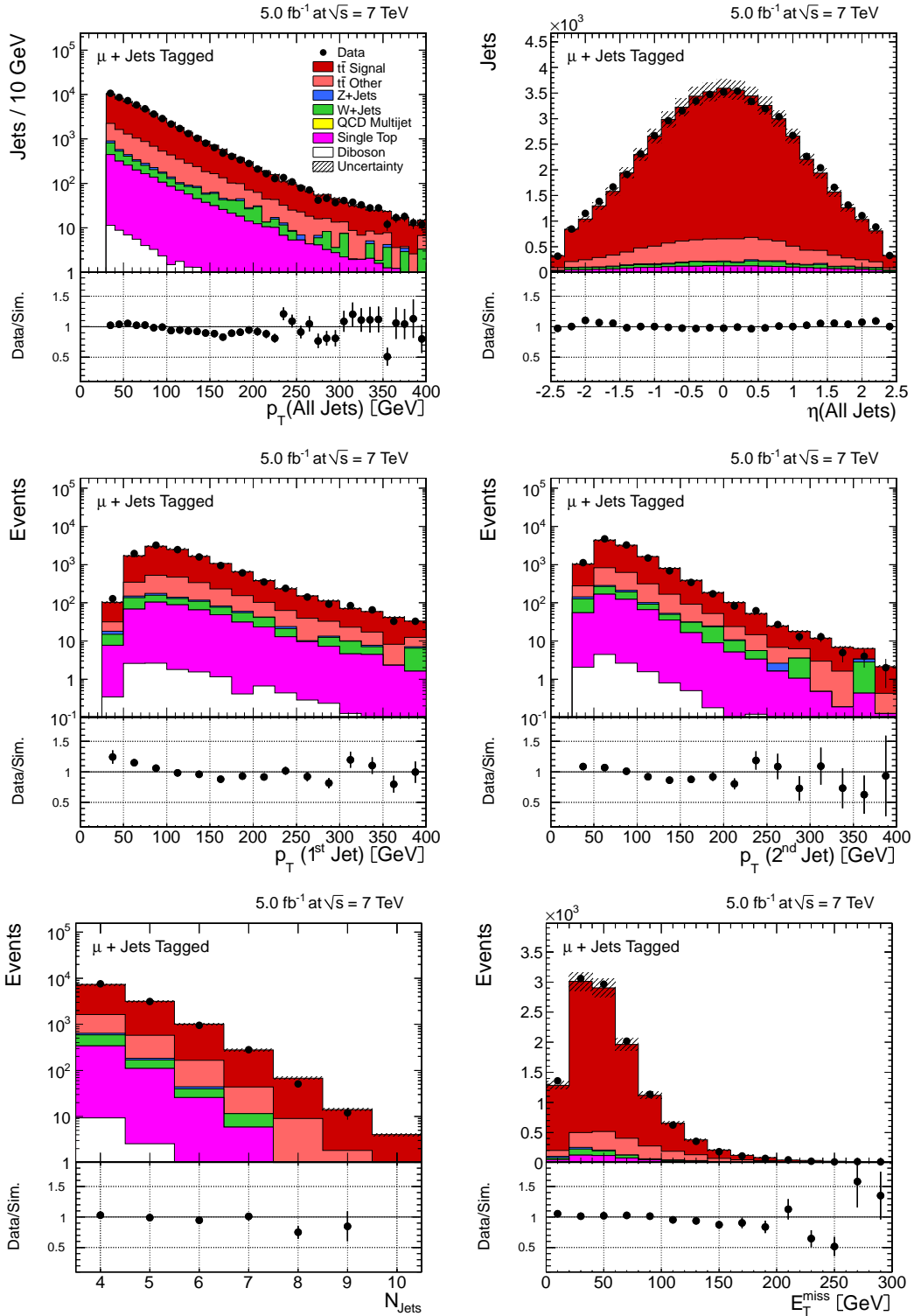
Figure 5.10: Kinematic jet variables and $E_{\mathrm{T}}^{\mathrm{miss}}$ after selection (after b tagging) in the muon channel. The error bars represent the statistical uncertainty of the data. The hatched error band of the simulated distributions corresponds to the uncertainty of the luminosity measurement and of the theoretical inclusive $t\bar{t}$ cross section. Data-driven corrections related to pile-up as well as to lepton-selection, trigger and b-tag efficiencies are applied to the simulation.

Figure 5.11: Kinematic jet variables and E_T^{miss} after selection (after b tagging) in the electron channel. The error bars represent the statistical uncertainty of the data. The hatched error band of the simulated distributions corresponds to the uncertainty of the luminosity measurement and of the theoretical inclusive $t\bar{t}$ cross section. Data-driven corrections related to pile-up as well as to lepton-selection, trigger and b-tag efficiencies are applied to the simulation.
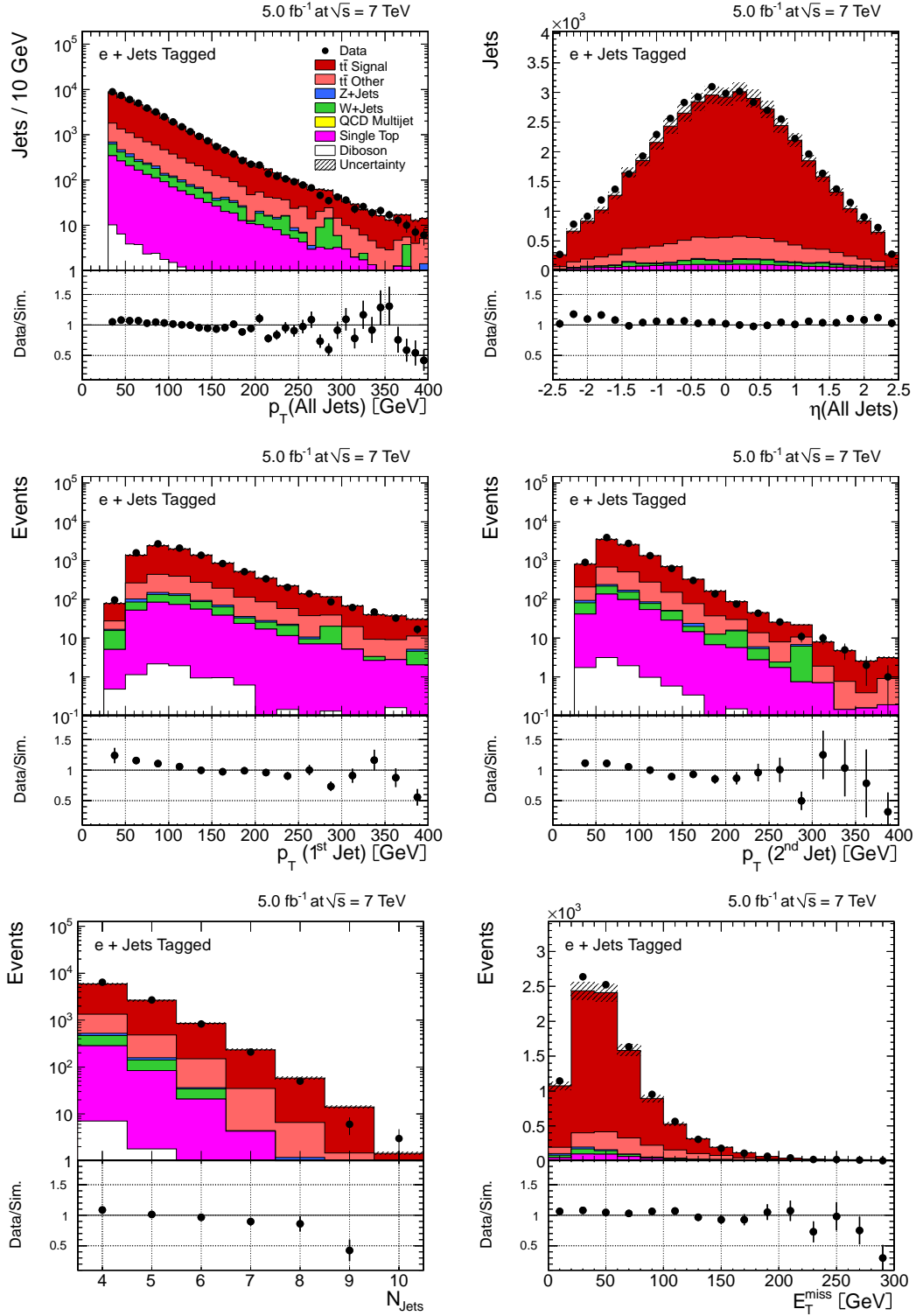
Chapter 6

Data-Driven Determination of Efficiencies

The main purpose of applying the signal selection is to reduce background events in order to obtain a clean signal sample. However, also signal events are cut away by this procedure. Moreover, also during triggering and reconstruction of the objects or simply due to limited geometric detector coverage (acceptance) a certain amount of signal events is lost. The ratio between the number of signal events that remain for analysis (reconstructed and selected, rec&sel) and the ones that are actually generated (gen) at the beginning is described by the efficiency:

$$\epsilon = \frac{N_{\text{rec\&sel}}}{N_{\text{gen}}}.$$ (6.1)

This efficiency can be factorised into the individual subefficiencies ϵ_{S_i} corresponding to each of the n steps S_i of the reconstruction and selection process:

$$\epsilon_{S_i[S_j]} = \frac{N_{S_i\&S_j}}{N_{S_j}}.$$ (6.2)

Note that these subefficiencies are relative to the selections S_j applied before (denoted in brackets). The total efficiency reads then:

$$\epsilon = \epsilon_{S_1} \cdot \epsilon_{S_2[S_1]} \cdot ... \cdot \epsilon_{S_n[S_1\&S_2\&...\&S_{n-1}]} = \frac{N_{S_1}}{N_{\text{gen}}} \cdot \frac{N_{S_1\&S_2}}{N_{S_1}} \cdot ... \cdot \frac{N_{S_1\&S_2\&...\&S_n}}{N_{S_1\&S_2\&...\&S_{n-1}}},$$ (6.3)

where $N_{S_1\&S_2\&...\&S_n} = N_{\text{rec\&sel}}$ from Eq. 6.1.

For the determination of the production cross section, the exact knowledge of the efficiency is of great importance (see Sec. 8.1).

The efficiency is determined by applying the whole analysis chain including triggering, reconstruction and selection to simulated signal events. However, the simulation

might not describe real data events perfectly, so that its validity needs to be checked in data and possible imperfections need to be corrected for.

One has to distinguish between the efficiency per object (e.g. lepton or jet) and the one per event. In the case of selecting exactly one object in the event selection (e.g. one lepton in this analysis), they are identical. However, in many cases more than one object is required, e.g. at least 4 jets and at least 2 b-tagged jets in this analysis. In that case, the event efficiency is a combination of the efficiencies of all objects in the event.

The efficiency determination in data requires either a clean background-free sample of events or objects of interest or the exact knowledge of the fraction of objects of interest with respect to the total number of objects in the sample. In many cases, these samples come from other processes than $t\bar{t}$ events. For instance, a pure sample of leptons (ℓ) for the determination of lepton-selection and trigger efficiencies is provided by $Z \to \ell\ell$ events, whereas the determination of b-tag efficiencies is usually done using di- or multijet events. These events have topologies that differ from $t\bar{t}$ events. Thus, the aim of these methods is not to determine absolute efficiencies, but to measure the ratio between the efficiency in data and the predicted one, which is also called *data-to-simulation scale factor* (SF):

$$SF = \frac{\epsilon_{\text{data}}}{\epsilon_{\text{sim}}} \tag{6.4}$$

It is assumed that this SF is largely caused by general imperfections in the detector modelling and therefore, in contrast to the efficiency itself, valid not only for the process for which it was determined, but for all processes including the signal and background ones. Furthermore, by constructing the ratio, systematic uncertainties or possible biases inherent to the method largely cancel. The SF is applied to all simulated samples used in this analysis as an event weight as explained in Sec. 4.3.

It is important to study the SF as a function of kinematic and topological variables of the objects of interest. On the one hand, this assures the validity of transferring the SF from the topologically different process used for the efficiency determination to the signal. And on the other hand, this is especially essential for differential cross sections that rely on the correct description of the efficiencies as a function of kinematic variables. For differential cross-section distributions normalised with the inclusive cross section, the shape of the SF is even the only relevant feature of interest as a flat SF cancels out completely (cf. Sec. 9). Also, the dependence on run conditions like pile-up is important to know.

As efficiencies can be regarded as binomial probabilities, their statistical uncertainties can be estimated by binomial errors. However, especially for efficiencies close to unity or zero and a low number of events, normal binomial errors are known to under-cover the desired confidence interval of 68% [131]. Thus, the values for the statistical uncertainties presented here refer to Clopper-Pearson confidence intervals [132], which guarantee the desired coverage and are therefore more conservative.

In the following, the data-driven determination of lepton-selection and trigger effi-

ciencies as well as b-tag efficiencies will be presented.

6.1 Lepton-Selection and Trigger Efficiencies

The lepton efficiencies are factorised into three components: lepton-reconstruction, -selection and -trigger efficiencies. They are determined subsequently with the *tag-and-probe* (T&P) method, which is explained below, i.e. as a first step the reconstruction efficiency, then the selection efficiency for already reconstructed leptons and lastly the trigger efficiency for already reconstructed and selected leptons:

$$\epsilon_\ell = \epsilon_{rec} \cdot \epsilon_{sel[rec]} \cdot \epsilon_{trig[rec\&sel]} \tag{6.5}$$

For the trigger efficiency in the electron channel it has to be considered that an electron-hadron cross trigger is used. It is assumed that it can be factorised into an electron and a jet leg. Thus, the electron-leg trigger efficiency is determined like in the muon channel as a part of the lepton efficiency with the T&P method, whereas the jet-leg trigger efficiency is determined with a separate method (see Sec. 6.1.3).

6.1.1 Tag-and-Probe Method

The *tag-and-probe* method is a well-established tool to determine efficiencies. Overviews on this method are given e.g. in [133, 134]. In its general version, it exploits a well-known correlation between two individually reconstructed objects. This correlation ensures that the precise identification of one of the objects using stringent selection criteria (called *tag*) automatically and unambiguously reveals the identity of the second object (called *probe*) without having imposed any requirements to be tested on the latter. Thus, this method is supposed to provide an almost background free and unbiased sample of objects that can be used for subsequent efficiency determination.

For the lepton-reconstruction, -selection and -trigger efficiencies, leptons from a resonance decaying into a dilepton final state, such as J/ψ or Z, can be utilised as one lepton ℓ is uniquely correlated with the other one via their invariant mass $m^{\ell\ell}$. For this analysis, Z-boson events are chosen as their topology is more similar to the one of $t\bar{t}$ events due to the larger mass of the Z boson. But still, leptons from inclusive dileptonic Z-boson decays have a softer p_T distribution and are less central due to the lower mass compared to the top quark. Furthermore, there is less hadronic activity close to the lepton in such events due to generally lower jet multiplicities on the one hand and the absence of a near b jet from the top-quark decay on the other hand. The latter might influence especially the isolation efficiency. Thus, the dependence of the SF on the kinematic variables p_T and η and the distance $\Delta R\,(\ell, \text{jet})$ between the lepton and the closest jet will be studied in detail to ensure the applicability of these results to $t\bar{t}$ events.

One well identified and isolated tag lepton is selected using the same tight criteria as for the analysis (see Sec. 5.1) in order to reduce background from multijet events

and misreconstructed leptons. In order to avoid a bias on the probe lepton, the tag is demanded to have fired the trigger (the leptonic part of it in case of a cross trigger), which is technically implemented by matching the offline muons to the HLT trigger objects using $\Delta R < 0.2$ as criterion. An oppositely-charged lepton candidate (requiring only very loose identification criteria; e.g. a PF lepton, see Sec. 5.1) is accepted as a *probe lepton* if the combined invariant mass of the two leptons lies within a narrow interval of ± 15 GeV around the Z-boson mass of 91 GeV (see Fig. 6.1). This sample of probe leptons can then be used to determine the efficiency for a certain selection relative to another one by counting the number of events that pass the selection of interest relative to the one applied before according to Eq. 6.2. If also the probe lepton fulfils the tight tag requirement, the event can be used twice by exchanging tag and probe. It has been checked that an alternative method using a fit to the resonance including a Voigtan[1] signal term and an exponential background term instead of simply counting event numbers yields comparable results. The background contribution obtained from the fit is found to be negligible due to the stringent tag selection and choice of the mass window (see Fig. 6.1). This justifies the use of the simpler cut-and-count method. Variations of the considered resonance-mass window (± 10 GeV or ± 20 GeV instead of ± 15 GeV around the Z-boson mass of 91 GeV) affect the results by maximally half a percent.

This procedure is applied to both data and the simulated Z+jets sample as listed in Sec. 4.2 in order to determine the SF.
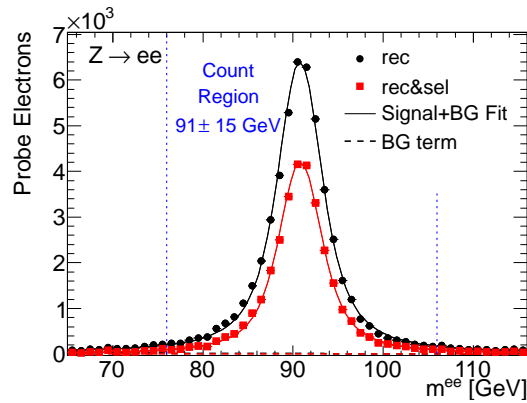

Figure 6.1: The distribution of probe electrons in data as a function of the invariant mass of probe and corresponding tag electron m^{ee} in the Z-boson resonance window. The probe electrons are shown after basic reconstruction as PF electrons (rec) and after passing additional identification and isolation selection (rec&sel). The counting region is indicated and the data is fitted with a Voigtan signal + exponential background (BG) term. The latter is almost zero ($<1\%$).

If not denoted otherwise, the following results are obtained in the phase space of this analysis, i.e. $p_T^\ell > 30$ GeV and $|\eta^\ell| < 2.1$. The simulation is reweighted in order to match the expected PU distribution in data. For this study, all PF leptons were

---

[1]Convolution of a Breit-Wigner resonance distribution with a Gaussian resolution term.

taken into account. However, in case jet information is needed like for the calculation of the distance ΔR between the lepton and the closest jet, a preselection of $I_{rel} < 0.2$ has to be applied to the lepton in order to have a clean jet definition using the PF top projections (see Sec. 5.1.5) consistent with the procedure of the analysis. However, the vast majority of events is included even after this preselection, so that the difference of the efficiency with or without preselection is only a few percent and much less for the SF. Also, cross checks were made using different lepton-jet cleaning approaches like top projections with a relaxed lepton isolation cut of $I_{rel} < 1$ or, alternatively, removing jets closer than $\Delta R = 0.3$ from the event. The thus obtained SF agrees well with the one from the standard procedure.

6.1.2   Muon Channel

Muon-Reconstruction Efficiency

The reconstruction efficiency has been extensively studied during the first run periods of CMS, e.g. in the course of the inclusive $W^{\pm}$- and Z-boson cross-section measurements [133], and those results are shortly presented here. The determination of the efficiency for the reconstruction of a muon in the inner-tracking region has been performed with good-quality stand-alone muons as probe muons. Vice-versa, the reconstruction efficiency for the tracks in the muon chamber has been studied using loose tracker muons as probes, i.e. well-reconstructed tracks that are only loosely-matched to muon-track segments. The efficiencies in data were found to be $(99.1 \pm 0.4)\%$ for the inner-tracking part and $(96.4 \pm 0.5)\%$ for the muon-chamber component and are well described by simulation with a SF consistent with unity. As the basic muon reconstruction is not process-dependent, the results of that measurement are considered applicable to this analysis as well. the muon reconstruction.

Muon-Selection Efficiency

The selection efficiency is defined relative to probe muons that are reconstructed as global and tracker muons. All the selection requirements listed in Sec. 5.1.3 are tested here, i.e. identification criteria (ID) regarding track quality and properties as well as the relative-isolation criterion (iso). In fact, the different parts of the selection can be evaluated separately with a factorising approach in order to learn more about their individual impact on the overall selection efficiency:

$$\epsilon_{sel[rec]} = \epsilon_{ID[rec]} \cdot \epsilon_{iso[rec\&ID]} \tag{6.6}$$

For the online selection of the events, the same triggers are used as for the analysis, i.e. IsoMu17 or IsoMu24(eta2p1) for data depending on the run range and IsoMu24eta2p1 for the simulation (see Tab. 5.3), which are demanded to be fired by the tag muon.

The average overall muon-selection efficiency is measured to be $(87.92 \pm 0.02)\%$ in data. It is well modelled by the simulation with an average SF of 0.9831 ± 0.0003. The

SF is flat within 1 to 2% as a function of all variables studied here. This can be seen from Fig. 6.2, which shows the overall selection efficiency and the corresponding scale factor as a function of p_T and η of the muon, the number of primary vertices (N_{PV}) in the event and the distance ΔR between the muon and the closest jet. Note that a preselection of $I_{rel} < 0.2$ is applied for the latter as jets are not well defined outside this region as explained above. The same plots separately for the factorised components (ID and iso) are shown in App. B.

A strong efficiency dependence on p_T is observed with an efficiency of $\approx 80\%$ around 30 GeV, which rises up to a plateau of $\approx 95\%$, which is reached around 60 GeV. This behaviour is caused by the fact that the isolation criterion is defined relative to the p_T of the muon, so that at low p_T the fraction of muons with a low relative isolation is larger, given an approximately constant amount of additional momentum in the cone around the muon. In contrast, the identification efficiency (cf. App. B) is observed to be flat in p_T. The SF tends to slightly lower values at low p_T, but the deviation is only at the percent level.

The selection efficiency as a function of η is quite constant with only slightly lower values in the central and outer region compared to the intermediate $|\eta|$. Also the SF does not show any dependence on η with fluctuations around its mean at the percent level.

The selection efficiency strongly depends on N_{PV} in the event, which is highly correlated with the number of PU interactions. It drops by 20% from low N_{PV} to $N_{PV} = 20$ as PU introduces additional particles that increase the value of I_{rel}. The general behaviour is well reproduced by the simulation, with the SF being 1 to 2% lower at high N_{PV} compared to the one at low N_{PV}. It becomes obvious that it is absolutely vital for the simulation to match the PU distribution in data as described in Sec. 4.3.

For a small distance ΔR between the muon and the jet, the efficiency drops significantly due to the isolation cut, which is well described by the simulation. Cross-checks using a different lepton-jet cleaning arrive at the same conclusion.

Muon-Trigger Efficiency

The trigger efficiency is defined relative to probe muons that pass the offline selection. The tag muon is defined as in the previous step and the probes are tested if they have fired the trigger using the same online-offline matching method as for the tag muon described above. Thus, effectively the combined L1+HLT trigger efficiency is tested. The efficiency is determined for the single-muon triggers that are used in this analysis, i.e. IsoMu17(24)(eta2p1) depending on the run range for data and IsoMu24eta2p1 for the simulation (see Tab. 5.3). It is reminded that the numbers indicate the p_T and $|\eta|$ trigger thresholds and that there is an absolute detector-based isolation criterion applied at trigger level (see Sec. 5.1.3, 5.2.2).

Fig. 6.3 shows the trigger efficiencies and the corresponding scale factors as a function of the same quantities as for the selection efficiency, averaged over the full run
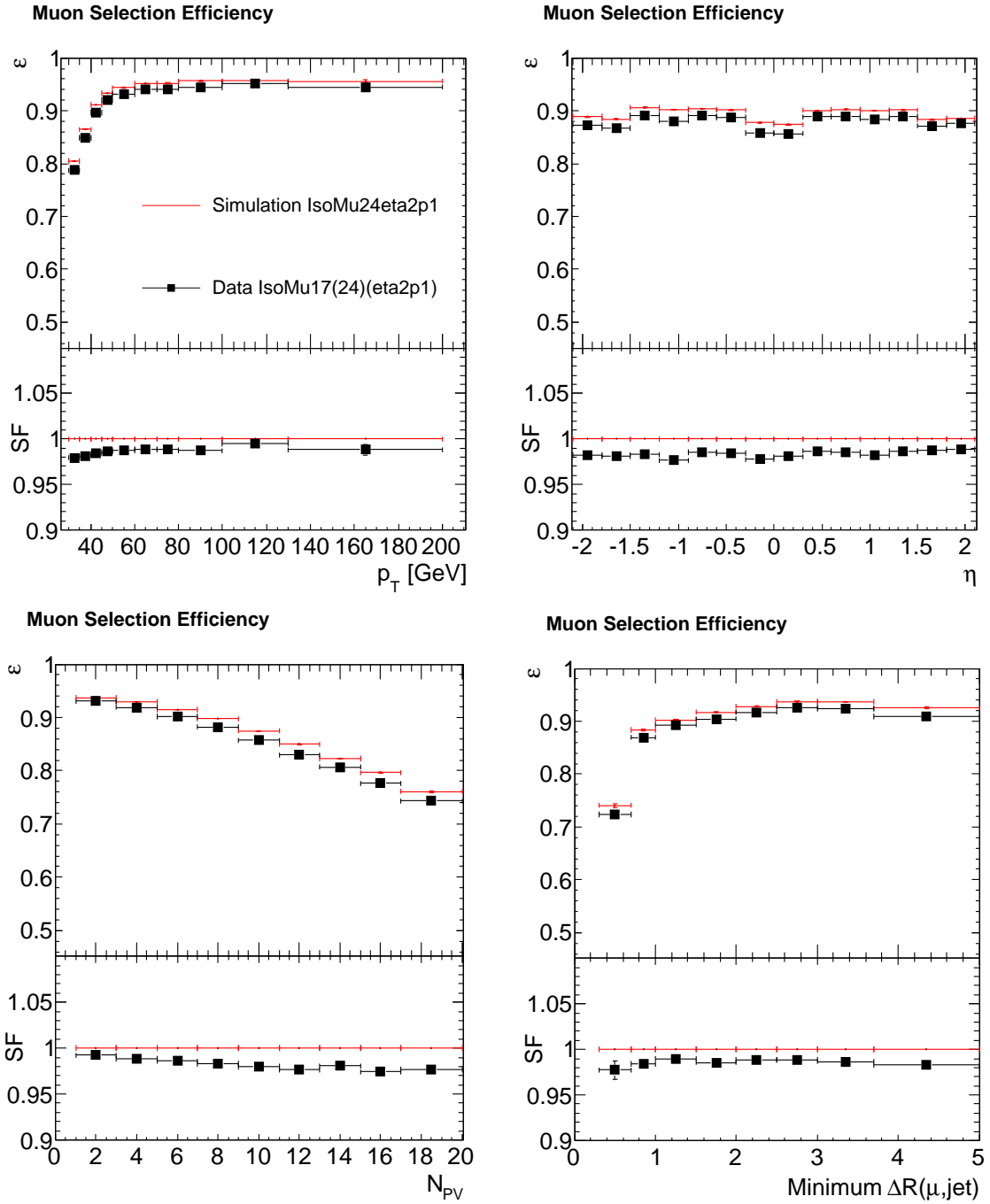
Figure 6.2: The muon-selection efficiency measured in data and the simulation with corresponding SF as a function of p_T (*top left*) and η (*top right*) of the muon, the number of primary vertices N_{PV} in the event (*bottom left*) and the distance between the muon and the closest jet (minimum $\Delta R(\mu, \text{jet})$, *bottom right*). A preselection of $I_{rel} < 0.2$ is applied to the ΔR distribution.
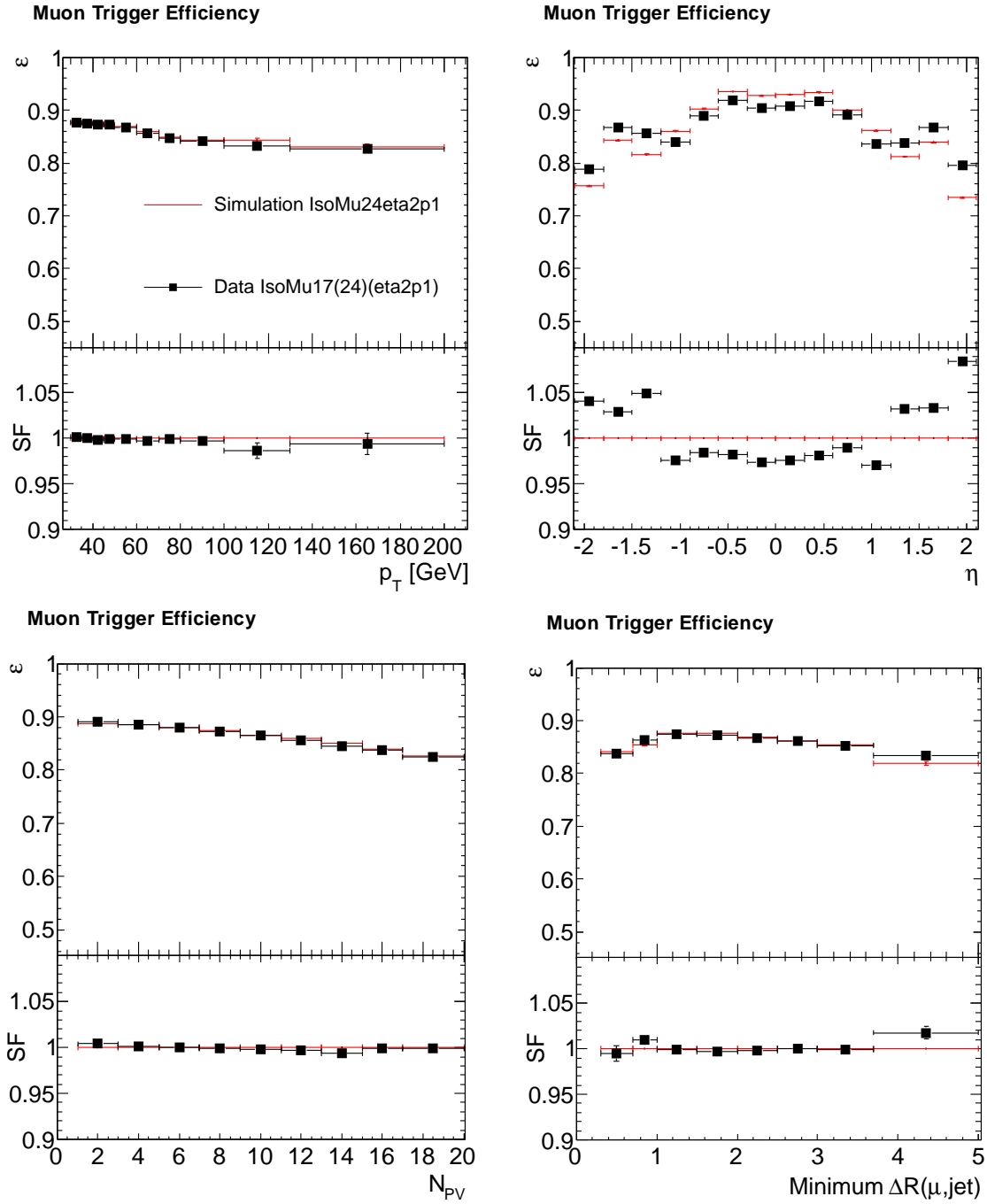
Figure 6.3: The muon-trigger efficiencies measured in data and the simulation with corresponding SF as a function of p_T (*top left*) and η (*top right*) of the muon, the number of primary vertices N_{PV} in the event (*bottom left*) and the distance between the muon and the closest jet (minimum $\Delta R(\mu, \text{jet})$, *bottom right*).

range. The average efficiency is measured to be $(87.27 \pm 0.02)\%$ in data with an average SF of basically unity (0.9992 ± 0.0004). However, as discussed below, the SF is observed to be strongly η dependent.

From the trigger efficiency as a function of p_T, it can be seen that the offline cut of 30 GeV is sufficiently high above the trigger thresholds to avoid turn-on effects[2], which are difficult to model. The efficiency even decreases from 88% at 30 GeV to about 83% between 100 and 200 GeV. Such an effect is not observed for non-isolated single-muon triggers. It is introduced due to the subtleties of different online and offline isolation criteria (absolute detector-based isolation vs. relative PF isolation). As this efficiency is measured on events having passed already the I_{rel} offline selection and as the absolute isolation is the relative one multiplied with p_T, the fraction of muons with a high value of absolute isolation is larger at high p_T than at low p_T. But it can be seen that the efficiency is well-described by the simulation with a SF that is flat in p_T at the percent level.

The efficiency is observed to be highly dependent on η with about 90% in the central region and 80% in the outer part around $|\eta| = 2.1$. The general trend is also described by the simulation, but it overestimates the data in the barrel and overlap regions up to $|\eta| = 1.2$ and underestimates it in the endcap part. The difference between the SF of these regions is up to 10%. In order to investigate this effect, one has to consider that the data efficiency is averaged over a lot of run periods with different trigger menus (see Sec. 5.2.2). On the one hand, different triggers are used depending on the run range, but even for the same trigger, there are different versions with changes in the trigger algorithms from one menu to another. Either improved algorithms were implemented or changes to reduce the trigger rate were necessary with increasing instantaneous luminosity. These modifications are reflected in a change of the trigger efficiency, which can be seen from Fig. **??**, where different run ranges are compared. Whereas the central region is hardly affected, there are substantial changes in the overlap and endcap regions. For instance, improvements in the L1-trigger algorithm related to CSC track finding and the quality criteria of the global muon trigger lead to an efficiency increase in the endcap region from the 5e32 to the 1e33 menu. In contrast, the introduction of muon-track-quality cuts at L2 for $0.9 < |\eta| < 1.5$ starting from the 2e33 menu leads to an efficiency drop especially in the overlap region. Moreover, a sophistication in the merging of L1 trigger muon objects coming from different muon chamber systems (RPC vs. DT/CSC), which is needed for the p_T determination of the L1 trigger muon, results in an efficiency increase from the 3e33A to the 3e33B menu, but this is mainly compensated by a decrease due to the higher PU in the 2011B run range.

The trigger version used in the simulation is similar to the one from the 3e33A menu. However, although the agreement is better when comparing the simulated efficiency to the efficiency in data for this trigger menu, residual differences remain.

Due to the isolation requirement of the trigger, which differs from the offline one, the efficiency depends on N_{PV}. The isolation criterion also introduces a slight dependence

---

[2]Trigger *turn-on* effects refer to the smearing of the threshold step function when the efficiency is shown as a function of variables of the offline objects. They arise from differences between online and offline object definitions.

on the distance between the muon and the closest jet. The SF as a function of these two variables is flat up to variations at the percent level.
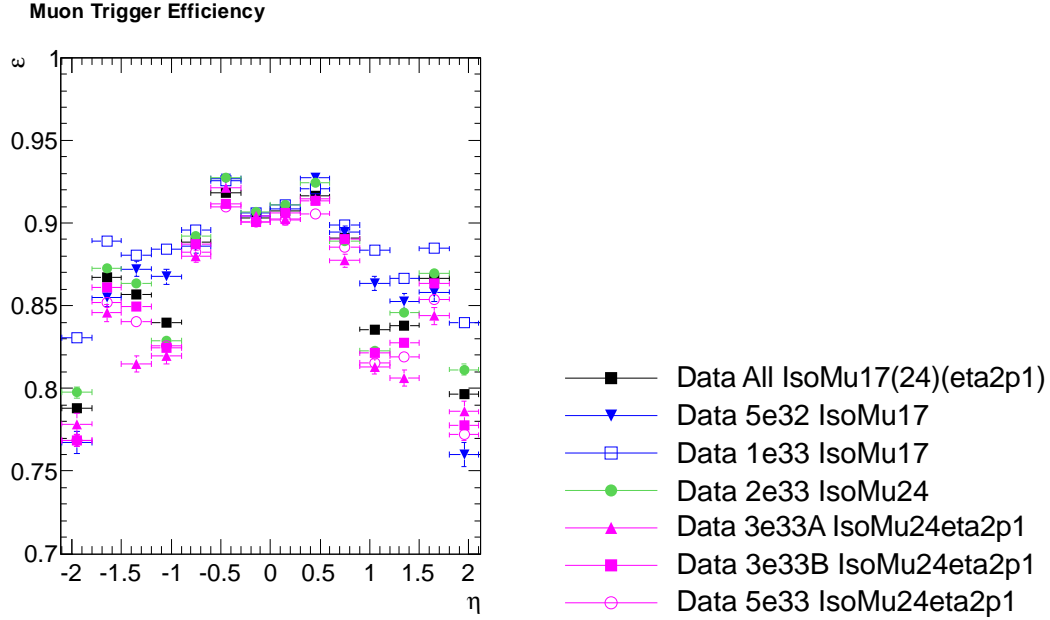

Figure 6.4: The muon-trigger efficiencies for different 2011 run ranges as a function of η. The different periods are according to the changing trigger menus deployed for data taking (see Tab. 5.2). The colours correspond to the different triggers used. The black marker corresponds to the average over the whole run range (the same as shown in Fig. 6.3, *top right*).

Final Efficiency Scale Factors in the Muon Channel

As the muon-trigger and selection efficiencies were obtained in a factorised approach, they can be combined by multiplication, i.e. by taking all probe leptons before any trigger and lepton selection as denominator and the leptons that pass these requirements as the numerator. The combined average efficiency scale factor including selection- and trigger-efficiency scale factors is measured as 0.9824 ± 0.0004. As the trigger-efficiency scale factor is highly η dependent, this is also valid for the combined scale factor. Thus, the scale factor is parametrised as a function of η in the bins as shown in Fig. 6.3 (*top right*) and applied as event weight to the simulation. The deviations from a flat SF in other distributions are observed to be small and are taken into account as systematic uncertainties (see Sec. 9.2.4).

6.1.3 Electron Channel

Electron-Reconstruction Efficiency

As in the muon channel, the reconstruction efficiency has been studied for the inclusive $W^{\pm}$- and Z-boson cross-section measurements [133]. It has been determined relative to probes made of ECAL superclusters with $E_T > 20\,\text{GeV}$ that are required to fulfil loose shower-shape and isolation criteria uncorrelated with the reconstruction efficiency. It was then tested, for how many of these probe clusters the reconstruction of GSF electron tracks is successful. An efficiency of $(98.6\pm0.5)\%$ and $(96.2\pm0.8)\%$ is measured for the barrel and the endcap region, respectively, which is well reproduced by the simulation with a SF compatible with one.

Trigger for the Determination of Electron-Selection and -Trigger Efficiency

In the electron channel, the electron-hadron (EleHad) cross triggers Ele25TriJet and IsoEle25TriJet are used in this analysis, which select online one electron with $E_T > 25\,\text{GeV}$ (isolated from menu 1e33v2 on) and at least three jets with $p_T > 30\,\text{GeV}$ (see Sec. 5.2.2). In simulated events, the version for isolated electrons is used. The use of a cross trigger makes the determination of the selection and trigger efficiencies more complicated. On the one hand, now also the efficiency of the hadronic part of the cross trigger needs to be determined. And on the other hand, also the determination of the efficiency of the leptonic part of the trigger and the electron-selection efficiency is complicated by the additional jets. There are two possible approaches:

Either suitable single-electron control triggers can be used. Ideally, this would be one with the same properties and threshold as the electron leg of the cross trigger, but unfortunately such is not available. But there are similar triggers with the same online ID and isolation requirements[3], but a slightly higher p_T threshold of 27 or 32\,GeV: IsoEle27(32). However, after $894\,\text{pb}^{-1}$, starting from menu 1.4e33, these are highly prescaled (by an average factor of 11 during menu 1.4e33 and typically a factor of 40 to 50 later) or missing completely, resulting in only $975\,\text{pb}^{-1}$ total effective luminosity.

A second approach is to use the subtrigger filter corresponding to the electron leg of the cross trigger itself. This has the advantage that the trigger in question is directly used, so that there is no problem with deviating properties or thresholds. Furthermore, the trigger is unprescaled for the whole run range[4]. But on the other hand, the additional triggering on jets also reduces the number of events available for efficiency determination as Z+jets events are rare, resulting in increased statistical uncertainties. However, electron-jet cleaning on trigger level is performed for only one electron, so that additional electrons are also regarded as trigger jets. Thus, in case of events with Z bosons decaying to two electrons, the IsoEle25TriJet trigger effectively

---

[3]This only refers to the isolated version; there are no suitable non-isolated single-electron control triggers available.

[4]But due to technical reasons, the subtrigger information corresponding to the electron leg is not available for trigger menu 5e32, i.e. the first $216\,\text{pb}^{-1}$.

behaves as an IsoEle25DiJet trigger selecting also events with only two additional jets. Another difference compared to single-electron triggers is a slightly higher level of PU for triggered events as jets from additional interactions are not removed at HLT level and increase the trigger probability of the jet trigger.

It needs to be checked that no bias is introduced by these effects. Therefore, both approaches are studied and compared in the following for the first run ranges during which the single-electron triggers are not yet highly prescaled. By this, the second approach can be validated with the first one and is subsequently applied to the whole data set.

Electron-Selection Efficiency

The selection efficiency is defined relative to probe electrons that are reconstructed as PF electrons. All the selection requirements listed in Sec. 5.1.4 are tested here, i.e. identification (d_0 cut and CiC ID), isolation and conversion-rejection criteria. Like for the muons, the different parts of the selection can be evaluated separately with a factorising approach:

$$\epsilon_{sel[rec]} = \epsilon_{d_0[rec]} \cdot \epsilon_{ID_{CiC}[rec\&d_0]} \cdot \epsilon_{iso[rec\&d_0\&ID_{CiC}]} \cdot \epsilon_{conv.rej.[rec\&d_0\&ID_{CiC}\&iso]} \qquad (6.7)$$

| | Electron-Selection Efficiency | |
Method	Data [%]	SF
Single-Electron Trigger	70.8 ± 0.1	0.977 ± 0.001
EleHad Trigger	68.0 ± 0.5	0.973 ± 0.007

Table 6.1: A comparison of the electron-selection efficiency and its corresponding SF as obtained with single-electron and EleHad triggers for the early run range defined by the trigger menus 1e33v2 and 1.4e33.

First, both methods (i.e. either using single-electron or EleHad triggers for online selection) are applied to the early run range defined by the trigger menus 1e33v2 and 1.4e33 (≈ 800 pb^{-1}). During this range, the IsoEle25 subtrigger information is already available on the one hand and the single-electron trigger is not yet (or only weakly) prescaled on the other hand. This facilitates the comparison of the two approaches under similar conditions, especially with respect to PU. The tag electron is required to have fired the trigger or, in the case of the cross trigger, the electron leg of it. As shown in Tab. 6.1, the average selection efficiency obtained using the cross trigger is about 3% lower than the one obtained with the single-electron trigger, probably due to the slight shift towards higher PU as explained above. However, this difference is well described by the simulation. Thus, the SFs differ by only 0.4%, which is well within the uncertainties, validating that both methods can be used alternatively. In the following, the results obtained with the unprescaled IsoEle25TriJet for the full available dataset are presented.

The average overall electron-selection efficiency is measured to be $(62.0 \pm 0.2)\%$ in data. Most inefficiencies come from the isolation and the conversion-rejection requirements as shown in Tab. 6.2, which displays the different components of the overall selection efficiency. It is well modelled by the simulation with an overall SF of 0.974 ± 0.004.

Selection Step	Data Efficiency [%]	SF
d_0	97.30 ± 0.07	0.9935 ± 0.0008
$\mathrm{ID_{CiC}}$	95.33 ± 0.09	0.987 ± 0.001
Isolation	84.4 ± 0.2	0.992 ± 0.002
Conv. Rej.	79.1 ± 0.2	1.001 ± 0.003
Overall Selection	62.0 ± 0.2	0.974 ± 0.004

Table 6.2: The factorised components of the average selection efficiency and their corresponding SFs as obtained with the T&P method using the IsoEle25TriJet trigger for the full available dataset.

Fig. 6.5 shows the overall selection efficiency and the corresponding scale factor as a function of p_T and η of the electron, the number of primary vertices N_{PV} in the event and the distance ΔR between the electron and the closest jet. Also here a preselection of $I_{rel} < 0.2$ is applied for the latter in order to have well-defined jets using the PF top projection as explained above. The same plots separately for the different efficiency components are shown in App. B. The general trend of the p_T dependence is similar to the one of the muons, being dominated by the I_{rel} cut: The efficiency increases with p_T up to a plateau at $80\,\mathrm{GeV}$. Within the barrel region, it rises by about 5% from the central part to $|\eta| = 1.5$, before it drops by 15% in the endcaps, which is dominated by the conversion-rejection efficiency due to the high track density in that region. The decrease of the efficiency with N_{PV} is mainly due to the isolation efficiency and also due to the conversion-rejection efficiency. The isolation criterion leads to a decrease of the efficiency at small ΔR (e, jet). The SF is flat within about $\pm 2\%$ as a function of all variables studied here. The statistical fluctuations are larger than for the muons due to less triggered events.

Electron-Trigger Efficiency

It is assumed that the electron and hadron leg of the (Iso)Ele25TriJet cross trigger are independent of each other, so that the efficiency of the cross trigger can be factorised into an electron and a hadron component. This assumption is challenged by the fact that an electron might be identified as a jet (enhanced by the incomplete online electron-jet cleaning of only one electron as described above) and vice-versa. However, it will be shown that the effect is small. On the one hand, the determination of the trigger efficiency of the electron leg is verified with single-electron triggers, which are independent of jet triggers. And on the other hand, the determination of the jet-leg efficiency is performed on events passing the $t\bar{t}$ selection of exactly one tight lepton (even vetoing the presence of looser ones), for which the lepton-jet cleaning is done
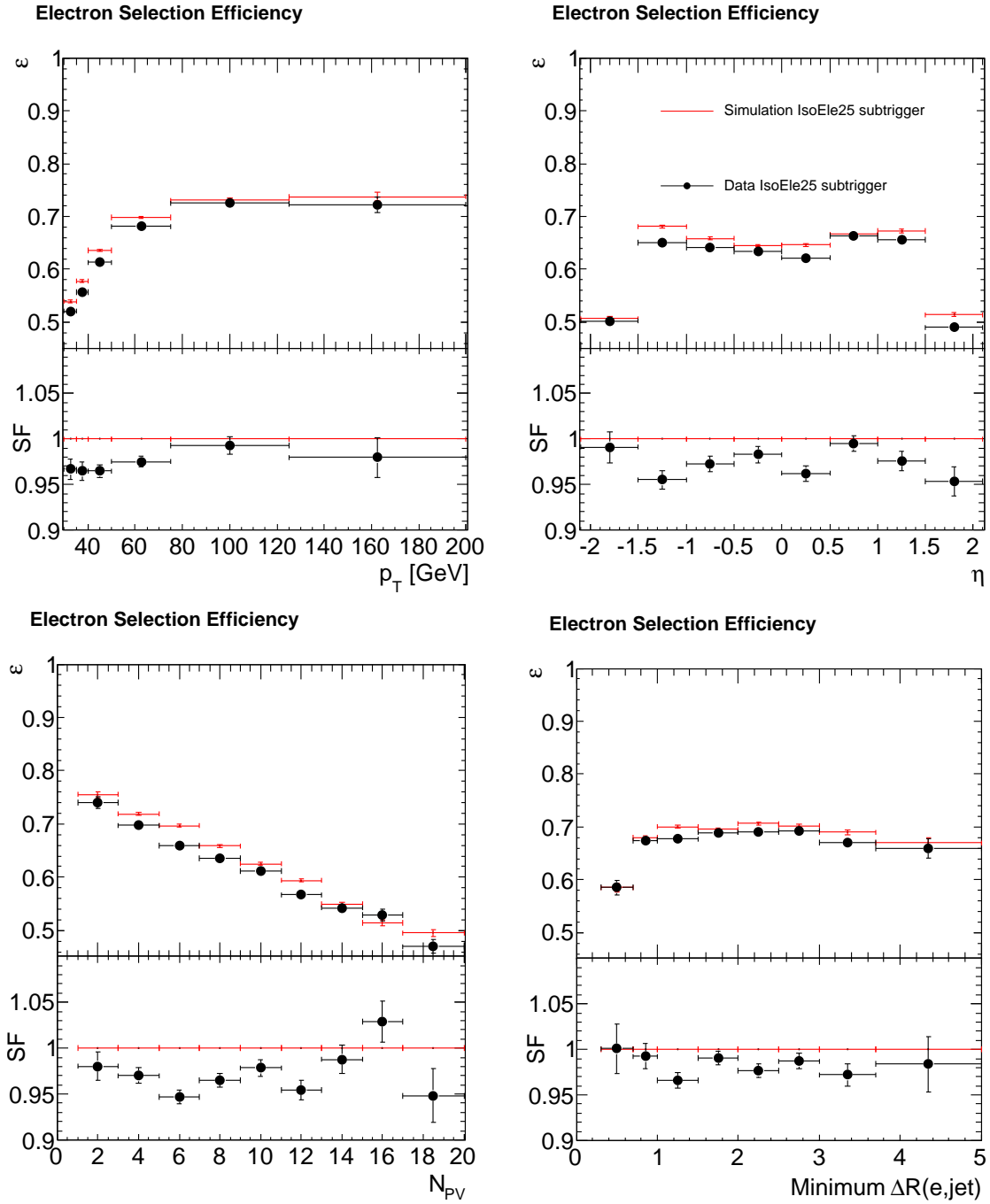
Figure 6.5: The electron-selection efficiency obtained with the IsoEle25TriJet cross trigger in data and the simulation with corresponding SF as a function of p_T (*top left*) and η (*top right*) of the electron, the number of primary vertices N_{PV} in the event (*bottom left*) and the distance between the electron and the closest jet (minimum $\Delta R(e, \text{jet})$, *bottom right*). A preselection of $I_{rel} < 0.2$ is applied to the ΔR distribution.

appropriately. Moreover, the latter is also studied using muon-jet cross triggers, for which the correlation between the lepton and the jet components are almost negligible.

Electron-Trigger Efficiency - Electron Leg

	Electron-Trigger Efficiency	
Method	Data [%]	SF
Single-Electron Trigger	96.63 ± 0.05	0.9956 ± 0.0006
EleHad Trigger	96.9 ± 0.3	0.997 ± 0.003

Table 6.3: A comparison of the electron-trigger efficiency and its corresponding SF as obtained with single-electron and EleHad triggers for the early run range defined by the trigger menus 1e33v2 and 1.4e33.

The trigger efficiency of the electron leg is defined relative to tight electrons that pass the requirements of the offline selection. The tag electron is defined as in the previous section and the probes are tested if they have fired the single-electron trigger or, in the case of the cross trigger, the electron subtrigger leg.

As for the selection efficiency, the two methods (single-electron trigger IsoEle32 vs. electron subtrigger leg of the cross trigger IsoEle25TriJet) are first applied to the early run range defined by the trigger menus 1e33v2 and 1.4e33 for which they can be compared under similar, unprescaled conditions. Only the isolated version of the cross trigger (from menu 1e33v2 on) is taken into account as the single-electron trigger has the same isolation requirements. Moreover, to ensure the comparability of triggers with different p_T thresholds ranging from 25 to 32 GeV, the results are compared for $p_T > 37$ GeV in order to be at least 5 GeV above the trigger threshold to be consistent with the $t\bar{t}$-event selection. As demonstrated in Tab. 6.3, a remarkable agreement between the two methods at the permille level is found, both for the efficiency and for the SF, which confirms that both can be used alternatively.

Fig. 6.6 shows the electron-trigger efficiency determined with the cross trigger IsoEle25TriJet and the corresponding scale factor for the full available dataset (i.e. from menu 1e33v2 on) as a function of the same quantities as for the selection efficiency. The average efficiency is measured to be $(96.1 \pm 0.1)\%$ in data. Only slight dependences on the shown quantities are seen as 30 GeV seems to be sufficiently high above the trigger threshold and the ID and isolation requirements on trigger level are sufficiently loose with respect to the offline selection. Thus, there is also hardly any dependence on PU observed. The simulation describes the data well with SFs close to one that deviate by typically 1% from the average value of 0.993 ± 0.001.

Due to technical reasons, the subtrigger information is only stored from menu 1e33v1 on. Thus, for the determination of the efficiency of the non-isolated version of the trigger (Ele25), which is used up to run 165970, the number of events available for the efficiency determination is very low leading to large uncertainties. Therefore, another approach is followed: the difference between the Ele25 and IsoEle25 subtrigger legs is studied in data for runs $165970 - 167913$, during which both Ele25TriJet (already
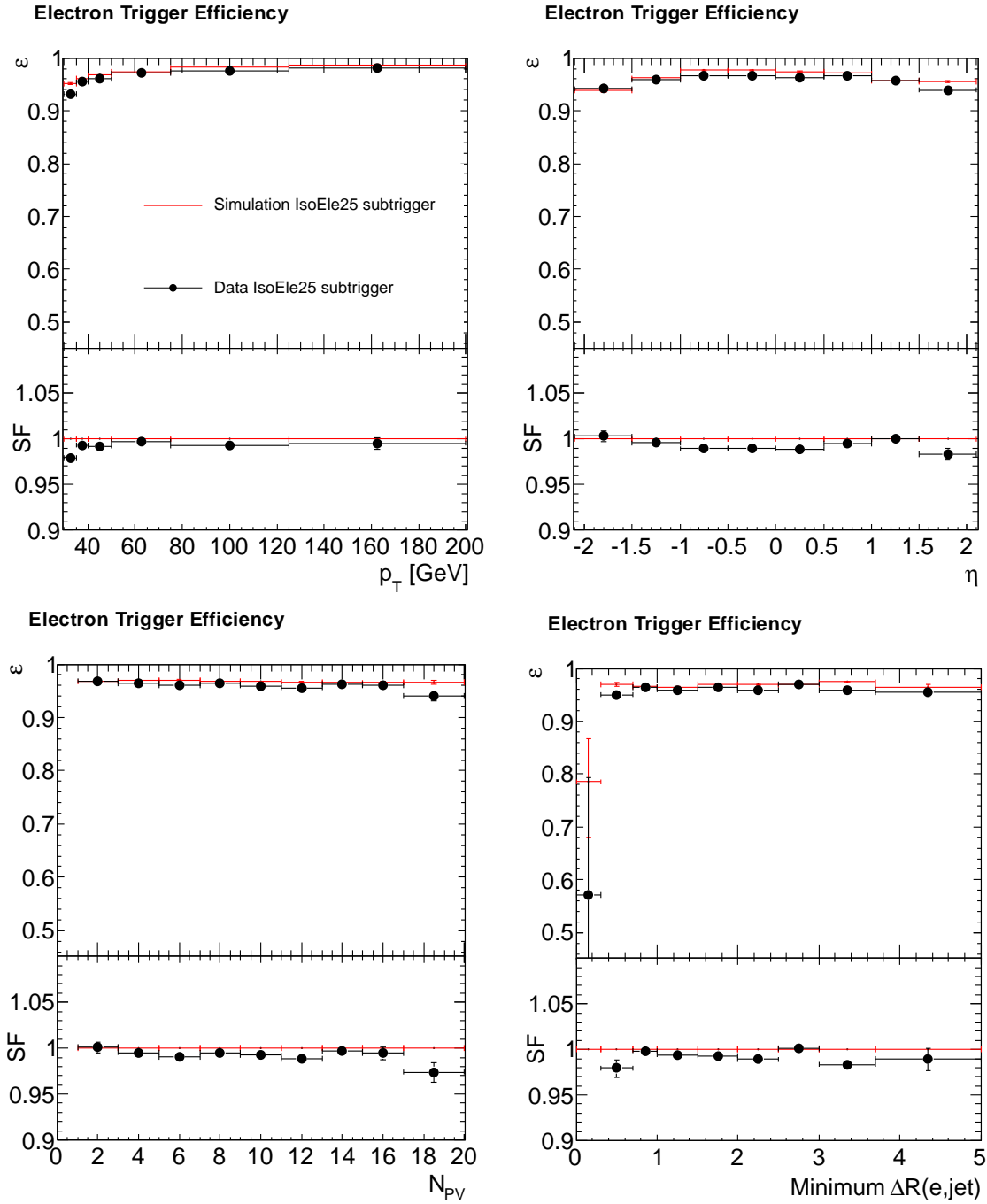
Figure 6.6: The trigger efficiency for the electron leg of the IsoEle25TriJet cross trigger measured in data and the simulation with corresponding SF as a function of p_T (*top left*) and η (*top right*) of the electron, the number of primary vertices N_{PV} in the event (*bottom left*) and the distance between the electron and the closest jet (minimum $\Delta R(\mathrm{e}, \mathrm{jet})$, *bottom right*).

prescaled) and IsoEle25TriJet are present in the trigger menu. The relative efficiency ϵ(IsoEle25TriJet wrt. Ele25TriJet) can be measured using the ratio of the number of events after the full pre-tagged $t\bar{t}$ selection that fire IsoEle25TriJet and Ele25TriJet. The ratio is flat as a function of all variables but the relative isolation. Thus, an I_{rel} dependent parametrisation is obtained by fitting a 2nd order polynomial:

$$\epsilon(\text{IsoEle25TriJet wrt. Ele25TriJet}) = 0.997 + 0.05 \cdot I_{rel} - 3 \cdot I_{rel}^2 \qquad (6.8)$$

This is used to correct the obtained SF (which so far only describes the difference between data and the simulation for IsoEle25) for the fact that the efficiency in data is slightly higher for early run ranges using Ele25, taking the exact luminosity weights into account (however, the overall effect is less than a permille).

Electron-Trigger Efficiency - Jet Leg

In addition to the electron leg of the cross trigger, the hadronic part needs to be studied. This is done using events recorded by a single-lepton reference trigger, which fulfil the pre-tagged ℓ + jets $t\bar{t}$-event selection. Subsequently, the jet-leg efficiency is determined as the fraction of these events that fire also the lepton-hadron (LepHad) cross trigger:

$$\epsilon(\text{Jet Leg}) = \frac{N_{SingleLep\&LepHad}^{pre-tagged}}{N_{SingleLep}^{pre-tagged}} \qquad (6.9)$$

This approach is valid if the single-lepton trigger is at least as tight and has at least the p_T threshold as the lepton leg of the cross trigger because in this case, the lepton-leg efficiency cancels.

Again, suitable single-electron reference triggers are IsoEle27(32), but as mentioned above, this trigger is highly prescaled or even missing after 1 fb^{-1}. An alternative is to perform the same study using muon-hadron cross triggers (Iso)Mu17TriJet with the same jet trigger requirements as the electron-hadron cross trigger. In that case, the signal triggers of the muon channel IsoMu17(24)(eta2p1) can be used as suitable unprescaled control triggers throughout the whole run range. For 1 fb^{-1}, i.e. for the range during which both channels have approximately unprescaled single-lepton triggers, it has been checked that the efficiencies and SFs in the different channels agree well with maximally 1% difference. Thus, for the full run range, the efficiency is determined using the jet leg of the muon cross trigger.

The method used here measures the effective event efficiency of the trijet trigger[5], which depends on the p_T of all jets in the event. To parametrise the efficiency as a function of only one variable, the p_T of the softest jet in the event is chosen in the following. The efficiency also strongly depends on the total number of jets in the event as for more than 3 jets the probability increases that at least 3 jets fulfil the trigger requirement. This can be seen from Fig. 6.7 (*top left*), which shows the

---

[5]In contrast to the trigger efficiency per jet.

effective event efficiency in data for events with 3, 4 and 5 offline jets as a function of the 3rd, 4th and 5th offline jet p_T, respectively. Note that the offline jets in this analysis are reconstructed as PF jets, whereas for the largest part of 2011 data taking, the trigger jets are built from calorimeter information only (see Sec. 5.1.5, 5.2.2). In combination with an offline p_T cut identical to the trigger threshold, this causes a pronounced efficiency turn-on curve for events with 3 jets as a function of the 3rd jet p_T, with efficiencies of 67 to 85% between 30 and 40 GeV, reaching a plateau of about 99% at 60 GeV. However, the effect is strongly mitigated in the case of 4 or more jets, which is relevant for this analysis: For events with 4 jets, only the range of a 4th jet p_T between 30 and 40 GeV differs by a few percent from unity ($\approx$ 97% efficiency in data). For events with 5 jets and more, the efficiency is hardly distinguishable from one.

Comparing this efficiency determined in data to the simulation (Fig. 6.7, *top right*, for $N_{jet} = 4$), one has to take into account that the event composition is a mixture of mainly $t\bar{t}$ and W+jets events at this step of the selection before b tagging (see Tab. 5.4). For the same p_T of the softest jet, the p_T of the harder jets tend to be lower in W+jets events than in $t\bar{t}$ events as jet production is dominated by higher-order radiation for W+jets, whereas it comes from the heavy top-quark decay in the case of $t\bar{t}$ events. Thus, the expected effective event efficiency is higher for $t\bar{t}$ events. In the following, the data is compared to a combination of both samples according to their predicted event composition. It can be seen that the general behaviour of the efficiency in data is well described by the simulation, but at low p_T the prediction overestimates the efficiency. From Fig. 6.7 (*bottom left*), which shows the efficiency for events with 4 jets and $30 < p_\mathrm{T}(\text{4th jet}) < 40$ GeV as a function of the 4th jet η, one can see that this discrepancy increases with increasing $|\eta|$. The *bottom right* plot displays the efficiency for 4 jet events as a function of N_{PV}. As PU is not corrected for at trigger level, it effectively decreases the trigger threshold, resulting in an increase of the efficiency. This is well reproduced by the simulation.

In order to steepen the jet turn-on curve, which is partly due to the difference between calorimeter jets online and PF jets offline, PF jets have been also introduced at trigger level during the last period of 2011B data taking (trigger menu 5e33). Fig. 6.8 shows a comparison of the efficiency for the 2011A run range and the first part of 2011B (menu 3e33), during which online calorimeter jets were used, and the second part of 2011B (5e33) with online PF jets. Whereas an efficiency increase from 2011A to 2011B 3e33 can be observed, which is expected due to higher PU as explained above, there is a significant drop in the first p_T bin when going from 3e33 to 5e33, both for N_{jet}=3 and 4 (*top row*). This is contrary to the expectation of an improved turn-on curve due to online PF jets. However, for $p_\mathrm{T} > 40$ GeV, the efficiency is higher for online PF jets. It seems that the turn-on curve is indeed steeper, but shifted to higher p_T. This is probably due to not- applied jet-energy corrections in case of online PF jets as mentioned in Sec. 5.1.5. It can be also seen in Fig. 6.8 (*bottom left*) that this efficiency drop becomes particularly pronounced for outer $|\eta|$ regions where the need for PF energy corrections is largest [124]. The behaviour is improved for the 2012 data taking after implementing online PF-jet-energy corrections.
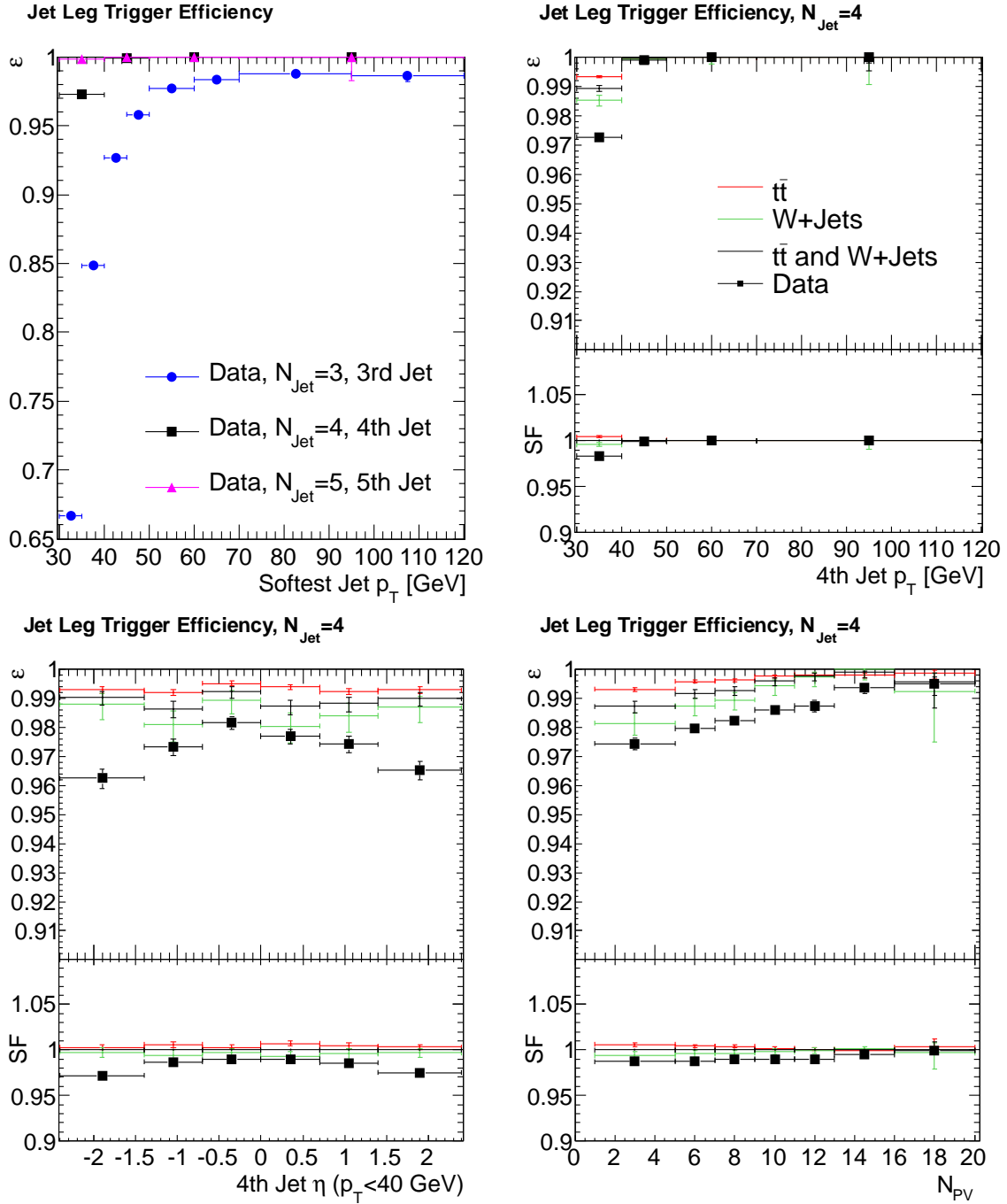
Figure 6.7: The jet-leg trigger efficiencies determined with muon (cross) triggers for the full run range. *Top left*: The efficiency measured in data for events with 3, 4 or 5 jets as a function of the p_{T} corresponding to the jet with lowest p_{T} in the event (i.e. 3rd, 4th, 5th jet, respectively). The other figures show the efficiency for events with 4 jets as a function of the p_{T} (*top right*) and η (*bottom left*, cut on $30 < p_{\mathrm{T}}(4\text{th jet}) < 40\,\mathrm{GeV}$) of the 4th jet and the number of PV (*bottom right*). For these, the data efficiency is compared to $t\bar{t}$ and W+jets simulations and a combination of both according to their event composition. Note that the jet quantities quoted here refer to offline PF jets.
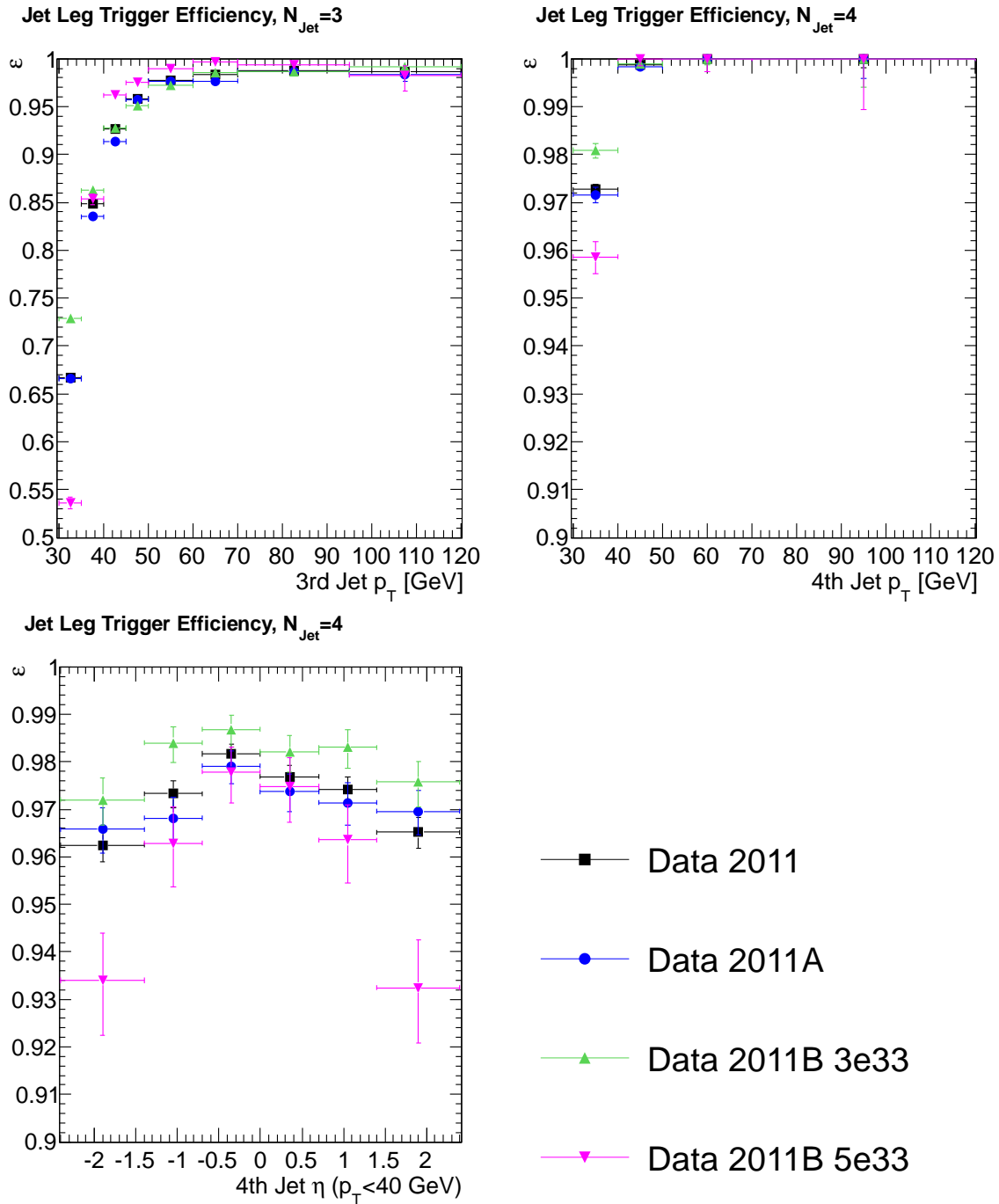
Figure 6.8: The jet-leg trigger efficiency determined with the muon trigger for different run ranges with online calorimeter jets (2011A, 2011B 3e33) and online PF jets (2011B 5e33). The figures show the efficiency dependence on the p_T of the 3rd jet for events with 3 jets (*top left*), on the p_T of the 4th jet for events with 4 jets (*top right*) and on η of the 4th jet for events with 4 jets with $30 < p_T(\text{4th jet}) < 40\,\text{GeV}$ (*bottom left*). Note that the jet quantities quoted here refer to offline PF jets.

Final Efficiency Scale Factors in the Electron Channel

The combined average efficiency scale factor including electron-selection and electron-leg-trigger efficiency scale factors is measured as 0.968 ± 0.004. As no significant dependence on p_T and η is observed, this flat SF is applied as event weight to the simulation. For the fraction of the data that uses a non-isolated-electron trigger (Ele25), the efficiency difference is taken into account as a function of I_{rel} (see Eq. 6.8). The SF for the jet-leg efficiency is observed to be consistent with unity except for events with 4 jets in the p_T bin between 30 and 40 GeV. Thus, only for that range a SF is applied, which is done separately for the central ($|\eta| < 1.4$) and the outer region ($|\eta| > 1.4$) to account for its η dependence.

6.2   B-Tagging Efficiency

Also the b-tag efficiency needs to be studied in data in order to correct for imperfections in the simulation using a SF. This becomes especially relevant for this analysis because at least 2 b-tagged jets are required, which increases the inefficiency and therefore the dependence on a correct description.

Several methods have been developed by the CMS b-tagging group to determine the b-tag efficiency and SF in a data-driven way, either using $t\bar{t}$ or di- or multijet events [127]. For this analysis, only the latter is considered in order to avoid possible correlations between the b-tag efficiency obtained from $t\bar{t}$ events with the $t\bar{t}$ cross section, which is the quantity under study in this analysis. A review of these methods and results is given in the following.

Four independent methods using multijet events to determine the b-tag efficiency are employed [127]. Three of them exploit a fit to distributions of a variable discriminating b jets from light and c jets in order to determine the number of b jets in the sample. This is performed before and after applying b tagging, with the ratio giving the efficiency. In two cases the variable is related to the kinematic properties of muons arising from semileptonic B-hadron decays (cf. Sec. 5.1.5), namely the component of the muon momentum transverse to the jet axis, p_T^{rel}, or the three dimensional impact parameter (IP3D). Both tend to be larger for b jets compared to other flavours. Alternatively, an independent reference lifetime tagger (LT) is used, which combines the impact-parameter information of all tracks in a jet. The fourth method solves a set of 8 equations (*System 8*) relating the weakly-correlated efficiencies of independent tagging criteria (including the tagger under study, p_T^{rel} and another lifetime tagger) to the event numbers before and after applying the taggers.

The p_T^{rel} and System-8 methods are only sensitive at low p_T up to 120 GeV, the IP3D method at high p_T and the LT method over the full range up to 670 GeV. The SFs obtained from these different methods are in good agreement with each other. Fig. 6.9 (*top*) shows the combination as a function of p_T of the tagged jet for the CSVM algorithm. Only a slight p_T dependence in the range of interest (30 to about 200 GeV) between SF=0.94 and 0.96 with uncertainties of 2-3% is observed. The average b-tag

SF in the phase space of $t\bar{t}$ events amounts to 0.95 ± 0.03. This is in good agreement with the value obtained from the b-tag SF measurement directly on $t\bar{t}$ events, giving 0.97 ± 0.04.

Also the mistag rate, i.e. the b-tagging efficiency of light jets, is measured in data [127]. Negative discriminator values of the tagger, which are rare in case of b jets, are used to measure a negative tagging rate, which is related to the mistag rate. The mistag SF as a function of p_{T} is shown in Fig. 6.9 (*bottom*). It is found to be typically about 1.1 ± 0.1.
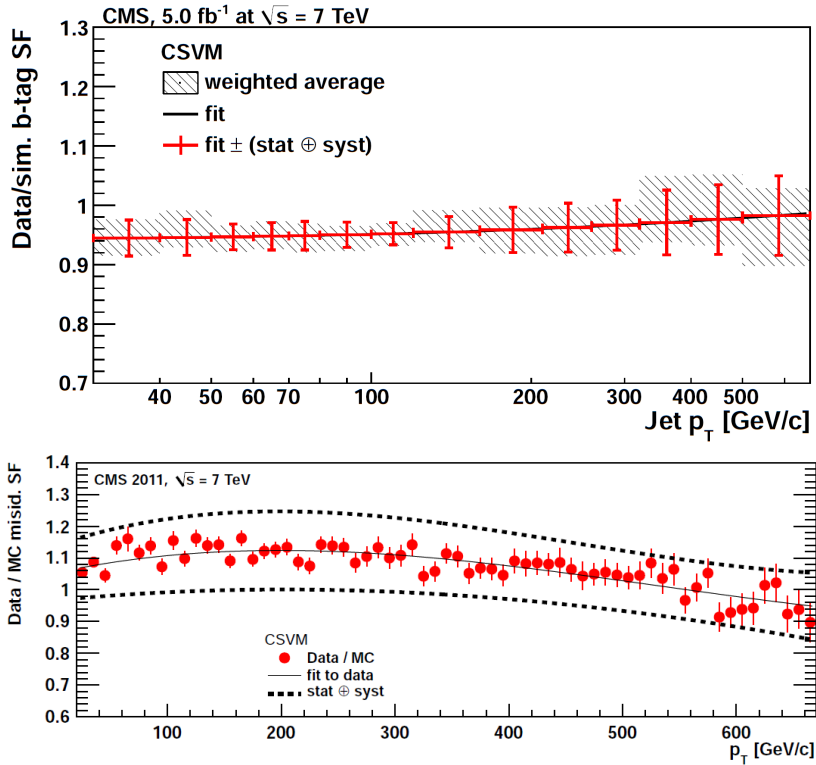
Figure 6.9: The data-to-simulation SF for the b-tag efficiency of b jets (*top*, labelled b-tag SF) and light jets (*bottom*, labelled misid. SF) using the CSVM tagger. The b-tag SF is a combination of the four methods explained in the text. The hatched area represents the combination and its overall uncertainty in each bin separately. The line is a fit to this; its error bars are taken from the uncertainties from the combination in each bin and are scaled and attached to the slightly different central value. The mistag SF is also fitted (solid line) and the dashed curve indicates the envelope of the overall statistical and systematic uncertainties. Taken from [127].

These SFs are applied to this analysis. However, as they give the b-tag efficiency SF per jet and this analysis selects events with at least two b-tagged jets, they need to be converted to an event SF. Eq. 6.10 shows how the efficiencies for single b, c or light (l) jets (ϵ_b, ϵ_c or ϵ_l) can be converted to b-tagging event efficiencies $\epsilon_{\geq 2b-tags}$. This is achieved by subtracting from unity the efficiency that no jet (1st row) and one jet (one b jet: 2nd row, one c jet: 3rd row, one l jet: 4th row) is b tagged:

$$
\begin{aligned}
\epsilon_{\geq 2b-tags} \quad = 1 \quad &- \prod_i^{N_b}(1-\epsilon_{b,i}) \prod_j^{N_c}(1-\epsilon_{c,j}) \prod_k^{N_l}(1-\epsilon_{l,k}) \\
&- \sum_h^{N_b} \epsilon_{b,h} \prod_{i\neq h}^{N_b}(1-\epsilon_{b,i}) \prod_j^{N_c}(1-\epsilon_{c,j}) \prod_k^{N_l}(1-\epsilon_{l,k}) \\
&- \sum_h^{N_c} \epsilon_{c,h} \prod_i^{N_b}(1-\epsilon_{b,i}) \prod_{j\neq h}^{N_c}(1-\epsilon_{c,j}) \prod_k^{N_l}(1-\epsilon_{l,k}) \\
&- \sum_h^{N_l} \epsilon_{l,h} \prod_i^{N_b}(1-\epsilon_{b,i}) \prod_j^{N_c}(1-\epsilon_{c,j}) \prod_{k\neq h}^{N_l}(1-\epsilon_{l,k})
\end{aligned}
\tag{6.10}
$$

This efficiency depends on the number of b, c and l jets (N_b, N_c, N_l) in the specific event. ϵ_b, ϵ_c and ϵ_l are parametrised as a function of p_{T} and $|\eta|$.

In a first step, the simulated $\epsilon_{b,sim}$, $\epsilon_{c,sim}$ and $\epsilon_{l,sim}$ are determined from the $t\bar{t}$ sample after the pre-tagged $t\bar{t}$-event selection. Subsequently, in order to obtain the event-efficiency scale factor $SF_{\geq 2b-tags}$, the event efficiency $\epsilon_{\geq 2b-tags}$ is calculated once from these uncorrected single-jet efficiencies from the simulation $\epsilon_{i,sim}$ and once from the data-corrected single-jet efficiencies using the per-jet scale factors SF_i, and the ratio is taken:

$$
SF_{\geq 2b-tags} = \frac{\epsilon_{\geq 2b-tags}(SF_i \cdot \epsilon_{i,sim})}{\epsilon_{\geq 2b-tags}(\epsilon_{i,sim})}.
\tag{6.11}
$$

The measured per-jet SF for b jets is assumed to be applicable also to c-jets.

$SF_{\geq 2b-tags}$ is calculated for each simulated event separately and used as a weight for this event. The average SF per event is found to be $\overline{SF}_{\geq 2b-tags} = 0.92 \pm 0.05$.

Chapter 7

Reconstruction of Kinematic Top-Quark Quantities

This analysis is intended to measure differential cross sections in kinematic variables of the top-quark decay products (charged lepton, b jets), the top quark itself and the $t\bar{t}$-pair system (see Tab. 1.1).

The kinematic quantities of the lepton and the b jets are direct observables in the detector. In contrast, to obtain the kinematic quantities of the top quark and the $t\bar{t}$ system, a complete reconstruction of the $t\bar{t}$-event topology as illustrated in Fig. 7.1 is needed: The measured leptons and jets need to be correctly assigned to the underlying particles from the $t\bar{t}$ decay and unmeasured quantities need to be recovered. In the $\ell + \text{jets}$ decay channel, the longitudinal momentum of the neutrino, represented by η, constitutes such an unmeasured quantity (assuming that the transverse components are represented by $E_{\mathrm{T}}^{\mathrm{miss}}$), and without additional jets from higher-order QCD radiation, there are four jets in the final state that need to be assigned. Two of them arise from b quarks of the top-quark decays and the other two from the hadronically decaying W boson. Moreover, in about 1/3 of the selected events, additional jets with $p_{\mathrm{T}} > 30\,\mathrm{GeV}$ are expected to be present, which need to be distinguished from the jets of the top-quark decay.

7.1 Kinematic Fit

As a tool for the event reconstruction, a constrained kinematic fit is used. Besides the desired $t\bar{t}$-event reconstruction including the estimation of the neutrino η, it provides the additional advantage of potentially improving the resolutions of the input objects (in case the right jet assignment is found). Details on the concept of the kinematic fit can be found in [136]. A common implementation in the CMS Top-Quark-Analysis Framework is used [137]. It was configured and adapted to this analysis by [135]. A short overview is given in the following.

The kinematic fit varies the kinematic parameters x_i (i.e. p_{T}, η and Φ) of the
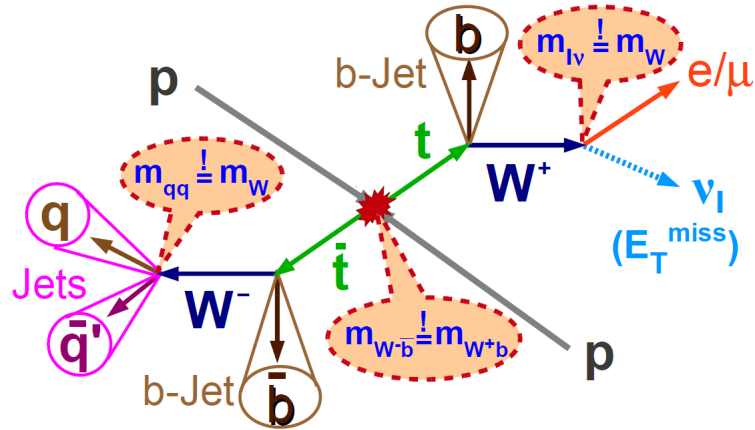
Figure 7.1: Illustration of a $t\bar{t}$ event and the constraints in the kinematic fit. Taken from [135].

measured input objects (lepton, $E_{\mathrm{T}}^{\mathrm{miss}}$ and jets; more details below) according to their estimated resolutions in order to fulfil certain constraints. This is implemented by the minimisation of a χ^2 function, which is composed of two expressions:

$$\chi^2(\vec{x}, \vec{\lambda}) = \underbrace{\sum_{i=1}^{n} \frac{(x_{i,fit} - x_{i,meas})^2}{\sigma_{x_i}^2}}_{\chi_0^2} + 2 \underbrace{\sum_{k=1}^{m} \lambda_k f_k(\vec{x})}_{\text{constraints}} \qquad (7.1)$$

The first term, χ_0^2, reflects the changes of the n object kinematics with respect to the initially measured values done by the fitting routine, normalised to their resolutions σ_{x_i}. The second term represents the m constraints f_k, which are introduced using Lagrangian multipliers λ_k. χ^2 is minimised with respect to $x_{i,fit}$ and λ_k using an iterative linearisation approach.

In this analysis, the measured four-momentum vectors of the selected muon or electron and the selected high-p_{T} jets are given as initial values to the kinematic fit (neglecting jet masses). The initial neutrino-four-momentum vector is constructed from the missing transverse momentum assuming $\eta = 0$. Thus, the actually unmeasured neutrino η is technically treated as measured, but assigned with basically infinite, i.e. very large, resolution. Consequently, de facto the fit determines η by means of the constraints and no contribution to χ^2 is obtained due to this term.

For this analysis, three constraints are used as illustrated in Fig. 7.1. The invariant mass of lepton and neutrino ($m^{\ell\nu}$) on the one hand and of the two light quarks ($m^{q\bar{q}'}$) on the other hand are constrained to reproduce the mass of the W boson of 80.4 GeV. Furthermore, the reconstructed top-quark masses of the leptonic and hadronic decay branch are required to be equal. Thus, the kinematic fit has 2 degrees of freedom (3 constraints minus 1 unmeasured parameter).

The object resolutions used in the kinematic fit are derived from the $t\bar{t}$ simula-

tion using the same jet and lepton definitions as in the analysis. They are obtained by comparing the kinematics of the reconstructed jets, charged leptons and $E_{\mathrm{T}}^{\mathrm{miss}}$ to the underlying generated partons, charged leptons and neutrinos, respectively. Light (including c) jets and b jets are treated separately. Only the cores of the residuum distributions (i.e. the difference between the generated and reconstructed quantity) are considered and fitted by a Gaussian. The resolutions are parametrised in different $|\eta|$ intervals as a function of p_{T}. For all quantities except the muon p_{T}, the functional form f corresponds to the standard calorimeter resolution parametrisation using a constant term with parameter C, a stochastic term with parameter S and a noise term with parameter N [19]:

$$f(p_{\mathrm{T}}) = \sqrt{C^2 + \frac{S^2}{p_{\mathrm{T}}} + \frac{N^2}{p_{\mathrm{T}}^2}} \qquad (7.2)$$

For the p_{T} resolutions, f corresponds to the relative resolution $\frac{\sigma_{p_{\mathrm{T}}}}{p_{\mathrm{T}}}$, whereas for the η and ϕ resolutions, f is taken to describe the absolute resolutions σ_η and σ_ϕ.

In contrast, the relative muon p_{T} resolution is dominated by the tracker, which is therefore parametrised linearly in p_{T} [19]:

$$f(p_{\mathrm{T}}) = A + B \cdot p_{\mathrm{T}} \qquad (7.3)$$

The actual parameter values used in this analysis can be found in [138]. The jet resolutions are scaled in order to match the ones measured in data as explained in Sec. 5.1.5. In general, the resolutions related to the charged leptons are superior to those of the jets, $E_{\mathrm{T}}^{\mathrm{miss}}$ or the chosen very large neutrino-η resolution. Thus, mostly jet and neutrino momenta are varied in the fit.

There are different possibilities of how to assign the measured jets to the underlying quarks. In order to keep the number of permutations at an acceptable level, only the four or, in case of events with additional hard jets, maximally five leading jets are considered in the kinematic event reconstruction. Furthermore, only b-tagged jets are considered as b quarks in the hypothesis and only non-b-tagged jets are considered as light quarks. Hence, the maximum number of total permutations amounts to four for four jets as input (2! from the exchange of the b quarks multiplied with 2! from the exchange of the light quarks), and twelve for five input jets (2! related to b quarks, 3! related to light quarks). In fact, it reduces to two and six relevant permutations, respectively, as the top-quark kinematics are invariant under exchange of the two light quarks from the hadronic W-boson decay. For every possible permutation, Eq. 7.1 is minimised, and the one with the lowest corresponding χ^2 (in the following referred to as *best combination*) is selected for further analysis.

After the reconstruction of the $t\bar{t}$-event topology, kinematic quantities related to the top quark and the $t\bar{t}$ system can be derived by summing up the reconstructed four-momentum vectors of the corresponding jets and leptons according to the best combination of the kinematic fit. The kinematic quantities of the top-quark decay products are taken from their adjusted four-momentum vectors after the kinematic

fit for a consistent treatment with the top-quark quantities and to profit from the improved resolution (at least for the correct permutation).

7.2 Performance of the Kinematic Event Reconstruction

As can be seen from Tab. 5.4, the events pass the kinematic fit routine in about 90% of the cases, consistently in data and simulation and in both channels. Most of the discarded events have less than two b jets or less than two light jets among the leading four or five jets that are given to the fit routine, thereby preventing a successful $t\bar{t}$-event reconstruction. The efficiency for passing the fit is similar for all simulated samples, thereby leaving the event composition unaffected. Only a small fraction of the discarded events is due to a failed fit convergence.

7.2.1 Jet Assignment
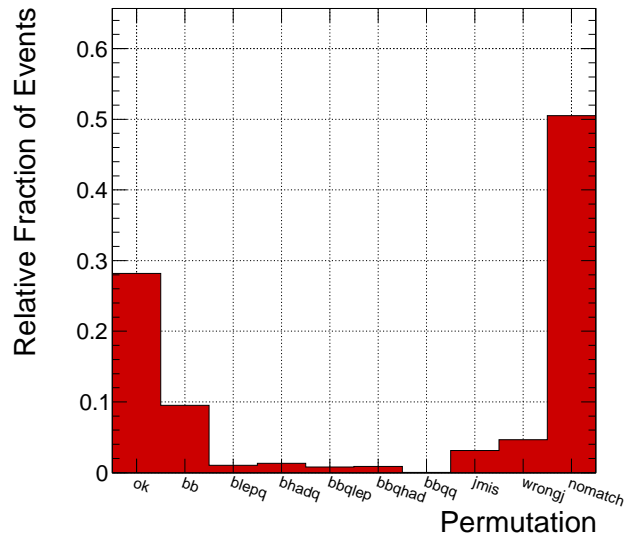
Figure 7.2: Performance of the kinematic fit regarding the jet assignment of the best combination for simulated $t\bar{t}$ signal events in the combined ℓ+jets channel: the fraction of events for different jet permutations obtained from jet-parton matching as described in the text. The last column corresponds to cases where the jet-parton matching is not successful.

The performance of the kinematic fit regarding the jet assignment of the best combination is studied in simulation for ℓ+jets $t\bar{t}$ events. The generated partons from the top-quark decay are matched to the closest reconstructed and selected jet in $\eta\Phi$. In

order to avoid ambiguities, i.e. possible mismatching to a jet originating from another parton, the distance ΔR(jet, parton) is required to be less than 0.3 and additionally, no other reconstructed jet is allowed within this distance. Otherwise, the parton is considered not matched.

As one can see from Fig. 7.2[1], after event selection and kinematic event reconstruction, the correct jet-parton assignment (*ok*) is obtained in about 28% of all events. The main combinatorial background is the permutation of the two b jets (*bb*), which occurs in about 10% of all cases. Other potential permutations involving the exchange of a b jet from the leptonic or hadronic decay branch with a light jet (*blepq*, *bhadq*) or the permutation of three or four jets (*bbqlep*, *bbqhad*, *bbqq*) are suppressed to 4% by exploiting the b-tag information in the jet assignment. In about 3% of all events, at least one jet from the $t\bar{t}$ decay is not among the five leading jets handed to the fitting routine (*jmis*), but among the remaining jets passing the event selection. In about 4% of all cases, the fit chooses an additional jet instead of a jet from a top-quark decay product out of the five leading jets (*wrongj*).

In about 51% of the cases, the jet-parton matching is not successful (*nomatch*). On the one hand, it might be still possible that the right combination is found by the fit and only the matching fails either due to an ambiguous assignment when two jets are near-by or due to ΔR(jet, parton) > 0.3. But on the other hand, also not or misreconstructed jets are possible reasons, in the case of which no correct $t\bar{t}$-event reconstruction is possible. This includes situations in which jets from the $t\bar{t}$ decay are merged, split or simply fail the selection criteria, i.e. are either out of acceptance (failing p_{T} or η requirements) or fail the jet-identification requirements. Looking at the residuum or χ^2 distributions of the unmatched cases (see below) suggests that they contain contributions from both correct permutations and misreconstructed events.

7.2.2 χ^2 and Probability Distributions

The distribution of χ^2 and the corresponding χ^2 probability[2] (for two degrees of freedom) of the selected best combination are shown in Fig. 7.3 for data and simulation.

Their agreement is found to be very good. For probability values above about 0.4, the probability distribution exhibits the flat behaviour expected for Gaussian-distributed parameters. A potential bias from the selection of the best combination towards higher values is not observed. However, the distribution is seen to increase for low probability values, which can be mainly explained by contamination from combinatorial and other backgrounds. Fig. 7.4 shows the distributions separately for the dominating permutations (*ok*, *bb*, *noMatch*) and for all permutations as obtained from the $t\bar{t}$ simulation. The distributions are normalised to unity to facilitate the comparison of their shapes. It can be seen that the unmatched cases and, to a lower extent, also

---

[1]From now on, the figures and numbers will be shown for the combined ℓ + jets channel. For important distributions and those with possible channel-specific differences, the separate channels are shown in the appendix.

[2]The χ^2 probability for a given value χ_0^2 is defined as the probability to observe events with $\chi^2 > \chi_0^2$. Thus, larger χ^2 values correspond to lower probabilities.
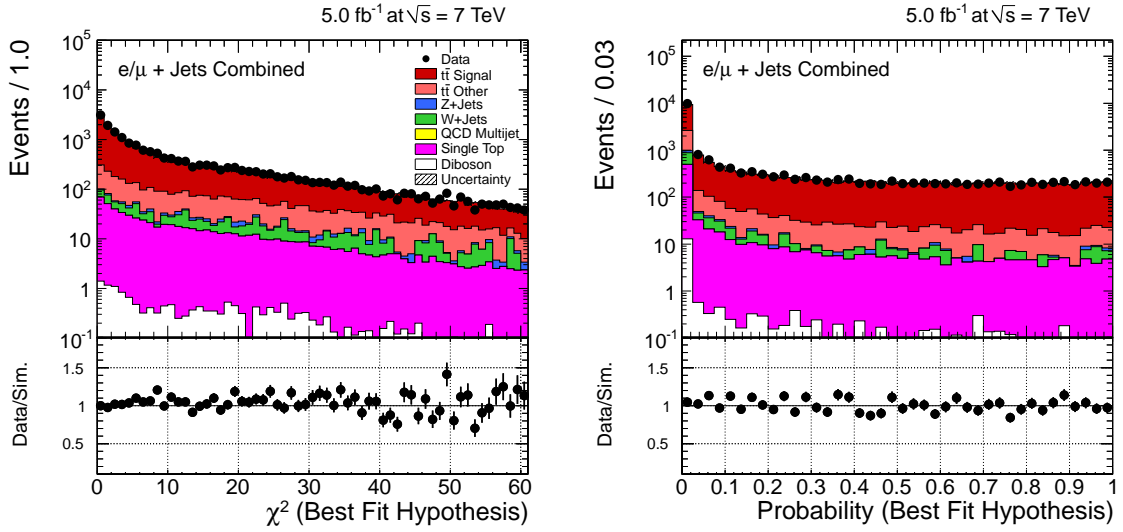
Figure 7.3: χ^2 (*left*) and corresponding probability (*right*) distribution in data and simulation for the combined $\ell +$ jets channel. Shown uncertainties and applied corrections are the same as detailed in Sec. 5.2.6.

the permutations with exchanged b jets tend to larger χ^2 and correspondingly lower probability values, mainly in the first bin around 0, than the correct permutations. This shows that a large part of the unmatched cases consists of badly reconstructed events.

For future developments of this analysis, it is envisaged to introduce a cut on the probability in order to reduce such backgrounds. As shown below, this would enhance the resolution. In the scope of this first analysis of differential $t\bar{t}$ cross sections, however, a cut is not performed to avoid an increase in complexity and a decrease of the number of selected events.

7.2.3   Comparison between Reconstructed and Generated Quantities

Figs. 7.5 and 7.6 display the residuum distributions for simulated events, i.e. the difference between a quantity as reconstructed by the kinematic fit and the underlying generated quantity (rec-gen). For p_T and mass quantities, the relative residuum (rec-gen)/gen is shown. Note that the generated quantities are defined at parton level for the top-quark and $t\bar{t}$ quantities, which require the $t\bar{t}$-event reconstruction, and at particle level for the leptons and b jets, which are directly measurable in the detector (see Sec. 8.1.3). In case there is both an object and its corresponding antiobject in the event like for the top quarks and b jets, the distributions include both entries. In this case, the assignment between the reconstructed and generated object is done as follows: For the top quarks, the lepton-charge information is used, as assigned by the kinematic fit. For the directly measurable b jets, however, it is advantageous not to rely on the
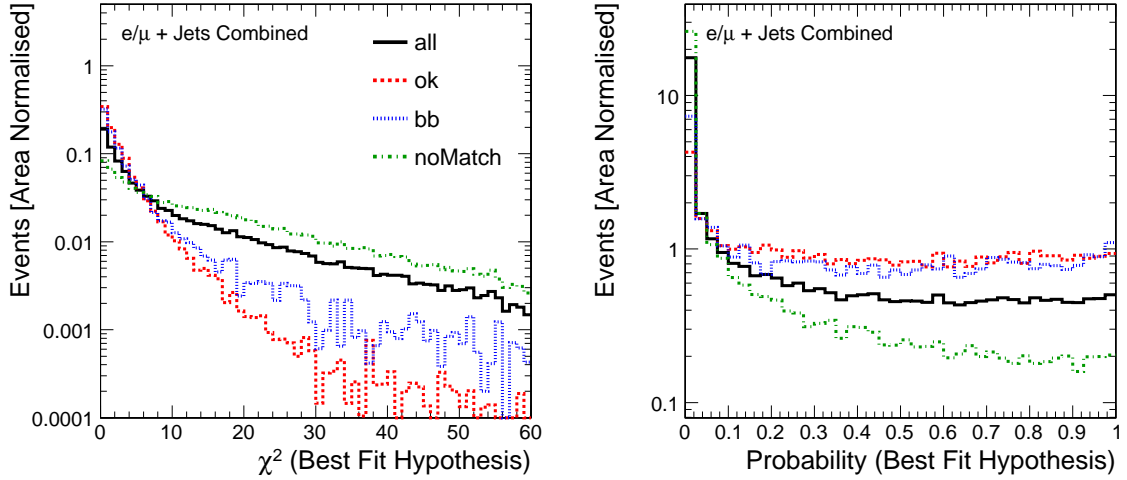
Figure 7.4: Distribution of χ^2 (*left*) and corresponding probability (*right*) for simulated $t\bar{t}$ signal events in the combined $\ell +$ jets channel, separately for the dominating permutations (*ok*, *bb*, *noMatch*) and for all permutations. The distributions are normalised to unity.

assignment information from the kinematic fit to avoid the permutations of swapped b jets. Thus, the two reconstructed b jets identified as coming from the top-quark decay by the kinematic fit (b_{rec}) are paired with the generated b jets (b_{gen}) by minimising the sum $\Delta R(b_{rec_1}, b_{gen_i}) + \Delta R(b_{rec_2}, b_{gen_j})$ for the two possible pairs ($i, j = 1, 2; i \neq j$). Generated jets are identified as b jets by requiring them to include a B hadron from the decay of one of the top quarks.

The residuum is calculated separately for each bin of the generated quantity of the final differential cross-section distributions (for the choice of binning see Sec. 8.2.4). As an example, the residua of two representative bins are shown for each quantity next to each other. Besides the distribution for all events, it is also displayed separately for the three most important permutations (*ok*, *bb*, *noMatch*).

The shape including all permutations differs significantly for the different quantities. Whereas it is similar to a Gaussian peak around 0 for the well measured lepton quantities, which are hardly affected by the jet permutations, there are large tails and partly asymmetric distributions with pronounced shoulders for the quantities reconstructed by the kinematic fit. However, a closer look reveals that for the right permutations, a pronounced peak around 0 is also maintained for these quantities. Thus, the tails and the asymmetric contributions mostly originate from the wrong permutations and the unmatched cases. However, it is interesting to note that the unmatched cases exhibit also a second component, which seems to peak around 0. This confirms the assumption made above that the unmatched cases consist of both correct permutations, for which the jets just cannot be matched unambiguously to the underlying partons, and cases in which the reconstruction of jets fails and therefore no correct reconstruction of the

$t\bar{t}$ event is possible.

Due to the largely non-Gaussian shapes, it is not possible to quote values for the resolution, when defined as the Gaussian standard deviation of the residuum distributions. However, the spread of these distributions directly affects the migration of events from one bin of the quantity into another one. Measures to quantify this migration such as the response matrix, purity and stability are defined and presented later in Sec. 8.2.1.

7.3　Reconstructed Kinematic Distributions

The event yields (i.e. the number of reconstructed and selected events) for the combined $\ell +$ jets channel as a function of the $t\bar{t}$ and top-quark quantities are shown in Fig. 7.7, the ones as a function of the lepton and b-jet quantities in Fig. 7.8.

In general, the distributions in data and simulation agree well. However, as already observed in the basic monitoring distributions before the kinematic reconstruction of the $t\bar{t}$ event in Sec. 5.2.6, the p_{T} distributions, mainly of the b jets and top quarks, are observed to be softer in data than predicted, i.e. they tend to lower p_{T} values. This propagates to the final differential cross-section distributions, which are discussed in Sec. 10.
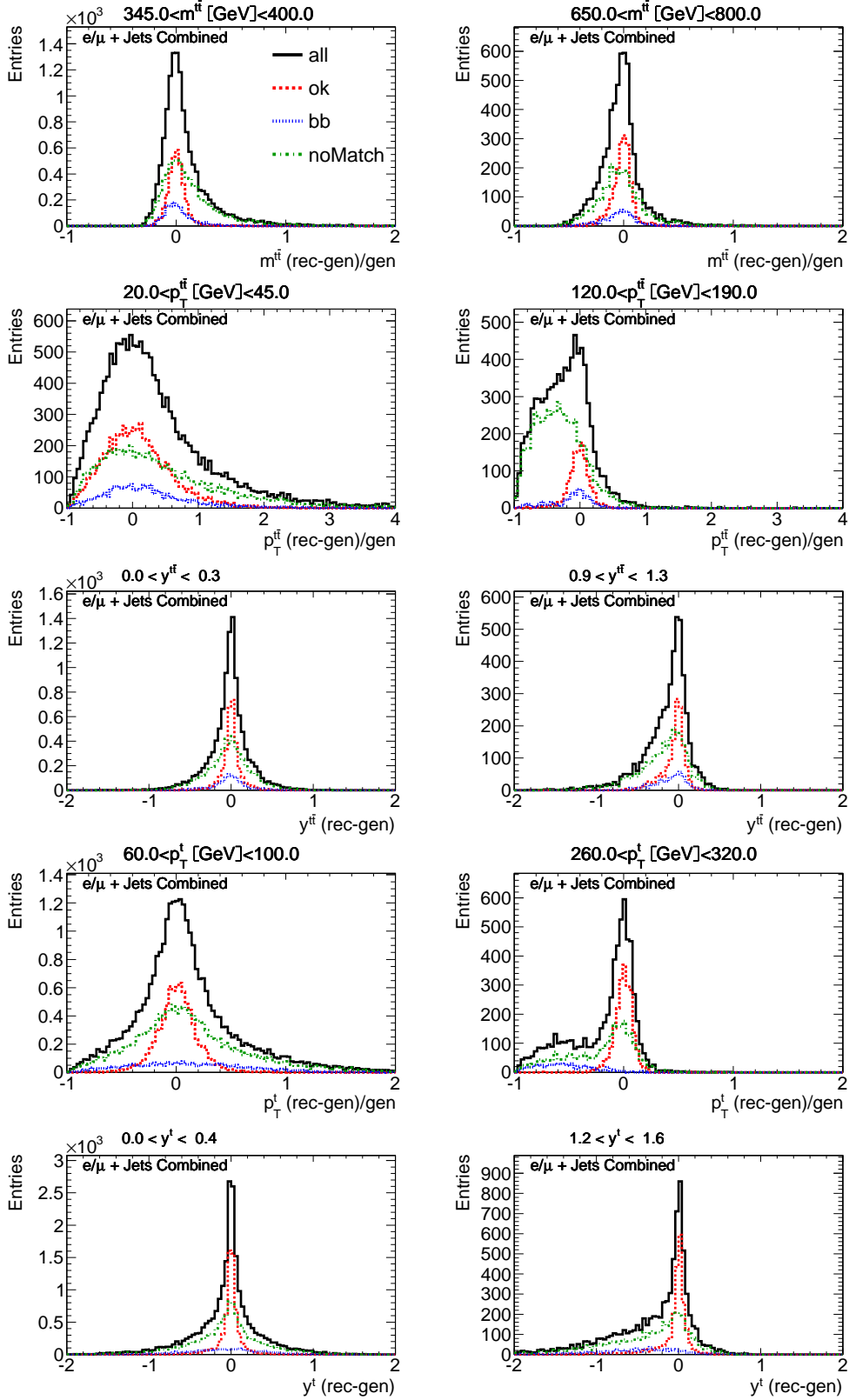
Figure 7.5: The residuum distributions (relative to the generated value in case of p_T and mass quantities) in the combined channel for the $t\bar{t}$ and top-quark quantities at parton level for the dominating permutations. This is shown for two selected bins of the generated quantity according to the final binning.
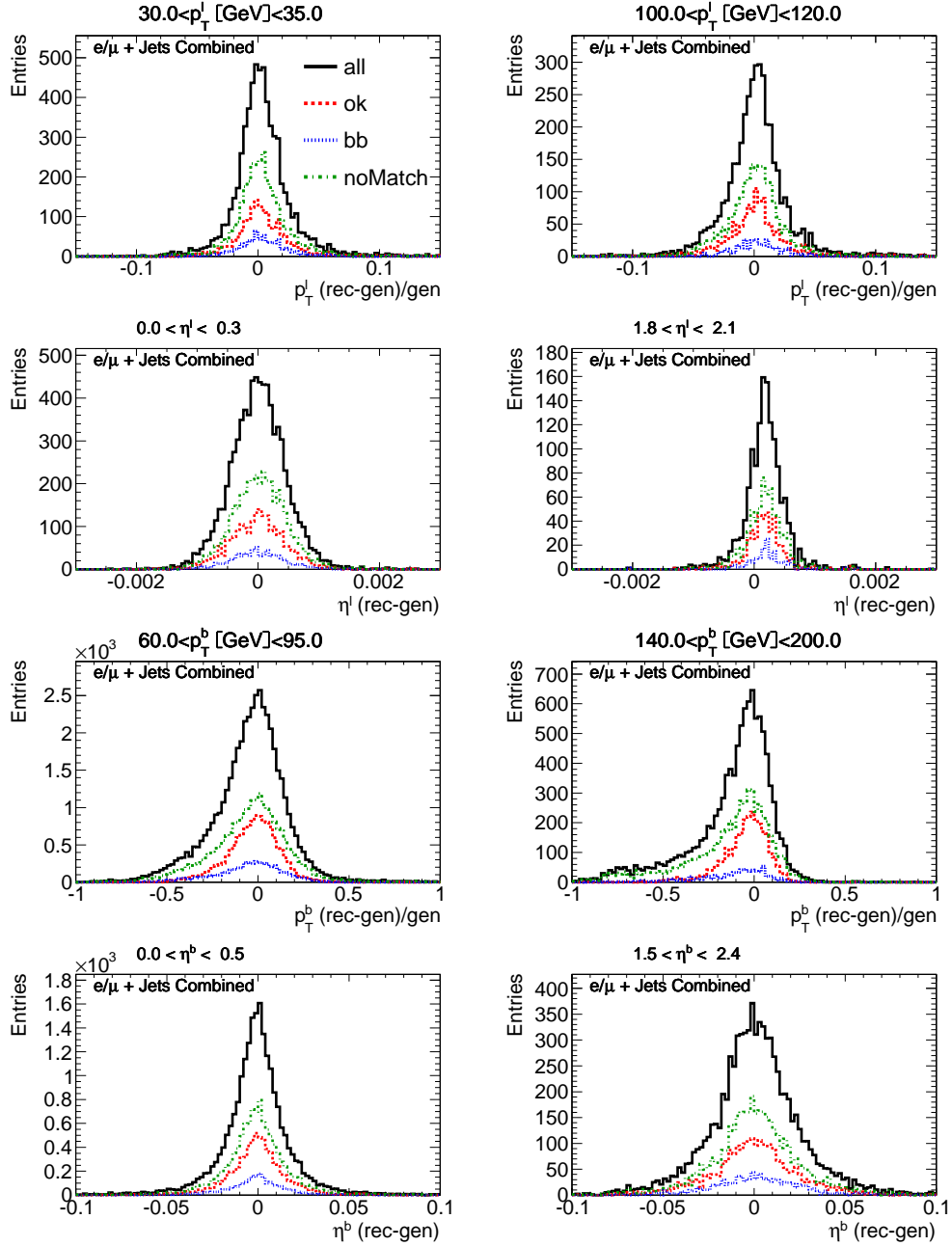
Figure 7.6: The residuum distributions (relative to the generated value in case of p_T quantities) in the combined channel for the lepton and b-jet quantities at particle level for the dominating permutations. This is shown for two selected bins of the generated quantity according to the final binning.
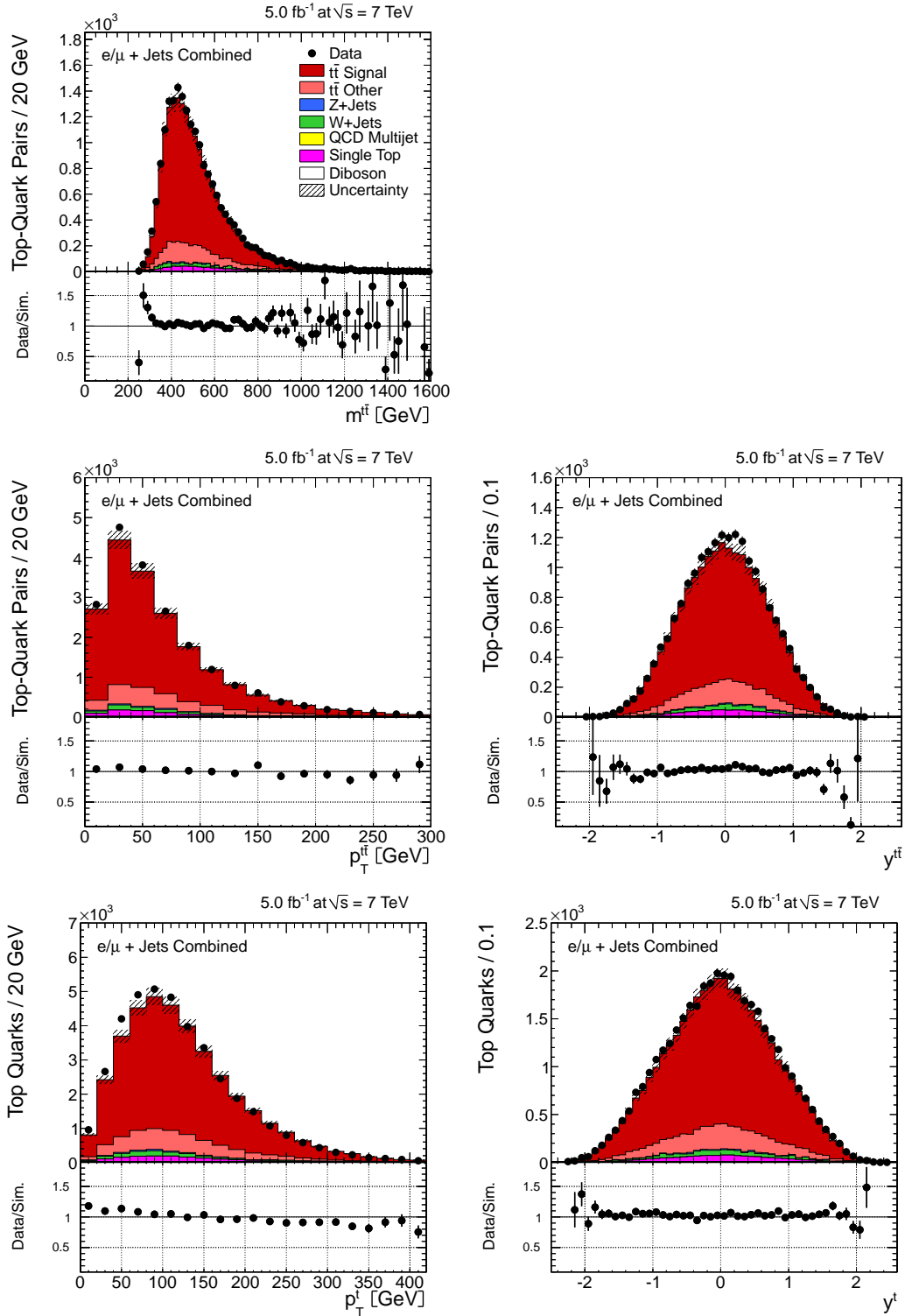
Figure 7.7: Event yields as a function of reconstructed quantities of the $t\bar{t}$ system and the top quarks in data and simulation for the combined channel. *First row*: invariant mass of the $t\bar{t}$ system; *second row*: transverse momentum (*left*) and rapidity (*right*) of the $t\bar{t}$ system; *third row*: transverse momentum (*left*) and rapidity (*right*) of the top quarks. Shown uncertainties and applied corrections are the same as detailed in Sec. 5.2.6.
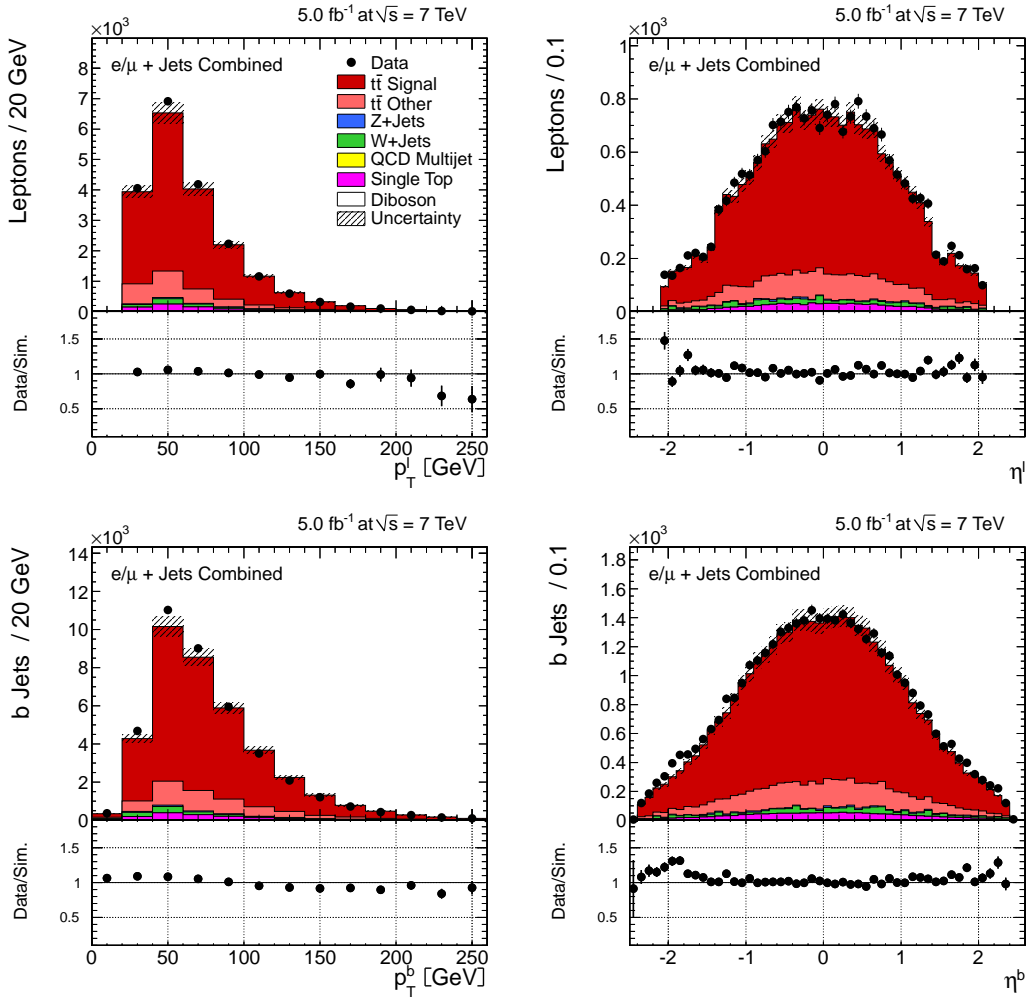
Figure 7.8: Event yields as a function of reconstructed lepton (*first row*: p_{T}^{ℓ}, η^{ℓ}) and b-jet (*second row*: p_{T}^{b}, η^{b}) quantities in data and simulation for the combined channel. Shown uncertainties and applied corrections are the same as detailed in Sec. 5.2.6.

Chapter 8

Cross-Section Definition and Unfolding

Yield distributions as shown in Sec. 7.3 can be used already for a first data-to-simulation comparison in order to judge the validity of the model used in simulation and possibly find hints of physics beyond the standard model. In fact, this is one of the most robust ways to do so as migration corrections of the data are avoided by folding the simulation instead. However, it thus requires a full detector simulation interfaced to the model of interest, which is time-consuming and only accessible to the collaboration of the respective experiment. Thus, in order to enable a direct comparison of the measurement to theoretical predictions without detector simulation, to facilitate comparison between different experiments and to better display the underlying physics corrected for detector effects, cross sections are calculated from the yield distributions.

The emphasis of this analysis is laid on differential $t\bar{t}$ cross sections as a function of kinematic quantities of the $t\bar{t}$ system, the top quarks and the top-quark decay products (lepton and b jets) as defined in Sec. 7.3. They are background subtracted and unfolded in a regularised way to correct for bin migrations and efficiencies. The cross sections are both measured in the visible phase space within the detector acceptance as well as extrapolated to the full phase space. The distributions of the directly measurable lepton and b-jet quantities are corrected back to particle level and the reconstructed quantities related to the top quarks and the $t\bar{t}$ system to parton level. As the main aim is the measurement of the distribution *shapes* (as opposed to their absolute normalisation), the differential cross sections are presented normalised to unity. By this, normalisation uncertainties correlated across all kinematic regions of the measurement largely cancel. In addition, also the inclusive cross section for the full phase space and corrected for the branching ratio is measured as a cross check.

8.1   Cross-Section Definition

For simplicity, the $t\bar{t}$-cross-section calculation is explained first for only one measurement interval, which corresponds to the inclusive cross section, before generalising to

104

the case of differential cross sections.

The cross section for inclusive $t\bar{t}$ production is given by

$$\sigma_{t\bar{t}} = \frac{(N_{\text{data}} - N_{\text{BG}}) \cdot f^{sig}}{\epsilon \cdot L \cdot BR}, \tag{8.1}$$

where N_{data} and N_{BG} refer to the number of selected data and non-$t\bar{t}$ background events, respectively, f^{sig} to the signal fraction to correct for background from other $t\bar{t}$ channels, ϵ to the efficiency to correct for detector effects, L to the integrated luminosity and BR to the branching ratio.

For differential cross sections, the cross section is measured as a function of a certain quantity X that is divided into a limited number n_{bins} of measurement intervals X_i. For each of them, the cross section is determined separately and divided by its bin width Δ_{X_i}. Furthermore, in addition to the efficiency, detector effects also lead to migration between the measurement intervals, which needs to be corrected for. This is done by generalising the efficiency to the detector response matrix $\mathbf{A}$, which is used for unfolding. As a result, the differential cross section for bin X_i (before normalisation) is given by

$$\frac{d\sigma}{dX_i} = \frac{\sum_{j=1}^{n_{bins}} \mathrm{A}_{\mathrm{ij}}^{-1} \left[(N_{\text{data,j}} - N_{\text{BG,j}}) \cdot f_j^{sig} \right]}{\Delta_{X_i} \cdot L \cdot BR} \tag{8.2}$$

Note that the direct inversion of the response matrix is only shown for illustration. In fact, a regularised unfolding approach is used as presented in Sec. 8.2.

Finally, the differential cross-section distributions are normalised to unity using the inclusive cross section σ in the same phase space, which is obtained as the sum over all bins of the corresponding differential cross-section distribution including under- and overflow bins:

$$\frac{1}{\sigma} \cdot \frac{d\sigma}{dX_i} = \frac{1}{\sum_{j=1}^{n_{bins}} \frac{d\sigma}{dX_j} \Delta_{X_j}} \cdot \frac{d\sigma}{dX_i} \tag{8.3}$$

Due to the normalisation, cross section terms that are the same for all bins like L, BR or flat correction factors cancel.

In the following, each component of the cross-section equations above is discussed in detail.

8.1.1 Event Yield: N_{data}

The event yield N_{data} corresponds to the number of events in data, which is obtained by counting the selected events after the full selection including b tagging and the kinematic fit (*Cut&Count* experiment). For differential cross sections, the yield is subdivided into bins of the measured quantity X according to the result of the kinematic fit (see Sec. 7.3).

8.1.2   Background Removal: N_{BG} and f^{sig}

Due to the tight event selection requiring at least two b tags, the expected amount of non-t$\bar{\text{t}}$ background events N_{BG} is very low, at the level of 8% (see Sec. 5.2.6). The largest fraction of it is expected to originate from single-top events, which is a rare process with a much lower cross section than t$\bar{\text{t}}$ production and a similar signature. Thus, a determination of this background from data is not feasible. As the background level is expected to be so low and control distributions show a good agreement between data and simulation (cf. Sec. 5.2.6), N_{BG}, is estimated directly from the background simulations.

From the remaining t$\bar{\text{t}}$ events, only the ones originating from prompt leptonic W-boson decays into one muon or electron (plus corresponding neutrino) are considered signal and are used for the determination of the cross section. The other t$\bar{\text{t}}$ events mainly derive from the τ+jets channel, in which one of the W bosons decays into a τ lepton as intermediate step before the τ lepton in turn decays further to a muon or electron, or from the τ+muon/electron channel with hadronic decay of the τ lepton. These events have different kinematic distributions compared to the ones with a prompt lepton. For instance, the τ+jets channel results in a lower p_{T} of the final-state lepton due to energy carried away by the additional neutrinos. Thus, these events are considered background and only the fraction of t$\bar{\text{t}}$ events that are prompt-lepton decays is used:

$$f^{sig} = \frac{N(\text{t}\bar{\text{t}} \text{ signal})}{\text{N}(\text{t}\bar{\text{t}} \text{ signal}) + \text{N}(\text{t}\bar{\text{t}} \text{ other})} \tag{8.4}$$

In contrast to a simple background subtraction of the expected other t$\bar{\text{t}}$ events, the application of the signal fraction f^{sig} avoids the use of the inclusive t$\bar{\text{t}}$ cross section, i.e. of the quantity that is intended to be measured.

8.1.3   Correction for Detector Effects: ϵ and A

Detector corrections are applied to take into account that only a fraction of the signal events produced in the collisions is observed, and possibly in another bin than originally generated. This is described for one bin by the efficiency ϵ introduced in Sec. 6 or, more generally in case of more bins, by the response matrix **A** given by:

$$A_{ij} = \frac{N_{gen,j \to rec,i}}{N_{gen,j}}. \tag{8.5}$$

$N_{gen,j \to rec,i}$ denotes the number of events that are generated in bin j and reconstructed[1] in bin i, whereas $N_{gen,j}$ gives the total number of events generated in bin j. From this, the efficiency for a generated bin j is obtained as the sum over the entries in column j, i.e. over all reconstructed bins:

---

[1] For simplicity, in this section the term "reconstructed" refers to the full event reconstruction and selection, which is not further distinguished here.

$$\epsilon_j = \sum_i A_{ij} = \sum_i \frac{N_{gen,j \to rec,i}}{N_{gen,j}}. \tag{8.6}$$

The efficiency or response matrix is estimated from the simulation and data-driven corrections are taken into account by applying the derived scale factors as event weights as described in Sec. 6. How the response matrix is used to unfold the data in a regularised way is described in Sec. 8.2.

Phase-Space Definition and Object-Evolution Level

At this point, one has to decide to which phase space and object-evolution level (as explained in Sec. 4.1) one intends to correct back, i.e. how the denominator $N_{gen,j}$ is defined. This determines the point at which theory and the measured cross section meet and are compared.

On the one hand, the cross section can be either extrapolated to the full phase space (full PS) or be restricted to the visible phase space (vis. PS) defined by the geometric and kinematic limitations in η and p_{T} due to the incomplete detector or trigger coverage. The efficiencies[2] of these two cases are related via the acceptance A:

$$\epsilon^{\mathrm{full\,PS}} = \frac{N_{rec}}{N_{gen}^{\mathrm{full\,PS}}} = \underbrace{\frac{N_{gen}^{\mathrm{vis.\,PS}}}{N_{gen}^{\mathrm{full\,PS}}}}_{A} \cdot \underbrace{\frac{N_{rec}}{N_{gen}^{\mathrm{vis.\,PS}}}}_{\epsilon^{\mathrm{vis.\,PS}}} \tag{8.7}$$

To determine the number of events in the visible phase space, $N_{gen}^{\mathrm{vis.\,PS}}$, phase-space cuts at generator level are performed.

On the other hand, one also needs to define the object-evolution level (parton or particle level, see Sec. 4.1) to which one would like to correct back. This affects the differential distributions of generated kinematic quantities $N_{gen,j}$, but also the acceptance cuts.

Depending on the choice of phase space and object-evolution level, different degrees of extrapolation are needed, i.e. the measured cross section might include certain corrections deduced from a specific model. Three different categories are used in this analysis:

Visible Phase Space at Particle Level

The least model-dependent version of an experimental cross-section measurement is restricted to the visible phase space and to the last level of object evolution before the measurement in the detector, which is the particle level. However, as no obvious definition for top quarks at particle level exist as they need to be reconstructed from

---

[2]For simplicity, only the efficiency for one bin is quoted here, but it applies also to the general case with several bins and the response matrix.

their decay products, this category is only well-defined for cross sections as a function of kinematic quantities of the final-state objects like leptons and jets.

For this level, generated stable leptons after radiation coming from a real W-boson decay are considered, along with generated jets, i.e. clustered from generated stable particles after radiation and hadronisation. For the jet clustering, stable leptons (including τ leptons) from a real W boson are excluded. In order to also avoid clustering of photons radiated off leptons into a jet containing only this photon itself, only generated jets with a minimum distance of $\Delta R(\text{jet, lepton}) > 0.4$ are taken into account. The phase-space cuts for the generated leptons and jets correspond to the lepton and jet selection at reconstruction level:

- generated lepton: $p_{\mathrm{T}}^{\ell} > 30\,\mathrm{GeV}$ and $|\eta^{\ell}| < 2.1$
                        $N_{\ell} = 1$

- generated jets: $p_{\mathrm{T}}^{\mathrm{jet}} > 30\,\mathrm{GeV}$ and $|\eta^{\mathrm{jet}}| < 2.4$
                        $N_{jets} \geq 4$, out of which $N_{b\ jets} \geq 2$

Generated jets are identified as b jets by a B hadron from a b quark from the decay of one of the top quarks, which is contained in the jet. If the same B hadron can be matched to more than one generated jet, the one with the highest p_{T} is considered as generated b jet. The efficiency of this identification procedure is about 99%.

Visible Phase Space at Parton Level

Measurements in this category are corrected for detector and hadronisation effects back to parton level. This allows for the definition of top-quark and $t\bar{t}$ quantities, but introduces some dependence on the hadronisation model. The exact correction level is defined at the point of the top-quark decay, i.e. top quarks are considered after their final state radiation.

The phase space is still restricted to the visible detector region, but the phase-space cuts, whose values are the same as above, are now imposed on the leptons and quarks at parton level directly after the top-quark decay.

Fully Extrapolated Phase Space at Parton Level

Presenting the parton-level top-quark and $t\bar{t}$ cross sections extrapolated to the full phase space allows for a direct and fast comparison to a variety of theory calculations from perturbative QCD that are not available for the visible phase space.

The efficiencies in the respective visible phase space for each generated bin, $\epsilon_j^{\text{vis. PS}}$, are presented in Figs. 8.1 to 8.5 (*top row*) for each distribution, as well as the corresponding acceptances A_j in case an extrapolation to the full phase space is performed. The average efficiency for the visible phase space at parton level amounts to 31% for the muon, 25% for the electron and 28% for the combined $\ell +$ jets channel, the corresponding average acceptance to 22% in all channels.

8.1.4 Luminosity and Branching Ratio

Finally, the cross section is calculated using the integrated luminosity L as measured by CMS [139] and the branching ratio for each $\ell + $ jets decay channel of $BR = 0.146$ [19]. However, both cancels again in the case of normalised differential cross sections.

8.1.5 Combination of Electron and Muon Channels

The combination of the electron and muon channel is done at the level of the yields, i.e. N_{data} is added for the two channels to obtain combined event numbers. The same applies to N_{BG}. An average $t\bar{t}$ signal fraction and efficiency or response matrix is calculated from the simulation after combining the simulated events with individual data-driven corrections for the different channels. For the calculation of the absolute inclusive cross section, the average effective luminosity recorded by the different triggers is taken (however, the recorded-luminosity difference between the channels is only 0.5%) and the double branching ratio is used.

8.2 Migration and Unfolding

The differential distributions are subject to bin migrations, i.e. events that are actually produced in bin $X_{gen,j}$ might be measured in another bin $X_{rec,i}$[3]. This is on the one hand due to the limited instrumental resolution of the variable X. But it can also result from kinematic changes induced by radiation and hadronisation effects if corrections from particle level back to parton level are applied. Thus, in the latter case, dependencies on the hadronisation model are introduced. As migrations can alter the distributions significantly, especially in the case of large slopes, they need to be corrected for.

Migrations are dealt with in the following way: At first, they are studied in terms of the migration matrix and the quantities purity and stability as determined from the simulation. The binning of the differential variables is chosen such that migration is limited to a reasonable amount as defined below. Subsequently, a regularised unfolding approach using the global-correlation coefficient as a criterion for the regularisation level [140] is used to correct for the remaining migration effects. An introduction to the topics of migration and unfolding can be found in [140–142].

8.2.1 Description of Migration

The response matrix $\mathbf{A}$ defined above (see Eq. 8.5) includes all detector effects, i.e. both efficiency and migration. If only migration effects are intended to be studied, it is useful to define the *migration matrix* $\mathbf{M}$ by factorising the efficiencies out. This can be achieved either by normalising the columns of $\mathbf{A}$ to 1 or, equivalently, by modifying

---

[3]Distributions of the generated and the reconstructed quantity are supposed to have the same bin boundaries and consequently also bin numbers in this analysis.

the denominator of Eq. 8.5 such that it includes only the number of events $N_{gen,j\rightarrow rec,*}$, which are generated in bin j and demanded to be reconstructed in any of the bins (denoted by $*$), i.e. not to be lost due to inefficiencies:

$$M_{ij} = \frac{N_{gen,j\rightarrow rec,i}}{N_{gen,j\rightarrow rec,*}}. \tag{8.8}$$

Stability s_i and purity p_i are measures of migration out of and into a bin i, respectively:

$$s_i = \frac{N_{gen,i\rightarrow rec,i}}{N_{gen,i\rightarrow rec,*}}$$

$$p_i = \frac{N_{gen,i\rightarrow rec,i}}{N_{gen,*\rightarrow rec,i}} \tag{8.9}$$

Stability describes the fraction of all the events generated in one bin (and not lost due to inefficiencies) that are also reconstructed in the same bin. It is equivalent to the diagonals of the migration matrix, M_{ii}. On the contrary, purity gives the fraction of all the events reconstructed in one bin that have been also generated in the same bin. Without migration effects, purity and stability would equal 1.

The migration matrix, stability and purity (along with efficiency and acceptance as already discussed above) are shown in Figs. 8.1 to 8.5 for all distributions of the combined channel in the final binning. It can be seen that migration effects are very limited for the directly measurable lepton and b-jet quantities: non-diagonal elements in the migration matrix are at a low level due to a high resolution (see Sec. 7.2.3), leading to high values of stability and purity. In contrast, in case of the reconstructed top-quark and $t\bar{t}$ quantities with a low resolution and large effects due to background from wrong permutations, significant non-diagonal elements in the migration matrix and correspondingly low values for stability and purity are observed despite a coarser binning. In fact, the final binning is mainly chosen according to the migration level observed here (see Sec. 8.2.4).

8.2.2   Covariance and Correlation

As correlations between the different bins of a differential distribution play a crucial role in the unfolding, a short introduction on their description is given here (cf. e.g. [140]).

If bins of a differential distribution represented by a vector $\vec{Y}$ are correlated with each other, their uncertainties (or better: variances) need to be generalised to the covariance matrix **cov** given by

$$\mathrm{cov}_{ij} = \mathrm{E}\left[(Y_i - \mathrm{E}[Y_i])(Y_j - \mathrm{E}[Y_j])\right], \tag{8.10}$$

where $E[\,]$ denotes the expectation value. The diagonal elements include the variances, i.e. the squared uncertainties of the respective bins: $\mathrm{cov}_{ii} = \mathrm{var}_i = \delta_i^2$.

Correlation coefficients with values ranging from -1 (completely anti-correlated) to +1 (completely correlated) with 0 denoting statistical independence can be deduced as

$$\rho_{ij} = \frac{\text{cov}_{ij}}{\sqrt{\text{cov}_{ii} \cdot \text{cov}_{jj}}} = \frac{\text{cov}_{ij}}{\delta_i \cdot \delta_j}. \tag{8.11}$$

To extend the correlation between two bins to a measure that gives the total amount of correlation between one bin Y_i and all other bins, the concept of the global-correlation coefficient ρ_i is defined [143]. It gives the maximum correlation between Y_i and every possible linear combination of all other bins and can be obtained as

$$\rho_i = \sqrt{1 - \frac{1}{(\mathbf{cov})_{ii} \cdot (\mathbf{cov}^{-1})_{ii}}}. \tag{8.12}$$

Its value ranges from 0 (uncorrelated with all other bins) to 1 (completely correlated with at least one linear combination of the other bins).

Finally, to take the global-correlation coefficients of all bins into consideration, the root of the mean squared (RMS) global correlation is calculated:

$$\bar{\rho} = \sqrt{\frac{1}{n_{bins}} \sum_{i=1}^{n_{bins}} \rho_i^2}. \tag{8.13}$$

8.2.3 Regularised-Unfolding Technique

The transformation of the original true distribution given by the vector $\vec{x}$ to the measured distribution $\vec{N}_{sig}$ (without background contribution) via the response matrix reads:

$$\mathbf{A}\vec{x} = \vec{N}_{sig}. \tag{8.14}$$

The aim of unfolding is to obtain the true distribution from the measured one, i.e. to solve Eq. 8.14 for $\vec{x}$, given the response matrix from the simulation. However, inversion problems are generally ill-posed and unstable [140]. Due to limited resolution, a measurement with a detector, i.e. mathematically the application of the response matrix, always involves a smearing of the original distribution, i.e. that peaks and high-frequency components are suppressed. The inversion needs to recover them. However, inevitable statistical fluctuations in the measurement can be mistaken as indications of such high-frequency structures of the true distribution and therefore introduce large unphysical oscillations. Thus, using a direct inversion of $\mathbf{A}$ leads to a large statistical variance of the solution and negative correlations between neighbouring bins. In order to suppress those, the solution needs to be *regularised*, i.e. a-priori constraints regarding the smoothness of the solution are introduced. Technically, this is performed

by rearranging and solving Eq. 8.14 in a minimum-χ^2 sense (χ_A^2) under inclusion of a *penalty or regularisation term (Reg)*:

$$\chi_{tot}^2 = \underbrace{(\mathbf{A}\vec{x} - \vec{N}_{sig})^T \mathbf{cov}_{\vec{N}_{sig}}^{-1}(\mathbf{A}\vec{x} - \vec{N}_{sig})}_{\chi_A^2(\vec{x})} + \underbrace{\tau(\mathbf{C}\vec{x})^T(\mathbf{C}\vec{x})}_{Reg(\vec{x})} = \text{min.} \qquad (8.15)$$

$\mathbf{cov}_{\vec{N}_{sig}}$ is the covariance matrix of the measured vector with the squared statistical uncertainties as diagonal elements only. $\mathbf{C}$ is a matrix that defines the type of the smoothness condition, whereas the regularisation parameter τ steers the relative weight of this condition with respect to χ_A^2.

In this analysis, the selection of $\mathbf{C}$ and the way how Eq. 8.15 is actually solved using Singular Value Decomposition (SVD) follows the method as detailed in [142] and implemented in the software package TSVDUNFOLD [144]. However, deviating from there, the optimisation of τ is based on the minimum-global-correlation method proposed in [140] and implemented by [145]. A short summary is given in the following.

First, instead of solving Eq. 8.15 directly for $\vec{x}$, the vector composed of

$$w_j = x_j/N_{gen,j}, \qquad (8.16)$$

i.e. relative to the simulated true distribution, is used:

$$\chi_{tot}^2 = \underbrace{(\mathbf{A}'\vec{w} - \vec{N}_{sig})^T \mathbf{cov}_{\vec{N}_{sig}}^{-1}(\mathbf{A}'\vec{w} - \vec{N}_{sig})}_{\chi_A^2(\vec{w})} + \underbrace{\tau(\mathbf{C}\vec{w})^T(\mathbf{C}\vec{w})}_{Reg(\vec{w})} = \text{min.} \qquad (8.17)$$

The response matrix is modified accordingly to $\mathbf{A}'$, which now includes the raw simulated event numbers instead of probabilities: $A'_{ij} = N_{gen,j\to rec,i}$. This assists the regularisation as the approximate smoothness of the solution without fluctuations is already assumed from the simulation and factorised out. It is assured that a possibly introduced bias towards the generated input distribution is small (see Sec. 8.2.5). After finding the mathematical solution for $\vec{w}$ by means of SVD, the desired distribution $\vec{x}$ is retrieved from this according to Eq. 8.16.

To obtain a criterion for "smoothness" for the regularisation term, the matrix $\mathbf{C}$ is chosen as

$$\mathbf{C} = \begin{pmatrix} -1 & 1 & 0 & & \\ 1 & -2 & 1 & 0 & \\ & \ddots & \ddots & \ddots & \\ & 0 & 1 & -2 & 1 \\ & & 0 & 1 & -1 \end{pmatrix} \qquad (8.18)$$

In this way, $\mathbf{C}\vec{w}$ is the discrete second derivative[4] of the solution $\vec{w}$, and its euclidian

---

[4]Assuming unity bin width to be precise, but any deviation therefrom is absorbed in the optimisation of the regularisation parameter τ.

norm $(\mathbf{C}\vec{w})^T(\mathbf{C}\vec{w})$ is a scalar measure for the global curvature of $\vec{w}$.

The regularisation parameter τ needs to be chosen carefully: $\tau = 0$ means no regularisation at all, leaving the large negative correlations between neighbouring bins of the original solution (under-smoothing). On the other hand, a very large τ dampens not only the oscillations induced by statistical fluctuations, but also possibly the fine structure of the distribution itself (over-smoothing). This leads to large positive correlations and a bias of the solution towards the underlying smoothness condition. Thus, the optimal τ can be found by demanding the correlations to be small. It is chosen such that the RMS global-correlation coefficient $\bar{\rho}$ (see Eq. 8.13) is minimised for each distribution. The correlation matrices needed for this calculation are obtained via error propagation using pseudo-experiments as explained in Sec. 9.1. They are shown for the normalised final results in App. A. Note, however, that for the calculation of $\bar{\rho}$, the correlation matrices before normalisation are taken (the normalisation can affect the correlations, which is, however, not related to the regularisation). A scan of $\bar{\rho}$ as a function of τ is shown in Figs. 8.1 to 8.5 (*bottom row*). It can be seen that for quantities that are not heavily affected by migration (especially the lepton quantities), the global correlation is already very low for small values of τ and the minimum is relatively shallow. In contrast, for quantities that are subject to substantial migration, the global correlation in the unregularised case is much higher and can be significantly reduced by choosing an optimum τ. The chosen τ is indicated in the figure.

8.2.4 Choice of Binning

In general, it is desirable to choose the measurement intervals as small as possible in order to maximise the gain of differential information and resolve the structure of the distributions as finely as possible. However, a trade-off needs to be found regarding the increasing statistical uncertainty (even without migration) and the increasing amount of bin migration when reducing the bin width. Despite the minimum-global-correlation condition for regularisation, the bin correlations, statistical uncertainties and a possible bias of the unfolded result can be large if migrations are too strong. Thus, for a good unfolding performance, stability and purity are required to stay at a level of typically 40 to 50% or above and to evolve approximately smoothly over the full range of the distributions (Figs. 8.1 to 8.5, *top row*). Additionally, it is required that the migration into the bins, which are not the next neighbours, are suppressed at the level of a few to maximally 15% (Figs. 8.1 to 8.5, *middle row*).

These constraints assure that the statistical uncertainties of the unfolded results remain below typically 5% (and hence below the systematic uncertainties, see Sec. 9.4) and the maximum bin correlations before normalisation typically below 40%. To distributions that are not limited by migrations like the lepton and partly the b-jet quantities, the constraint of a statistical uncertainty below the systematic one is directly applied. Finally, it is required that the systematic-uncertainty distributions as displayed in Sec. 9.4 do not show significant spikes in any of the bins as this would indicate a statistical deficit in the simulated sample (and hence in the response matrix) that is used to assess that uncertainty. In rare cases like in peripheral regions, the requirements are
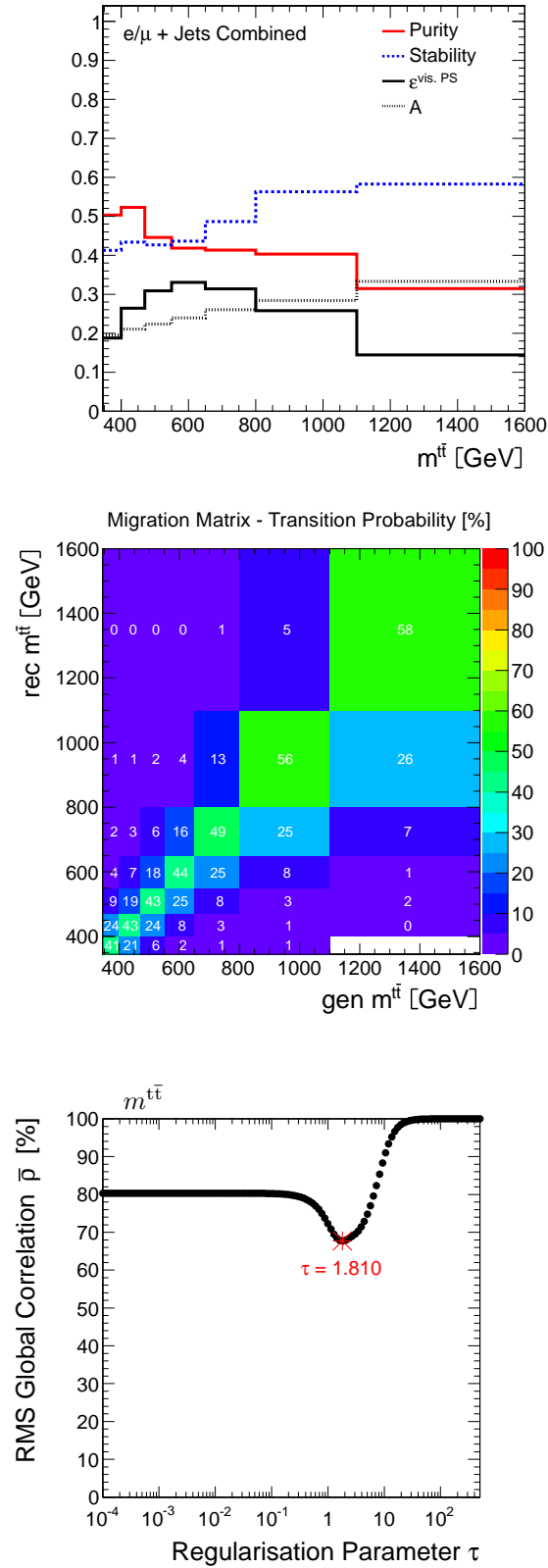
Figure 8.1: Detector effects and unfolding plots for the $t\bar{t}$ quantity $m^{t\bar{t}}$ in the combined channel (gen. quantity at parton level). *Top row*: purity, stability, efficiency $\epsilon^{\mathrm{vis.\,PS}}$ and acceptance A; *middle row*: migration matrix $\mathbf{M}$; *bottom row*: RMS global correlation $\bar{\rho}$ as a function of the regularisation parameter τ.
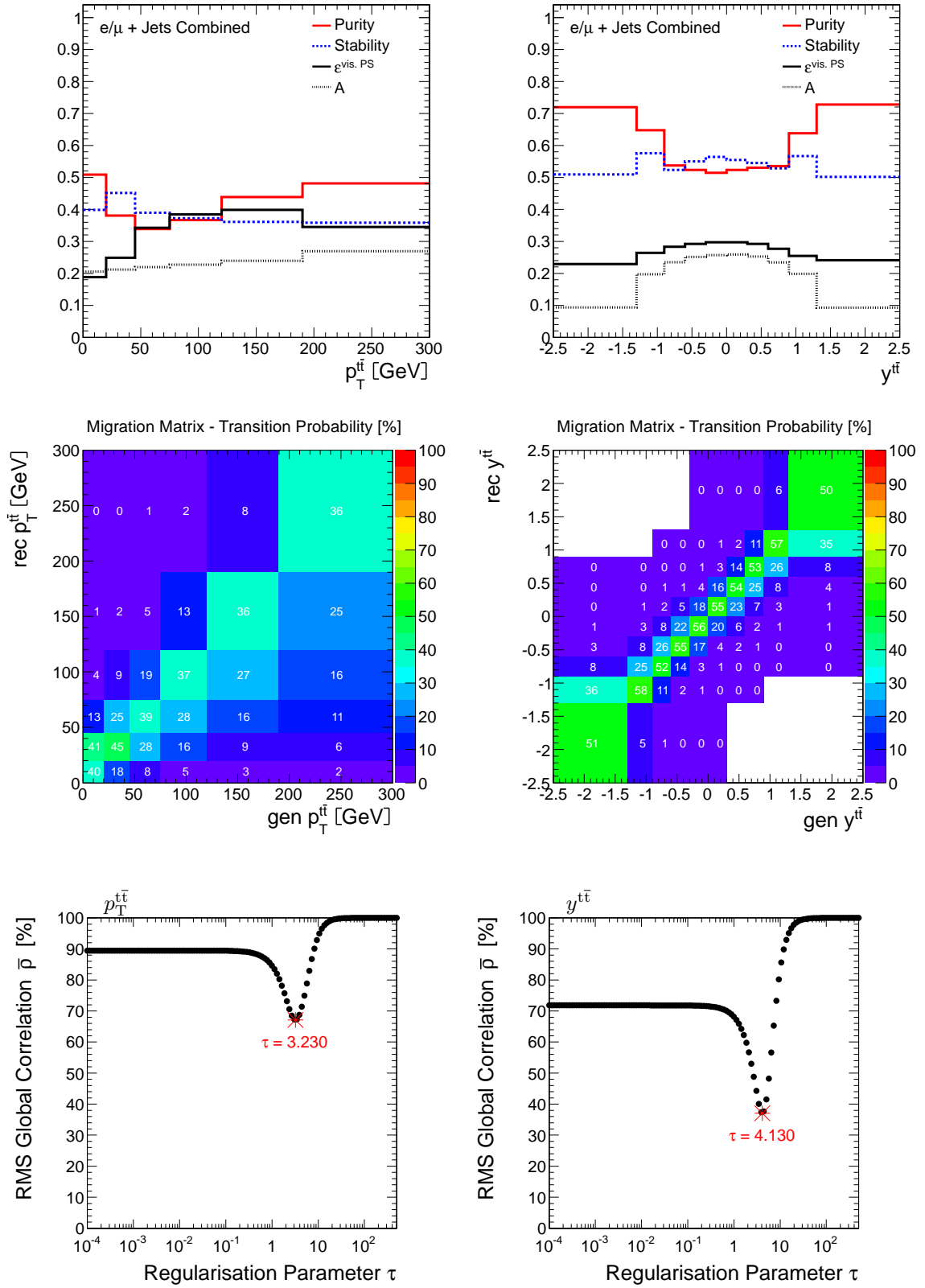
Figure 8.2: Detector effects and unfolding plots for the $t\bar{t}$ quantities $p_T^{t\bar{t}}$ (*left*) and $y^{t\bar{t}}$ (*right*) in the combined channel (gen. quantities at parton level). *Top row*: purity, stability, efficiency $\epsilon^{\mathrm{vis.\,PS}}$ and acceptance A; *middle row*: migration matrix $\mathbf{M}$; *bottom row*: RMS global correlation $\bar{\rho}$ as a function of the regularisation parameter τ.
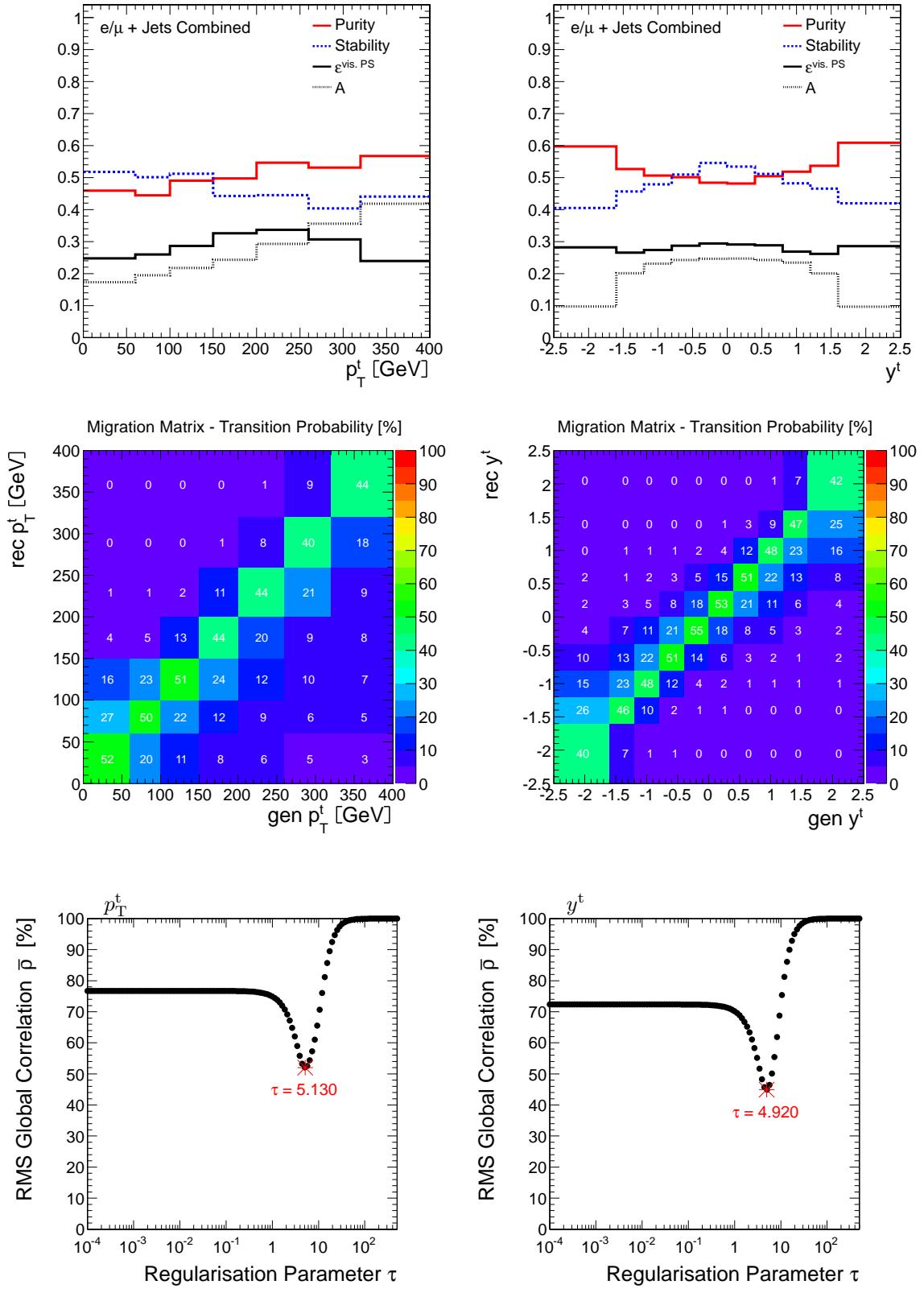
Figure 8.3: Detector effects and unfolding plots for the top-quark quantities p_T^t (*left*) and y^t (*right*) in the combined channel (gen. quantities at parton level). *Top row*: purity, stability, efficiency $\epsilon^{\text{vis. PS}}$ and acceptance A; *middle row*: migration matrix $\mathbf{M}$; *bottom row*: RMS global correlation $\bar{\rho}$ as a function of the regularisation parameter τ.
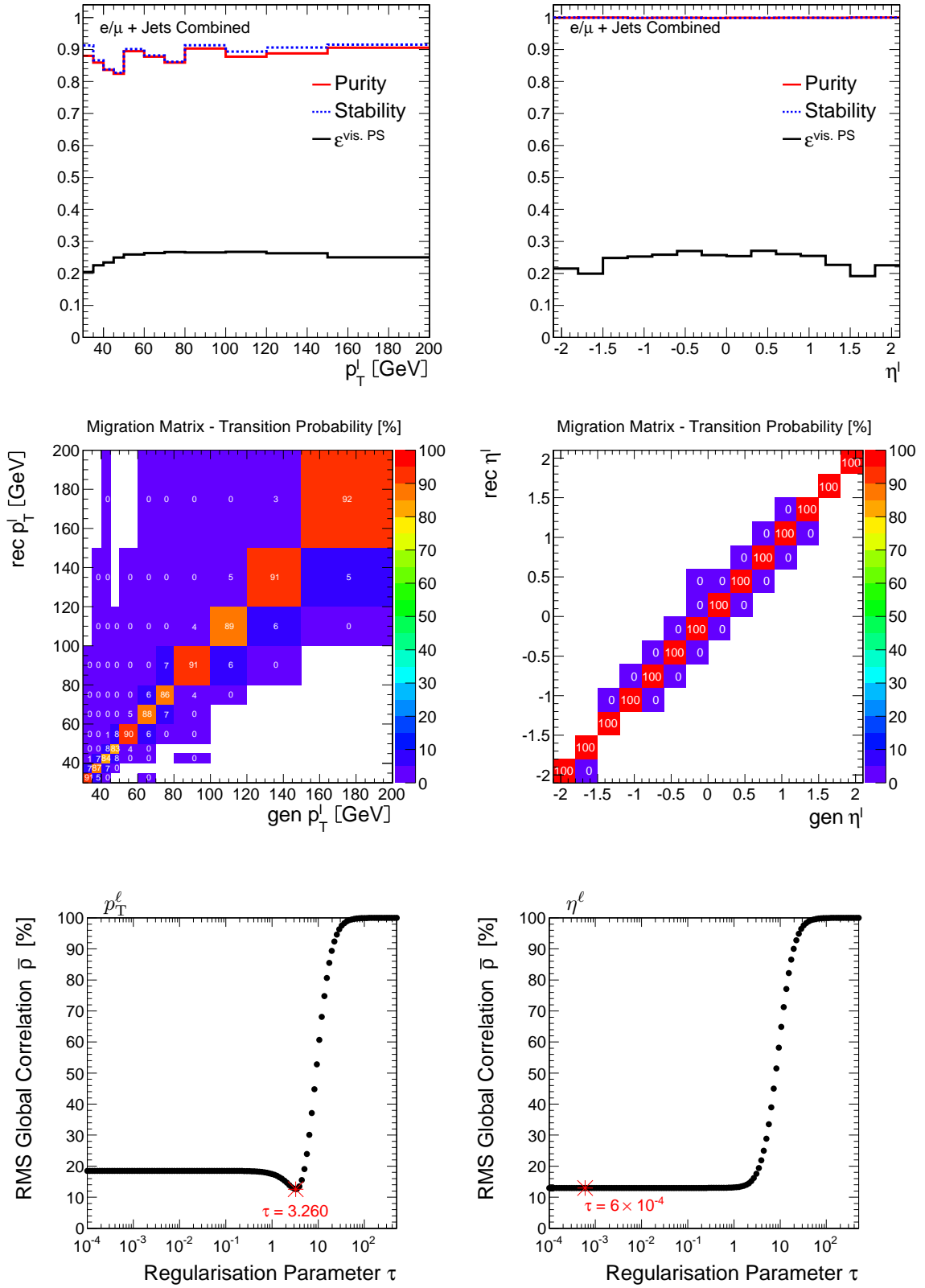
Figure 8.4: Detector effects and unfolding plots for the lepton quantities p_T^ℓ (*left*) and η^ℓ (*right*) in the combined channel (gen. quantities at particle level). *Top row*: purity, stability and efficiency $\epsilon^{\text{vis. PS}}$; *middle row*: migration matrix $\mathbf{M}$; *bottom row*: RMS global correlation $\bar{\rho}$ as a function of the regularisation parameter τ.
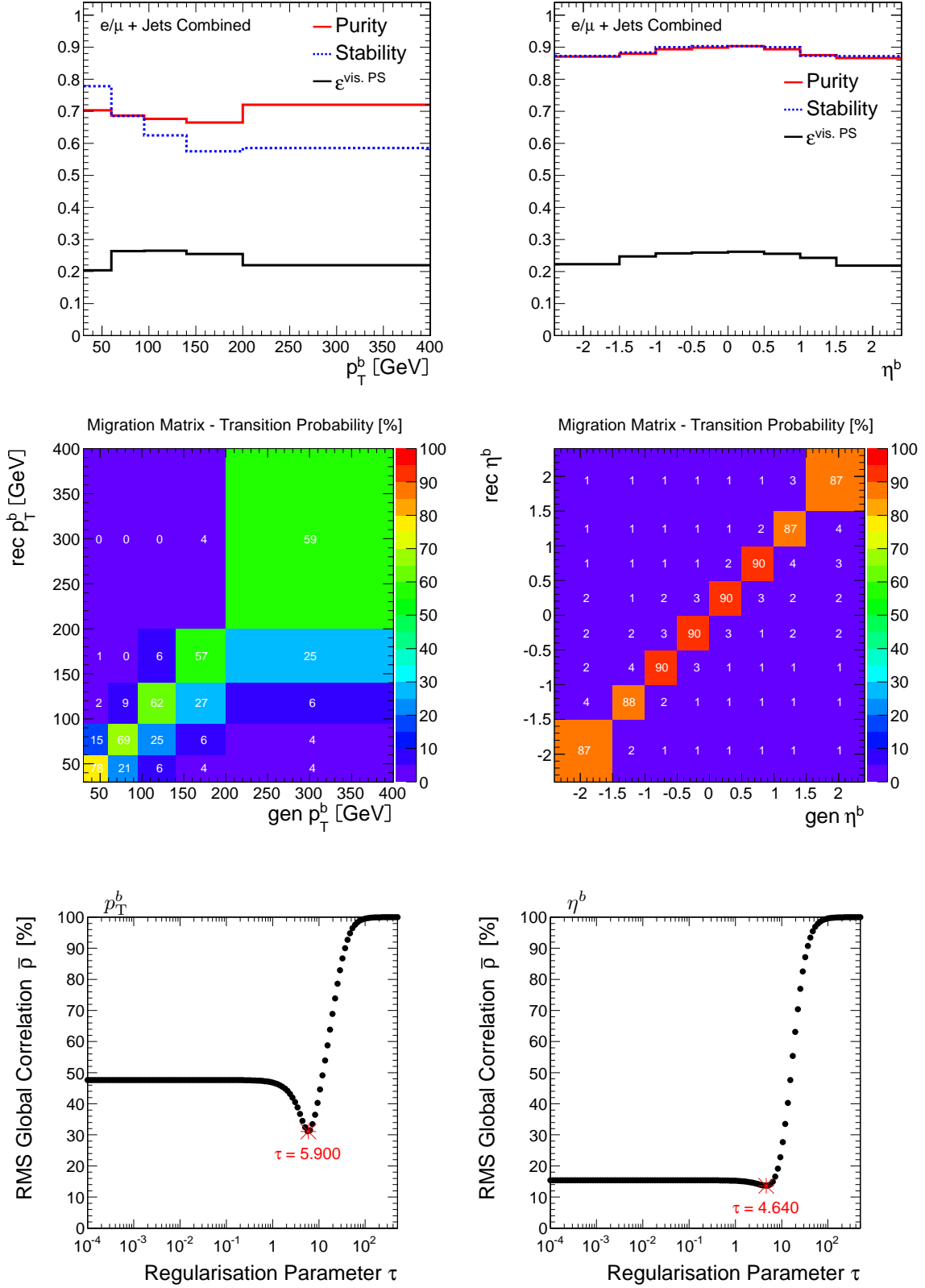
Figure 8.5: Detector effects and unfolding plots for the b-jet quantities p_T^b (*left*) and η^b (*right*) in the combined channel (gen. quantities at particle level). *Top row*: purity, stability and efficiency $\epsilon^{\text{vis. PS}}$; *middle row*: migration matrix **M**; *bottom row*: RMS global correlation $\bar{\rho}$ as a function of the regularisation parameter τ.

exceptionally allowed to be softened to enable a measurement there.

8.2.5 Unfolding Closure and Stability Tests

As explained above, regularisation introduces an a-priori assumption regarding the unfolded solution. In this analysis, the curvature of $\vec{w}$, i.e. of the unfolded result relative to the simulated true distribution (cf. Eq. 8.16), is constrained. However, the minimum-global-correlation condition for the determination of the regularisation parameter and the limitation of migration by the choice of binning are expected to keep a possible bias towards the input model at a low level. Several closure tests are performed to verify that the unfolding applied here produces consistent results and that the introduced bias is negligible. Note that these tests here only investigate effects due to the unfolding technique itself, especially the regularisation, and do not address the question whether the underlying detector and hadronisation models used to construct the response matrix are correct. The latter is studied separately and is finally taken into account as systematic uncertainties as described in Sec. 9. The tests presented here are done in the full phase space at parton level.

First, an unfolding closure test is performed on simulated events. For the unfolding, the same setup as in the real data analysis is used: the standard $t\bar{t}$ MADGRAPH sample is taken to construct the response matrix and the denominator in $\vec{w}$, which serves as curvature reference for the regularisation. Moreover, also all other analysis steps including binning, background removal, normalisation, decay-channel combination etc. follow the same procedure as in the real data analysis. Only the input data that is unfolded is not from real collisions, but taken from reconstructed simulated events scaled to the standard luminosity of this analysis.

In a first step, it is verified that the unfolded reconstructed distribution of the standard MADGRAPH $t\bar{t}$ simulation reproduces the underlying generated true distribution. The agreement is found to be better than a permille.

Subsequently, distributions with shapes that are significantly different from the standard $t\bar{t}$ simulation are unfolded and compared to their underlying generated true distributions. Two qualitatively different shape distortions are studied. On the one hand, the shape of the distribution is altered globally by reweighting the $m^{t\bar{t}}$ distribution such that it becomes either softer (i.e. tends to lower $m^{t\bar{t}}$ values) or harder (i.e. tends to higher $m^{t\bar{t}}$ values). Alternatively, the distribution is only locally distorted by adding a simulated Z' signal to the SM prediction, thereby testing the sensitivity of the unfolding to narrow, delta-pulse-like resonances.

The weights for the global-shape distortion are calculated for each simulated event k as a function of the generated $m^{t\bar{t}}$ [in GeV]:

$$w_{prel,k} = 1 \pm (m_k^{t\bar{t}} - 350) \cdot 0.015$$
$$w_{norm,k} = w_{prel,k} \cdot \frac{N}{\sum_{i=1}^{N} w_{prel,i}} \tag{8.19}$$

The preliminary weights w_{prel} are normalised (w_{norm}) such that the total number of events in the sample N stays unchanged. Applying the plus sign in the equation results in a harder spectrum, the minus sign in a softer one.

The distorted generated spectrum is compared to the original one in Fig. 8.6 after normalisation. Due to correlations of $m^{t\bar{t}}$ with other quantities, the reweighting also changes other distributions, especially p_T^t and moderately also $y^{t\bar{t}}$, which is also shown. It should be noted that these shape distortions are extreme examples significantly larger than the observed differences between the measured and the standard simulated distributions (cf. final results presented in Sec. 10). The data points in these figures correspond to the reconstructed reweighted distributions after unfolding with statistical uncertainties corresponding to the standard luminosity of this analysis (5 fb^{-1}). Thus, they are expected to match with the respective reweighted generated distribution. It can be seen that despite the extreme shape distortions, the agreement is very good and no visible bias is introduced. Residual deviations are well within the statistical uncertainties.

A completely different shape distortion is introduced by the presence of a narrow resonance-like signal. To simulate this, a hypothetical leptophobic topcolour Z$'$ signal [60] with a mass of 750 GeV and 1.2% width (much less than the $m^{t\bar{t}}$ reconstruction resolution) as simulated by MADGRAPH is added to the standard t$\bar{t}$ sample. To study the dependence of the unfolding on the strength of such a resonance signal, the predicted cross section of 3.2 pb is varied with applied factors ranging from 0.03 to 4. Fig. 8.7 shows the originally generated t$\bar{t}$ distribution used in the unfolding setup, the combined generated distribution of t$\bar{t}$ +Z$'$ (*magenta line*) and the reconstructed combined t$\bar{t}$ +Z$'$ distribution after unfolding for Z$'$ cross sections of 3.2 pb (*top*) and 4×3.2 pb (*bottom*). The $m^{t\bar{t}}$ spectrum (*left*) exhibits the resonance most prominently. The generated normalised cross section in the bin including the simulated Z$'$ mass ($650 < m^{t\bar{t}}$ [GeV] < 800), is enhanced by about 25% and 100% for a Z$'$ cross section of 3.2 pb and 4×3.2 pb, respectively. But also the p_T^t spectrum (*right*) is affected by such an additional signal.

It can be seen that the unfolding reproduces the originally generated distributions including an additional Z$'$. The bias, i.e. the difference between the unfolded and the generated t$\bar{t}$ +Z$'$ cross section in this bin, is very small as displayed in Fig 8.8: Only 2% for a normalised cross section enhancement of 25% in this bin and 6% for an enhancement of 100%. It should be emphasised again that these are extreme examples and the observed difference between real data and SM predictions is much less, thereby justifying the assumption of a negligible bias. Furthermore, note that this analysis is intended and therefore optimised to measure the t$\bar{t}$ cross section and not to set limits on resonance signals, which would require e.g. other signal efficiencies due to different topologies. A dedicated CMS analysis for resonance searches can be found elsewhere [146]. However, it is reassuring to note that such signals would manifest themselves as clear deviations of the measured normalised differential cross section from the SM t$\bar{t}$ prediction.

Besides the closure tests on simulated events, further tests are performed on real data to study the stability of the unfolding. For one test, the measured distribution in
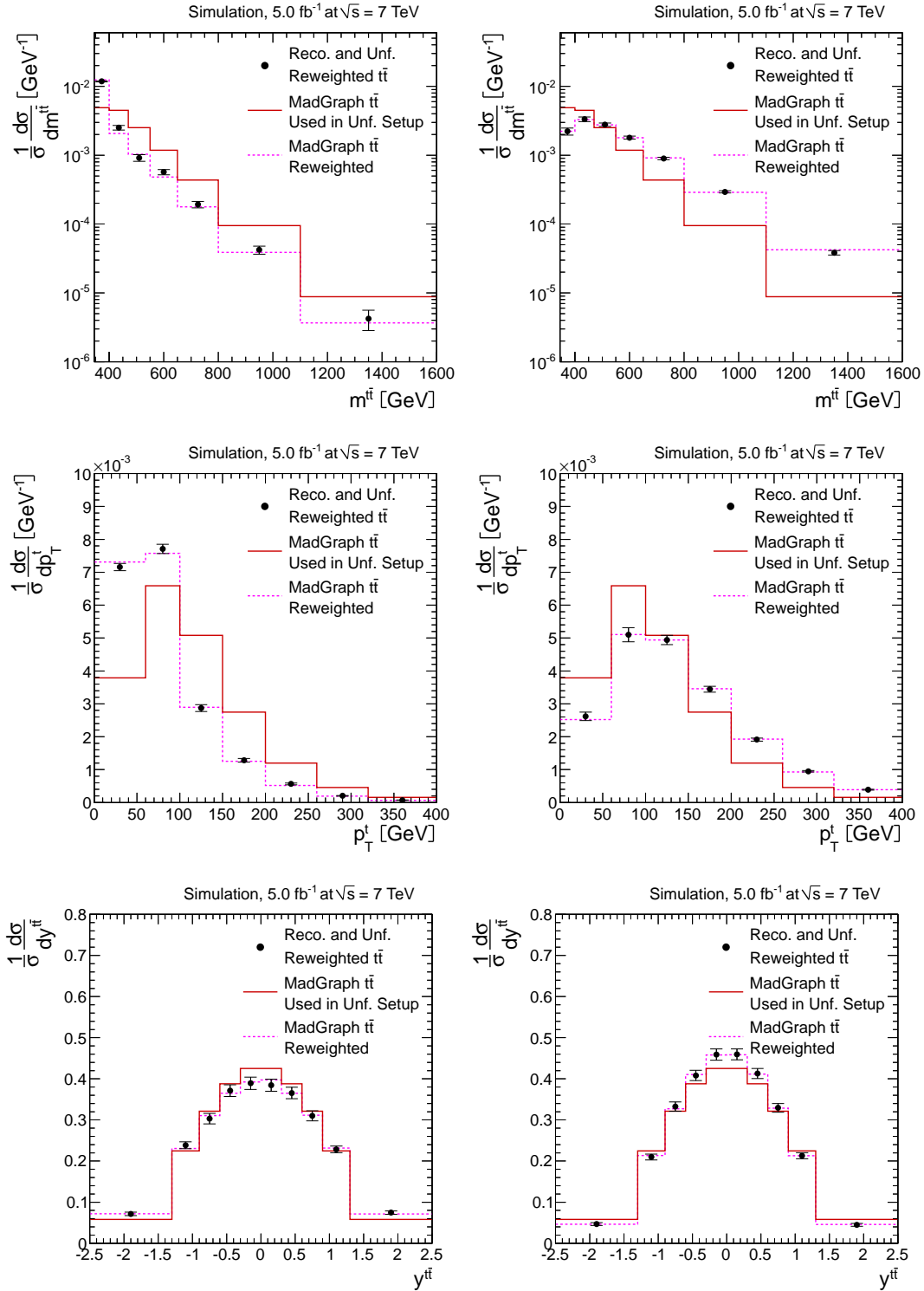
Figure 8.6: Unfolding closure test with a reweighted $m^{t\bar{t}}$ spectrum: Softer (*top left*) and harder (*top right*) $m^{t\bar{t}}$ spectrum. Further variables that change during the $m^{t\bar{t}}$ reweighting in a correlated way include p_T^t (*middle row*) and $y^{t\bar{t}}$ (*bottom row*). The originally simulated $t\bar{t}$ distribution used in the unfolding setup (*red line*), the reweighted distribution (*magenta line*) and the reconstructed and unfolded reweighted distribution (*points*) are compared. The shown distributions are normalised differential cross sections for the combined ℓ + jets channel.
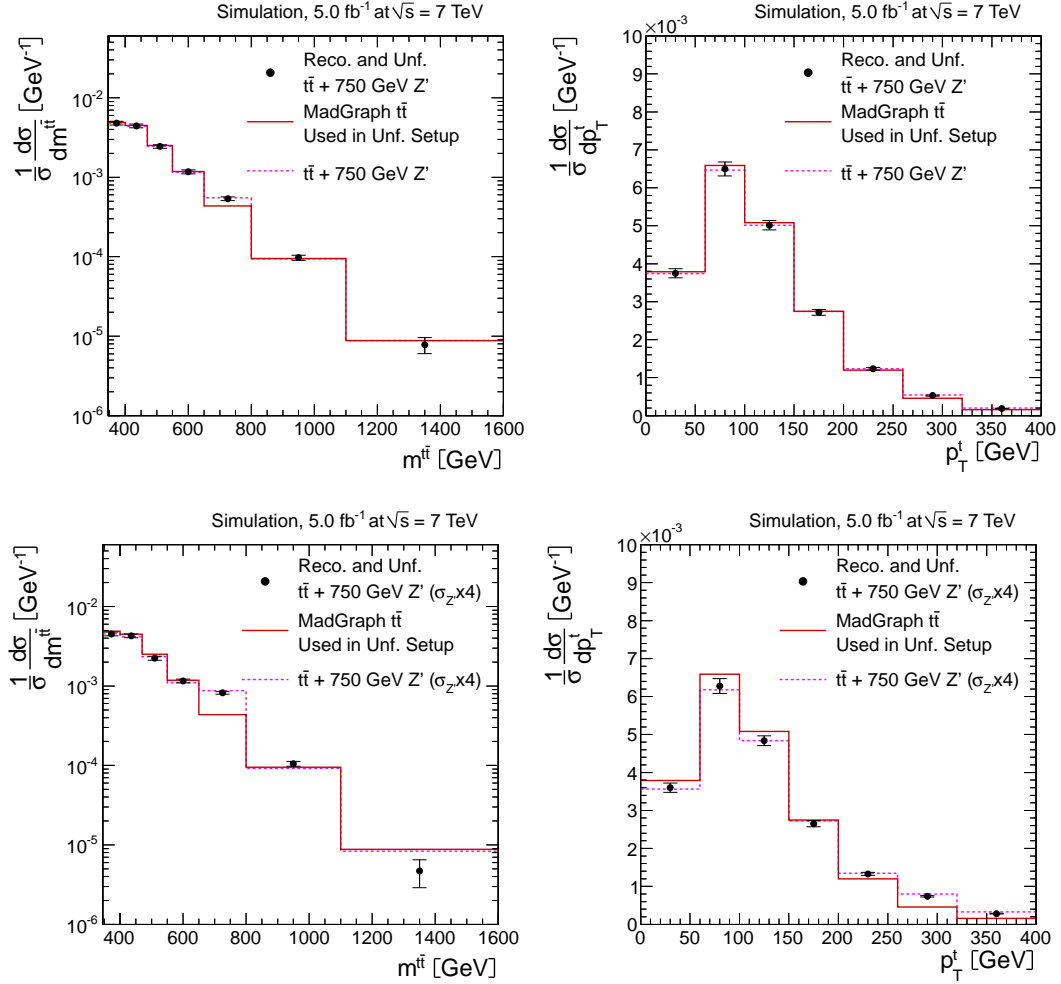
Figure 8.7: Unfolding closure test with an additional Z′ signal for the $m^{t\bar{t}}$ (*left*) and p_T^t variable (*right*). The *top row* uses the nominal Z′ cross section of 3.2 pb predicted by [60], the *bottom row* a cross-section value of 4×3.2 pb. The originally generated t$\bar{t}$ distribution used in the unfolding setup (*red line*), the combined generated distribution of t$\bar{t}$ +Z′ (*magenta line*) and the reconstructed and unfolded combined t$\bar{t}$ +Z′ distribution (*points*) are compared. The shown distributions are normalised differential cross sections for the combined ℓ + jets channel.
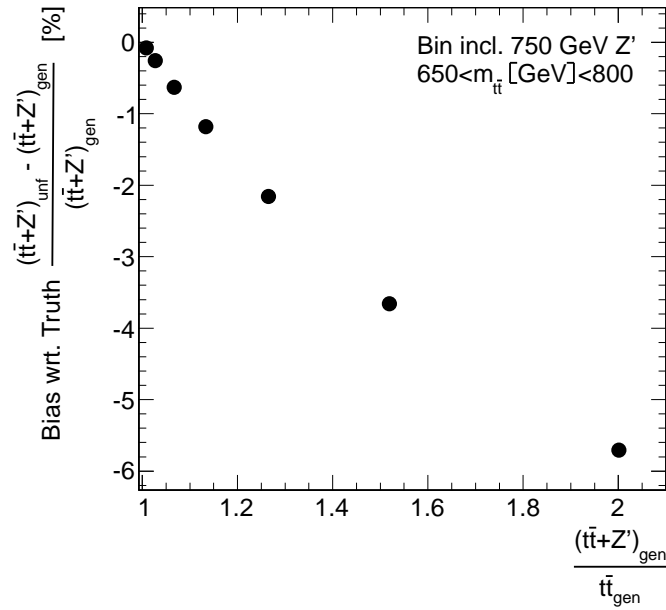
Figure 8.8: The unfolding bias in the presence of a resonance, defined as the relative difference between the unfolded and generated normalised differential cross section in the bin including the Z′ with a simulated mass of 750 GeV. It is shown as a function of the cross-section enhancement given by the ratio of the generated normalised differential cross section with Z′ to the one without. The corresponding Z′ cross sections are *from left to right*: 0.03, 0.1, 0.25, 0.5, 1, 2 and 4 times the nominal cross section of 3.2 pb.

data is unfolded in a regularised way and folded again with the simulated response matrix. The difference with respect to the original measurement is found to be negligible for all distributions, proving the stability and consistency of the regularisation.

Another test involves the reweighting of the simulation (both generated and reconstructed distributions) such that the generated distribution matches the measured cross section from data after a first unfolding step. Subsequently, further iterations of unfolding the original data are performed using the reweighted simulated distributions as new input for the unfolding setup, i.e. for the construction of the response matrix and as denominator of $\vec{w}$ in Eq. 8.16. The difference between the iterations is typically below the percent level and converges fast to 0. Even for top-quark p_{T}, which turns out to be the distribution, for which the deviation between the measured and predicted cross section is largest (cf. Sec. 10), the iteration change is typically at the percent level and thus well within the statistical uncertainties. This can be seen from Fig. 8.9, which shows the generated and the unfolded cross section after 1, 2 and 3 iterations (*left*) and the ratio between subsequent iterations (*right*).

To conclude, the chosen binning and level of regularisation lead to stable and consistent unfolded results with negligible bias towards the input model. Thus, no bias
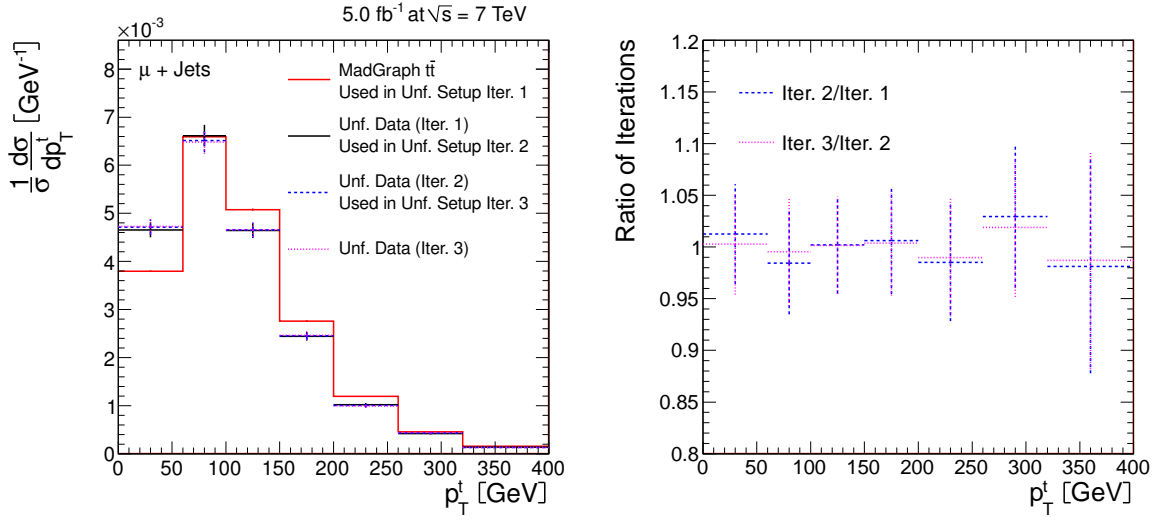
Figure 8.9: Unfolding stability test on data using different unfolding iterations for the p_T^t normalised differential cross section in the μ+jets channel. *Left*: comparison of the originally generated distribution used in the unfolding setup for iteration 1, and the unfolded measured data after 1, 2 and 3 unfolding iterations, which are subsequently used in the unfolding setup of the next iteration, respectively. *Right*: the corresponding ratio between subsequent iterations. The error bars correspond to statistical uncertainties.

corrections need to be applied.

Chapter 9

Uncertainties

The individual quantities used to calculate the cross sections (Eq. 8.1, 8.2) are not known perfectly. It is important to estimate their uncertainties in order to know the precision of the measurement when comparing to other experimental results or theoretical models.

Uncertainties can either be of statistical nature, originate from limited precision in the correction for detector effects or arise from theoretical uncertainties in the unfolding, acceptance extrapolation and background determination. They have different effects on absolute and normalised cross sections because the uncertainties common to all bins of the measurement (i.e. normalisation uncertainties concerning luminosity, flat scale factors etc.) cancel for the normalised case, or at least reduce significantly. Thus, only uncertainties uncorrelated between the bins, which affect only the shape of the differential distributions, remain.

The systematic uncertainties are generally determined by up and down variations of the uncertainty-afflicted quantity by one standard deviation or other conventional amounts. Subsequently, the shift is propagated to the cross section (in some cases by repeating the whole analysis chain) and the difference to the central value is considered as the systematic uncertainty of the cross section. In case the uncertainty values for the up and down variations differ, the uncertainty is symmetrised to the mean value. This procedure is done separately for each uncertainty source and the individual contributions are finally added in quadrature. The uncertainties of the normalised differential distributions are determined separately for each bin from the difference between the normalised shifted and normalised central value.

The uncertainties taken into account are discussed in the following. An overview is given in Tab. 9.1 and Figs. 9.1 and 9.2.

9.1   Statistical Uncertainty

The statistical uncertainty of the event yield is given by the Poissonian standard deviation $\sqrt{N_{\text{data}}}$. For the inclusive cross section, it is propagated to the final result using

simple Gaussian error propagation as approximation. For the reconstructed differential distributions, the squared statistical uncertainties of all bins (i.e. the variances) constitute the diagonal elements of the measured covariance matrix $\mathbf{cov}_{\vec{N}_{sig}}$ (see Sec. 8.2.2). As each bin is measured independently, no off-diagonal elements are present. The covariance matrix of the unfolded result $\mathbf{cov}_{\vec{x}}$ is determined by error propagation using pseudo-experiments. The measured yield distribution $\vec{N}_{sig}$ is overlaid with random noise according to its statistical uncertainty. Each altered distribution is unfolded again and the differential cross section is recalculated. From a sample of 1000 of such pseudo-experiments, the covariance matrix for each differential cross-section distribution is obtained according to Eq. 8.10. It includes non-zero off-diagonal entries because the elements of the unfolded distributions are correlated with each other due to limited resolution and migration. The statistical correlation matrices for each distribution after normalisation are given in App. A (they are related to the covariance matrices via Eq. 8.11). For the graphical presentation of the differential cross-section distributions, the square root of the diagonal covariance elements are taken as statistical uncertainties.

9.2 Experimental Systematic Uncertainties

9.2.1 Luminosity

The uncertainty of the luminosity measurement is determined to be 2.2%, which is dominated by scan-to-scan variations of the Van-der-Meer calibration and afterglow effects [89]. For the normalised differential cross sections, the luminosity cancels largely. Only a small fraction remains due to subtracting the luminosity-scaled simulated background events from data.

9.2.2 Pile-Up

As explained in Sec. 4.3, the pile-up (PU) model estimates the mean number of PU interactions to be about 9.5 events for 2011 data. An uncertainty of 8% is assigned to cover the uncertainties related to the inelastic proton-proton cross-section, the instantaneous luminosity, the PYTHIA PU-model and the reweighting process [147]. Such variations lead to new PU distributions in data and consequently new event weights, which are applied to the simulation. Also the lepton-efficiency scale factors are redetermined using the new event weights, which mitigates the influence of the PU uncertainty on the lepton selection as in all cases the efficiencies are scaled to the data.

9.2.3 Jet Energy

As at least four jets are required in this analysis, the uncertainties related to the jet energy (both scale and resolution, see Sec. 5.1.5) have a large influence on the selection efficiency.

Jet-Energy Scale

To estimate the effect of the jet-energy scale (JES) uncertainty, the reconstructed jet energy in the simulation is shifted by its uncertainty of typically 1 to 3% depending on p_T and $|\eta|$ (see Sec. 5.1.5). This shift is also propagated to the measurement of the missing transverse energy.

Jet-Energy Resolution

As mentioned in Sec. 5.1.5, the jet-energy resolution (JER) in simulation is corrected using the $|\eta|$-dependent data-to-simulation scale factor displayed in Tab. 5.1. The analysis is repeated with scale factors shifted according to their uncertainties of typically 5 to 8%. This shift affects both the selection efficiency and the resolutions used for the kinematic fit.

9.2.4   Trigger, Lepton-Selection and B-Tagging Efficiencies

The trigger, lepton-selection and b-tagging efficiencies from the simulation are corrected using data-to-simulation scale factors (SFs), which are partly parametrised as a function of kinematic variables as presented in Sec. 6.

For the determination of normalisation uncertainties, which are dominant for absolute cross sections, the efficiency SFs are varied in the same direction (up or down) within their uncertainties simultaneously in all kinematic regions. Such a correlated treatment of the variations across all bins yields the most conservative estimate for the uncertainty of the inclusive cross section. In contrast, it has hardly any effect on normalised cross sections as it mostly cancels in the ratio. In cases in which it is not guaranteed that all parts of the SF uncertainty are completely correlated in all kinematic regions, this might underestimate the uncertainty on the normalised differential cross sections.

Thus, for a conservative estimate, the effect of additional SF shape uncertainties is determined. The SF distribution is divided into two p_T or $|\eta|$ bins and the SF is shifted up in one bin and simultaneously down in the other one, and vice-versa. The bins are chosen such that they are divided by the median of the respective distribution in the phase space of the selection (55 GeV (65 GeV) for the lepton (b-jet) p_T distributions, 0.7 for lepton and b-jet $|\eta|$ distributions). Other divisions such as one bin containing one quarter of the events or bin divisions according to the detector geometry (barrel/endcap) are found to yield similar results.

The normalisation variation as well as the p_T- and $|\eta|$-dependent shape variations are performed individually and their maximum is taken as final uncertainty to avoid double-counting.

Trigger and Lepton-Selection Efficiencies - Muon Channel

The uncertainties on the muon-selection and trigger efficiencies arise from almost negligible statistical tag-and-probe uncertainties, systematic method uncertainties (resonance fit or cut-based count, Z-boson mass-window definition) and dominantly from about 1%-level deviations from a flat SF in case the SF is not parametrised like for the η-dependent trigger efficiency (cf. Sec. 6.1.2). Thus, uncertainties in both normalisation and shape are conservatively assessed by SF variations of $\pm 1\%$.

Trigger and Lepton-Selection Efficiencies - Electron Channel

The statistical uncertainties and deviations from a flat SF for the selection and trigger efficiencies are observed to be larger in the electron than in the muon channel (cf. Sec. 6.1.3). Both normalisation and shape uncertainties are conservatively assessed by $\pm 2\%$ SF variations.

For the efficiency of the jet part of the trigger, a SF is only applied to events with 4 jets and p_{T}(4th jet) between 30 and 40 GeV. For those, a 1% variation is performed as systematic uncertainty mainly to account for the difference between the efficiencies determined with the muon- and electron-hadron cross triggers. In order to determine a shape uncertainty as a function of $|\eta|$ of the 4th jet, the SF of the two $|\eta|$ bins (divided by $|\eta|$=1.4) is shifted up and down in opposite directions by 0.5%.

B-Tagging Efficiency

The b-tagging efficiency scale factor per jet is determined as a function of b-jet p_{T} (see Sec. 6.2). For the determination of the normalisation uncertainty, the SF is varied by its uncertainty of 2–3%. As a part of this uncertainty might be uncorrelated across the bins, additional shape variations are performed with half of this uncertainty.

In addition, the mistag rate is varied according to its uncertainty (see Sec. 6.2), which has only a small effect on the cross sections.

9.3 Systematic Modelling Uncertainties

The estimation of modelling uncertainties largely follows the general approach in the CMS Top-Quark-Physics Analysis Group as presented in [107] and summarised in the following.

9.3.1 Signal Modelling: Hard-Scattering Scale Q^2 and Matching Threshold

The uncertainty on the modelling of the kinematics of the $t\bar{t}$ signal process is evaluated by varying the hard-scattering scale Q^2. As explained in Sec. 4.2, this comprises the

renormalisation and factorisation scale. The initial parton-shower evolution scale is varied by the same factor in a correlated way. Furthermore, the effect of additional jet production in MadGraph is studied by varying the matching threshold between jet production at matrix-element level and in parton showering (see Secs. 4.1.2 and 4.2). Thus, both variations cover uncertainties on initial- and final-state radiation modelling. Both Q and the matching threshold are varied up and down by the conventional factor of two and 0.5 with respect to their nominal values, respectively. Dedicated simulated samples generated with these variations are used (see Tab. 4.1).

9.3.2 Background Modelling and Normalisation

As the background is estimated from simulated samples, model uncertainties also apply to them. Thus, the variation of the Q^2 scale and matching threshold is also studied for W- and Z-boson events. These two samples are varied simultaneously. This allows for associating both a shape and normalisation uncertainty. For single-top events, only Q^2-scale variations are considered (as POWHEG is used as a generator, no matching threshold is applied). For the other minor background contributions of diboson and QCD-multijet events, the uncertainty is assessed by varying the background normalisations by $\pm 30\%$ and $\pm 50\%$, respectively.

9.3.3 Hadronisation Model

The difference in kinematic distributions of jets at parton and particle level can, to a large extent, be attributed to the hadronisation process. For the distributions measured at parton level, the unfolding procedure corrects for this effect via the response matrix. Since those corrections are determined from simulated $t\bar{t}$ events, a dependence on the hadronisation model of the simulation can be present, which differs e.g. between PYTHIA and HERWIG as explained in Sec. 4.1.3. To evaluate the size of this uncertainty, cross-section distributions obtained by unfolding the background-subtracted data with response matrices from POWHEG + PYTHIA are compared to those obtained by unfolding with response matrices from MC@NLO + HERWIG. The difference is taken as the hadronisation uncertainty, assuming that differences between POWHEG and MC@NLO in describing $t\bar{t}$ production, which are formally beyond NLO accuracy, are negligible. Since PYTHIA and HERWIG include different parton-showering techniques, there is possibly some unavoidable overlap with the hard-scattering-scale (Q^2) and the matching-threshold uncertainty, making this a rather conservative estimate. As the inclusive cross section does not rely on unfolding, this uncertainty is not taken into account for it.

9.3.4 Parton-Distribution Functions

For the simulation of the $t\bar{t}$ signal with MadGraph, the LO CTEQ6L1 parton-distribution-function (PDF) set is used. The impact of PDF-model uncertainties on

the measurement, including α_s variations, is evaluated following the PDF4LHC prescription [148].

As a first step, the PDF uncertainties are determined for the predicted $t\bar{t}$ cross sections using the MC@NLO event generator (the recommended PDF error sets are only available at NLO). This is performed separately for the three NLO PDF-error sets CT10 [149], MSTW2008 [46] and NNPDF2.1 [150]. For each set, each of the corresponding PDF parameters is varied within its uncertainty and the effect on the predicted cross-section distributions (for normalised cross sections after normalisation) is evaluated by PDF reweighting as described in [148]. These individual uncertainties of each parameter are added in quadrature. Subsequently, the envelope of the individual uncertainty bands of the three considered PDF sets is determined. From the ratio of the upper and lower envelope to the central value, event weights are calculated as a function of each measured kinematic quantity. These weights are used to vary the corresponding distribution of the MADGRAPH $t\bar{t}$-signal simulation and the analysis is repeated.

9.3.5   Top-Quark Mass

The predicted kinematic distributions of the produced top quarks and their decay products, and hence the acceptance and unfolding, depend on the exact value of the top-quark mass. To evaluate the uncertainty due to the assumed top-quark mass of $172.5\,\text{GeV}$ in the simulation, the analysis is repeated using $t\bar{t}$ MC samples with top-quark masses of $161.5\,\text{GeV}$ and $184.5\,\text{GeV}$. To take into account that the latest combination of the top-quark-mass measurement already achieves a precision of $0.9\,\text{GeV}$ [21], the uncertainty is linearly rescaled by a factor of $0.9/\Delta m_t$, with Δm_t being the difference between m_t in the samples with varied and central top-quark mass.

9.4   Typical Values and Distributions of the Uncertainties

In Tab. 9.1, relative values for the various sources of uncertainties are given, both for the normalised differential cross-section distributions and the absolute inclusive cross section in the combined channel. The values for the top-quark and $t\bar{t}$ quantities are given for the full phase space at parton level (for the visible phase space similar numbers are obtained), the values for the lepton and b-jet quantities for the visible phase space at particle level. For the differential cross sections, the table quotes the median of the uncertainties, which vary from bin to bin, as a representative value. The exact uncertainty dependence on all differential quantities is shown for the statistical, total systematic and total uncertainty in Figs. 9.1 and 9.2. As can be seen, the uncertainties tend to be larger for peripheral bins.

The table indicates that the model uncertainties, especially related to the Q^2 scale and matching threshold for both $t\bar{t}$ signal and V+jets background, are the dominant

	Uncertainties [%]									
	Normalised Differential Cross Sections									Incl.
Unc. Source	$m^{t\bar{t}}$	$p_T^{t\bar{t}}$	$y^{t\bar{t}}$	p_T^t	y^t	p_T^ℓ	η^ℓ	p_T^b	η^b	$\sigma_{t\bar{t}}$
Luminosity	<0.5	<0.5	<0.5	<0.5	<0.5	<0.5	<0.5	<0.5	<0.5	2.5
PU	<0.5	1.0	<0.5	<0.5	<0.5	0.5	<0.5	<0.5	<0.5	1.0
JES	3.5	4.5	0.5	1.5	0.5	<0.5	<0.5	2.0	0.5	5.5
JER	1.0	2.0	0.5	0.5	0.5	<0.5	<0.5	<0.5	<0.5	<0.5
Lep.&Trig. Eff.	0.5	<0.5	<0.5	1.0	<0.5	1.5	0.5	<0.5	<0.5	1.5
B-Tag&Mistag Eff	1.5	<0.5	1.0	1.0	1.0	<0.5	<0.5	2.0	1.0	5.0
Q^2 (t$\bar{\text{t}}$)	2.5	4.0	1.5	2.0	2.0	1.5	2.0	1.0	1.0	4.0
Match. (t$\bar{\text{t}}$)	5.5	1.5	2.0	2.5	2.5	1.5	2.0	1.0	1.0	1.5
Q^2 (V+Jets)	3.0	3.0	2.0	2.0	2.0	1.0	1.5	1.0	1.5	2.0
Match. (V+Jets)	4.5	5.0	3.0	2.0	1.5	1.5	3.0	1.0	1.5	0.5
Q^2 (Single Top)	<0.5	<0.5	0.5	<0.5	<0.5	<0.5	<0.5	<0.5	<0.5	<0.5
Diboson&QCD	<0.5	<0.5	<0.5	<0.5	<0.5	<0.5	<0.5	<0.5	<0.5	<0.5
Top-Quark Mass	0.5	<0.5	<0.5	<0.5	<0.5	<0.5	<0.5	<0.5	<0.5	1.0
PDF	0.5	<0.5	1.0	<0.5	0.5	<0.5	<0.5	<0.5	0.5	1.0
Hadronisation	1.5	3.5	1.0	1.0	1.0	1.5	1.0	2.5	<0.5	n/a
Total Systematic	9.5	9.5	5.0	4.5	4.5	3.5	4.5	4.5	3.0	9.5
Statistical	5.5	4.0	3.5	2.5	3.0	2.5	2.5	2.0	2.0	1.0

Table 9.1: List of relative uncertainties for the combined normalised differential cross sections and the absolute inclusive cross section. The quoted values refer to the uncertainty median of the respective distributions, rounded to half an integer. The values for the t$\bar{\text{t}}$ and top-quark quantities are given for the full phase space at parton level (for the visible phase space similar numbers are obtained), the values for the lepton and b-jet quantities for the visible phase space at particle level.

uncertainties for normalised differential cross sections. However, a part of this is attributed to the limited number of events of the dedicated simulated samples[1] that are used to evaluate these uncertainties, which introduces statistical fluctuations. These are also clearly visible in Figs. 9.1 and 9.2 for the systematic-uncertainty distributions. All uncertainties not affecting the shape of a distribution largely cancel. Thus, many uncertainties that are dominant for the inclusive cross section play only a minor role for the normalised differential cross sections. This is for example the case for the b-tagging efficiency and luminosity uncertainties and partly also for the JES uncertainty. However, the latter strongly depends on the type of quantity. It is negligible for the (pseudo-)rapidity quantities and the lepton p_T, but highly relevant for $p_T^{t\bar{t}}$ and $m^{t\bar{t}}$ as the JES variations change the shapes of their distributions. Also other systematic variations can have different effects on different distributions. The total systematic uncertainty amounts to typically 3 to 5%, except for the $p_T^{t\bar{t}}$ and $m^{t\bar{t}}$ distributions with typically about 10%, similar to the inclusive cross section.

The statistical uncertainty is already at a level well below the systematic uncer-

---

[1]The simulated samples for the Q^2-scale and matching-threshold variations have only about 12% (4%) of the generated events of the central sample for W+jets (Z+jets), cf. Tab. 4.1.

tainties for the inclusive cross section ($< 1\%$). However, due to the splitting into many measurement intervals and the unfolding, it amounts to typically 2 to 5% for the differential cross sections. For the lepton quantities, which are not strongly affected by migration, it is the limiting factor preventing a finer binning (see Sec. 8.2.4). However, for some of the quantities, whose binning is limited by migration such as p_T of the $t\bar{t}$ system and $m^{t\bar{t}}$, the statistical uncertainty is already lower than the systematic one, like for the inclusive cross section. Thus, decreasing the systematic uncertainties is required for the improvement of the precision.

However, already now the measurement achieves an overall precision in the order of typically 4 to 11%.
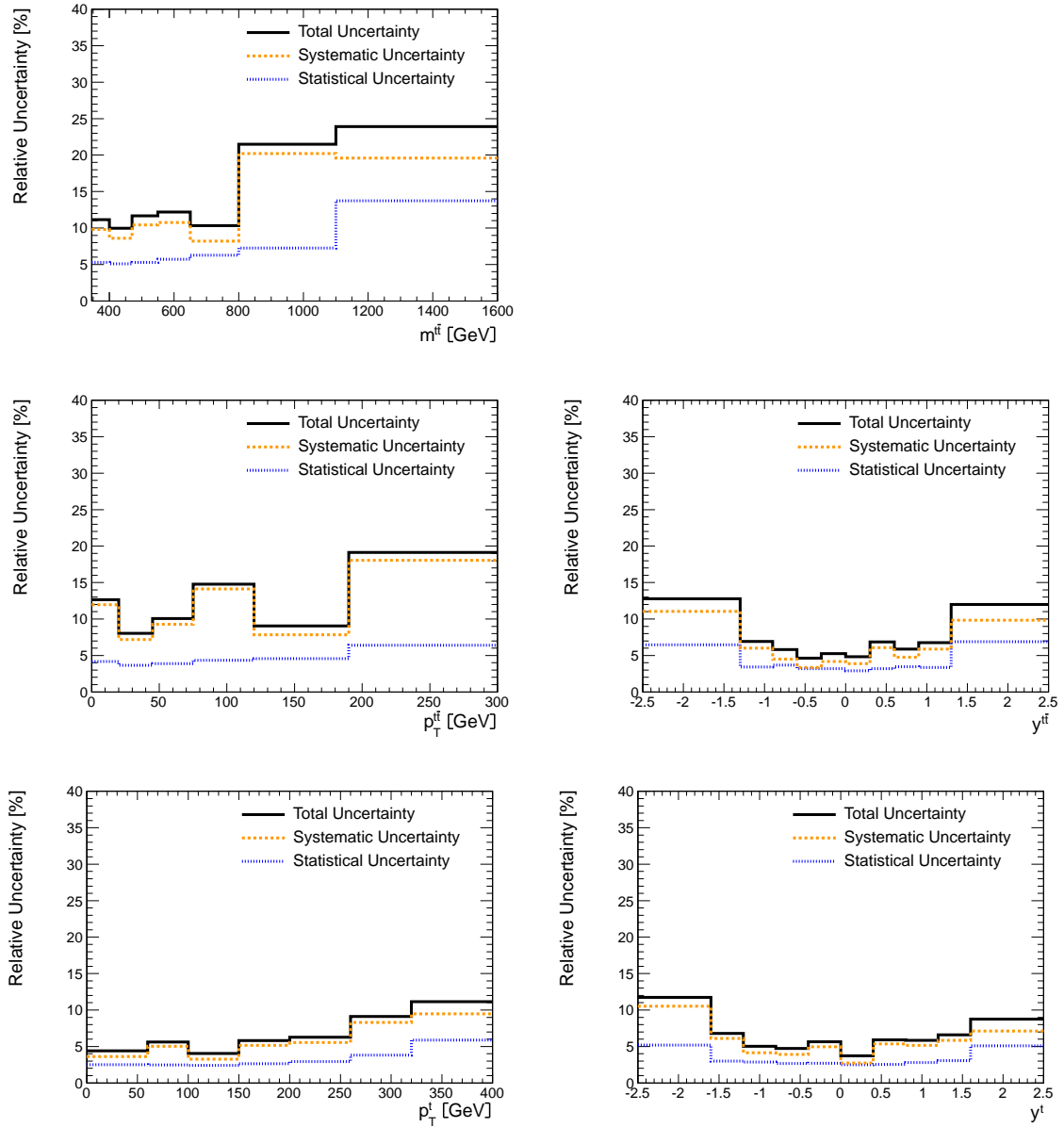
Figure 9.1: Distributions of statistical, total systematic and total uncertainty for the combined normalised cross sections as a function of the $t\bar{t}$ and top-quark quantities extrapolated to the full phase space at parton level.
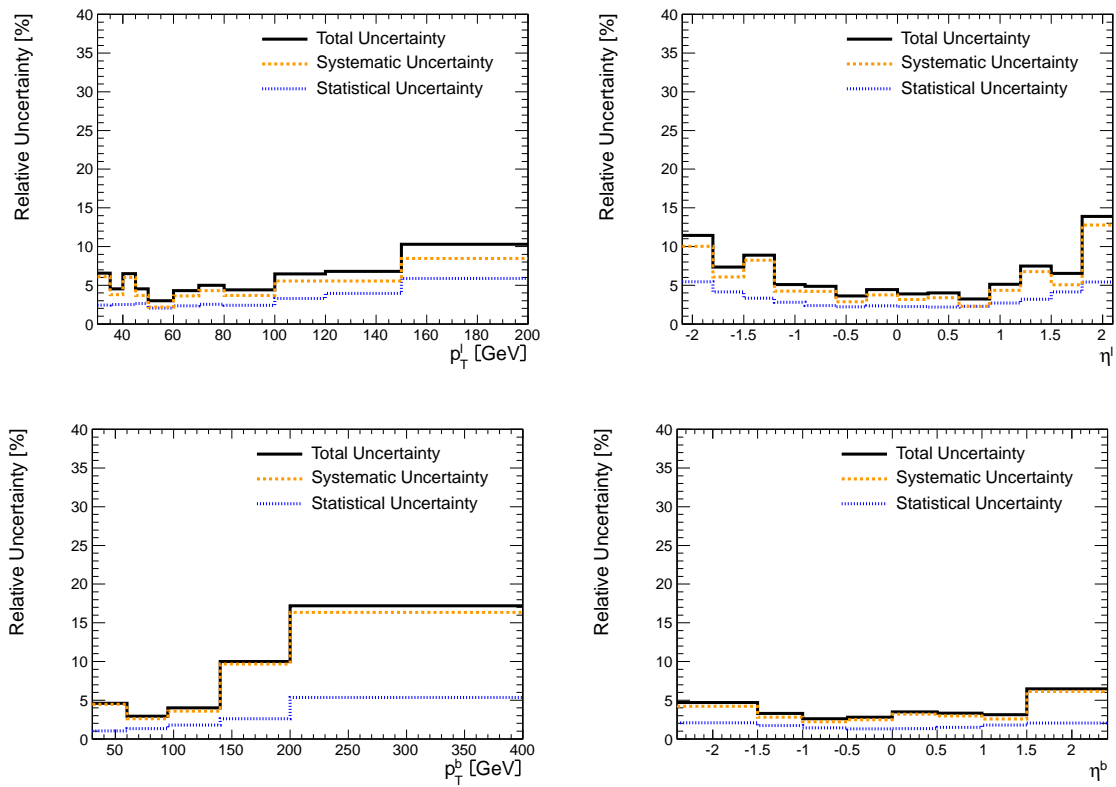
Figure 9.2: Distributions of statistical, total systematic and total uncertainty for the combined normalised cross sections as a function of the lepton and b-jet quantities in the visible phase space at particle level.

Chapter 10

Results - $t\bar{t}$ Production Cross Section

In this section, the results for the $t\bar{t}$-production cross sections are presented. They include normalised differential cross sections as a function of kinematic quantities of the $t\bar{t}$ system, the top quarks and top-quark decay products (b jets and lepton), which are published in [6], as well as the inclusive $t\bar{t}$ cross section.

10.1 Normalised Differential Cross Sections

The measured normalised differential cross sections $\frac{1}{\sigma} \cdot \frac{d\sigma}{dX}$ are presented for the combined ℓ + jets channel. For reference, the results of the individual muon+jets and electron+jets channel are included in App. E. They agree well with each other and with the combined channel for all kinematic quantities. The results are compared to various model predictions as well as to the results in the dilepton channel and those of the ATLAS experiment.

For the kinematic quantities $m^{t\bar{t}}$, $p_T^{t\bar{t}}$ and $y^{t\bar{t}}$ of the $t\bar{t}$ system and p_T^t and y^t of the top quarks, the results are obtained at parton level as the top quark decays before hadronisation as explained in Sec. 8.1.3. They are shown both restricted to the visible phase space in Fig. 10.1 and extrapolated to the full phase space in Fig. 10.2. The latter facilitates the comparison to model predictions not available in the visible phase space. The distributions for top-quark quantities include entries for both the top and the antitop quark in the event. For the $p_T^{t\bar{t}}$ and p_T^t distributions in the full phase space, the measurement is also shown after a variable transformation to $\frac{1}{\sigma} \frac{d\sigma}{dp_T^2}$ in Fig. 10.3. As $dp_T^2 = 2p_T dp_T$, this transformation eliminates the contribution from the phase-space term proportional to p_T, which forces the $\frac{1}{\sigma} \frac{d\sigma}{dp_T}$ distribution to zero at $p_T = 0$.

For the kinematic quantities of the top-quark decay products, the cross sections are obtained in the visible phase space at particle level. This avoids model dependencies induced by extrapolations to non-measured regions and to the parton level. The differential variables include the charged-lepton quantities p_T^ℓ and η^ℓ and the b-jet quantities p_T^b and η^b. The latter refer to both the b and anti-b jet collected in one distribution. They are shown in Fig. 10.4.

The data points are shown with error bars corresponding to the statistical (inner bars) and total (outer bars) uncertainties. A detailed table with the results including their uncertainties and correlation matrices is given in App. A.

The measurements are compared to theory predictions in the same phase space and at the same object-evolution level (parton or particle level). For all distributions, predictions from the Monte-Carlo event generators MADGRAPH + PYTHIA with CTEQ6L1 LO PDF, MC@NLO + HERWIG and POWHEG + PYTHIA, both with CTEQ6M NLO PDF, are shown, as introduced in Sec. 4. Whereas the MADGRAPH sample has also been used to derive the efficiency and migration corrections in this analysis, the predictions from MC@NLO and POWHEG provide a completely independent data-to-theory comparison. In the extrapolated phase space, the measurement of $m^{t\bar{t}}$ is additionally compared to an NLO+NNLL QCD prediction [42], and the ones of $p_{\mathrm{T}}^{\mathrm{t}}$ and y^{t} to an approximate NNLO prediction [43, 44], all using MSTW2008 NNLO PDF (see Sec. 2.2.1). For other distributions, no theoretical calculations to this perturbative order are available. For the MC@NLO predictions, an uncertainty band corresponding to PDF, Q^2-scale and top-quark-mass variations is attached [151]. Below each cross-section distribution, theory-to-data ratios are shown to facilitate the comparisons. The error bars correspond to the statistical (inner bars) and total (outer bars) uncertainty of the measurement.

The theory curves are presented in the same binning as the measurement to enable a direct comparison. To illustrate the continuous behaviour of the prediction, a smooth curve according to MADGRAPH with much finer binning is overlaid. To keep the same vertical data-to-theory deviation for both the smooth and the binned curve, horizontal bin-centre corrections are applied, i.e. the data point in each bin is displayed at the horizontal position at which the smooth MADGRAPH curve intersects the binned one [152]. As this position is determined with respect to a specific theory, the bin-centre-corrected data can only be compared to one smooth curve at the same time.

10.1.1 Discussion

Distributions of $t\bar{t}$-System and Top-Quark Quantities

The $t\bar{t}$ and top-quark quantities are measured both in the visible (Fig. 10.1) and full (Fig. 10.2) phase space, which affects the shapes of the distributions. As can be seen, the phase-space restriction leads to harder p_{T} and $m^{t\bar{t}}$ spectra and more central rapidity distributions as the low-p_{T} and high-$|\eta|$ leptons and jets are not considered. However, the general trend of the distributions and the data-to-theory agreement is the same in both cases. The following discussion will focus on the full phase space, for which approximate NNLO calculations are available for the top-quark distributions.

The invariant mass of the $t\bar{t}$ system $m^{t\bar{t}}$ is a measure for the centre-of-mass energy $\sqrt{\hat{s}}$ of the partonic collision (at leading order, $m^{t\bar{t}}$ equals $\sqrt{\hat{s}}$). The $m^{t\bar{t}}$ distribution is measured starting from about twice the top-quark mass (345 GeV), which is the production threshold for real $t\bar{t}$ pairs. Production below this threshold would be due to the finite decay width of the top quark (about 1 GeV) and is therefore highly suppressed.
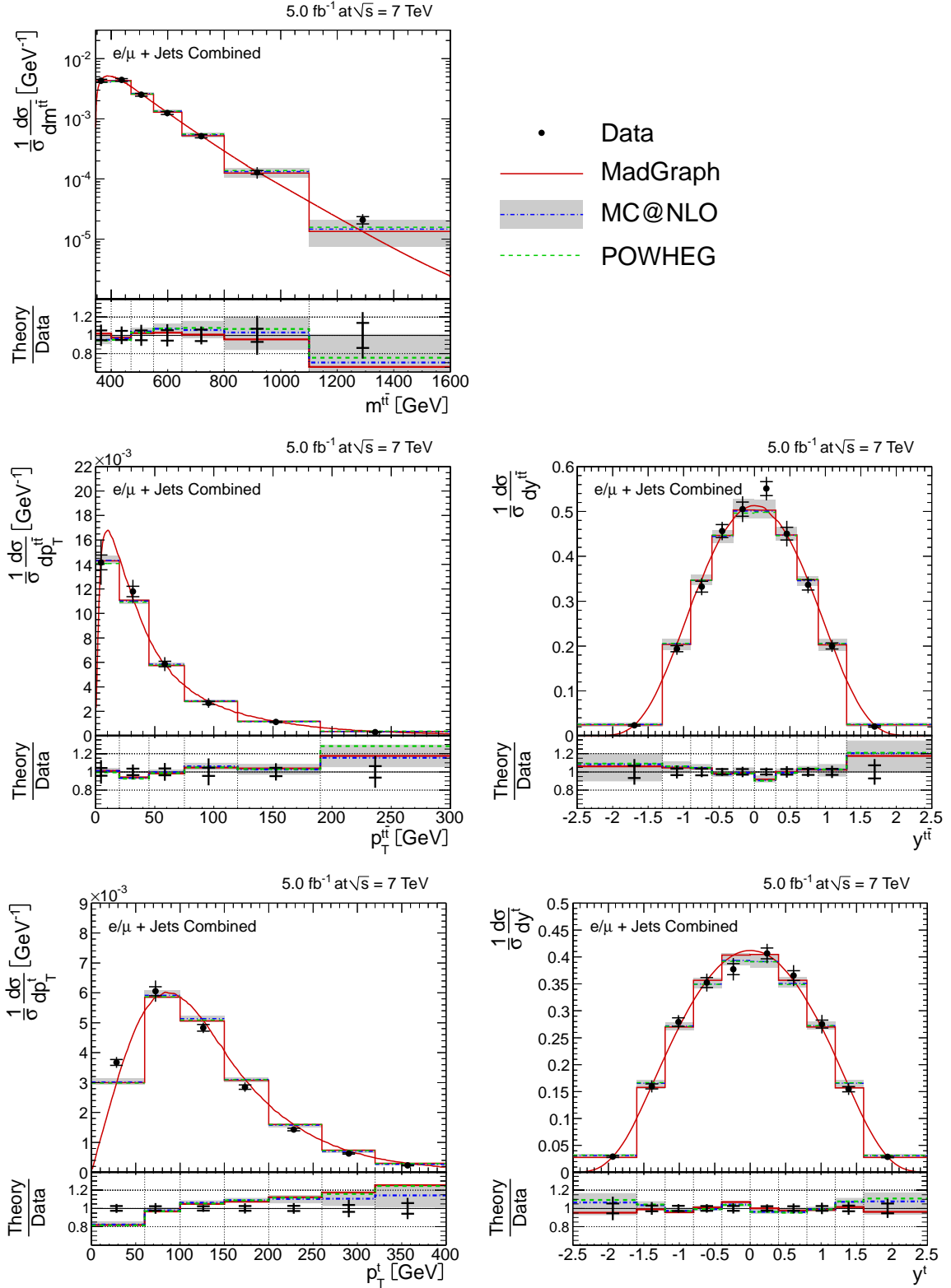
Figure 10.1: Normalised differential cross sections for the **t$\bar{\text{t}}$** (*top and middle row*) and **top-quark** (*bottom row*) quantities (*left*: p_{T} or invariant mass, *right*: y) in the **visible phase space at parton level**, compared to MadGraph, mc@nlo and powheg predictions. A smooth curve is added for MadGraph, wrt. which horizontal bin-centre corrections are applied to the data points.
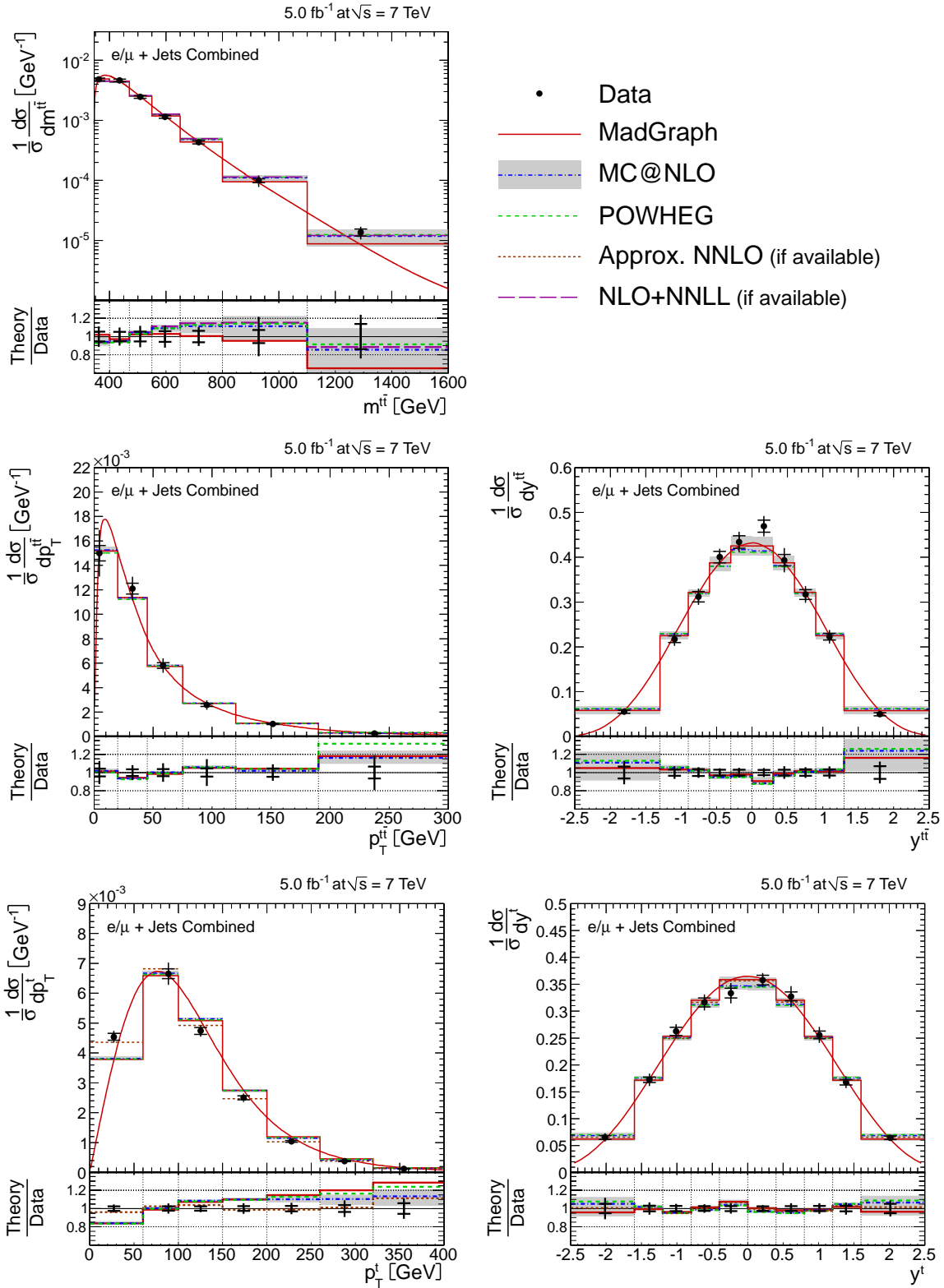
Figure 10.2: Normalised differential cross sections for the **t$\bar{\text{t}}$** (*top and middle row*) and **top-quark** (*bottom row*) quantities (*left*: p_{T} or invariant mass, *right*: y) in the **full phase space at parton level**, compared to MADGRAPH, MC@NLO, POWHEG and for p_{T}^{t} and y^{t} also approx. NNLO predictions. A smooth curve is added for MADGRAPH, wrt. which horizontal bin-centre corrections are applied to the data points.
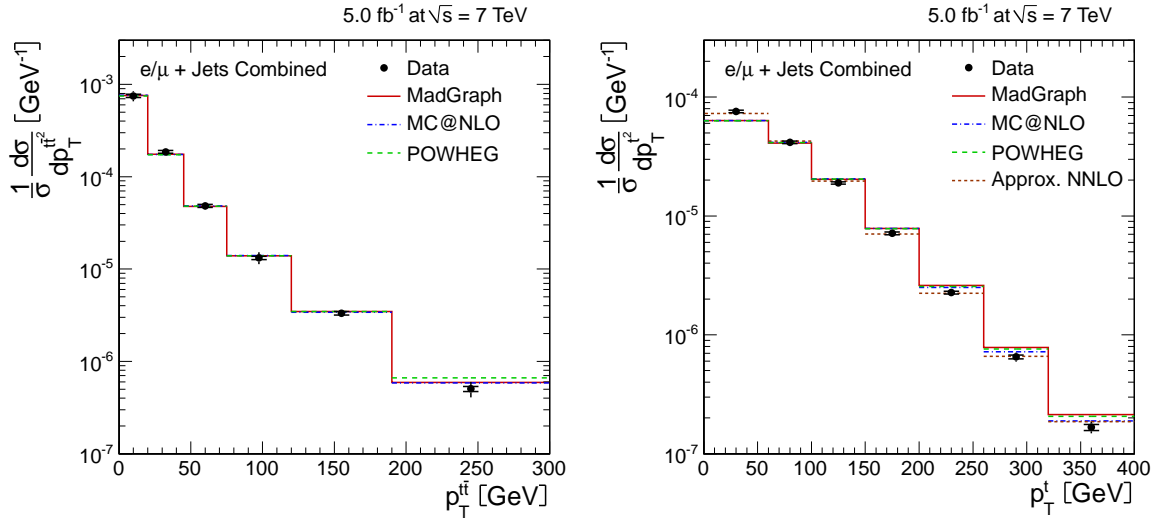
Figure 10.3: Normalised differential cross sections $\frac{1}{\sigma}\frac{d\sigma}{dp_{\mathrm{T}}^2}$ as a function of $p_{\mathrm{T}}^{t\bar{t}}$ (*left*) and p_{T}^{t} (*right*) in the full phase space at parton level.

As the detector and kinematic-reconstruction resolution are much larger than these effects (see Fig. 7.5), this measurement is not sensitive to it. Moreover, the top-quark decay width is set to 0 in the MADGRAPH event generator, which is used for the unfolding. The cross section decreases by more than two orders of magnitude up to the last measured bin, which includes events up to 1600 GeV. Very few events are found above this value due to the fast decrease of the spectrum and an efficiency drop due to jet merging arising from highly boosted top quarks [153]. It can be seen that already the last shown bin suffers from large statistical and systematic uncertainties, adding up to more than 20% (compared to about 10% at lower $m^{t\bar{t}}$). The SM predictions agree well with the measurement, in particular MADGRAPH, which is found to be a bit softer than MC@NLO and POWHEG. Thus, no indications of heavy resonances or other new physics effects that have the potential to show up most prominently in the invariant-mass distribution are observed.

The transverse-momentum distribution of the t$\bar{\text{t}}$ system $p_{\mathrm{T}}^{t\bar{t}}$ is sensitive to higher-order effects as it balances the p_{T} of additionally radiated partons (at leading order, the t$\bar{\text{t}}$ system would be at rest in transverse direction). The measurement is performed up to $p_{\mathrm{T}}^{t\bar{t}} = 300$ GeV, beyond which both the uncertainties and resolutions increase too much. The distribution decreases from its maximum in the first bin by a factor of 50 to the last bin. In addition to $\frac{1}{\sigma}\frac{d\sigma}{dp_{\mathrm{T}}^{t\bar{t}}}$ in Fig. 10.2, the measurement is also shown after a variable transformation to $\frac{1}{\sigma}\frac{d\sigma}{dp_{\mathrm{T}}^{t\bar{t}^2}}$ in Fig. 10.3. A good agreement is observed between the measurement and the predictions. It is in particular notable that radiation is well-described irrespective of the different techniques applied by MADGRAPH + PYTHIA, MC@NLO + HERWIG and POWHEG + PYTHIA. One can conclude that a significant fraction of t$\bar{\text{t}}$ events is accompanied by hard-parton emission with a p_{T} between 10 and several 100 GeV, e.g. to a larger extent than Z-boson production, which exhibits

a softer p_T^Z spectrum (as measured in [154]). This is due to the high energy scale of t$\bar{\text{t}}$ production in combination with predominantly gluons in the initial state, which have a larger colour factor than quarks.

The top-quark p_T reflects the p_T of the top quarks in the t$\bar{\text{t}}$ rest frame, convoluted with the p_T of the t$\bar{\text{t}}$ system. The latter is discussed above, and the first is determined by the total-momentum magnitude of the top quarks (given by $\sqrt{\hat{s}/4 - m_t^2}$ at leading order) and the scattering angle in the t$\bar{\text{t}}$ rest frame. The distribution increases from low p_T to its maximum in the second bin (60 GeV $< p_T <$ 100 GeV), before it falls again. Again, to eliminate the contribution from the phase-space term proportional to p_T, which forces the $\frac{1}{\sigma}\frac{d\sigma}{dp_T^t}$ distribution to zero at $p_T^t = 0$, the $\frac{1}{\sigma}\frac{d\sigma}{dp_T^{t2}}$ distribution is shown in Fig. 10.3, which decreases monotonically. The available number of events allows a measurement up to 400 GeV. Beyond this, both the spectrum falls off too steeply and the efficiency as well as the reconstruction resolution decrease due to jet merging at such highly-boosted top quarks. Compared to the predictions of the Monte-Carlo event generators, the distribution in data is observed to be significantly softer. This trend was consistently already observed at the level of the reconstructed yield distributions after the kinematic fit (see Fig. 7.7). However, the approximate NNLO calculation largely improves the description and is in good agreement with the data. This suggests that the deviations of the event generators are due to missing higher-order corrections and can hence be described within the SM.

The rapidity distributions are related to the momentum component in the direction along the beam (see Sec. 2.2.1). The $y^{\text{t}\bar{\text{t}}}$ distribution represents the longitudinal boost of the t$\bar{\text{t}}$ system due to the different proton-momentum fractions x of the colliding partons: $y^{\text{t}\bar{\text{t}}} = 1/2 \cdot \ln(x_1/x_2)$ (see Eq. 2.5). It exhibits a pronounced maximum at zero and falls off symmetrically to both sides. The measurements are performed up to absolute rapidity values of 2.5, beyond which almost no events are selected because of the falling distribution and decreasing acceptance due to the $|\eta|$ cuts for the lepton and jets. The observed distribution indicates that t$\bar{\text{t}}$ production is very central, in contrast to e.g. Z-boson production, which exhibits a much flatter rapidity distribution [154]. This is mainly due to the large top-quark mass, which leads to the requirement of a large proton-momentum fraction of both initial partons, preventing a strong boost along the beam (the maximum possible $y^{\text{t}\bar{\text{t}}}$ at 7 TeV amounts to 3 as shown in Sec. 2.2.1). Another reason is the dominance of the gluon-gluon-fusion production mechanism with symmetric PDFs in both initial protons over the quark-antiquark annihilation with asymmetric PDFs (quarks mainly from valence quarks with typically large x and antiquarks from the sea partons with small x). In general, due to the PDF dependence, $y^{\text{t}\bar{\text{t}}}$ is especially sensitive to the underlying PDF sets, in particular for gluon PDFs at high x. The measured distribution is observed to be slightly more central than the predictions. As the MADGRAPH prediction is as well a bit more central than the other ones, it agrees slightly better with the measurement. However, the achieved sensitivity makes it difficult to draw reliable conclusions.

The y^{t} distribution is a convolution of the $y^{\text{t}\bar{\text{t}}}$ distribution with the one of the rapidity of the top quarks in the t$\bar{\text{t}}$ rest frame. Thus, it is slightly broader than the $y^{\text{t}\bar{\text{t}}}$ distribution. The MADGRAPH and approximate NNLO predictions are slightly more

central than MC@NLO and POWHEG, but all are consistent with each other and the measurement within uncertainties.

Distributions of Decay-Product Quantities
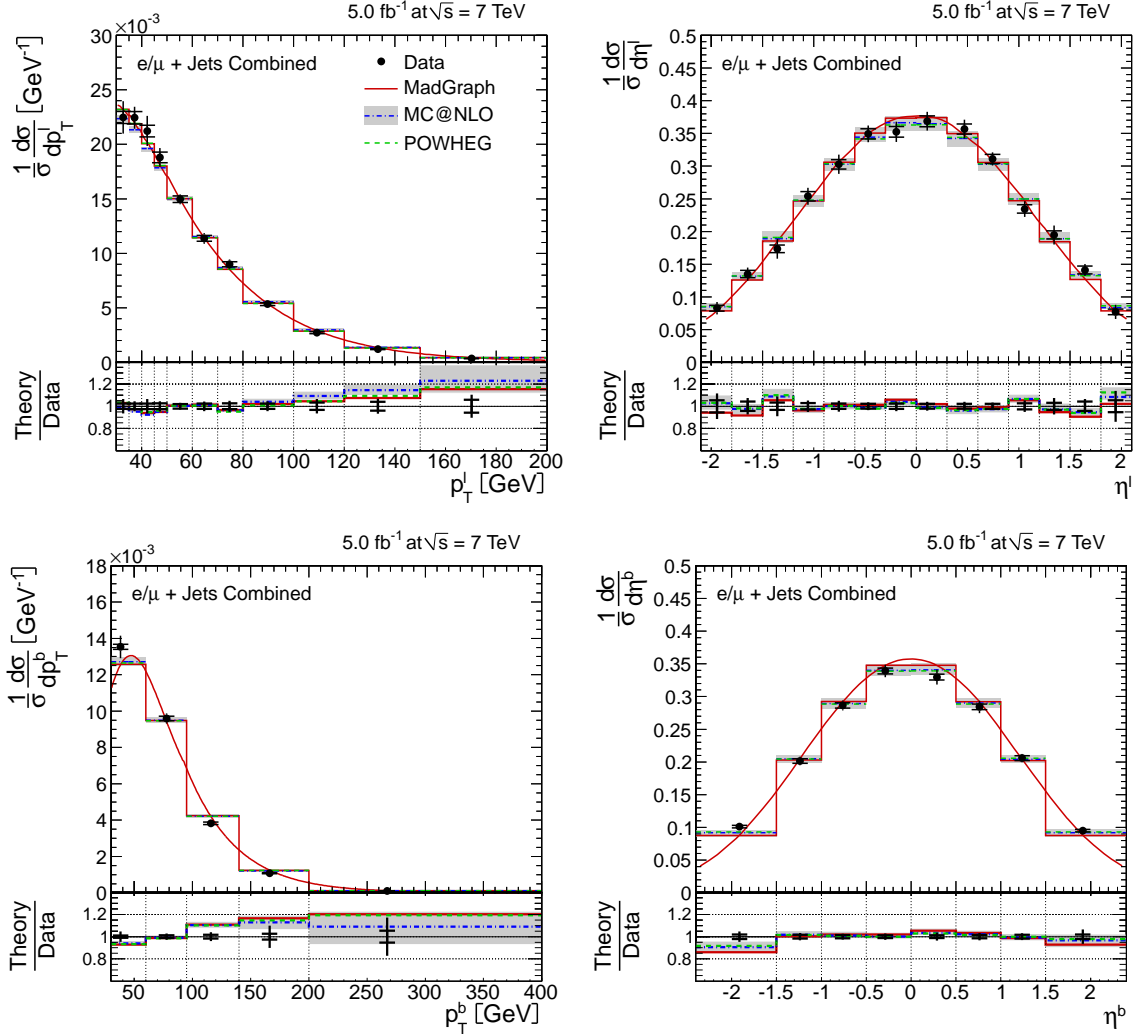
Figure 10.4: Normalised differential cross sections for the **lepton** (*top row*) and **b-jet** (*bottom row*) quantities (*left*: p_T, *right*: η) in the **visible phase space at particle level**, compared to MADGRAPH, MC@NLO and POWHEG predictions. A smooth curve is added for MADGRAPH, wrt. which horizontal bin-centre corrections are applied to the data points.

The kinematic distributions of the final decay products of the top quarks (shown in Fig. 10.4 in the visible phase space at particle level) are convolutions of the distributions of the top quarks with the ones of the decay products in the top-quark rest frames.

Their ranges are limited by the phase-space acceptance except for the upper ranges

of the p_T distributions, which are limited by a lack of measured events at higher p_T. At the given integrated luminosity, measurements can be performed up to $p_\mathrm{T}^\ell = 200$ GeV and $p_\mathrm{T}^b = 400$ GeV. The first p_T bin (30 to 35 GeV for the leptons, 30 to 60 GeV for the b-jets) is the one with the highest measured and predicted cross section. Towards higher p_T, the cross section is monotonically decreasing as predicted. The p_T distributions in data tend to be slightly softer than predicted by all event generators, although the achieved sensitivity makes it difficult to judge reliably, especially in case of the leptons. This effect is consistently visible at the level of control plots after the basic selection (Fig. 5.4, 5.5) and in the yield distributions after the kinematic fit (Fig. 7.8). As discussed above, a similar trend is observed for the p_T distribution of the top quark, which probably propagates to the distributions of the decay products. For the p_T^t distribution, an approximate NNLO prediction is found to significantly improve the description of the data, but such is unfortunately not available for distributions of the decay products.

The η distributions exhibit a maximum at 0 and fall off symmetrically to both sides. It indicates that the top-quark decay products are very central due to the central production of the top quarks as shown above. These distributions are generally well-reproduced by the predictions.

10.1.2   Comparison to Other Measurements

Normalised Differential t$\bar{\text{t}}$ Cross Sections in the Dilepton Channel at CMS

Complementary to these measurements in the $\ell+$jets channel, the same analysis is also performed in the dilepton channel (ee, µµ and eµ) for the same dataset at CMS [6, 7]. As explained in Sec. 2.2.2, the event signature is on the one hand very clean, so that a high-purity t$\bar{\text{t}}$ sample can be already obtained by requiring only one b-tagged jet. Thus, despite a 6 times lower branching ratio, the selected number of events is only 1.5 times lower compared to the $\ell +$ jets channel. However, the two neutrinos from the W-boson decays lead to a less constrained kinematic system of equations compared to the $\ell +$ jets channel, requiring a channel-optimised reconstruction of the kinematic event topology. It also results in generally lower resolutions, which make the choice of larger bins necessary, applying the same criteria as in this analysis.

Fig. 10.5 shows a comparison between the two channels. For this, the $\ell +$ jets analysis is redone in the wider bins of the dilepton analysis. Due to the different final states and phase space, a comparison is only possible for top-quark and t$\bar{\text{t}}$ quantities extrapolated to the full phase space. It can be seen that the results are consistent with each other. In particular, the measurement of a softer p_T^t spectrum compared to the predictions by the MC generators up to NLO (MadGraph, mc@nlo and powheg) and an improved description by the approx. NNLO calculation is observed in both channels. Due to less migration and more selected events, this analysis is more precise.
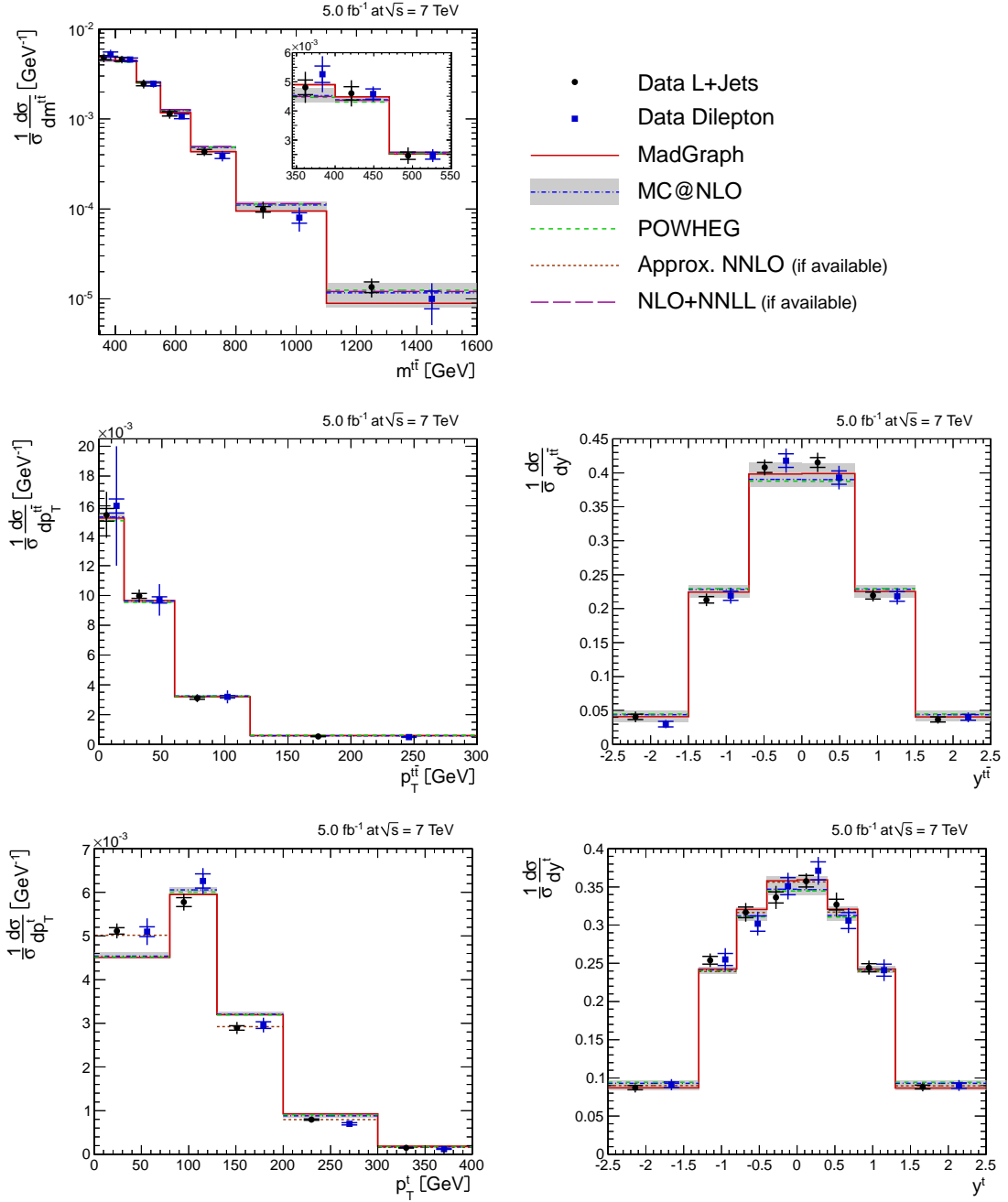
Figure 10.5: Comparison of normalised differential cross sections in the $\boldsymbol{\ell}+$ **jets** (*black points*) and **dilepton** [6] (*blue squares*) channel for the t$\bar{\text{t}}$ and top-quark quantities in the full phase space at parton level.

Normalised Differential t$\bar{\text{t}}$ Cross Sections for t$\bar{\text{t}}$ Quantities at ATLAS

The ATLAS collaboration presents a measurement of normalised differential cross sections for the quantities $m^{\text{t}\bar{\text{t}}}$, $p_{\text{T}}^{\text{t}\bar{\text{t}}}$ and $y^{\text{t}\bar{\text{t}}}$ of the t$\bar{\text{t}}$ system in the ℓ + jets channel for 2.05 fb^{-1} at $\sqrt{s} = 7$ TeV [155]. In contrast to this analysis, only one b-tagged

jet is minimally required in the event selection and MC@NLO is used to extract the simulation-based migration and efficiency corrections. Direct matrix inversion without regularisation is applied for unfolding. Wider bins than in this analysis are chosen. Fig. 10.6 shows a comparison between this analysis (CMS) and the ATLAS measurement, with this analysis redone in the bins of the ATLAS analysis. A good agreement is observed. This analysis exhibits smaller statistical and systematic uncertainties than the ATLAS measurement.
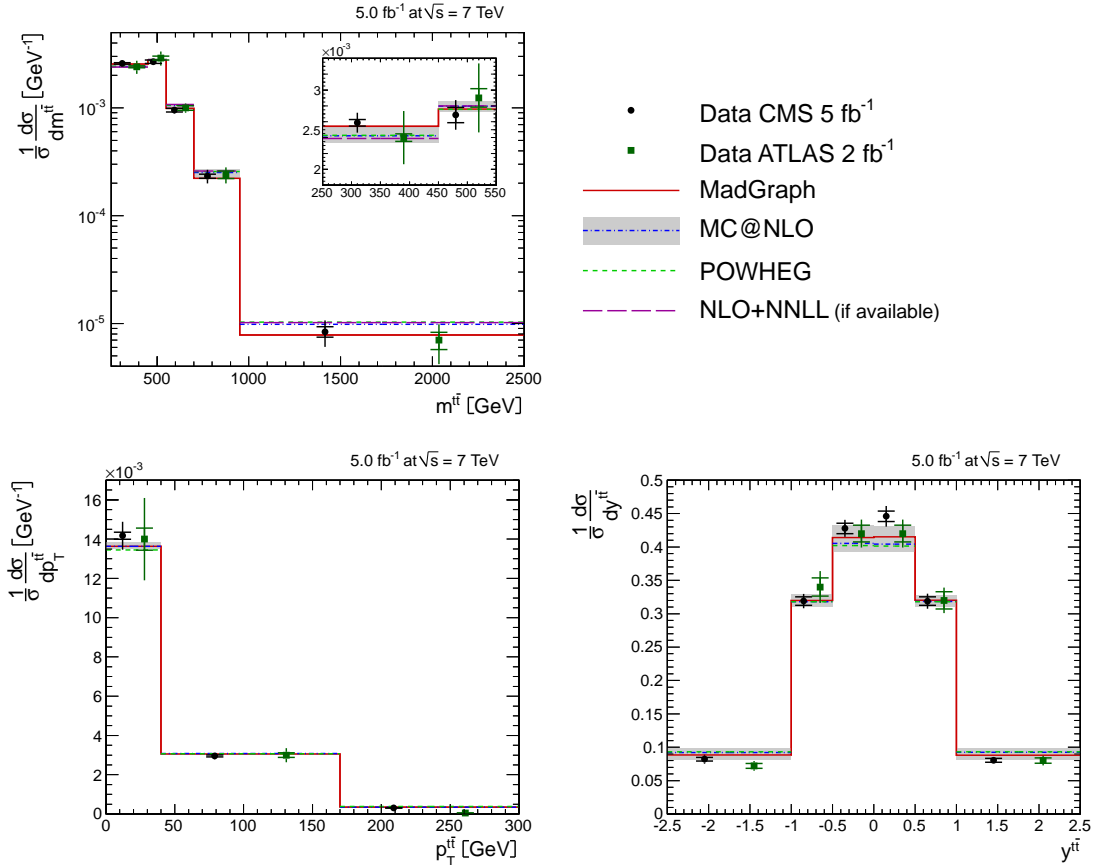
Figure 10.6: Comparison of normalised differential cross sections in the ℓ+jets channel measured by **CMS** (*black points*) and **ATLAS** [155] (*green squares*) for the t$\bar{t}$ quantities in the full phase space at parton level. For the ATLAS measurement, the last shown bin of the $m^{t\bar{t}}$ distribution extends up to 2700 GeV (in contrast to 2500 GeV for this analysis), and the one of the $p_T^{t\bar{t}}$ distribution up to 1100 GeV (in contrast to 300 GeV), thereby complicating a direct comparison in those bins.

Differential t$\bar{t}$ Cross Sections in $p\bar{p}$ Collisions at 1.8 or 1.96 TeV at the Tevatron

The Tevatron experiments CDF and D0 present measurements of differential t$\bar{t}$ cross sections in p$\bar{p}$ collisions at $\sqrt{s}$ =1.8 or 1.96 TeV for the p_T^t and $m^{t\bar{t}}$ distributions.

Due to the different initial state and centre-of-mass energy, the distributions differ from the ones measured in this analysis. This allows for an independent cross check of t$\bar{\text{t}}$ kinematics in another energy regime and via another dominating production mechanism (q$\bar{\text{q}}$).

After an early measurement of the differential cross section as a function of $p_{\mathrm{T}}^{\mathrm{t}}$ with only 106 pb^{-1} at $\sqrt{s}$ =1.8 TeV by CDF [1], D0 measures this distribution on a larger dataset corresponding to 1 fb^{-1} at $\sqrt{s}$ =1.96 TeV [2]. A good agreement is observed with all considered SM predictions (NLO and approx. NNLO calculations, MC@NLO, PYTHIA, ALPGEN). The achieved sensitivity does not yet allow for a discrimination between the different models. Also, the differential cross section as a function of $m^{\mathrm{t}\bar{\mathrm{t}}}$ as measured by the CDF collaboration with 2.7 fb^{-1} at $\sqrt{s}$ =1.96 TeV shows no deviation from the SM prediction according to PYTHIA 6 [3].

10.2   Inclusive Cross Section

Whereas the focus of this analysis is laid on the measurement of normalised differential cross sections, the measurement of the inclusive t$\bar{\text{t}}$ cross section within the same analysis framework is also presented. On the one hand, it is used for the normalisation of the differential cross sections, and on the other hand, it represents a cross check that can be compared to other measurements.

The inclusive cross section is calculated from all events after event selection including b tagging and kinematic event reconstruction using a cut-based counting method as explained in Sec. 8.1. It should be noted that one inclusive event yield number with corresponding inclusive efficiency is used for the values presented here. This agrees well with the integrals over the differential distributions before normalisation. The measurement is extrapolated to the full phase space and all decay channels, facilitating the comparison to other results. The following cross sections are obtained for the different channels:

μ + jets:	174.5 ± 1.8 (stat.) ± 15.8 (syst.) ± 4.2 (lumi.) pb
e + jets:	180.6 ± 2.0 (stat.) ± 17.1 (syst.) ± 4.3 (lumi.) pb
ℓ + jets combined:	177.3 ± 1.4 (stat.) ± 16.3 (syst.) ± 4.3 (lumi.) pb

10.2.1   Comparison to Other Results

The obtained result is in good agreement with the theory prediction of 172.0^{+8}_{-9} pb at NNLO+NNLL (using $m_t = 173.3$ GeV and MSTW2008 NNLO PDF, including hard-scattering-scale, PDF and top-quark-mass uncertainties) [41].

It can be also compared to the published CMS result in the same channel (combined ℓ+jets) of 158.1±2.1 (stat.)±10.2 (syst.)±3.5 (lumi.) pb [156], which uses a subset of 2.3 fb^{-1} of the data of this analysis. It should be noted that the analysis strategies are optimised in completely different ways. The derivation of the inclusive cross section does not demand such a high signal purity as this analysis. In contrast, the published

CMS analysis includes background-dominated low-jet and low-b-tag multiplicity bins (obtained with another b tagger than in this analysis) in a likelihood fit to determine parameters such as the background normalisation, b-tag efficiency and jet-energy scale in-situ from data. As peculiarity of such a multi-dimensional fit, the result of the fitted combined channel does not need to envelope the results of fits to the separate channels, which amount to 164.2 ± 2.8 (stat.) ± 10.1 (syst.) ± 3.6 (lumi.) pb for μ+jets and 160.6 ± 3.2 (stat.) ± 11.2 (syst.) ± 3.5 (lumi.) pb for e+jets. Due to the different approaches, the difference between this and the published analysis can be explained by uncorrelated systematic uncertainties, e.g. related to the b-tagging efficiency and background contributions.

ATLAS measures a cross section of 179.0 ± 9.8 (stat.+syst.) ± 6.6 (lumi.) pb in the ℓ+jets channel with 0.7 fb^{-1} [157], which is in good agreement with this measurement.

It should be emphasised again that the magnitude of the inclusive cross section does not have any effect on the normalised differential cross sections presented in Sec. 10.1 as it cancels in the ratio, such that only the shapes of the kinematic distributions are measured.

A summary and outlook of the differential t$\bar{\text{t}}$-cross-section analysis is given in Sec. 15.

Chapter 11

Basics of Silicon Detectors

11.1 Introduction to Silicon Detectors at the HL-LHC

High-resolution silicon (Si) detectors provide precise and efficient track and vertex reconstruction for all major LHC experiments (and beyond). This constitutes the basis of particle-momentum and -direction determination, pile-up mitigation, particle-flow reconstruction techniques, b-jet identification etc. This is vital for each particle-physics analysis as demonstrated by the top-quark cross-section measurement presented in the last sections. For that analysis, for instance, the secondary-vertex reconstruction is especially important as at least two b tags are required.

Due to this importance of the silicon tracking detectors, their performance and reliability has to be maintained over the whole lifetime of the experiments. Radiation damage presents a challenge for this. This is especially true for trackers at the high-luminosity upgrade of the LHC (HL-LHC) [8]. Fig. 11.1 shows the expected fluences for the CMS tracker as a function of radius with respect to the beam line. For the innermost pixel layer at radii of about 4–5 cm (which is especially important for secondary-vertex reconstruction), maximum particle fluences of $(1\text{--}2){\cdot}10^{16}$ cm^{-2} are predicted after the envisaged 3000 fb^{-1}, which is an order of magnitude higher than expected for the present CMS pixel system. In the inner part (up to radii of 40–60 cm), the radiation is dominated by charged hadrons from the primary interactions, whereas neutrons, mainly backscattered from secondary interactions in the calorimeters, dominate in the outer part.

The introduction of radiation-induced defects in the Si bulk leads to a change of the effective doping concentration, an increase in leakage current and the trapping of signal charge carriers. The latter effect is expected to be the limiting factor at HL-LHC fluences, leading to a large degradation of the signal. As the noise increases simultaneously, especially due to increasing leakage current, the signal-to-noise ratio is challenged from both sides, potentially rendering the detectors inoperable.

In this second part of the thesis (Sec. 11 to 14), the novel effect of radiation-induced charge multiplication in silicon detectors is studied as an option to overcome the signal degradation due to trapping.

147
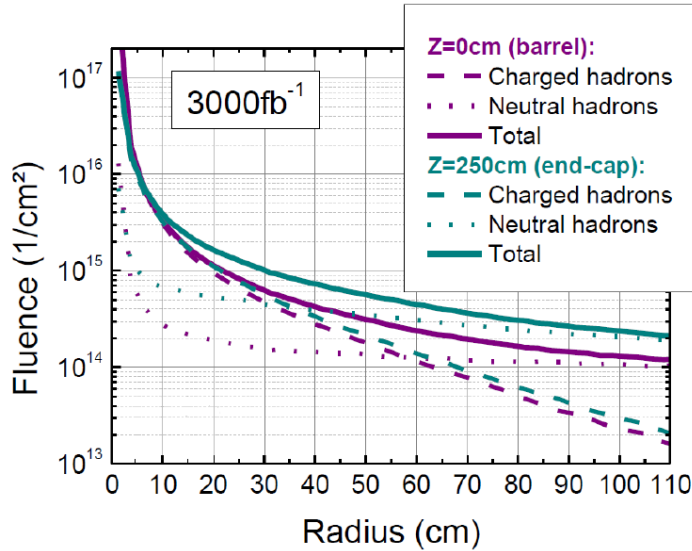
Figure 11.1: Expected equivalent fluence as a function of radius with respect to the beam line for the CMS tracker at the HL-LHC after a luminosity of 3000 fb^{-1}. The charged, neutral and total hadron fluence is shown. It is displayed both for $z = 0$ (barrel region) and $z = 250$ cm (end caps). Taken from [164].

A detailed introduction and motivation to this topic is given already in Sec. 1. The CMS silicon tracker is described in Sec. 3.2.1. More background information on silicon detectors and radiation damage can be found in [158–163], on which the following sections are based. This thesis carries on a previous work of the author [9]. Parts of Secs. 11 to 13 are reproduced from there.

11.2   Overview of Silicon Detectors in Particle Physics

Semiconductor detectors act as solid-state ionisation chambers as illustrated in Fig. 11.2. An incident ionising particle liberates electron-hole (e-h) pairs inside the semiconductor bulk. The average number of e-h pairs is the absorbed energy E_{abs} divided by the mean ionisation energy E_i. The charge carriers move under the influence of an applied electric field to the respective electrodes. This induces a measurable current in the external electric circuit, which is typically amplified, shaped and read out electronically.

In energy-spectroscopy measurements, the particle is stopped inside the detector, so that the signal is proportional to its initial energy. In high-energy tracking experiments, the particle traverses a detector with finely segmented electrodes (strip or pixel detectors), which yields a high-resolution position information ($\sigma_x \approx 10$ μm). Multiple layers of detectors make a track reconstruction possible. For testing purposes, e.g. in this work, also simple, large-area pad detectors are used instead of segmented devices.

The signal-to-noise ratio (SNR) is considered the figure-of-merit of a detector. It determines the detection efficiency of a traversing particle at a given noise occupancy (fake rate). Moreover, it has a large influence on the spatial resolution if charge sharing
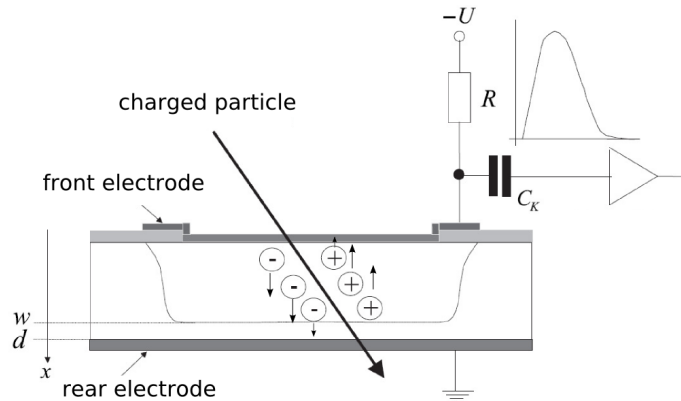
Figure 11.2: Principle of a semiconductor detector. Taken from [167] and modified.

between pixels or strips is exploited with clustering algorithms [165, 166]. In that case, the resolution $p/\sqrt{12}$ for binary readout is improved, depending on the SNR (the pitch p refers to the distance between the segments). The signal of a minimum-ionising particle is mainly determined by the thickness of the sensitive detector region and the charge-collection efficiency (CCE) of the detector. For minimising the noise, a low capacitance and low quiescent detector current are required.

Compared to other detectors like gas ionisation chambers, the advantages of semi-conductors are the low mean ionisation energy (3.6 eV for Si, >30 eV for gas) and the large density, which result in a high number of created charge carriers per traversed distance (MPV[1] ≈ 73 e-h pairs/μm in 300 μm Si for a minimum-ionising particle [19], see Sec. 11.4.1). Thus, only a small thickness of about 100–300 μm is required for a sufficiently large signal (MPV ≈ 22 ke in units of elementary charge e, corresponding to 3.5 fC, for 300 μm). This and the large mobility of charge carriers in semiconductors lead to short charge-collection times (t_C ≈1–10 ns) and consequently a fast readout.

Silicon in particular is a very suitable material and is widely used in semiconductor industries, so that the detector manufacturers can profit from the highly developed technologies and the great experience gained from mass-market production. This ensures also low costs of Si detectors compared to competing semiconductor materials.

However, the resistivity of commercially available Si material is limited to about 20 kΩcm [19], which would lead to a much too high detector current and hence noise. The solution is to use Si diode structures with large sensitive detector regions depleted from free charge carriers. This is established by a reverse-biased p-n junction.

---

[1]Most probable value of the deposited charge.

11.3   Electric Properties of Silicon Diodes

11.3.1   Intrinsic and Extrinsic Semiconductors

Semiconductors are characterised by their forbidden energy gap between valence band and conduction band ($E_g = 1.12\,\text{eV}$ for Si at room temperature). In intrinsic Si, only few electrons are thermally excited from the valence into the conduction band at room temperature, so that there are only few free charge carriers. The large benefit of semiconductors is the possibility of tailoring the conductivity by deliberately introducing impurities into the Si lattice. This procedure is called doping. If a Si atom is replaced by a so-called shallow donor with five valence electrons such as phosphorus (P) or antimony (Sb), four of these will form the covalent bonding with the neighbouring Si atoms. The remaining electron is only loosely bound ($\approx 45\,\text{meV}$ ionisation energy for P), so that it can be easily excited into the conduction band at room temperature. In this way, both a positively charged P ion and a free negative charge carrier are created. Hence, the material is called n-type. In a similar manner, p-type material with free positive charge carriers (holes) can be produced by adding shallow acceptors with only three valence electrons, e.g. boron (B).

11.3.2   p-n Junction
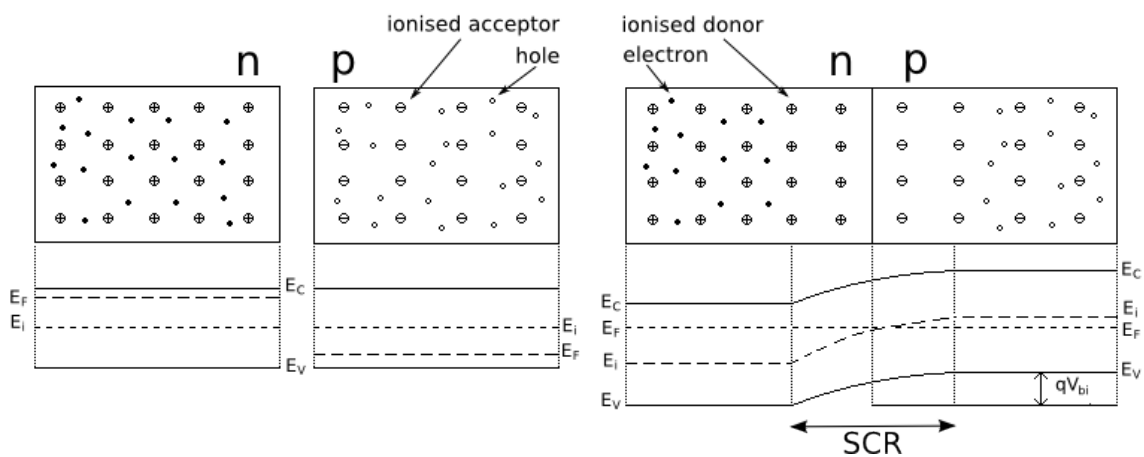
Figure 11.3: Sketch of the formation of a p-n junction. *Left:* An n-type and p-type semiconductor separately with their respective energy band diagrams. *Right:* The p-n junction with the space-charge region (SCR). Taken from [168].

Fig. 11.3 shows a separated p-type and n-type material with their respective energy band diagrams (*left*). If these two materials are joined together (*right*), there will be a charge-carrier-concentration gradient due to the different doping types. As a result, the free electrons from the n-side in the junction region will diffuse to the p-side and recombine, and vice versa for the holes from the p-side. The non-mobile positively ionised donors, however, are left on the n-side and the negatively ionised acceptors on
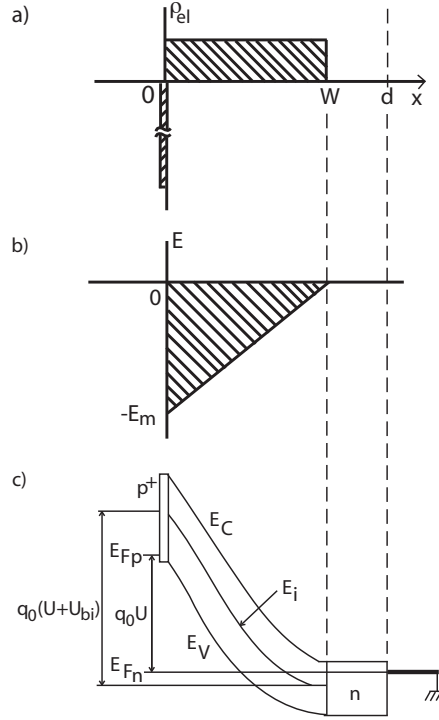
Figure 11.4: Schematic figure of a one-sided abrupt p$^+$-n junction (taken from [163, 168]): space-charge density (*top*), electric-field distribution (*middle*), electron potential energy (*bottom*).

the p-side. An electric field builds up, which acts against the diffusion. Eventually, an equilibrium between the diffusion current and the drift current is reached. In this way, a bipolar space-charge region (SCR) depleted from free charge carriers is formed around the junction. The potential difference is called built-in voltage U_{bi} and corresponds to the difference between the fermi level E_F[2] on the n-side (E_{F_n}) and the one on the p-side (E_{F_p}). The electric-field strength E and the electric potential Φ can be obtained from solving Poisson's equation. For Si detectors, one usually uses a one-sided abrupt p$^+$-n junction, where the p$^+$ denotes that the p-side is much more heavily doped than the n-side (or vice versa for n$^+$-p junctions) as sketched in Fig. 11.4 (*top*). It follows from charge neutrality that in this case, the depleted region of thickness W extends much further into the less heavily doped n-side of the diode. If one assumes the free charge-carrier density to be zero, Poisson's equation[3] reads

$$ -\frac{d^2\Phi(x)}{dx^2} = \frac{\rho_{el}}{\epsilon\epsilon_0} = \frac{eN_{eff}}{\epsilon\epsilon_0}, \qquad (11.1) $$

where $N_{eff} = N_D - N_A$ is the effective doping concentration, i.e. the difference between

---

[2]The Fermi level E_F is the energy level with occupation probability 1/2 in thermal equilibrium.

[3]For simplicity, only the one-dimensional case is considered. It represents a good approximation far away from the edges of p^+ implantations, i.e. in particular for pad diodes. Close to the edges of strip or pixel implantations, however, the field lines bend and the field strength is enhanced. In this case, more-dimensional calculations are needed.

the ionised donor and acceptor concentration in the n-type space-charge region, $\epsilon\epsilon_0$ the dielectric constant ($\epsilon = 11.9$ for Si) and e the elementary charge.

By integrating Eq. 11.1 with the boundary condition $E(x = W) = -\frac{d}{dx}\Phi(x = W) = 0$, one obtains an expression for the electric-field distribution. For a homogeneous space-charge density ρ_{el}, the field develops linearly inside the space-charge region from its maximum absolute value at $x = 0$ to 0 at $x = W$ (see Fig. 11.4, *middle*):

$$E(x) = \frac{eN_{eff}}{\epsilon\epsilon_0}(x - W), \qquad 0 \le x \le W \text{ and } W \le d. \tag{11.2}$$

A second integration with the boundary condition $\Phi(x = W) = 0$ gives a parabolic behaviour of the potential:

$$\Phi(x) = -\frac{1}{2}\frac{eN_{eff}}{\epsilon\epsilon_0}(x - W)^2, \qquad 0 \le x \le W \text{ and } W \le d. \tag{11.3}$$

Fig. 11.4 (*bottom*) shows the corresponding electron potential energy $-e\Phi$. For no applied external bias voltage, $\Phi(x = 0)$ corresponds to U_{bi}. In the case of an applied reverse bias voltage U, one has to set $\Phi(x = 0) = U_{bi} + U$, so that the width of the space-charge region as a function of U is given by

$$W(U) = \sqrt{\frac{2\epsilon\epsilon_0}{e\,|N_{eff}|}(U + U_{bi})}, \qquad W \le d. \tag{11.4}$$

The electric field and the development of the space-charge region play a paramount role for detector operation. Moreover, high-field values constitute the condition for charge multiplication, which is the subject under study in this thesis (see Sec. 11.4.4). Thus, it is instructive to consider the dependence of the field distribution, its maximum value and the space-charge width on the applied bias voltage U, effective doping concentration N_{eff} and thickness d.

As one can see from Fig. 11.5 (*left*), the space-charge region extends further into the detector with increasing reverse bias voltage ($W \propto \sqrt{U}$), until the back contact is reached and the detector is fully depleted. Until that point, the maximum value of the electric field at the junction increases as $E_{max} \propto \sqrt{U}$. The voltage necessary for a full depletion of the whole detector depth is called *depletion voltage* U_{dep}. With the approximation $U_{dep} \gg U_{bi} \approx 0.5\,\mathrm{V}$, which will be always assumed in the following, the following relation between U_{dep}, $|N_{eff}|$ and d is obtained:

$$U_{dep} = \frac{e}{2\epsilon\epsilon_0}|N_{eff}|d^2. \tag{11.5}$$

If the applied voltage is larger than the depletion voltage (*overdepletion*), the part of U that exceeds U_{dep} creates a homogeneous field $E = -\frac{(U - U_{dep})}{d}$ in addition to the field $E(x)|_{W=d}$ from Eq. 11.2:

$$E(x) = \frac{1}{d}\left[U_{dep}\left(\frac{2x}{d} - 1\right) - U\right], \qquad U \ge U_{dep}. \tag{11.6}$$
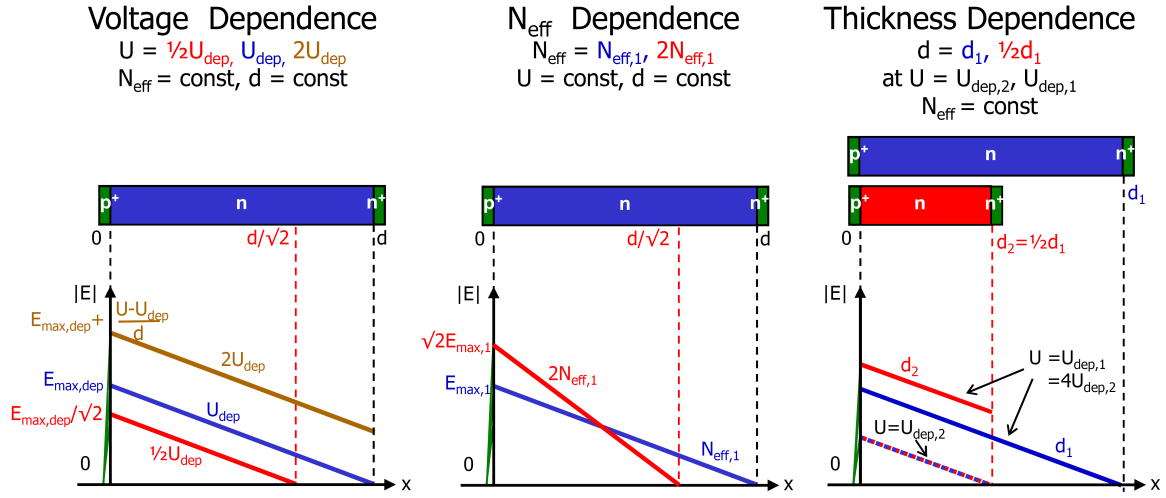
Figure 11.5: Sketch of the dependence of the electric-field distribution $E(x)$ on the applied bias voltage U (*left*), the effective doping concentration N_{eff} (*middle*) and the thickness d for two different voltages (*right*). For simplicity, the polarity of the electric field is ignored and only its absolute value is shown.

Fig. 11.5 (*middle*) shows the dependence of the field distribution on N_{eff}: Its slope depends linearly on N_{eff}. Thus, its maximum develops as $E_{max} \propto \sqrt{N_{eff}}$ and the depletion width as $W \propto 1/\sqrt{N_{eff}}$. The depletion voltage depends linearly on N_{eff}.

In Fig. 11.5 (*right*), the field dependence on the thickness is illustrated for two different regimes: Up to full depletion of the thinner detector (maximally $U = U_{dep,2}$ in the example), the electric field is independent of thickness. However, due to the thickness-dependent term $E \propto 1/d$ for the overdepleted case (see Eq. 11.6), the field increases for decreasing detector thickness once overdepletion is reached (shown for $U = U_{dep,1} = 4U_{dep,2}$). The depletion voltage depends quadratically on the thickness (see Eq. 11.5).

11.3.3 Capacitance

As the depletion layer exhibits an insulating behaviour, effectively separating the electrodes, a diode acts as a capacitor. Its capacitance C is an important detector parameter since it highly influences the noise (see Sec. 11.4.5) and can be used to determine the depletion voltage.

The capacitance is defined as the incremental change of the depletion-layer charge dQ on each side of the junction upon an incremental change of the applied voltage dU:

$$C = \frac{dQ}{dU}. \tag{11.7}$$

For abrupt junctions, the space charge Q can be written $Q = e|N_{eff}|AW$, where A denotes the effective area of the diode. Hence, its incremental change is given by $dQ = e|N_{eff}|AdW$. Together with the derivative of Eq. 11.4, this gives

$$C = \frac{dQ}{dU} = \frac{dQ}{dW}\frac{dW}{dU} = A\sqrt{\frac{\epsilon\epsilon_0 e|N_{eff}|}{2U}} = \epsilon\epsilon_0\frac{A}{W(U)}, \qquad U \leq U_{dep}. \tag{11.8}$$

This results in the following capacitance-voltage (CV) characteristic: For $U \leq U_{dep}$, the capacitance decreases as $C \propto 1/\sqrt{U}$. If the applied voltage exceeds the depletion voltage, C reaches a constant final value

$$C_{end} = \epsilon\epsilon_0\frac{A}{d}, \tag{11.9}$$

which is also called the *end capacitance* or *geometrical capacitance* since it is only dependent on the detector geometry and not on the voltage. Due to this specific CV characteristic, it is possible to obtain the depletion voltage from the kink in the doubly logarithmic CV plot.

11.3.4 Reverse Current

The *reverse current* or *leakage current* I_{rev} denotes the current of a reverse-biased diode. It is an important detector parameter as well because it has also a large effect on the noise and the power consumption of a detector.

In an ideal diode, the reverse current is only determined by diffusion of charge carriers from the non-depleted region into the space-charge zone (saturation current $I_S \approx \text{pA}$). However, in real diodes, the dominant contribution comes from charge carriers thermally generated by process- and radiation-induced defects near the middle of the band gap (see Sec. 12.4) and interface or surface states. The latter are neglected in the following and only the bulk generation current is taken into account. As it arises from defects in the depleted volume, $I_{bulk} \propto W \propto \sqrt{U}$ for $U \leq U_{dep}$ and it saturates if the applied reverse bias is larger than the depletion voltage. Furthermore, it is determined by the generation life time τ_g, whose reciprocal is a measure for the temperature-dependent probability of e-h pair generation. Eventually, the reverse current can be written

$$I_{rev} \approx I_{bulk} = \frac{en_iW(U)A}{\tau_g}, \tag{11.10}$$

where n_i is the intrinsic charge-carrier concentration.

As it is a thermal process, the reverse current is strongly temperature dependent:

$$I_{rev}(T) = I_{rev}(T_R) \cdot \left(\frac{T}{T_R}\right)^2 \exp\left(-\frac{E_{g,eff}}{2k_B}\left[\frac{1}{T} - \frac{1}{T_R}\right]\right), \tag{11.11}$$

where k_B is Boltzmann's constant, T_R a reference temperature and $E_{g,eff}$ an effective band gap energy found to be 1.21 eV [169]. I_{rev} doubles for every temperature increase by 7°C.

11.4   Signal and Noise

11.4.1   Charge Creation

Charged particles create e-h pairs along their paths. The mean energy loss absorbed in the material as a function of[4] $\beta\gamma$ is described by the Bethe-Bloch equation (see e.g. [19]).

At low $\beta\gamma$, particles are highly ionising. Thus, particles that are stopped in the material such as α particles from radioactive sources lead to densely ionised regions at the end of their path (*Bragg peak*).

A minimum of the energy loss is reached around $\beta\gamma \approx 3$. Beyond this point, for a wide range of energies, the energy loss is increasing only slightly. Such particles, which are the ones typically measured in high-energy tracking detectors, are referred to as *minimum ionising* (MIP). The actual energy loss per event, however, is subject to large fluctuations. This is typically described by a Landau distribution with a pronounced tail towards higher energy loss. Thus, the most-probable value (MPV) of the distribution is lower than its mean.

Also photons can create free charge carriers due to different mechanisms depending on their energy. Infrared and visible light with energies just slightly larger than the band gap can be absorbed by electrons in the valence band and excite them to the conduction band (possibly with the help of phonons). The absorption of photons in Si and thus also the generated charge carrier density $n(x)$ is given by

$$n(x) = \frac{N_{e-h}}{\lambda A_i} \exp\left(-\frac{x}{\lambda}\right), \tag{11.12}$$

where N_{e-h} is the number of created e-h pairs, A_i the illuminated area and λ the attenuation length of light in Si.

Higher-energy photons can create fast electrons (which in turn ionise the material) via the photo effect (X rays in the keV range), Compton effect or e^+e^- pair creation (γ rays).

More information on the absorption and depth profile of deposited charge for the radiation used in this thesis is given in Sec. 13.5.1.

11.4.2   Signal Formation and Charge Collection

If an electric field E is applied, the liberated electrons and holes drift with velocity $\vec{v}_{dr_{e,h}}(E)$ to the positive and negative electrode, respectively. The drift of a charge q at position $\vec{r}$ induces a current in the circuit of a readout electrode i, which is given by the *Shockley-Ramo theorem* [170, 171] as

---

[4]β is the velocity in units of the speed of light, $\gamma = 1/\sqrt{1-\beta^2} = E/m$ the relativistic Lorentz factor.

$$I_i(t) = q\vec{v}_{dr}(\vec{E}(\vec{r}(t))) \cdot \vec{E}_{i,w}(\vec{r}(t)). \qquad (11.13)$$

$\vec{E}(\vec{r}(t))$ is the electric field at point $\vec{r}$ and $\vec{E}_{i,w}(\vec{r}(t))$ the so-called weighting field of the ith electrode at the same point. The weighting field is defined as the negative gradient of the weighting potential $\Phi_{i,w}(\vec{r})$, which can be obtained as a solution of Laplace's equation $\Delta\Phi_{i,w}(\vec{r}) = 0$ using a unit potential at the ith electrode and 0 at the other electrodes.

Large differences are observed for different electrode geometries (see Fig. 11.6). A pad detector has a linear weighting potential with the field simply given by the inverse detector thickness $1/d$. Thus, in the case of a pad detector, on which the following discussion focuses, the induced current of $N_{e,h}(t)$ electrons or holes simplifies to

$$I_{e,h}(t) = \frac{eN_{e,h}(t)}{d}v_{dr_{e,h}}(t), \qquad (11.14)$$

The weighting potential under strips and, even more pronounced, under pixels, however, strongly peaks in the vicinity of the segmented electrode. That means that charge drifting in that region induces more current than charge drifting with the same velocity far away from the segments.
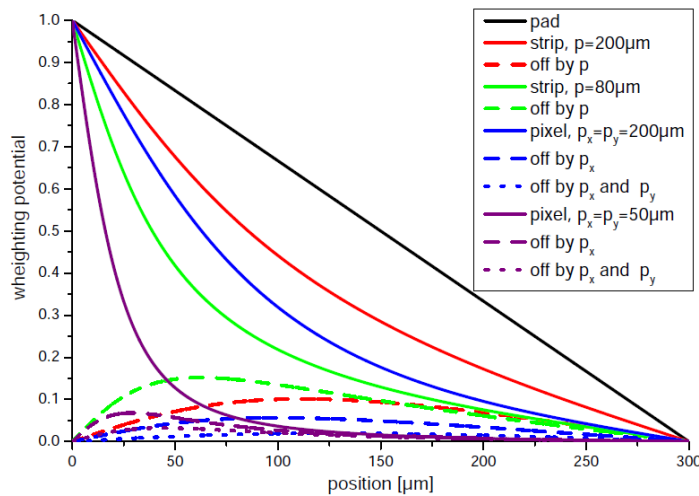
Figure 11.6: The weighting potential for different electrode geometries (a pad detector and strips and pixels of different pitches) as a function of the detector depth under the centre of the readout electrode (*solid lines*). For the strips and pixels, also the weighting potential beneath the neighbouring electrodes is shown (*dashed lines*). Taken from [172].

Drift Velocity

The drift velocity above is only an implicit function of time. In reality, it is a function of the electric field that in turn depends on the position of the charge inside the detector:

$v_{dr}\left(E\left(x\left(t\right)\right)\right)$. Hence, the trajectory $x(t)$ of the particle must be known, which can be obtained via the solution of its inverse $t(x)$:

$$v_{dr} = \frac{dx}{dt} \qquad \Rightarrow \qquad t(x) = \int_{x_0}^{x} \frac{1}{v_{dr}\left(E\left(x'\right)\right)} dx', \qquad (11.15)$$

with x_0 being the position where the charge carrier has been created. The charge-collection time after which electrons and holes reach their respective electrode is obtained by $t_{C_e} = t(d)$ and $t_{C_h} = t(0)$, respectively.

The drift velocity is due to different scattering mechanisms (impurities, phonons etc.) a non-trivial function of the electric field. For low-field values, the velocity depends linearly on the field via the low-field mobility μ_0: $v_{dr} = \mu_0 E$. For high-field values around $4 \cdot 10^4$ V/cm, the velocity saturates: $v_{dr} = v_{sat} = const$. Usually, parametrisations interpolate between the low-field and the high-field regime [173].

For Si at room temperature, the low-field mobility of electrons ($\mu_{0,e} = 1605\,\mathrm{cm}^2/\mathrm{Vs}$) is about three times higher than the one of holes ($\mu_{0,h} = 486\,\mathrm{cm}^2/\mathrm{Vs}$) [173]. The saturation velocities, however, are close to each other with $v_{sat,e} = 1.1 \cdot 10^7$ cm/s and $v_{sat,h} = 0.8 \cdot 10^7$ cm/s.

Charge-Collection Efficiency

In practice, one is usually not so much interested in the instantaneous current, but rather in the *collected charge* Q[5], i.e. the integrated current:

$$Q = \int_{0}^{t_{C_e}} I_e(t)dt + \int_{0}^{t_{C_h}} I_h(t)dt = \int_{x_0}^{d} \frac{eN_e(t(x))}{d}dx + \int_{x_0}^{0} -\frac{eN_h(t(x))}{d}dx. \quad (11.16)$$

After the second equal sign, the integration variable dt has been substituted by $\frac{dx}{v_{dr}}$, assuming that all e-h pairs have been created at position x_0 at $t = 0$.

The *charge-collection efficiency*

$$\mathrm{CCE} = \frac{Q}{Q_0}, \qquad (11.17)$$

is defined as the ratio between collected charge Q and deposited charge $Q_0 = eN_0$. If the number of charge carriers remains constant during the drift, i.e. $N_e(t) = N_h(t) = N_0$, it follows from Eq. 11.16 that the collected charge is the same as the deposited one, giving CCE = 1. However, the number of charge carriers can decrease or increase with time due to trapping and charge-multiplication effects, as explained in the following.

---

[5]Note that the collected charge is not limited to the charge actually arriving at the electrodes, but it refers to the total integrated current induced by the drifting charge carriers.

11.4.3 Trapping

Charge carriers can be trapped by defects with energy levels in the silicon band gap during their drift. The decrease of $N_{e,h}$ can be described by a charge-carrier lifetime called *effective trapping time* $\tau_{eff_{e,h}}$:

$$dN_{e,h} = -N_{e,h}\frac{dt}{\tau_{eff_{e,h}}}, \tag{11.18}$$

If τ_{eff} is constant, i.e. does not depend on time or, alternatively, on the position inside the detector, the solution of the differential equation reads

$$N_{e,h}(t) = N_{0_{e,h}} \exp\left(-\frac{t}{\tau_{eff_{e,h}}}\right). \tag{11.19}$$

The loss of charge carriers during their drift leads to a lower induced current and collected charge if the detrapping of charge carriers is slower than the integration time. In this case, the CCE becomes less than unity.

Trapping becomes especially relevant after strong irradiation due to the introduction of defects acting as trapping centres, which is described in more detail in Sec. 12.4.

11.4.4 Charge Multiplication

Under the influence of high electric fields, charge carriers can gain so much energy that they are able to create further e-h pairs by impact ionisation. As the newly created charge carriers might ionise again and so forth, such a process is also called an avalanche effect and can lead to a large multiplication of the original numbers of charge carriers N_0 (charge multiplication, CM). Such internal amplification mechanisms are well-known in gaseous detectors, but are also exploited in certain Si devices, such as avalanche photodiodes (APD) or silicon photomultipliers (SiPM). The occurrence in highly-irradiated silicon-tracking detectors, however, is a novel effect and is studied in this thesis. Overviews on the properties of impact ionisation can be found e.g. in [158, 174].

The probability for an electron or hole to create an additional e-h pair by ionisation per unit distance is given by the ionisation coefficients $\alpha_{e,h}(E)$, respectively. They are a strong function of the electric field (see Fig. 11.7). If one considers for simplicity the situation that only one carrier type multiplies (as is the case in Si at low fields as discussed below), the change of the number of charge carriers N is given by

$$dN = N\alpha dx. \tag{11.20}$$

Thus, the multiplication factor (also called gain) $M = N/N_0$ is obtained as

$$M(x_0) = \exp\left(\int_{x_0}^{d} \alpha(E(x))dx\right), \tag{11.21}$$

It depends on the location x_0 where the charge carrier is injected. A generalisation for both charge carriers contributing to multiplication (for electron injection at $x_0 = 0$) leads to [158]:

$$M = \frac{1}{1 - \int_0^d \alpha_e(E(x)) \exp\left(-\int_x^d (\alpha_e(E(x)) - \alpha_h(E(x)))dx'\right) dx}. \qquad (11.22)$$

The behaviour is qualitatively different. In the case of multiplication of only one carrier type (Eq. 11.21), M remains finite for a finite field value, although it obviously can become very large. In this case, the multiplied charge is proportional to the deposited charge. In contrast, if both carriers multiply, M can become infinite for a finite field value if the denominator of Eq. 11.22 becomes zero, i.e. for $\alpha d = 1$ in the simplified case of $\alpha = \alpha_e = \alpha_h$ and a constant field. This situation is called junction breakdown. If quenching is provided, some devices such as single-photon APDs or SiPMs can operate in this regime, which is also called Geiger mode.
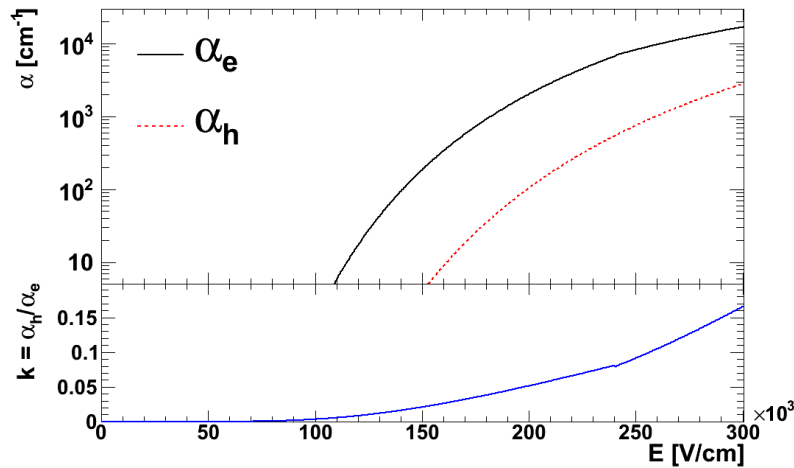
Figure 11.7: The ionisation coefficients for electrons and holes $\alpha_{e,h}(E)$ and their ratio $k = \alpha_h/\alpha_e$ at room temperature as a function of electric field E according to [175].

$\alpha_{e,h}(E)$ are typically parametrised by the Chynoweth expression [176]:

$$\alpha_{e,h}(E) = A_{e,h} \exp\left(-\frac{B_{e,h}}{E}\right). \qquad (11.23)$$

Experimentally obtained values for $A_{e,h}$ and $B_{e,h}$ vary significantly among different groups [175–179]. In the following, the values measured at room temperature by [175] are taken as a reference (see Fig. 11.7). For increasing temperatures, the ionisation coefficients are found to decrease. Recent results also hint at a decrease of the coefficients after heavy radiation [180] (but no parametrisation is provided).

It is important to note that the electron ionisation coefficient α_e is much larger than α_h, although the difference decreases with increasing electric-field value: the ratio

$k = \alpha_h/\alpha_e$ rises from 0.02 at $1.5 \cdot 10^5\,\mathrm{V/cm}$ to 0.09 at $2.5 \cdot 10^5\,\mathrm{V/cm}$. Thus, for low fields, the assumption of only electrons multiplying is a good approximation.

If the onset of CM is defined by the condition of 10% more charge carriers at the end of a 10 μm or 1 μm thick multiplication region ($M = 1.1$), it follows from Eq. 11.21 that (homogeneous) α values of 10^2 or $10^3\,\mathrm{cm}^{-1}$ are needed, respectively. For electron multiplication, this corresponds to electric fields of $1.4 \cdot 10^5\,\mathrm{V/cm}$ or $1.8 \cdot 10^5\,\mathrm{V/cm}$, respectively. The corresponding hole multiplication sets in only at the higher fields of $2.0 \cdot 10^5\,\mathrm{V/cm}$ or $2.6 \cdot 10^5\,\mathrm{V/cm}$, respectively.

CM in irradiated sensors can be beneficial if it increases the signal and thus potentially compensates trapping. However, it can also increase the noise as discussed below.

11.4.5   Detector Readout and Noise

When measuring MIPs, the signal in the order of 10 ke needs external amplification. Thus, the detector is readout using a charge-sensitive, i.e. current-integrating, preamplifier.

Inherent to each measurement is background noise, which is defined as the root mean square (RMS) of the measured charge in absence of a signal. It is typically given in units of equivalent noise charge (ENC). Noise can arise from various sources in the sensor or readout chain. It originates mainly from fluctuations of the sensor current due to the discrete nature of charge emission (shot or current noise) and fluctuations of the velocity of charge carriers in resistors (thermal or voltage noise). The current spectral density of shot noise is given by $i_{n,sh}^2 = 2eI_{rev}$, the voltage spectral density of thermal noise by $e_{n,th}^2 = 4k_B TR$. It turns out that the voltage noise is highly influenced by the detector capacitance C_d when propagated to the amplifier output.

To determine the final noise of a detector-readout system, one needs to fold the spectral densities with the frequency-dependent transfer function of the system. To enhance the SNR, the signal after the preamplifier is usually shaped with a differentiating capacitance-resistor (CR) circuit followed by a chain of RC integrators. As the first one acts as a high-pass and the second one as a low-pass, tailored for the signal frequencies, the signal is filtered against the background noise. However, also other constraints such as the duration of the shaped signal have to be taken into account. This is especially relevant for the LHC with a designed 25 ns bunch-crossing time in order to avoid signal pileup. The noise of a sensor-readout system can be written

$$\sigma_{noise} = \sqrt{\sigma_{sh}^2 + \sigma_{C_d}^2 + \sigma_{res}^2} = \sqrt{aI_{rev}\tau_p + (b + \frac{c}{\tau_p}C_d)^2 + \sigma_{res}^2}, \qquad (11.24)$$

where a, b and c are readout-specific parameters, τ_p is the peaking time of the shaped signal and σ_{res} are residual noise sources, which are usually not dominant. The shot noise increases and σ_{C_d} decreases for increasing τ_p. Thus, for detectors at the LHC with τ_p in the order of the bunch crossing time, σ_{C_d} is by far the dominant contribution for unirradiated detectors with low I_{rev}.

Typical noise values are about 200–300 e for pixel and 1000 e for strip detectors at the LHC [73, 76, 162]. The latter exhibit more noise due to the larger cell size, which increases both the current and capacitance. Pad detectors show even more noise due to their size. At such low pixel noise levels, the pixel readout threshold (typically about 3000 e) is usually determined by other effects such as signal cross talk in the readout chip [181].

Due to irradiation, the current increases strongly (see Sec. 12.4.1). However, the shot noise can be controlled by cooling down to about -10°C at the LHC due to the strong temperature dependence (see Eq. 11.11), so that the total noise increase is only moderate at LHC fluences [76, 162].

11.4.6 Spectrum Broadening and Noise in the Charge-Multiplication Regime

In the CM regime, the discrimination between signal and noise can be complicated due to different mechanisms: statistical fluctuations in the multiplication process, the multiplication of the leakage current or an increased rate of microdischarges. Thus, it has to be studied in detail whether the beneficial effect of an increasing signal is not compensated by these adverse effects.

Firstly, the signal spectrum can be broadened (independently of the broadening due to a possible background noise increase) as M is only the average multiplication. Due to the stochastic nature of CM, the multiplication factor M undergoes statistical fluctuations described by the excess noise factor [174, 182, 183]

$$F(M) = \frac{\overline{M^2}}{\overline{M}^2} = \frac{\overline{M^2}}{M^2}. \tag{11.25}$$

For electron injection, $F(M)$ is given approximately by

$$F(M) = kM + (2 - \frac{1}{M})(1 - k). \tag{11.26}$$

If only electrons multiply ($k = 0$), which is valid for low fields just above the CM threshold, F increases from 1 at $M = 1$ to only 2 at large values of M. For $k > 0$, however, F increases steeply with M, e.g. $F = M$ for $k = 1$.

Moreover, the shot noise is expected to increase because not only the signal is multiplied, but also the bulk leakage current $I_{rev}(M') = M'I_{rev,M'=1}$. Here, $I_{rev,M'=1}$ is the current without CM and M' a multiplication factor that might be different from M for the signal. It should be noted that the shot noise in the CM regime cannot be obtained by inserting this multiplied leakage current into Eq. 11.24, which would give $\sigma_{sh}(M') \propto \sqrt{M'}$. Instead, the whole current noise spectrum is multiplied, leading to $\sigma_{sh}(M') \propto M'$. Moreover, an excess noise factor $F' = F(M')$ due to statistical fluctuations of M' also applies here and further enhances the noise. Thus, it is finally given by

$$\sigma_{sh}(M') = \sigma_{sh,M'=1}M'\sqrt{F'} = \sqrt{aI_{rev}\tau_p M'^2 F'}. \qquad (11.27)$$

The total noise is the sum of this multiplication-dependent shot noise and other noise contributions σ'_{noise} which are not influenced by CM, such as σ_{C_d}. Thus, the mean SNR can be expressed as

$$SNR = \frac{\bar{Q}}{\sigma_{noise}} = \frac{\bar{Q}}{\sqrt{\sigma_{sh}(M')^2 + \sigma'^2_{noise}}} = \frac{M\bar{Q}_{M=1}}{\sqrt{\sigma^2_{sh,M'=1}M'^2 F' + \sigma'^2_{noise}}}, \qquad (11.28)$$

where $\bar{Q}$ and $\bar{Q}_{M=1}$ is the mean collected charge with and without CM, respectively. Thus, it depends on the relative size of the different terms whether CM can improve the SNR. For $M \approx M'$, the SNR improves as long as $\sigma_{sh}(M') < \sigma'_{noise}$. If $\sigma_{sh}(M') \gg \sigma'_{noise}$ the SNR can only improve if $M > M'\sqrt{F'}$.

Another critical issue are microdischarges, i.e. randomly occurring current peaks due to short, uncontrolled, localised CM. This is in general independent of radiation-induced CM and can even occur in unirradiated sensors at local high electric fields, e.g. at the edges of implantations or other boundaries. However, it needs to be studied if the rate increases in the presence of generally higher electric fields in the CM regime after high irradiation. Microdischarges are particularly detrimental as they lead to non-Gaussian noise tails and potentially detector damage.

11.5   Silicon Materials

There are three main growing techniques of silicon crystals for electronics and sensors: the *Czochralski (Cz)*, *Float Zone (FZ)* and *epitaxial (EPI)* process [158]. The different amounts of process-induced impurities, especially oxygen, play a decisive role in the creation of radiation damage, as shown in Sec. 12.

11.5.1   Czochralski Material

The Czochralski method begins with polysilicon that is melted in a rotating quartz crucible. A monocrystalline seed crystal is placed on the surface and slowly drawn upwards while being rotated. At the interface between crystal and melt, the Si solidifies in a single crystal with the same crystal orientation as the seed. By varying the drawing speed and temperature, the diameter is controlled.

The drawback of the Cz method is the high amount of impurities, especially O, C, P, B and Al. During the process, molecules from the crucible and the graphite susceptor dissolve into the melt and lead to an enrichment of the Si with impurities. For a long time, it was impossible to produce detector-grade Cz Si with resistivities >100 Ωcm. However, this is now achieved by applying a magnetic field in vertical or horizontal

direction. This can improve the situation by preventing convection and thus avoiding a mixing of the dirty melt near the crucible with the purer Si in the centre. This method is called *magnetic Czochralski (MCz)*. But the concentrations of impurities are still high compared to other materials ($[O] \approx (7\text{–}8) \cdot 10^{17} \, \text{cm}^{-3}$, $[C] \lesssim 2 \cdot 10^{16} \, \text{cm}^{-3}$ [163]). A certain fraction of the oxygen exists not as a single atom O but as a dimer O_2.

However, especially the high concentration of oxygen can be also advantageous for radiation hardness due to the *oxygen effect* (see Sec. 12.4.2). Moreover, MCz material is available at low cost and widely used in microelectronics.

11.5.2 Float-Zone Material

The float-zone method is based on the zone-melting principle and takes place either under vacuum or in an inert gaseous atmosphere. A high-purity polycristalline rod and a single-crystal seed are brought into close contact in a vertical position and rotated. With a radio-frequency field, the region around the contact is melted (*floating zone*). Slowly, the melted zone is shifted away from the contact so that the Si can solidify gradually in a single crystal from the seed as a starting point.

Contrary to the Cz method, there is no contact to other materials than the ambient gas so that a higher purity and consequently resistivity is achieved ($[O] \approx 10^{16} \, \text{cm}^{-3}$, $[C] \approx 5 \cdot 10^{15} \, \text{cm}^{-3}$).

However, as it turned out that a high oxygen concentration is beneficial in terms of radiation hardness, a deliberate adding of oxygen to standard float-zone material *(STFZ)* is preferred. This oxygen enrichment can be done by a diffusion process at 1150°C that lasts between 24 h and 72 h, resulting in an oxygen concentration up to a level of $10^{17} \, \text{cm}^{-3}$. This material is called *diffusion oxygenated float zone (DOFZ)* and is one of the best examples of defect engineering (see Sec. 12.5.2).

11.5.3 Epitaxial Material

Epitaxy denotes the growing of a thin layer on a single-crystal substrate. The epitaxial layer adopts the crystal orientation of the substrate and is monocrystalline. If the layer and the substrate are of the same semiconductor material, it is called homoepitaxy, if they are different the process is called heteroepitaxy.

There are different epitaxial growing methods, but the most relevant with respect to detector-grade Si is the *vapour-phase epitaxy (VPE)*, sometimes also called *chemical-vapour deposition (CVD)*, which has also been used by the manufacturer ITME [184] for the material in this work. At temperatures around 1200°C, Si is obtained by decomposition of a gaseous compound (most commonly *silicon tetrachloride $SiCl_4$*) with the help of hydrogen and arranges itself on the crystal substrate:

$$SiCl_4(\text{gas}) + 2H_2(\text{gas}) \rightarrow Si(\text{solid}) + 4HCl(\text{gas}). \tag{11.29}$$
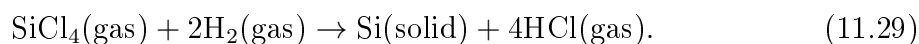
As there are also competing reactions with $SiCl_4$ that etch the Si away, the growth

rate is reduced and the $SiCl_4$ concentration has to be chosen carefully. A typical growth rate is approximately 1 μm/min. The doping of the layer is done by introducing gaseous compounds such as diborane (B_2H_6) or phosphine (PH_3) for p-type and n-type material, respectively.

As a substrate, usually highly-doped Cz material is chosen for the following reasons: The high doping guarantees a low resistivity, so that the serial resistance of the substrate can be neglected and the sensitive region is determined by the epitaxial layer alone. During the crystal growth impurities can out-diffuse from the substrate into the EPI layer. While the diffusion of unwanted impurities remains on a moderate level, especially oxygen (O and also a large amount of O_2) with its high diffusion constant is introduced in the layer in a high concentration as Cz material is very oxygen-rich. So naturally, the oxygen concentration of EPI material is higher than the one of STFZ. However, the distribution of oxygen is very inhomogeneous throughout the layer (see Fig. 13.1). In order to improve the homogeneity and to increase the average oxygen density, oxygenation can be performed also for epitaxial material in a similar way as for FZ: The diffusion of oxygen from the Cz substrate on the one side and from the SiO_2 at the surface on the other side is stimulated at about 1100°C, thereby transforming *standard epitaxial material (EPI-ST)* into *diffusion oxygenated epitaxial material (EPI-DO)*.

Chapter 12

Defects in Silicon and Radiation Damage

In the last section, the macroscopic parameters that determine the detector performance like capacitance, depletion voltage, reverse current and charge-collection efficiency were introduced. Energy levels in the forbidden band gap arising from microscopic defects like impurities or lattice distortions can have large effects on those macroscopic parameters. Some of the defects are inherent as even today's purest Si contains a considerable amount of impurities like oxygen or carbon, which is sometimes even desired as in the case of gettering or deliberate doping with phosphorus and boron. Normally, this can be well controlled and many of the defects are not even electrically active. However, in the case of the application in high-luminosity colliders as the LHC, radiation damage can occur, i.e. the introduction of new electrically active defects which pose a considerable threat on the detector performance.

Radiation damage can be divided into surface and bulk damage. The first one is mainly relevant for photon science and the readout electronics, but this is expected not to be of major relevance at the HL-LHC. Therefore, the following discussions will focus on bulk damage, which degrades the performance of Si detectors at hadron colliders.

12.1 Damage Mechanism

The interaction of hadronic and higher-energetic leptonic particles with the Si lattice atoms can cause such a high energy transfer from the incoming particle to a so-called *primary knock-on atom (PKA)* that the latter one can be displaced from its lattice site. For an incoming particle of energy E and mass m, the maximal transferable energy can be calculated in a nonrelativistic approach as

$$E_R^{max} = 4E \frac{m \cdot m_{Si}}{(m + m_{Si})^2},$$

(12.1)

where m_{Si} is the mass of a Si atom. The minimum energy that needs to be imparted to the PKA in order to cause a displacement is $E_d \approx 25\,\text{eV}$ [185]. In this way, a Si

interstitial (I) and a left-over vacancy (V) are created (*Frenkel pair*). If the recoil energy of the PKA is large enough, it can knock out further Si atoms and thus create cascades of defects as illustrated in Fig. 12.1. At the end of the path of a heavy recoil atom, the cross section for elastic scattering increases as the velocity decreases, resulting in a dense agglomeration of defects (*clusters*). The threshold recoil energy required for cluster generation is approximately 5 keV.
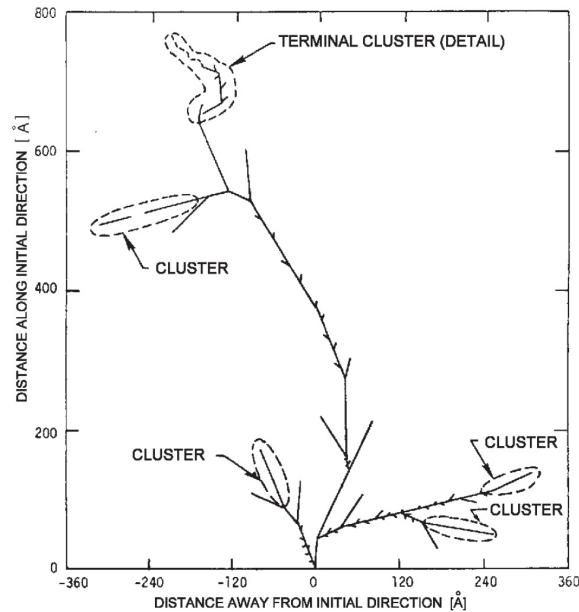
Figure 12.1: Monte-Carlo simulation of a cascade caused by a recoil atom with a primary energy of $E_R = 50$ keV. This energy corresponds to the average kinetic energy that a 1 MeV neutron transfers to a PKA. Taken from [185].

12.2   Comparison of Different Radiation Types

The question arises how the damage effects of irradiation with different particle types and energies can be compared. This is a difficult task because depending on the irradiation type and energy, there are different interactions with the Si atoms. Charged hadrons interact primarily via ionisation, which is a fully reversible process in the Si bulk[1]. The part of the interaction that does result in displacement damage in the lattice is called *non-ionising energy loss (NIEL)*. For low-energetic protons (e.g. 10 MeV), this is mostly due to Coulomb interaction, which transfers the energy in small fractions, so that mainly point defects are created. On the contrary, neutrons as non-charged particles interact only via nuclear reactions. This imparts a large fraction of the energy of the neutron to the PKA, resulting dominantly in cluster effects. High-energetic protons, e.g. the 24 GeV protons used in this work, cause both point defects and cluster damage.

---

[1]However, ionisation can cause radiation-induced surface damage, but this is not considered in this work.

12.2.1 The NIEL-Scaling Hypothesis

The NIEL-scaling hypothesis assumes that any displacement-damage-induced change in the material properties scales with the energy imparted in displacing collisions, irrespective of the type and interaction process of the imparting particle. This can be expressed by the *displacement-damage cross section* or *damage function*

$$D(E) = \sum_\nu \sigma_\nu(E) \cdot \int_{E_d}^{E_R^{max}} f_\nu(E, E_R) P(E_R) dE_R. \tag{12.2}$$

The index ν runs over all possible reactions with cross section σ_ν between the impinging particle of energy E and the Si atoms, which can lead to displacements in the lattice. $f_\nu(E, E_R)$ is the probability for the generation of a PKA with recoil energy E_R by a particle with energy E in the reaction with index ν. The so-called Lindhard partition function $P(E_R)$ gives the portion of energy available for displacement damage by a PKA with recoil energy E_R and can be calculated analytically [186]. The integration is done over all possible recoil energies ranging from the displacement threshold E_d to the maximum transferable energy E_R^{max}.
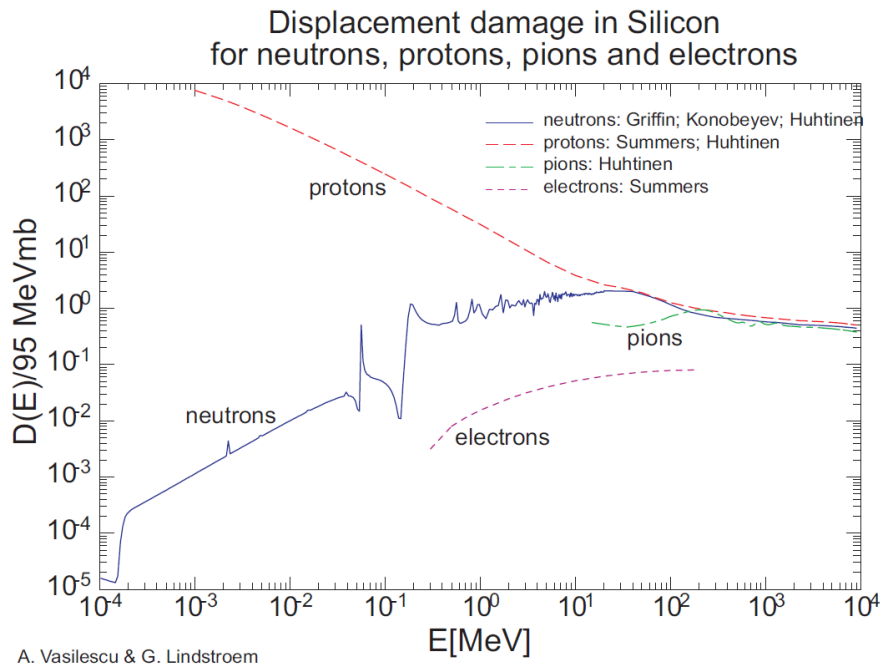
Figure 12.2: Displacement-damage cross section for different particle types as a function of energy, normalised to 1 MeV neutrons. Taken from [187].

With the help of $D(E)$ it is now possible to compare the displacement damage for different particle types and energies as shown in Fig. 12.2. As one is usually dealing with different irradiation sources with continuous energy spectra $\Phi(E)$, it is convenient to define a so-called *hardness factor* κ that integrates $D(E)$ over the energy spectrum and scales it to the equivalent displacement-damage cross section of mono-energetic 1 MeV neutrons:

$$\kappa = \frac{\int D(E)\Phi(E)dE}{D(E_n = 1\,\text{MeV}) \cdot \int \Phi(E)dE}. \tag{12.3}$$

Hence, it is possible to calculate the *equivalent fluence* of 1 MeV neutrons, which would have created the same displacement damage, as

$$\Phi_{eq} = \kappa\Phi = \kappa \int \Phi(E)dE. \tag{12.4}$$

It should be noted that NIEL-scaling violating behaviour is observed for specific macroscopic damage (see below) as the scaling assumption neglects e.g. the different effects of point defects and clusters as it takes only the total displacement energy into account.

12.3 Evolution of Defects and Annealing

12.3.1 Creation of Point and Cluster-Related Defects with Influence on Detector Properties

The primary Si interstitials and vacancies are not the defects that influence the detector properties. The damage process evolves further as the defects are highly mobile at temperatures above 150 K. On the one hand, damage is reduced as a large fraction of the produced Frenkel pairs recombine, namely approximately 60% of the overall produced pairs and even 75-95% in cluster regions [188]. On the other hand, the remaining interstitials and vacancies migrate through the lattice and many of them undergo further reactions both with each other and with impurities in the Si crystal. An overview on some of the possible resulting point defects is given in Fig. 12.3. The properties of the resulting defect clusters, however, are not yet well understood [189, 190]. But it is known that cluster-related defects acting similarly to point defects emerge in or close to the disordered regions. Due to the huge amount of vacancies and interstitials in clusters, cluster-related defects are of silicon-intrinsic nature and do not depend on impurity concentrations.

12.3.2 Annealing

The evolution of defects does not only happen directly after irradiation, but is a continuous process. Also the above described secondary point and cluster-related defects are mobile, depending on the temperature. Hence, the radiation-induced defects and their impact on the detector performance develop further as a function of time. This process is called *annealing*.

Three processes may happen during annealing:
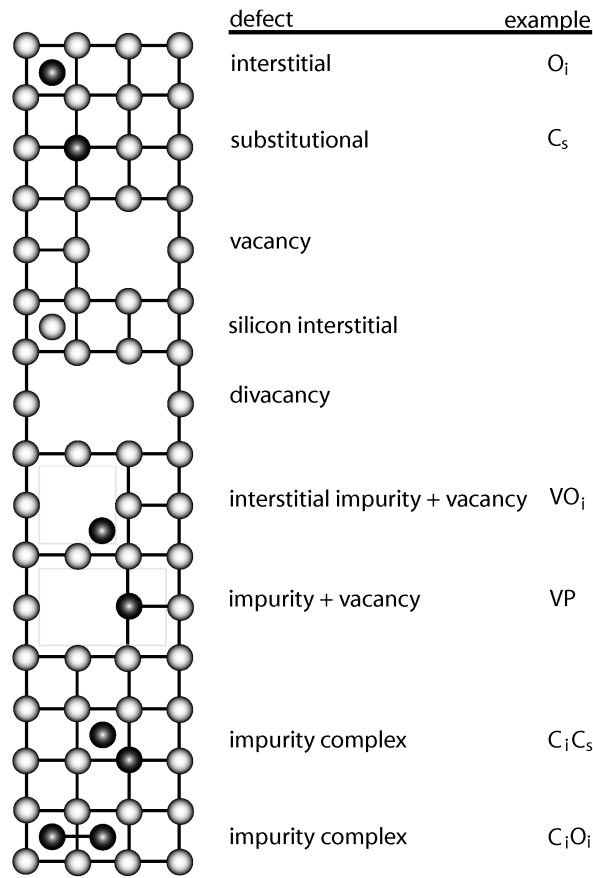
Figure 12.3: Schematic representation of some point defects. The index i stands for *interstitial*, the index s for *substitutional*. Taken from [168].
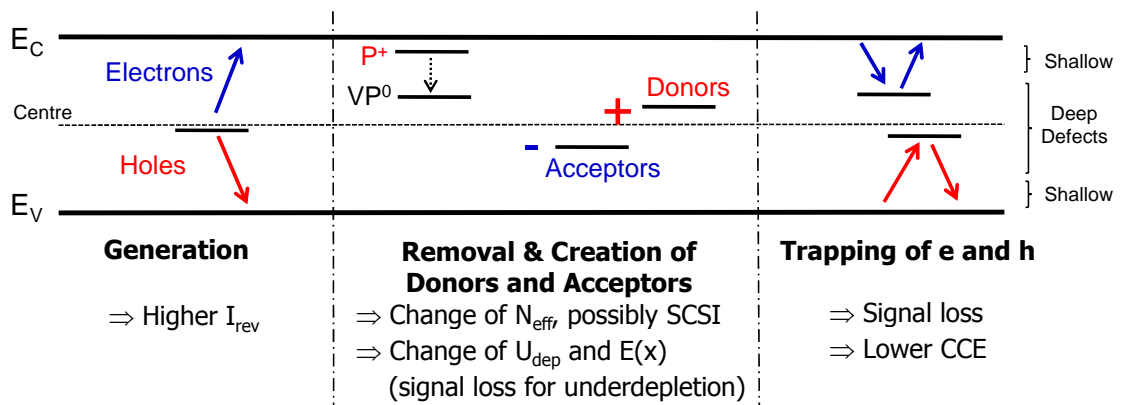
Figure 12.4: Effects of defect levels in the band gap on electrical properties and macroscopic detector parameters.

- *Migration*
  Depending on temperature, defects become mobile and migrate through the Si lattice until trapped by sinks (e.g. surface, dislocations, etc.).

- *Complex Formation*
  Migrating defects can react with other defects or impurities. Some of them can recombine (e.g. $V + Si_i \rightarrow Si_s$), others form new defect complexes (e.g. $V + O_i \rightarrow VO_i$).

- *Dissociation*
  A defect complex consisting of more than one component can dissociate into its single constituents if the energy of the absorbed phonon is larger than the binding energy of the complex. The new fragments in turn can migrate, recombine or build other defects.

Annealing studies are important because of two reasons. On the one hand, the annealing behaviour of defects can provide further information besides the characterisation of electrical properties, which might help in identifying the microscopic nature of a defect. On the other hand, depending on the process and its time constant, the reactions can develop slowly, so that even years after irradiation still changes may occur. Especially for detectors at particle colliders, this is a factor potentially limiting their application and has to be well-understood.

12.4   Influence of Defects on Detector Properties

Both point defects and cluster-related defects can have discrete, electrically active energy levels E_t in the Si band gap. Such energy levels are able to alter the macroscopic detector parameters. The main effects are illustrated in Fig. 12.4 and are explained in further detail below. The probabilities of these processes and of the occupation of defects can be calculated with the help of Fermi-Dirac statistics in thermal equilibrium or Shockley-Read-Hall statistics (for further details see [163]).

12.4.1   Generation of Charge Carriers: Increase of I_{rev}

As mentioned in Sec. 11.3.4, defects with energy levels close to the middle of the band gap act as generation centres for e-h pairs (see Fig. 12.4, *left*). As the number of generation centres increases during irradiation, the reverse current also rises. It was found that the change in reverse current $\Delta I = I_{irr} - I_0$ is linear to the equivalent fluence, irrespective of the type and energy of fast hadron irradiation and Si material [163]:

$$\Delta I(\Phi_{eq}) = \alpha \Phi_{eq} V, \tag{12.5}$$

with the sensitive detector volume V and the *current-related damage parameter* α. For measurements at room temperature, a value of $\alpha = (3.99 \pm 0.03) \cdot 10^{-17}$ A/cm was

found after annealing of 80 min at 60°C (corresponding to 8 min at 80°C). The validity of this relation is believed to be so precise that it is in turn often used to determine or cross-check the fluence of an irradiated sample via the current. The current is observed to decrease during annealing.

Recently, progress has been made in identifying the microscopic origin of the radiation-induced current increase [190]. It was found that the cluster-related defects $E4/E5$ and $E205a$ are responsible for a part of it. $E4/E5$ were identified as tri-vacancy V_3.

12.4.2 Change of Acceptor and Donor Concentrations

Radiation-induced defects can change the concentration of donors and acceptors.

On the one hand, the original doping impurities like P or B can form new defect complexes with other radiation defects. Thereby, they might become electrically inactive if the new complex is neutral at the measurement temperature. This is e.g. the case for phosphorus undergoing the reaction $V + P \rightarrow VP$. Such processes are called donor (or acceptor) removal.

On the other hand, the defect states can be acceptor- or donor-like. Acceptors are negatively charged if occupied by an electron and neutral otherwise, whereas donors are neutral if occupied by an electron and positively charged otherwise. Whether the states are occupied (and hence charged) or not is determined in thermal equilibrium by the relative position of the energy level compared to the Fermi level E_F (an energy level is more likely to be occupied by an electron if $E_t < E_F$ and to be not occupied if $E_t > E_F$).

The change of the effective doping concentration $N_{eff} = N_D - N_A$ can go so far that the initial doping type can invert. For example, if in an initially n-type diode so many acceptors are induced by irradiation that they exceed the original and newly generated donors, this material effectively changes to p-type (see Fig. 12.5, *left*). This phenomenon is called *type inversion* or *space-charge-sign inversion (SCSI)*. After type inversion, the junction moves from one contact to the other (in the simplest case; after strong irradiation, also effects like double junctions are observed as explained below). This can imply adverse effects on the detection efficiency and position resolution, which has to be taken into account when deciding at which electrode to read out.

The annealing behaviour is described by the *Hamburg model* [163] as a superposition of a constant term N_C and a short-term (N_A) and long-term (N_Y) annealing component:

$$
\begin{aligned}
\Delta N_{eff}(\Phi_{eq}, t_a) &= N_{eff,0} - N_{eff}(\Phi_{eq}, t_a) & (12.6) \\
&= N_A(\Phi_{eq}, t_a) + N_C(\Phi_{eq}) + N_Y(\Phi_{eq}, t_a). & (12.7)
\end{aligned}
$$

$N_{eff,0}$ is the initial doping concentration. The constant term can be parametrised as

$$
N_C(\Phi_{eq}) = N_{C,0} \left(1 - \exp(-c\Phi_{eq})\right) + g_C \Phi_{eq}. \tag{12.8}
$$

The first term describes an incomplete donor removal with $N_{C,0} \leq N_{eff,0}$ being the removable doping concentration and c being the so-called removal constant that describes the removal velocity. The second term represents a fluence-proportional introduction of space charge ($g_C > 0$ for effective acceptor introduction, $g_C < 0$ for donor introduction).

Impact on Detector Parameters

The change in N_{eff} has a large impact on the depletion voltage ($U_{dep} \propto |N_{eff}|$, see Sec. 11.3.2) and possibly on the size of the sensitive detector region if the depletion voltage exceeds the maximum operating voltage. In that case, the collected charge decreases and the capacitance increases, leading to more noise. Moreover, N_{eff} also influences the slope of the electric-field distribution and thereby its maximum value (see Fig. 11.5, *middle*). This can lead to charge multiplication effects as demonstrated by the results of this thesis.

Material Dependence

In the frame of the CERN-RD48 (ROSE) collaboration, it was found that the change of N_{eff} highly depends on material and irradiation type, thereby violating the NIEL-scaling hypothesis [191].

In n-type STFZ, a large donor removal and acceptor introduction rate was measured for proton and neutron irradiation. The material inverts already at equivalent fluences around $10^{12}\,\mathrm{cm}^{-2}$ to a few $10^{13}\,\mathrm{cm}^{-2}$, depending on the initial doping concentration (see e.g. Fig. 12.5, *left*). After this point, N_{eff} and hence U_{dep} increase approximately linearly. At a few $10^{14}\,\mathrm{cm}^{-2}$, the maximum operation voltage of $600\,\mathrm{V}$ for most LHC experiments is reached, thereby disqualifying this material already for the innermost layers of the current LHC tracker, and even more for the HL-LHC.

However, it was found that after oxygen enrichment, the increase of acceptor concentration at high fluences is suppressed by about a factor of three with respect to STFZ after charged-hadron and lepton irradiation [163, 191]. Thus, n-type DOFZ is used for the innermost layers of the current LHC trackers.

N-type MCz and EPI materials, which exhibit even higher oxygen concentrations, usually do not type-invert at all after charged-hadron irradiation, and at high fluences, N_{eff} increases due to the predominant creation of donors instead of acceptors [9, 192–194] (see Fig. 12.5, *right*). However, after neutron irradiation, acceptor introduction dominates also here and type inversion takes place. This behaviour could be related to the radiation-type dependent introduction rate of the donors $E(30K)$ and BD in comparison to the acceptors $H(116K)$, $H(140K)$ and $H(151K)$ found in microscopic measurements [190, 194].

The annealing behaviour was found to be qualitatively similar for all materials: the short-term component is characterised by a decrease of radiation-induced acceptors or an increase of donors, whereas predominantly acceptors are introduced during the

long-term annealing [190, 194].
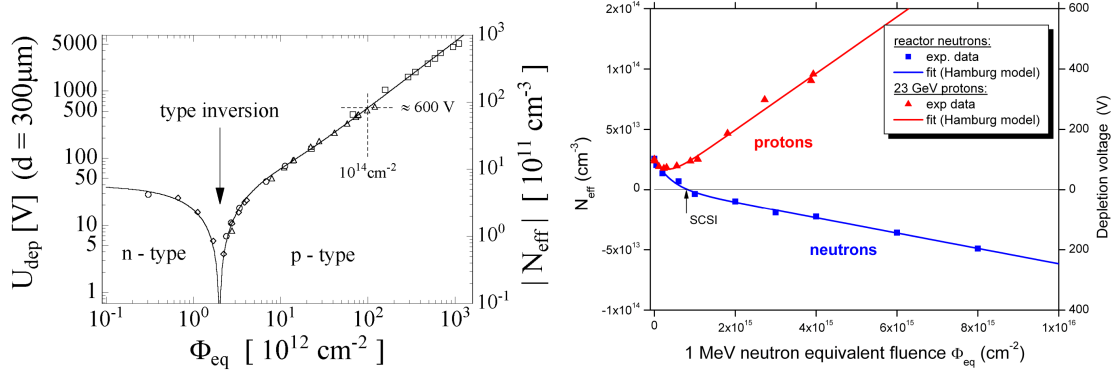
Figure 12.5: The development of N_{eff} and U_{dep} with equivalent fluence. *Left:* $|N_{eff}|(\Phi_{eq})$ and $U_{dep}(\Phi_{eq})$ in 300 μm thick n-type STFZ diodes, directly measured after neutron irradiation [195]. *Right:* $N_{eff}(\Phi_{eq})$ and $U_{dep}(\Phi_{eq})$ in 75 μm thick n-type EPI-DO diodes after neutron and proton irradiation [194].

Double Junction and Electric Field in Neutral Bulk Region in Highly Irradiated Material

The effective doping concentration N_{eff} (i.e. the difference between *ionised* donor and acceptor concentration) is not only determined by the number of radiation-induced defects, but also by their occupation. Thus, the N_{eff} and electric-field distributions are more complicated in highly irradiated sensors with a high leakage current. This leads to a large density of free charge carriers, which can be captured and hence change the occupation of acceptors and donors. As holes drift in the direction of the p^+ electrode and electrons to the n^+ electrode under reverse bias, this occupation change (and hence N_{eff}) depends on the position in the sensor. It can even happen that the material type-inverts locally, leading to a double junction [196] at both electrodes. Consequently, the electric-field distribution is not linear anymore as for a constant N_{eff}, but exhibits a double peak structure. A simulation of this effect is shown in Fig. 12.6. The effect of the reverse current on the electric-field distribution is clearly demonstrated by switching it on and off in the simulation. Moreover, it can be also seen that at lower temperatures, where current generation is suppressed (see Sec. 11.3.4), the double peak is less pronounced.

Another effect in highly irradiated sensors is the emergence of an electric field in the neutral bulk region in the middle between the two space-charge regions of a double junction [198]. This is caused by the fact that after irradiation and introduction of a large amount of deep defects, the bulk material becomes highly resistive. In the presence of a large leakage current, this leads to a voltage drop according to Ohm's law, which implies an electric field. Thus, in such a sensor it is possible to have an electric field everywhere inside the sensor even without being fully depleted.

These effects show that the concept of a constant N_{eff} as single parameter describing the depletion zone and the electric field of the whole diode is questionable under
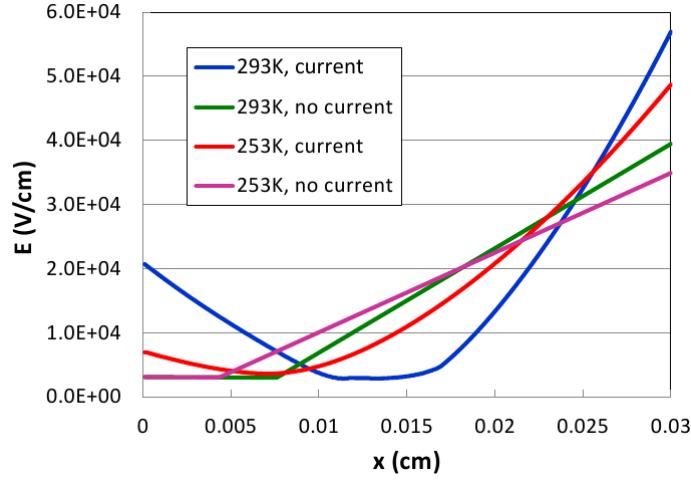
Figure 12.6: Development of a double junction: Simulation of the electric-field distribution in an irradiated sensor at different temperatures (253 and 293 K) with and without taking the reverse current into account. Taken from [197].

such conditions. However, in lack of a better alternative concept, it is still frequently used.

12.4.3   Trapping

In principle, all electrically active defects can trap charge carriers and re-emit them later. Especially harmful are those defects which have a high capture cross section and whose emission or detrapping time constant is large with respect to the integration time of the readout. This results in effective signal-charge-carrier loss and hence in a degraded charge-collection efficiency (see Sec. 11.4.2).

The charge is captured with the probability $\frac{1}{\tau}$ (inverse trapping time constant), depending on the concentration of the trap N_t, its electron- or hole-capture cross section $\sigma_{e,h}$ and its electron-occupation probability f_t:

$$
\begin{aligned}
\frac{1}{\tau_{e,i}} &= N_{t,i} \cdot (1 - f_{t,i}) \cdot \sigma_{e,i} \cdot v_{th,e} && \text{for electrons and} \\
\frac{1}{\tau_{h,i}} &= N_{t,i} \cdot f_{t,i} \cdot \sigma_{h,i} \cdot v_{th,h} && \text{for holes.}
\end{aligned}
\tag{12.9}
$$

$v_{th,e,h}$ is the thermal velocity. The overall effective trapping probability is the sum over the probability of individual traps: $\frac{1}{\tau_{eff,e,h}} = \sum_i \frac{1}{\tau_{i,e,h}}$.

It has been shown experimentally that the effective radiation-induced trapping probability is proportional to the equivalent fluence [199, 200]:

$$
\frac{1}{\tau_{eff,e,h}} = \beta_{e,h} \Phi_{eq},
\tag{12.10}
$$

where $\beta_{e,h}$ is referred to as *trapping-related damage parameter*. The values for $\beta_{e,h}$ measured in FZ material up to fluences of about 10^{15} cm^{-2} are shown in Tab 12.1.

They are slightly temperature dependent and decrease by about 20–30% over a range from 220 to 294 K [199]. The annealing behaviour of β is different for electrons and holes [199]. β_e decreases by about 35% from the value as irradiated to a saturation value reached after about 30 h at 60°C annealing. On the contrary, β_h increases by about 30%. No dependence on impurity concentrations was found. So far, no clear microscopic identification of the defects responsible for trapping could be made [190].

	β_e [10^{-16} cm^{2}ns^{-1}]	β_h [10^{-16} cm^{2}ns^{-1}]
Neutrons	3.7 ± 0.6	5.7 ± 1.0
Charged hadrons	5.4 ± 0.4	6.6 ± 0.9

Table 12.1: The trapping-related damage parameter $\beta_{e,h}$ at -10°C, taking into account the results of measurements by different groups as compiled in [201].

Trapping is expected to be the limiting factor at HL-LHC fluences. This can be illustrated by the expected trapping time constants and corresponding mean drift distances $\ell_{eff} = v_{dr}\tau_{eff}$ before being trapped, assuming $v_{dr} = v_{sat}$ in the following. At a fluence of 10^{15} cm^{-2}, the trapping time constants are less than 2 ns for charged-hadron irradiation, leading to $\ell_{eff} \approx 200$ μm. This is already shorter than the thickness of most sensors currently used at the LHC. For 10^{16} cm^{-2}, the extrapolated trapping times of less than 0.2 ns lead to very short drift distances of only $\ell_{eff} \approx 20$ μm. For electric fields too low for a saturated velocity, ℓ_{eff} is even shorter, especially for holes with only 1/3 of the low-field mobility of electrons. Thus, a dramatic degradation of the CCE is expected.

However, recent results have shown that charge collection in highly irradiated detectors is higher than expected from above considerations. This was seen both for the EPI diodes under study in this work [9, 202] as well as for segmented sensors [203]. Probably two different reasons account for this. At high fluences and voltages, this can be explained by CM (see following sections). However, charge collection is also anomalously high at lower fluences and voltages below the expected CM threshold [9, 202, 204]. In particular, the deviation between measured and expected charge is increasing with voltage. This behaviour can be modelled assuming a voltage- [9, 204, 205] or field-dependent [202, 204] τ_{eff} in contrast to the commonly assumed constant trapping times. Possible explanations include a field-dependent capture cross section, field-enhanced detrapping (e.g. phonon-assisted trap-to-band tunnelling [206, 207], Poole-Frenkel effect [208]) or trap filling due to the capture of charge carriers in the presence of high currents (a similar effect as the one leading to a double junction, see above).

12.5   Improving Radiation Hardness

The CERN-RD50 collaboration [209, 210] as well as the tracker collaborations of the experiments at the LHC perform extensive R&D programmes to develop detectors able to survive the harsh radiation environments of the HL-LHC. In the following, some strategies of how to improve the radiation hardness are presented.

12.5.1   Change of Operating Conditions

Some of the effects of radiation damage can be mitigated by changing the operating conditions.

The most prominent example is cooling of the sensors to compensate the radiation-induced increase of the leakage current to limit power consumption and noise (see Eq. 11.11). The Si detectors at the LHC are designed for cooling down to -10°C using fluorocarbons, whereas a CO_2 cooling system is being developed for the HL-LHC, which can achieve lower temperatures down to -20°C [211].

Another important parameter is the applied bias voltage. It needs to be increased if the depletion voltage rises. Moreover, the electric field increases for higher voltage. This increases the drift velocity (if not saturated yet) and hence the effective drift distance of charge carriers before being trapped. Further, as mentioned in Sec. 12.4.3 and shown in the following sections, charge collection is enhanced at high voltages due to charge multiplication (and supposedly also due to a lower trapping probability even below the multiplication regime as mentioned in Sec. 12.4.3). For these reasons, it is desirable to increase the current voltage limit of the LHC trackers of about 600 V, which is, however, difficult with the current plan of re-using the existing support structures. But e.g. the ATLAS Insertable B-Layer (IBL) [212] is designed with a limit of 1000 V.

Further alternative detector-operation concepts include operation under forward bias [213] or at cryogenic temperatures [214].

12.5.2   Choice of Material - Defect Engineering

As described in the last sections, the types and concentrations of existing impurities play an important role in defect generation. Thus, it is very important to understand the underlying microscopic mechanisms of radiation damage in order to tailor the material and its concentration of impurities in such a way that the effect of radiation damage is minimised. This approach is called *defect engineering* and has already proven to be successful in the case of oxygen-rich Si (DOFZ, MCz, EPI), which exhibits a lower increase of depletion voltage with fluence (see Sec. 12.4.2). Thus, DOFZ is used for the innermost layers of the LHC trackers. Furthermore, other strategies like hydrogenation and p-type Si are investigated. However, the leakage current and trapping are not found to depend on the Si material. Thus, also completely different materials like diamond [215] are investigated.

12.5.3   Device Engineering

Radiation hardness of Si detectors can also be improved by device optimisation, i.e. by changing the geometry of the wafer or the electrodes.

For example, sensors with n-type segmentation (n-in-n or n-in-p technology) profit from the fact that electrons, which are less susceptible to trapping due to a higher drift velocity and trapping time constant, drift towards the readout electrode [216, 217].

This is the most important region for signal formation in segmented sensors due to the maximum of the weighting field (see Fig. 11.6), as well as of the electric field (in n-in-n sensors after type inversion). The pixel detectors of ATLAS and CMS are made of n-in-n sensors. Detectors with n-in-p technology are a candidate for large parts of the HL-LHC trackers [218].

In 3D detectors, the readout electrodes are arranged as doped columns penetrating through the thickness of the detector [219, 220]. This decouples the thickness of the sensor, which determines the amount of deposited charge for a MIP (see Sec. 11.2), from the distance between the electrodes, which determines the depletion voltage and maximum drift distance, and hence the susceptibility to trapping. 3D detectors are envisaged for 25% of the ATLAS IBL and are a candidate for the innermost pixel layer at the HL-LHC.

Another option is the use of thin detectors ($d < 300~\mu$m). There are three approaches to produce them: physical thinning of processed FZ and MCz wafers down to 50 μm, deep diffusion of dopants from the backside [190] and epitaxial growing of a thin Si layer (25–150 μm) on a thicker Cz substrate (see Sec. 11.5.3). The latter is used in this work. Using thin detectors reduces the leakage current ($I_{rev} \propto d$) and especially the depletion voltage ($U_{dep} \propto N_{eff} \cdot d^2$) significantly (cf. Sec. 11.3). Furthermore, Si with a higher initial doping concentration $N_{eff,0}$ can be used, which delays the effect of dopant removal and is easier to produce. Another great advantage is the reduced susceptibility to trapping due to the smaller drift distance, the larger weighting field $1/d$ and the larger drift velocity as the average electric field is higher at a given voltage above full depletion ($E \propto U/d$). The latter also enhances charge multiplication. However, for a MIP, there is the drawback that the deposited charge Q_0 is also reduced ($Q_0 \propto d$), which decreases the signal in non- and low-irradiated sensors. But at very high fluences with mean drift distances before trapping of $\ell_{eff} \ll d$, the collected charge in response to MIPs becomes independent of the sensor thickness (see e.g. [220] for a derivation). Another drawback of thin detectors, the increased capacitance ($C \propto A/d$), can be overcome by a smaller sensor-cell size, which is envisaged anyway because of the high hit occupancies at the HL-LHC luminosity.

To conclude, epitaxial detectors as studied in this work combine both the approaches of defect engineering (high oxygen concentration) and device engineering (thin).

Chapter 13

Investigated Devices and Experimental Methods

13.1 Diode Samples

In this work, standard and oxygen-enriched epitaxial pad diodes of three different thicknesses (75, 100 and 150 μm) were studied.

13.1.1 Material

The main parameters of the used materials are listed in Tab. 13.1. The epitaxial layers were grown by ITME [184] on a Cz substrate of about 500 μm thickness. The substrate is highly doped with antimony (Sb, $0.02\,\Omega$cm) in order to provide a good ohmic contact and to prevent it from acting as a sensitive detector region. The crystal orientation of EPI 75 μm is <111>, the one of EPI 100 μm and EPI 150 μm is <100>. The initial doping concentration $N_{eff,0}$ with phosphorus is deliberately chosen to vary between $2.6 \cdot 10^{13}\,\mathrm{cm}^{-3}$ for 75 μm, $1.5 \cdot 10^{13}\,\mathrm{cm}^{-3}$ for 100 μm and $8 \cdot 10^{12}\,\mathrm{cm}^{-3}$ for 150 μm in order to obtain approximately the same initial depletion voltage $U_{dep,0}$ of about 100–150 V for all thicknesses.

Fig. 13.1 shows the oxygen-concentration depth profile obtained from *secondary ion mass spectrometry (SIMS)* measurements performed by [221]. For EPI-ST, it is clearly visible that there is an out-diffusion of oxygen from two sides, mainly from

Material	d [μm]	Wafer	Orientation	$N_{eff,0}$ [P] [10^{12} cm^{-3}]	ρ [Ωcm]	$U_{dep,0}$ [V]	[O] [10^{16} cm^{-3}]	[C] [10^{15} cm^{-3}]
EPI-ST 150	147	261636-13	<100>	8.8	490	145	4.5	<2.8
EPI-DO 150	152	261636-09	<100>	8	538	140	14.0	<1.6
EPI-ST 100	102	261636-05	<100>	15	287	118	5.4	<3.9
EPI-DO 100	99	261636-01	<100>	15	285	113	28.0	<1.7
EPI-ST 75	74	8364-03	<111>	26	165	110	9.3	<1.9
EPI-DO 75	72	8364-07	<111>	26	167	103	60.0	<1.6

Table 13.1: Properties of the used materials (average values).

the Cz substrate, but also from the SiO_2 surface layer. This results in an inhomogeneous distribution with a concentration variation of more than one order of magnitude between the minimum and the maximum. The average concentration increases for decreasing thickness ($4.5 \cdot 10^{16} \, \mathrm{cm}^{-3}$ for 150 μm, $9.3 \cdot 10^{16} \, \mathrm{cm}^{-3}$ for 75 μm) because in a thin layer the ratio of diffusion range (if assumed to be constant) and thickness is larger. Homogeneity and average concentration are largely improved for EPI-DO after oxygenation at 1100°C for 24 h. For these diodes, the average concentration varies between $1.4 \cdot 10^{17} \, \mathrm{cm}^{-3}$ for 150 μm and $6.0 \cdot 10^{17} \, \mathrm{cm}^{-3}$ for 75 μm.

The results for the carbon concentration were found to vary between $1.2 \cdot 10^{15} \, \mathrm{cm}^{-3}$ and $5 \cdot 10^{15} \, \mathrm{cm}^{-3}$ for the different processing procedures, but such small concentrations are expected to be below the detection limit of the SIMS method [222].
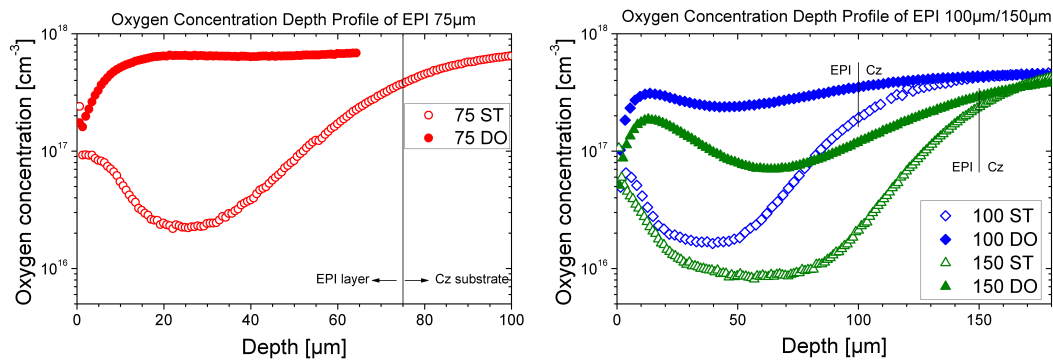
Figure 13.1: Oxygenconcentration depth profiles (SIMS measurements).

13.1.2 Pad Diodes

The diodes were processed by the company CiS [223]. For this work, pad diodes were used, which are displayed in a top-view and side-view sketch in Fig. 13.2. Pad detectors are large simple planar diodes without segmentation, which are easy to produce and handle, so that they are very suitable test structures for material investigations.

The p-n junction is produced by boron implantation that creates a 1 μm thick p^+ layer with a high doping level of about $10^{19} \, \mathrm{cm}^{-3}$ at the front side. The junction is fabricated in such a way that there is one central pad diode in the middle of either $0.5 \times 0.5 \, \mathrm{cm}^2$ or $0.25 \times 0.25 \, \mathrm{cm}^2$ size[1] and a guard-ring structure surrounding it. The guard ring, which has to be kept at the same potential as the pad, has two main functions. On the one hand, it helps keeping the area of the central pad and the electric field well-defined. On the other hand, it shields the pad from surface and edge leakage currents. The guard ring is 100 μm wide with a distance of 10 μm to the pad. Often, there are further smaller potential rings around the main guard ring, which are operated in floating mode to lower the potential difference between the central pad and the edges of the detector.

---

[1]Labelled as *big* and *small*, respectively, in the following.

The metallisation of the front contact is done with aluminium, but leaving a hole of 2 mm diameter in the middle for optical charge-carrier injection. The back side is coated with an aluminium mesh, which also allows optical illumination for other materials that do not have a substrate. The parts of the detector that are not metallised are covered with silicon oxide (SiO_2) for passivation and protection.
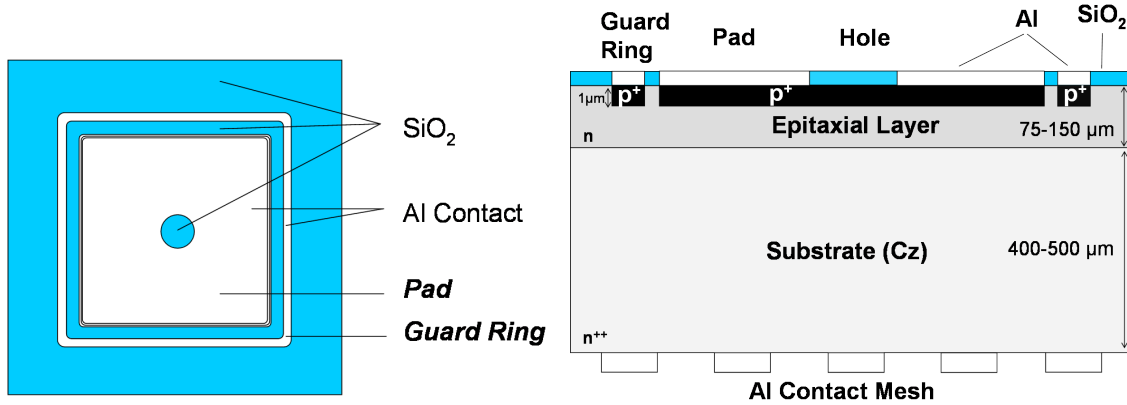
Figure 13.2: Schematic top view *(left)* and cross section *(right)* of the used pad diodes (not to scale).

13.2   Irradiation

In the context of this work, diodes irradiated with 24 GeV protons in an equivalent-fluence range between 10^{14} and 10^{16} cm^{-2} were studied (see Tab. 13.2). The irradiation was performed with the Proton Synchrotron (PS) T7 beam line at the IRRAD-1 irradiation facility at CERN [224, 225]. The samples were mounted on a cardboard slide and transported automatically by a shuttle into the beam. Homogeneous irradiation can be achieved by sweeping the beam at a constant rate over the samples. This results in an average proton flux of about $(3\text{–}9)\cdot10^{9}$ p cm^{-2} s^{-1}. Thus, for high fluences long irradiation times were needed: up to several days for equivalent fluences around 10^{15} cm^{-2} and several weeks for 10^{16} cm^{-2}. As irradiations were performed at about 27 to 29°C, self-annealing effects already during irradiation occur.

The achieved fluences were measured by aluminium activation. One Al foil of 5×5 mm^2 and one of 10×10 mm^2 size were placed together with the samples in the beam and activated by the reactions ^{27}Al(p,3pn)^{24}Na and ^{27}Al(p,3p3n)^{22}Na. The half-lives of ^{24}Na and ^{22}Na are 15 h and 2.6 years, respectively. The intensity of the gamma emission lines of ^{24}Na ($E_\gamma = 1369$ keV) and ^{22}Na ($E_\gamma = 1275$ keV) as measured by a NaI or Ge spectrometer can be used to obtain the activity. This is proportional to the received proton fluence if the time between irradiation and activity measurement is taken into account. The systematic error of the measured fluence is reported to be about 10%. Equivalent-fluence values were obtained using a hardness factor of $\kappa = 0.62$ for the PS 24 GeV proton source.

$\Phi_p[cm^{-2}]$	$\Phi_{eq}[cm^{-2}]$	$\Phi_{eq}[cm^{-2}]$ simplified notation
$4.88 \cdot 10^{14}$	$3.03 \cdot 10^{14}$	$3 \cdot 10^{14}$
$8.94 \cdot 10^{14}$	$5.54 \cdot 10^{14}$	$6 \cdot 10^{14}$
$1.44 \cdot 10^{15}$	$8.93 \cdot 10^{14}$	$9 \cdot 10^{14}$
$1.73 \cdot 10^{15}$	$1.07 \cdot 10^{15}$	$1 \cdot 10^{15}$
$4.40 \cdot 10^{15}$	$2.73 \cdot 10^{15}$	$3 \cdot 10^{15}$
$6.25 \cdot 10^{15}$	$3.88 \cdot 10^{15}$	$4 \cdot 10^{15}$
$1.06 \cdot 10^{16}$	$6.57 \cdot 10^{15}$	$7 \cdot 10^{15}$
$1.71 \cdot 10^{16}$	$1.06 \cdot 10^{16}$	$1 \cdot 10^{16}$

Table 13.2: The denoted proton fluence Φ_p as measured by Al activation, the corresponding equivalent fluence Φ_{eq} using $\kappa = 0.62$ and the simplified notation of the equivalent fluence that will be used in the following for fast reference.

13.3   Annealing Experiments

Isothermal annealing experiments at 80°C were performed to investigate how the radiation damage develops over time. The temperature of 80°C has been chosen in order to speed up the annealing (e.g. for FZ the N_{eff} reverse annealing is accelerated by a factor of 7430 with respect to room temperature, assuming an activation energy of 1.33 eV [163]). At higher temperatures there would be the danger of other annealing reactions that do not occur at room temperature.

For annealing, the test structures were heated up in a circulating-air oven. The temperature stability of the oven was around ±1°C. Between the measurements, the irradiated samples were stored at -25°C to avoid unwanted annealing.

13.4   Overview on the U_{dep} and N_{eff} Behaviour of the Irradiated Diodes

The dependence of I_{rev} and U_{dep} as a function of fluence and annealing time for the diodes studied here was extensively investigated in a previous work [9]. Only the results that are of importance for this thesis are shortly reviewed here.

Fig. 13.3 (*left*) shows the depletion voltage measured with the CV method at room temperature and 10 kHz as a function of annealing time at 80°C for two different fluences. Fluences higher than $4 \cdot 10^{15}$ cm^{-2} could not be measured due to large currents. In the simplified picture of a constant N_{eff}, neglecting effects like double junctions (see Sec. 12.4.2), it shows the typical behaviour of non-type-inverted diodes with a rise in U_{dep} during short-term annealing (dominated by out-annealing of acceptors), a maximum at typically 8 min (slightly later for higher fluences), and a decrease during long-term annealing (dominated by acceptor introduction [194]). However, due to the latter, type-inversion can happen at large annealing times, leading to an increase of

U_{dep} thereafter.

Fig. 13.3 (*right*) displays U_{dep} at 8 min at 80°C annealing, which is believed to represent the stable-damage component. It exhibits donor removal at low fluences and donor introduction at large fluences. A fit according to the Hamburg model (see Eq. 12.8) reveals that the donor introduction rate $-g_C$ is higher for EPI-DO than for EPI-ST at a fixed thickness and higher for 75 μm than for 100 and 150 μm for the same material (probably also due to the higher O concentration in 75 μm diodes). The results are shown in Tab. 13.3.
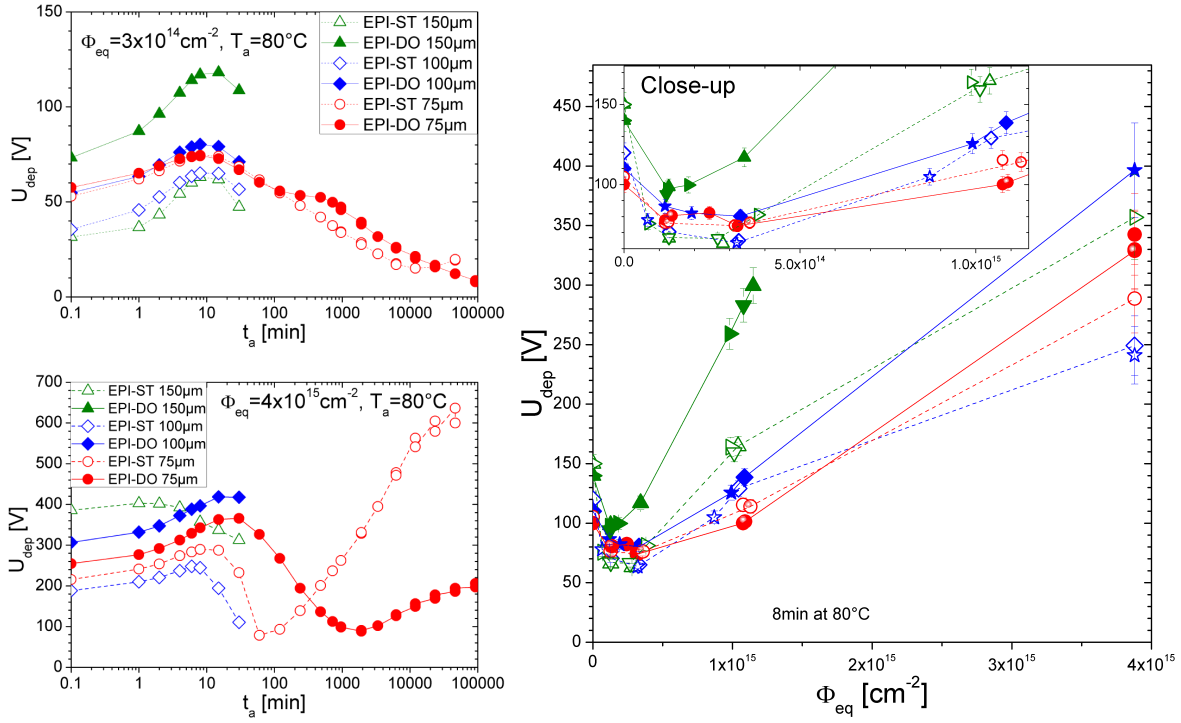
Figure 13.3: *Left:* U_{dep} annealing curves at fluences of $3 \cdot 10^{14}$ cm^{-2} (*top*) and $4 \cdot 10^{15}$ cm^{-2} (*bottom*). *Right:* U_{dep} after 8 min at 80°C annealing. Taken from [9].

Material	$N_{eff,0}$ [10^{12} cm^{-3}]	[O] [10^{16} cm^{-3}]	$N_{C,0}$ [10^{12} cm^{-3}]	c [10^{-14} cm^{-2}]	g_C [10^{-2} cm^{-1}]
ST 150 μm	8.75	4.5	6.4 ± 0.6	2.22 ± 0.85	-0.71 ± 0.07
DO 150 μm	8.17	14	6.6 ± 0.3	0.84 ± 0.06	-1.36 ± 0.04
ST 100 μm	15.00	5.4	8.8 ± 0.7	1.50 ± 0.40	-0.70 ± 0.07
DO 100 μm	15.14	28	9.4 ± 0.7	0.73 ± 0.09	-1.13 ± 0.06
ST 75 μm	25.82	9.3	14.4 ± 1.1	0.78 ± 0.13	-1.52 ± 0.09
DO 75 μm	26.17	60	23.1 ± 2.2	0.32 ± 0.04	-2.08 ± 0.15

Table 13.3: The stable-damage parameters in EPI diodes: removable doping concentration $N_{C,0}$, removal constant c and space-charge introduction rate g_C from a fit according to the Hamburg model (see Eq. 12.8). The initial doping concentration $N_{eff,0}$ and average oxygen concentration [O] are also displayed. Taken from [9].

13.5   Transient-Current Technique and Charge-Collection Measurements

In this thesis, charge collection in highly-irradiated silicon diodes is studied in response to laser light of different wavelengths as well as to alpha and beta particles. The measurements were performed with different methods: either with the transient-current technique, which measures the instantaneous signal current due to the drifting charge carriers (the collected charge is then obtained in an offline analysis as integral over the current pulse), or with a low-noise shaping readout, which measures only the integrated charge.

13.5.1   Penetration of Different Types of Radiation

Various types of electromagnetic and ionising radiation with different penetration properties were used. The general charge-deposition mechanisms are explained in Sec. 11.4.1. The initial distributions of deposited e-h pairs as a function of detector depth measured from the p^+n junction at the front side are shown in Fig. 13.4. As mentioned above, for the epitaxial diodes used in this work, only front illumination is possible for low-penetrating radiation due to the thick insensitive Cz substrate at the back side.

On average, MIPs deposit charge uniformly over the whole detector depth. Thus, the current signal is due to both electrons and holes drifting to the respective electrodes. Such a penetration can be mimicked by 1060 nm laser light as its attenuation length [226] of about 1 mm at room temperature exceeds by far the detector thickness.

In contrast, red laser light of 660 or 670 nm wavelength has a short attenuation length of ≈ 3 μm at room temperature. Thus, charge carriers are produced close to the illuminated surface. For front illumination of n-type material (i.e. from the junction side) as used in this work, the current signal is almost entirely due to the drift of electrons towards the back side.

The penetration of 830 nm laser light with an attenuation length of ≈ 13 μm at room temperature lies in between.

For lower temperatures, the attenuation length increases.

As explained in Sec. 11.4.1, 5.8 MeV α particles from a ^{244}Cm source feature a Bragg peak about 26 μm deep inside the detector for perpendicular incidence. The penetration as shown in Fig. 13.4 was simulated with SRIM [227], taking energy loss before the sensitive layer in 2 mm air, 100 nm SiO_2 and 1 μm p^+ implantation into account. Polyethylene (PE) absorbers of different thicknesses (12 and 24 μm) can be inserted between the source and the sample in order to deliberately modify the penetration and shift the Bragg peak closer to the surface. However, there is also unintended reduction of effective penetration depth for part of the beam due to about 50° divergence allowed by the collimator (see below). Moreover, single α particles with lower energy ($\approx 5\%$ of the beam) were observed in measurements, possibly caused by
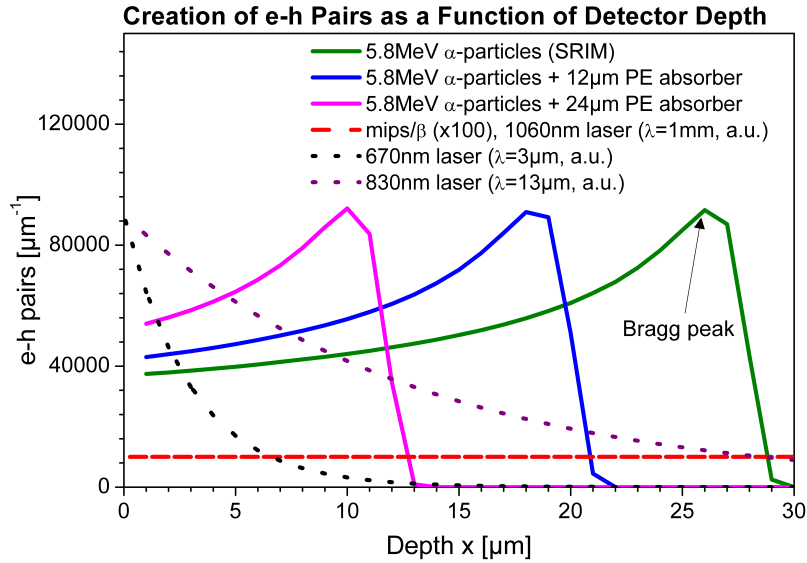
Figure 13.4: Distribution of initially created e-h pairs in Si as a function of detector depth for different types of radiation (MIPs/β particles; α particles with different PE absorbers; 670, 830 and 1060 nm laser light). The normalisation of the laser-induced e-h pairs is arbitrary, it depends on the energy and focus of the laser pulse.

energy loss at the edge of the plastic collimator. These two effects were not taken into account in the simulation.

13.5.2   Transient-Current Technique

Basic Principle

With the Transient-Current Technique (TCT), the induced current due to the drift of free charge carriers according to Eqs. 11.13 and 11.14 is directly measured. Any current distortion needs to be minimised. This requires the use of fast, high-bandwidth electronics, e.g. a current-sensitive amplifier (if at all) and the minimisation of filtering elements. This method allows a deep insight into the signal formation in the sensor, in particular into the electric field and trapping. Such investigations for the diodes studied here were performed and described in detail in a previous work [9]. In this thesis, however, TCT was mainly used to study the amount of collected charge Q, which was obtained in an offline analysis as the integral over the TCT current pulse (see Fig. 13.5). Typically, an integration window of about 10 ns was used. The charge-collection efficiency can then be obtained by normalising the measured charge Q in an irradiated detector by the charge Q_0 in an unirradiated reference detector (see Eq. 11.17) if the amount of deposited charge is well-reproducible.
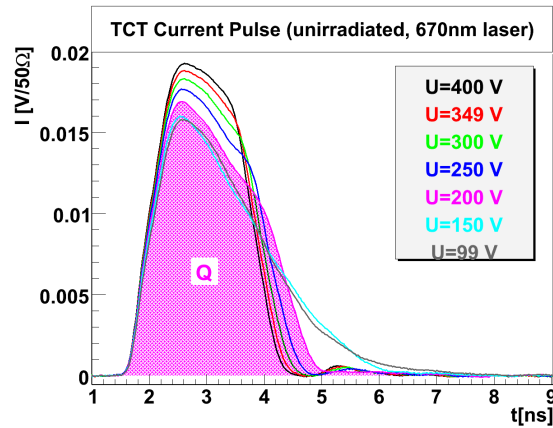
Figure 13.5: TCT current pulses in an unirradiated EPI-ST-150 μm diode in response to red laser light at different applied voltages. The integral corresponds to the collected charge Q.

TCT Setups

The TCT setups at the Detector Lab of the University of Hamburg are sketched in Fig. 13.6. The readout was very similar for all TCT measurements, but the detector mounting was different for TCT with α particles and laser light.

In the case of α particles, the diode was mounted in a brass box with metal bars surrounding it at each side to fix it at a well-defined position (see Fig. 13.6, *bottom left*). It was biased and the signal was read out at the p^+ front side via a small needle on a cantilever spring. The back side was kept at ground level. The ^{244}Cm-α source was in the middle of the plastic lid, which served also as a collimator allowing about 50° beam divergence. The lid was put on the box during the measurements, so that the source was about 2 mm above the injection hole of the diode. A Keithley 6517A served as a voltage source up to 1000 V and simultaneously as a current meter. A low-pass filter box was used to cut off the high-frequency noise of the voltage source. A Picosecond Pulse Lab 5531 bias-T was employed to decouple the voltage source from the input of a current-sensitive amplifier (Phillips Scientific Model 6954 with a gain of 10 or 100 and a bandwidth of 1.8 GHz or 1.5 GHz, respectively). This was connected to a Tektronix DPO 4104 oscilloscope with 1 GHz bandwidth and 5 GS/s. The temperature was measured with a Pt 100 sensor in combination with a Keithley 2001. The emission of α particles occurred randomly, so that self-triggering was needed. The trigger level was set to 8 or 80 mV for an amplifier gain of 10 or 100, respectively, to be above the noise level and trigger on the signal only. In the offline analysis of the data, the voltage drop at the resistors in the filter box and bias-T was taken into account. The advantage of charge deposited by α particles is the good reproducibility due to the mono-energetic spectrum, which allows the measurement of the CCE using a reference detector. The SRIM simulation mentioned above predicts a deposited charge inside the sensitive region of 5.5 MeV corresponding to $1.5 \cdot 10^6$ e-h pairs, taking energy loss in the 2 mm air gap, 100 nm SiO_2 and 1 μm p^+ implantation into account. The measured average charge was about 15% lower due to a small fraction of pulses
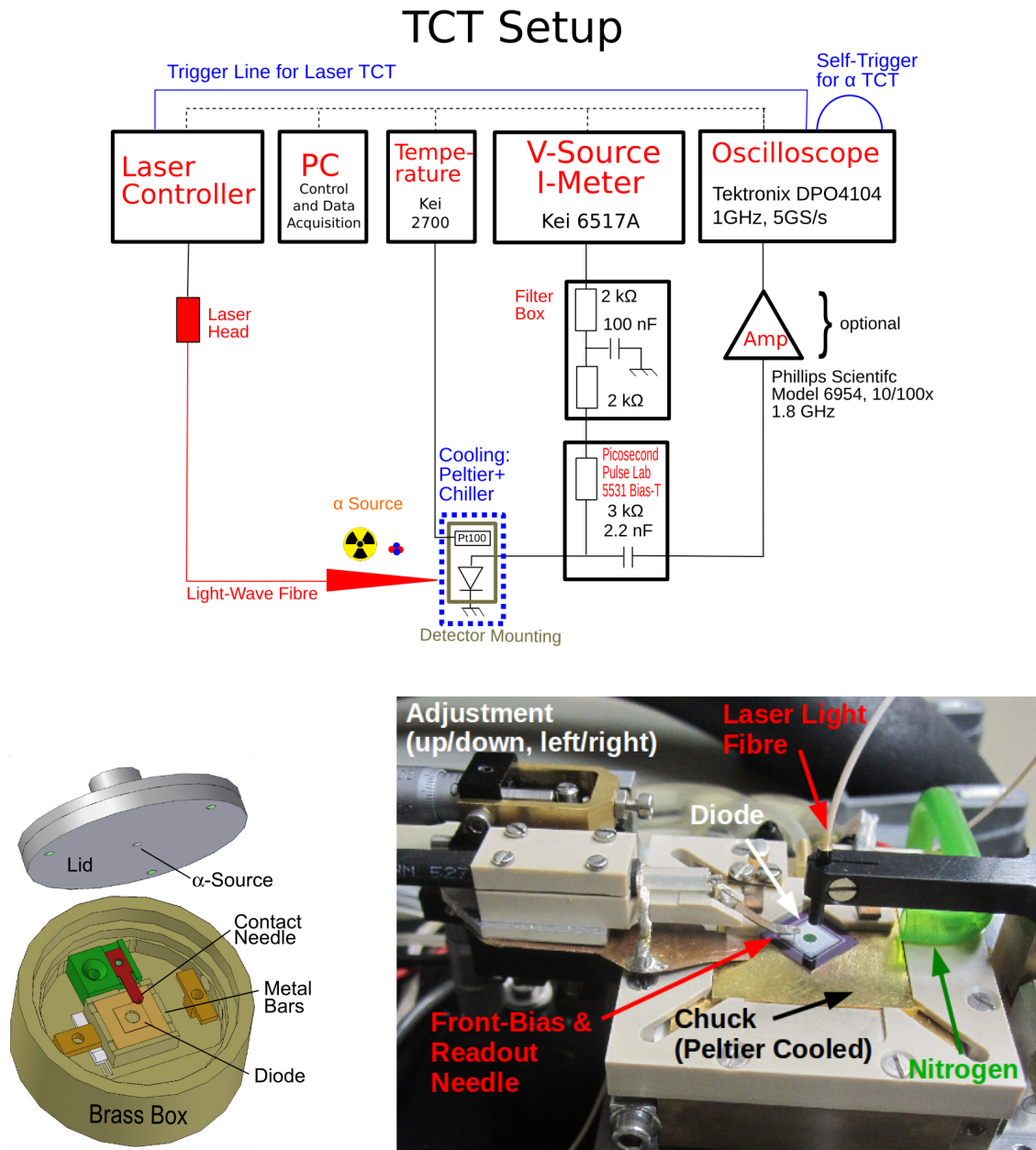
Figure 13.6: The TCT setups. *Top:* Basic principle of the TCT setups including readout chain. *Bottom:* Detector mounting for the setup with α particles (*left*) and laser light (*right*).

with significantly lower signal, probably due to additional unwanted absorption (see Sec. 13.5.1). Optionally, polyethylene (PE) absorbers of 12 and 24 μm thickness could be inserted, which deliberately enhanced the energy loss. A CCE precision of 3% was estimated from reproducibility studies involving demounting and mounting and from varying the integration time window.

In the case of laser light (see Fig. 13.6, *right*), the diode was fixed on a chuck with customisable plastic bars and vacuum at a well-defined position. The light was guided

via an optical fibre from the laser head to the illumination window without additional focussing to avoid high charge-carrier densities. The repetition rate was chosen to be 50 Hz and triggering was provided externally by the laser driver. The readout was basically the same as in the case of α particles. Optionally, the bias voltage could be also applied at the back side of the detector, allowing a readout at the front side without a bias-T. The difference was found to be negligible.

For 670 and 1060 nm light, lasers from Advanced Laser Systems with a pulse width below 100 ps (FWHM) were used. The laser intensity was tunable both with the laser driver and with additional optical attenuators, so that $(0.8$ to $50){\cdot}10^6$ e-h pairs could be produced in the diode with the 670 nm laser with about $1.8{\cdot}10^6$ e-h pairs chosen as standard. For 1060 nm laser light, the deposited charge depends on the diode thickness and temperature, but usually not more than a few 10^6 e-h pairs were produced. For 830 nm light, a laser diode was driven with a pulse generator and delivered light pulses of about 1 ns duration, which produced about $4.5{\cdot}10^6$ e-h pairs.

Another setup developed for multi-channel TCT was used in order to perform x-y scans over the illumination window in the front surface. This setup is described in more detail in [172]. The light of a 660 nm Picoquant laser with less than 100 ps pulse width (FWHM) and 1 kHz repetition rate was focused to a measured spot size of $\sigma_{spot}{=}20$ μm. Only $6{\cdot}10^5$ e-h pairs were injected to avoid effects of high charge-carrier densities. The sample was movable on x- and y-tables with 0.1 μm precision. Front-side readout as explained for the above setups was applied with a Tektronix DPO 7254 oscilloscope with 2.5 GHz bandwidth and 40 GS/s.

In contrast to earlier measurements presented in [9], the reproducibility of a charge measurement when demounting and mounting again was greatly improved with the help of the new mounting system and new stable lasers. After a laser-warming time of about 3 h, a reproducibility of about 2% was achieved. Thus, it was possible to perform CCE measurements with this precision.

To all setups, cooling could be applied either by a chiller with a temperature precision of around 0.3°C or by a chiller in combination with a Peltier element, which improved the precision to better than 0.1°C. If not stated otherwise, the measurements were done at -10°C in a nitrogen atmosphere in order to reduce the high leakage current and operate the diode under LHC conditions.

The noise can be largely reduced by averaging a large number of current pulses. This was always done for 512 pulses in the following, unless denoted otherwise.

The guard ring was not connected during these measurements.

13.5.3 Setup for Charge-Collection Measurements with β Particles and Low-Noise Charge Readout

In a real (HL-)LHC experiment, the signal is typically created by MIPs, which induce charge of about 5–20 ke for 75–300 μm thick sensors. This needs to be measured with a low-noise charge readout using a shaper (see Sec. 11.4.5). Thus, to study the
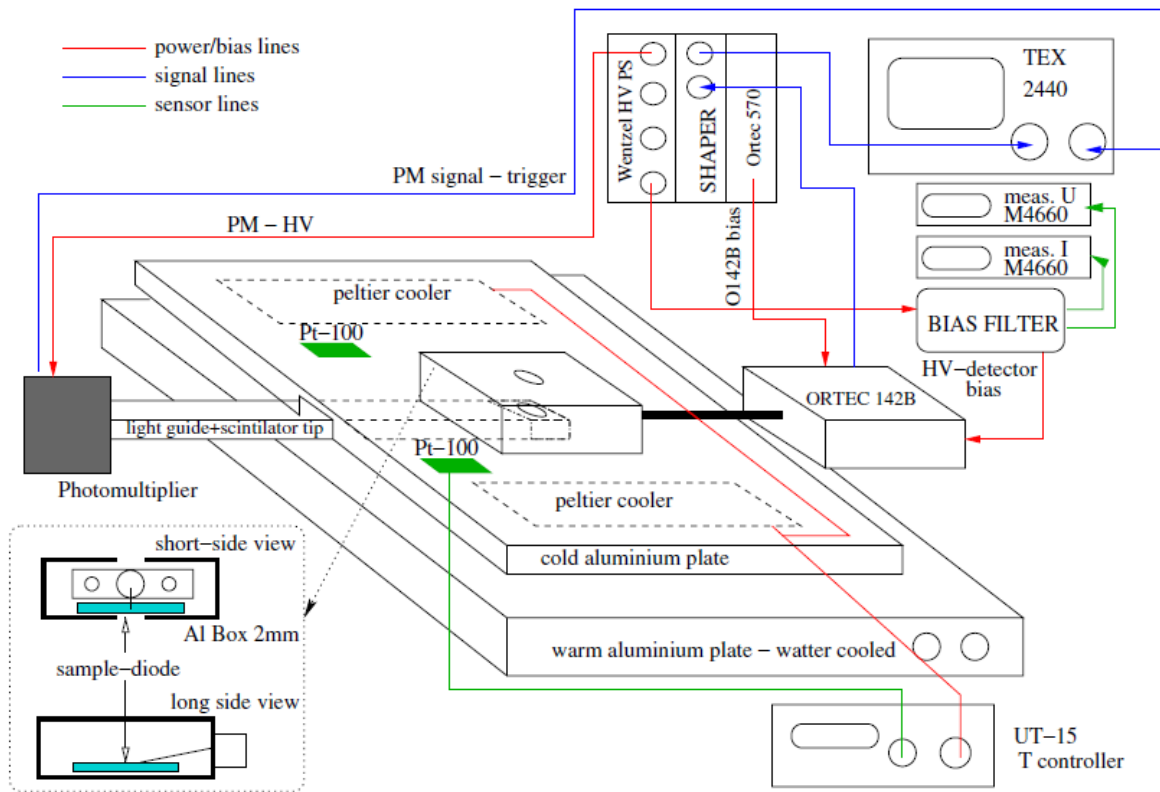
Figure 13.7: Sketch of the charge-collection setup for β particles with low-noise charge readout. Taken from [228].

sensor signal under more realistic conditions and to obtain absolute charge values in response to MIP-like particles, measurements with fast β particles using a charge-sensitive preamplifier connected to a shaping amplifier were performed.

For these measurements, the β setup of the Jožef Stefan Institute was used. It is described in [228] and a short overview is given in the following.

A radioactive 3.7 MBq ^{90}Sr source was employed. ^{90}Sr undergoes β decay with a half life of 29 a to ^{90}Y [19]. ^{90}Y in turn is also a β source with a half life of 2.7 d. The emitted β particles of ^{90}Sr and ^{90}Y have a typical continuous three-body energy spectrum with maximum energies of 0.5 MeV and 2.3 MeV, respectively. Whereas electrons with the highest energies can be considered as good representatives of a MIP, the lower-energetic part of the spectrum is highly-ionising and needs to be filtered out using a trigger as explained below.

A sketch of the setup is shown in Fig. 13.7. The diodes were mounted in an Al box, which was placed on an Al support plate. Cooling down to about -29°C could be provided by Peltier elements in combination with water cooling with a precision of about 0.1°C. Small holes of about 2 mm diameter in the lid and bottom of the box and in the support plate served as a collimator for the β particles. A plastic scintillator in combination with a photomultiplier under the cold plate provided a trigger with a high purity of $> 97\%$. This enabled measurements also at low signal-to-noise ratios of the

silicon detector, even below 1. Most of the unwanted lower-energetic particles of the β spectrum were stopped or substantially decelerated in the silicon material, thereby failing the trigger threshold. An effective trigger rate of about 30–50 Hz was obtained. The signal pulse was sent to a charge-sensitive Ortec 142B preamplifier and a custom-made shaping amplifier with 25 ns peaking time, corresponding to the design LHC bunch-crossing time. Finally, the shaped signal was recorded by a digital oscilloscope (Tektronix 2440) and analysed offline. At least 2500 signals were measured for each data point, for low SNR up to 7500 signals. The pulse-height-to-charge calibration was performed with 59.5 keV photons from an ^{241}Am source using an unirradiated diode.

Examples of measured single waveforms of an unirradiated big EPI-ST 150 μm diode are shown in Fig. 13.8 (*top*). The signal is at about $t = 50$ ns. It is overlaid with noise. However, it can be seen that after averaging, the SNR is greatly improved (*middle*). By this, the signal remains well determinable even after strong irradiation with much lower SNR of the single waveforms. The signal spectrum (*bottom*) is obtained from the height of the single waveforms at the position of the maximum of the averaged waveform. It is fitted with a convolution of a Landau function with a Gaussian as defined in ROOT [229]. The Gaussian accounts for both the noise and the fact that the real straggling distributions are only approximated by a Landau function [19]. The small peak of the signal spectrum at 0 is due to trigger impurities. The noise spectrum is sampled on the part of the acquired waveform before arrival of the trigger ($t = -100$ ns) after common mode correction. It is fitted with a Gaussian.

An occasional problem during measurements with both the TCT and the β-particle setup were microdischarges (see Sec. 11.4.6). They sometimes occurred at high voltages of both irradiated and unirradiated diodes. The occurrence and frequency were not reproducible. In the case of external triggering, the microdischarges interfered with the signal only in extreme cases. In the case of TCT with α particles relying on self-triggering, however, microdischarges could produce signals above the trigger threshold and in case of a high discharge rate, no measurements were possible.
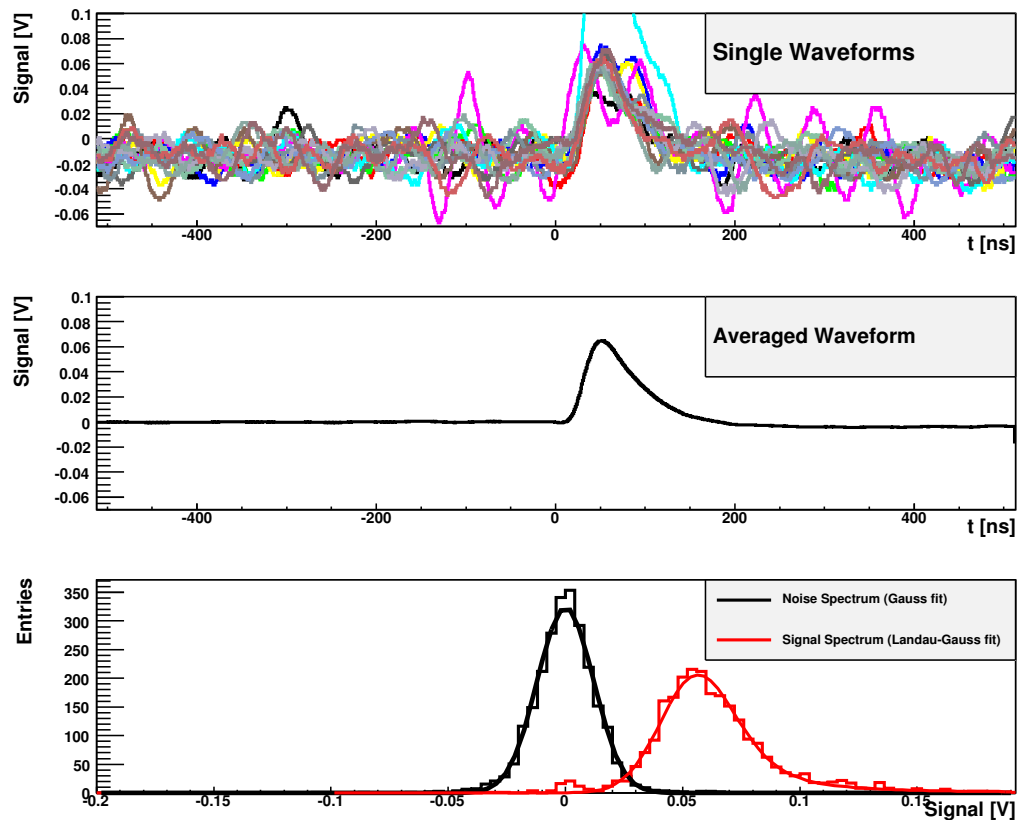
Figure 13.8: Measurement of an unirradiated big EPI-ST 150 μm diode with the setup for β particles: Measured single (*top*) and averaged waveforms (*middle*) as well as noise and signal spectrum (*bottom*) with fits using a Gauss and Landau-Gauss function, respectively.

Chapter 14

Results - Charge Multiplication in Irradiated Silicon Detectors

The results of the charge-collection measurements in proton-irradiated epitaxial diodes with a TCT setup and with a setup using β particles are presented in Secs. 14.1 and 14.2, respectively. The investigations focus on the novel effect of charge multiplication (CM) after heavy irradiation. Thus, typically diodes at the highest available fluence of 10^{16} cm^{-2} are studied as they exhibit pronounced CM effects. For investigations of general properties of CM (i.e. independent of material and thickness), typically a big diode of this fluence and of n-type EPI-ST 75 μm material is taken, labelled ST75-1E16 in the following. If not denoted otherwise, the measurements were done after 30 min annealing at 80°C in order to be at a well-defined point beyond the short-term annealing and where possible self-annealing effects during irradiation can be neglected. The TCT measurements were usually performed at -10°C, the ones with the β setup at -29°C, if not denoted otherwise.

14.1   Measurements with the TCT Setup

Parts of the results obtained with the TCT setup are published in [230, 231]. The following sections include material from there with some adaptations and extensions.

14.1.1   Formation and Location of the CM Region

Charge multiplication in epitaxial diodes was first observed in charge-collection efficiency (CCE) measurements with α particles [9]. Repeating this measurement with radiation of different penetrating properties (see Sec. 13.5.1) can give valuable indications concerning the formation and localisation of the CM region with respect to the detector depth.

Fig. 14.1 shows the CCE as a function of bias voltage for ST75-1E16 measured with 670, 830 and 1060 nm laser light, as well as with α particles with 12 and 24 μm

191
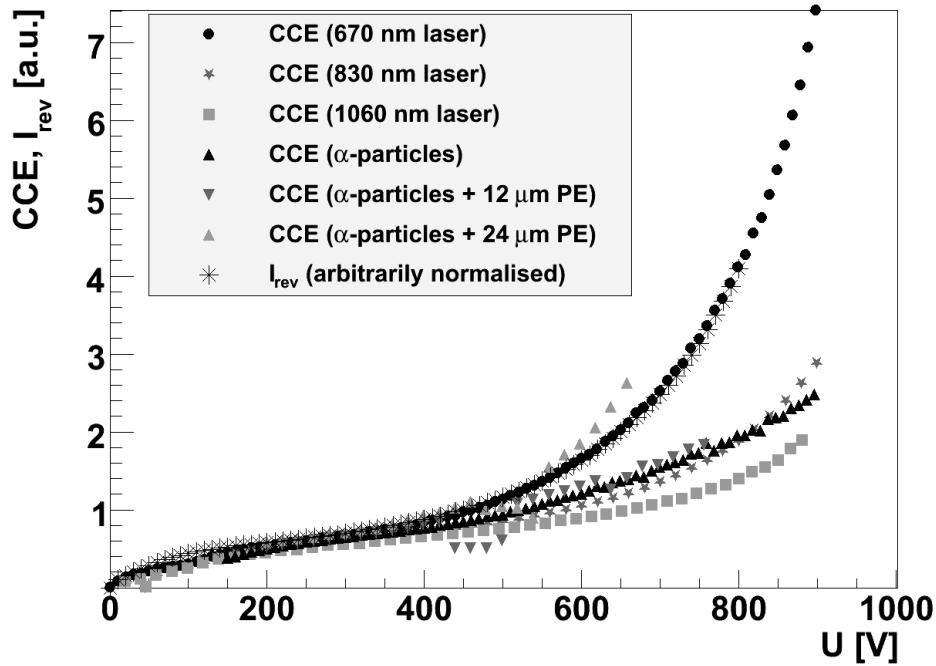
Figure 14.1: The CCE as a function of bias voltage in 75-1E16 measured with different types of radiation and I_{rev} (arbitrarily normalised).

thick PE absorber and without. The self-triggered measurements with α particles with 12 and 24 μm absorber gave sometimes low values in certain voltage ranges due to suddenly occurring microdischarges. Also the voltage dependence of the reverse current (obtained from a dedicated IV measurement with connected guard ring) is added for comparison (arbitrary units).

At high voltages, the CCE of all types of radiation increases strongly and eventually exceeds unity, clearly indicating CM. Also the reverse current does not saturate, but rises strongly due to CM, similarly to the curve for 670 nm laser light. However, there are large differences in the increase rate between the different radiation types. It can be seen that at high voltages, the CCE of 670 nm laser light and α particles with 24 μm absorber is highest, followed by α particles with 12 μm absorber and without absorber and by 830 nm laser light. The lowest CCE, but still exceeding 1, was measured for 1060 nm laser light. To conclude, the CM depends on the position where the e-h pairs have been initially deposited: The closer the charge carriers have been produced to the p$^+$ implant at the front surface, the stronger the CM.

The following simplified considerations on the formation of the radiation-induced CM region show that this is what one would expect because the high-field region in non-type-inverted p$^+$n diodes is located at the front surface. For a first rough estimation, a linear field dependence with a depletion voltage of 750 V due to uniform radiation-induced space charge is assumed. Unfortunately, U_{dep} could not be directly measured for this sample due to high leakage currents, but needed to be extrapolated from measurements of the stable damage parameters in lower irradiated diodes after
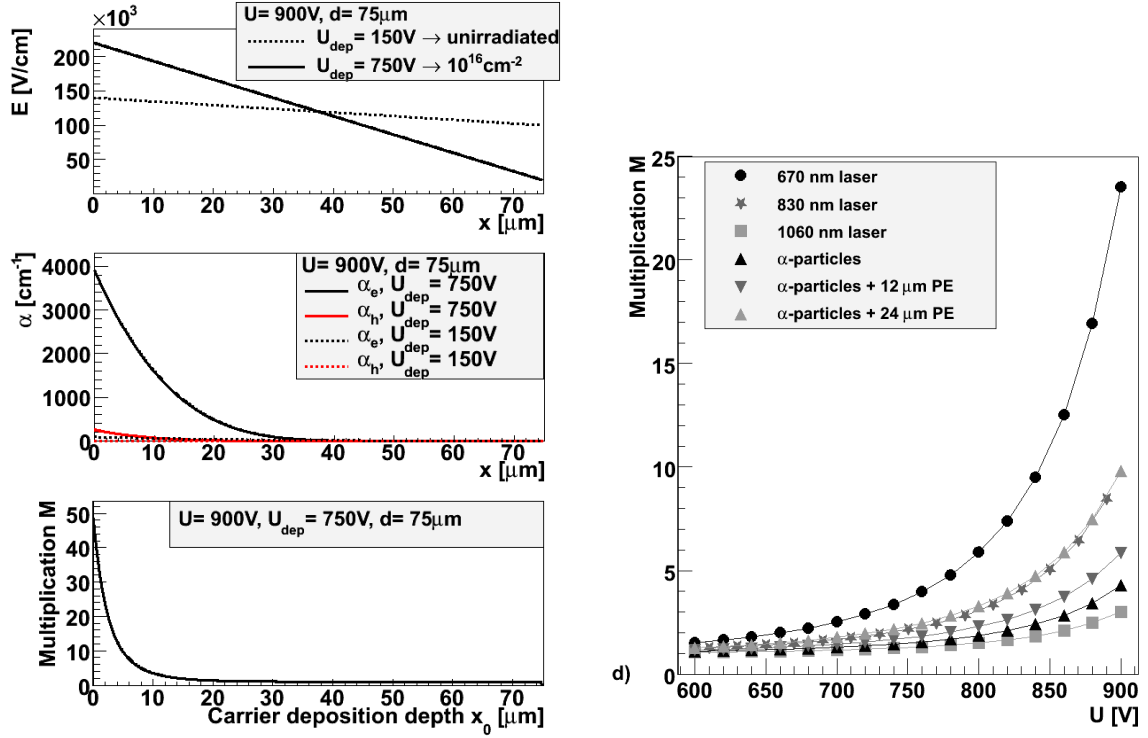
Figure 14.2: Qualitative explanation for the development of a radiation-induced CM region. *Top left:* Electric-field distribution $E(x)$ in the linear model for an unirradiated 75 μm diode and for ST75-1e16 at 900 V. *Middle left:* The corresponding distributions for the ionisation coefficients $\alpha_e(x)$, $\alpha_h(x)$ at room temperature[1] [175] (see Fig. 11.7). *Bottom left:* The resulting multiplication M as a function of deposition depth x_0. *Right:* M for different types of radiation as a function of bias voltage.

8 min annealing at 80°C (see Sec. 13.4). Also the assumption of a linear electric-field dependence is only a rough approximation in highly-irradiated diodes as the high level of reverse current modifies the electric-field distribution by changing the space charge and leading to a voltage drop over the neutral bulk region, which becomes highly-resistive after irradiation (see Sec. 12.4.2). Double peak electric-field structures have been observed in 150 μm thick EPI diodes irradiated with fluences around 10^{15} cm^{-2} [9].

Neglecting this, Fig. 14.2 (*top left*) shows the assumed field at 900 V compared to the one of an unirradiated diode with $U_{dep} = 150$ V. The maximum of E at the front side is higher for ST75-1E16 than for the unirradiated case. As the ionisation coefficient $\alpha(E)$ is a strong function of the electric field (see Sec. 11.4.4), such a difference in E leads to considerable values[2] of α_e for electrons in ST75-1E16 in a 30 μm thick layer (Fig. 14.2, *middle left*). In contrast, α_h for holes in ST75-1E16 is much less and the α-values in

---

[1]Room temperature is chosen because the temperature dependence in [175] is only measured for $T > 22$°C. If extrapolations to the measurement temperature of -10°C are done, $\alpha_{e,h}$ are about 40% higher. M for 670 nm laser light would be about twice as high at 900 V.

[2]As already mentioned in Sec. 11.4.4, different parametrisations of $\alpha(E)$ [175, 177–179] vary significantly. However, all but [179] eventually clearly predict charge multiplication ($M > 1$) similarly to the parametrisation chosen here.

the unirradiated case both for electrons and holes are basically 0. The consequences of such a distribution of α_e for CM is shown in Fig. 14.2 (*bottom left*) where the multiplication factor (or gain) $M(x_0)$ is displayed (neglecting hole multiplication, see Eq. 11.21). $M(x_0)$ gives the number of collected charge carriers in the absence of trapping for one e-h pair that has been initially deposited at x_0. It can be seen that considerable values of $M \gg 1$ arise in a thin, approximately 10 μm thick layer at the front side. If $M(x_0)$ is convoluted with the respective distributions of deposited charge from Fig. 13.4, multiplication factors for the different kinds of radiation can be calculated, which is shown in Fig. 14.2 (*right*) as a function of voltage. It is obvious that for a realistic calculation of the CCE, trapping effects and a parametrisation of $\alpha_{e,h}$ as a function of temperature have to be included. But if Fig. 14.2 (*right*) is qualitatively compared to the CCE measurements in Fig. 14.1, one can see that the order of the curves for different laser-light wavelengths is well-reproduced, as well as the order of the curves for α particles with different absorbers. Only when cross-comparing the curves for laser light and α particles, inconsistencies occur as the curves for α particles are measured to be higher than simulated compared to the laser curves. This can be explained by the components of the α beam with effectively shallower penetration due to its divergence or low-energy component (cf. Section 13.5.1). They undergo stronger multiplication, which is not taken into account for the calculation of M. Moreover, the calculated curves might look different if trapping is taken into account as also the effect of trapping depends on the distribution of deposited charge carriers.

A more detailed simulation for 660 nm laser light and the linear-field model from above, including trapping effects and the contribution of hole multiplication, can be found in [172]. Also there, the different parametrisations for $\alpha_{e,h}$ [175, 177–179] lead to largely different predictions. Although all describe the general trend of a CCE increasing with voltage, none of them match the shape and normalisation of the data. For more realistic simulations, a better description of the electric field and the trapping (possibly field or voltage dependent) is required. A simulation developed for n-in-p strip detectors including double-junction effects (see Sec. 12.4.2) predicts a quenching of CM at high voltages due to a negative feedback of the multiplied reverse current on the maximum electric-field value [232]. More insights into the electric-field distribution might be experimentally derived from the newly developed method of Edge-TCT [233].

As the effect of CM is largest for 670 nm laser light due to its shallow penetration, the CM properties are best studied with this type of radiation, so that most of the following measurements were performed with it.

14.1.2   Charge-Multiplication Dependence on Fluence, Material and Thickness

Fig. 14.3 shows the CCE as a function of voltage measured with 670 nm laser light for different fluences in all available materials (ST, DO) and thicknesses (75, 100 and 150 μm). These measurements with 670 nm laser light are more sensitive to CM effects than previous ones with α particles [9] due to the shallower penetration (see last section).

Fluence Dependence

It can be seen that at low voltages (e.g. 200 V), the CCE is trapping dominated: it decreases significantly with increasing fluence. The CCE for fluences up to 10^{15} cm^{-2} seems to saturate at high voltages, at least up to the voltages where measurements were still possible (at higher voltages, microdischarges or large currents prevented to measure further). In contrast, from $4 \cdot 10^{15}$ cm^{-2} on, the CCE increases strongly at high voltages (in some cases after a previous saturating behaviour) and exceeds unity for all materials and thicknesses. This indicates clearly that CM overcompensates trapping in this regime.

From the discussion in the last section, it is expected that CM occurs only in highly-irradiated diodes where the space charge is high enough to create a large electric field at the junction. However, once CM has set in at a certain fluence, the further fluence dependence is not so clear anymore. Whereas in 75 and 100 μm detectors, the CCE in the CM regime of $7 \cdot 10^{15}$ cm^{-2} and 10^{16} cm^{-2} is always significantly higher than the CCE of $4 \cdot 10^{15}$ cm^{-2}, the situation is different in the 150 μm detectors, with $4 \cdot 10^{15}$ cm^{-2} in EPI-DO 150 μm exhibiting the highest CCE. But also in 75 and 100 μm detectors, the CCE of $7 \cdot 10^{15}$ cm^{-2} is always higher than the one of 10^{16} cm^{-2} at very high voltages, although at intermediate voltages, the CCE of 10^{16} cm^{-2} is temporarily highest in DO. To understand this complicated behaviour, one has to take trapping effects into account, which increase with fluence and compete with CM. Moreover, it is also mandatory to have a detailed knowledge of the electric field and its dependence on voltage and fluence. As discussed in Sec. 12.4.2, the electric field depends on the level of reverse current, which increases with fluence. Simulations for n-in-p strip detectors including these two effects predict indeed a maximum of collected charge at a certain fluence (between 10^{15} and $5 \cdot 10^{15}$ cm^{-2}) for a fixed voltage [234].

Material Dependence

Already from Fig. 14.3, the dependence of CM on the material and thickness of the devices is clearly visible. To facilitate the comparison, Fig. 14.4 (*top*) shows the CCE as a function of bias voltage for different materials and thicknesses at a fixed fluence of 10^{16} cm^{-2} measured with 670 nm laser light. For a fluence of $7 \cdot 10^{15}$ cm^{-2}, the same material and thickness dependence is found.

In the CM regime, the CCE of DO material is observed to be higher than the CCE of ST material with the same thickness. The ratio between the CCE of DO and ST material for the same thickness is shown in Fig. 14.4 (*bottom left*). It increases similarly for all thicknesses from values below 1 at low voltages to around 2.5 at high voltages. This can be explained by a higher donor-introduction rate for DO material compared to ST material as discussed in Sec. 13.4, which leads to higher space-charge densities and therefore higher maximum field values at the p-n junction. Probably also the different distributions of oxygen concentration over the detector depth affect the space charge and consequently the field distribution.
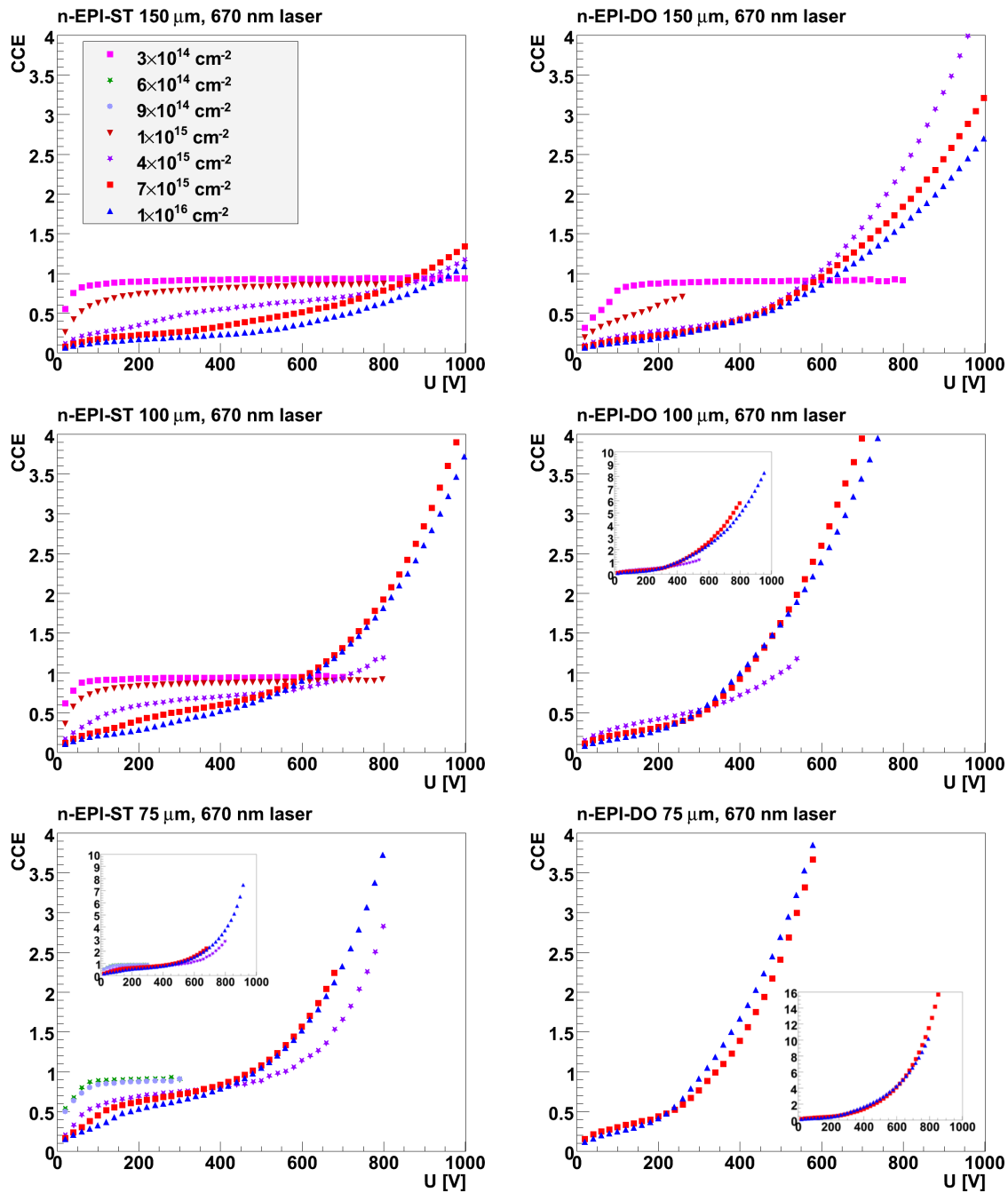
Figure 14.3: The CCE measured with 670 nm laser light as a function of bias voltage for different fluences in all available materials (ST *left*, DO *right*) and thicknesses (150 μm *top*, 100 μm *middle*, 75 μm *bottom*). Not for all fluences in the legend, a measurement was done in diodes of all materials and thicknesses. Where necessary, a plot with an extended CCE axis over the whole measured range is added.
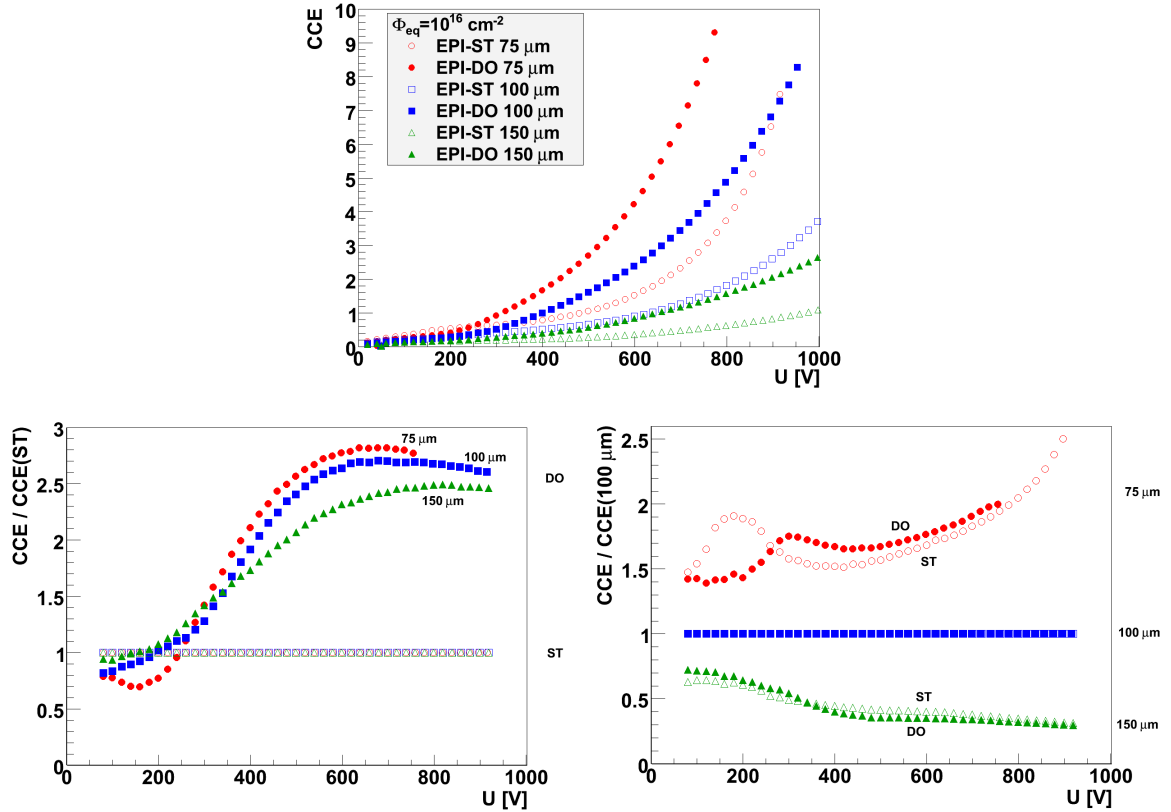
Figure 14.4: *Top:* The CCE as a function of bias voltage for different materials and thicknesses at a fluence of $\Phi_{eq} = 10^{16}$ cm^{-2} measured with 670 nm laser light. *Bottom:* The CCE normalised to the CCE of ST material with the same thickness (*left*) and to the CCE of 100 μm for the same material (*right*).

Thickness Dependence

The CCE of thinner diodes is found to be higher than the CCE of thicker samples for the same Si material. This can be seen easiest from Fig. 14.4 (*bottom right*), which shows the CCE normalised to the CCE of the respective 100 μm detector of the same material.

However, not the whole difference can be attributed to a difference in CM. Also the strong trapping in combination with the different weighting fields $1/d$ must be taken into account. Assuming for simplicity that all charge carriers are created and multiplied with M at the junction (x=0) and trapped after the mean drift distance $\ell_{eff} \approx 20$ μm $\ll d$ for all thicknesses d studied[3], the CCE is given by $CCE = M \cdot \ell_{eff}/d$. Considering the thickness ratio only, one would expect CCE(75 μm)/CCE(100 μm)=1.33 and CCE(150 μm)/CCE(100 μm)=0.66. However, e.g. at 600 V the measured CCE ratios are 1.7 and 0.37, respectively, and the difference between the thickness ratio and the actually measured CCE ratio increases with voltage. This suggests that M is higher

---

[3]Assuming a constant drift with the saturation velocity and a constant trapping time of 0.2 ns (see Sec. 12.4.3).

for thinner diodes. However, some care is needed to explain this effect. The simple expectation that electric fields are higher in thinner sensors at the same applied voltage is only valid if the field extends over the whole sensor thickness. Below full depletion, the electric-field distribution $E(x)$ in the linear model does not depend on the thickness, but only on the space-charge density (see Fig. 11.5). In fact, none of the extrapolated depletion voltages of the diodes studied here is below 600 V. But modifications to the linear field like double peak and voltage drop over the neutral bulk region are expected to lead to non-zero field values over the entire diode thickness far below the nominal depletion voltage. Moreover, in the case of 75 μm diodes, another reason for higher maximum fields could be the higher donor-introduction rate than in thicker materials (see Sec. 13.4), which is probably due to the larger average oxygen concentration. However, in the case of 100 and 150 μm diodes, the donor-introduction-rates were found to be very similar.

14.1.3　Annealing Behaviour
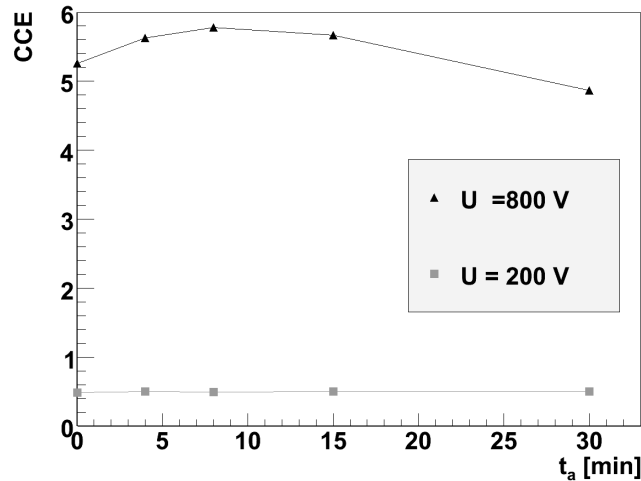
Figure 14.5: The CCE at 200 and 800 V as a function of annealing time t_a for a small EPI-ST 75 μm diode at 10^{16} cm^{-2}. Annealing was performed at 80°C and CCE measured with 670 nm laser light.

The annealing behaviour at 80°C of CCE in the CM regime was studied using 670 nm laser light for EPI-ST diodes of 75 μm and 100 μm thickness and fluences of 6 or $7 \cdot 10^{15}$ cm^{-2} and 10^{16} cm^{-2}. They all show such a characteristic behaviour as displayed in Fig. 14.5 for the example of EPI-ST 75 μm at 10^{16} cm^{-2}. In the CM regime, e.g. at 800 V, the CCE increases from its value as irradiated up to a maximum at 8 min before it decreases again. This is exactly the same behaviour as observed for the annealing of U_{dep} and the space-charge density (see Sec. 13.4), at least at lower fluences of up to $4 \cdot 10^{15}$ cm^{-2}, where CV measurements at room temperature were still possible. This shows again that CM and its underlying high electric fields are closely connected to the space charge which is built up during irradiation and altered

during annealing. The annealing behaviour at lower voltages (e.g. 200 V), where CCE is trapping- instead of CM-dominated, is completely different and the CCE does hardly change.

14.1.4   Temperature Dependence
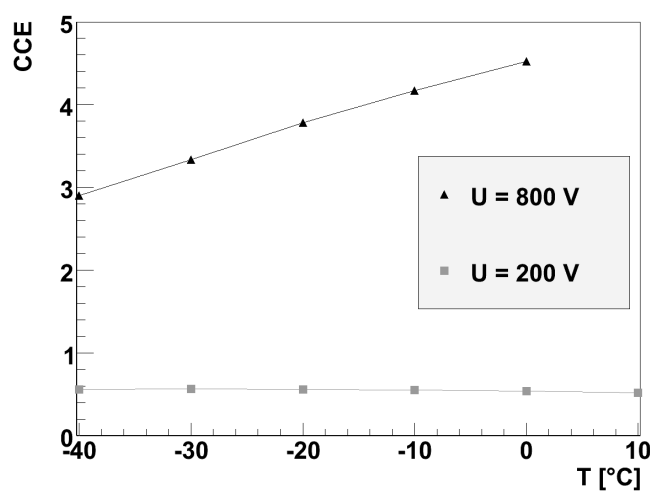
Figure 14.6: The CCE at 200 and 800 V as a function of temperature for ST75-1E16 measured with 670 nm laser light.

Fig. 14.6 shows the temperature dependence of the CCE below and in the CM regime measured with 670 nm laser light. At low voltages (e.g. 200 V), where trapping dominates the charge collection, no large sensitivity on temperature can be observed, similarly to the temperature behaviour of CCE at lower fluences [9]. In contrast, at voltages above 300 V a systematic decrease of CCE for decreasing temperature was found. Naively, one would expect the opposite behaviour as the ionisation coefficients increase for decreasing temperature [175]. However, on the one hand, the absorption length of 670 nm laser light increases slightly for decreasing temperature (according to [226] from 3.1 μm at 0°C to 3.6 μm at -40°C), so that at lower temperatures a smaller fraction of charge is produced in the region with the highest electric field at the very front side. Indeed, the effect was found to be less pronounced for 1060 nm laser light and α particles, for which the charge-deposition distribution in the CM region is less or not temperature dependent, respectively. However, the trend is the same and a simulation based on the simple model from Sec. 14.1.1 suggests that the temperature-dependence of the absorption length is only a minor correction and cannot compensate for the expected change in the ionisation coefficient. On the other hand, the electric field could change with temperature. It can be seen from Fig. 12.6 in Sec. 12.4.2 that the lower level of reverse current at lower temperatures can decrease the maximum electric-field value in case of a double junction.

14.1.5   Linearity of Multiplication
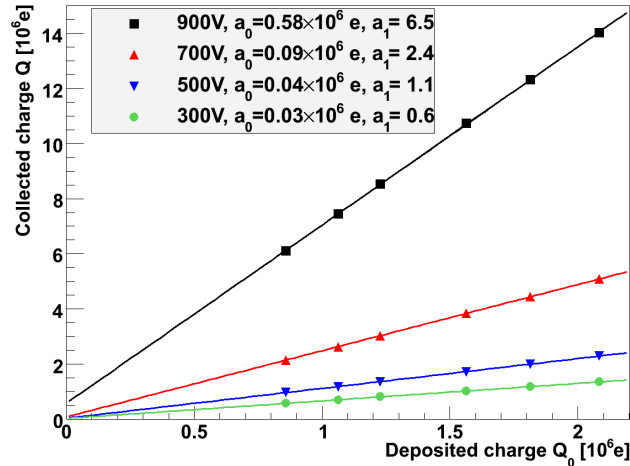
Figure 14.7: The collected charge as a function of deposited charge with linear fits $Q = a_0 + a_1 \cdot Q_0$ at different voltages. Measured with 670 nm laser light in ST75-1E16.

To find out whether a highly-irradiated diode in the CM regime operates in proportional or in Geiger mode (see Sec. 11.4.4), the measured charge Q was determined as a function of deposited charge Q_0 in the range from $(0.8$ to $2.1) \cdot 10^6$ e for 300, 500, 700 and 900 V (see Fig. 14.7). 670 nm laser light was used. An approximately proportional behaviour can be observed. The linear slope corresponds within 10% to the CCE results in Sec. 14.1.1 at the respective voltage. For Geiger mode, a substantial multiplication contribution of holes and therefore higher electric fields with a higher k-value (α_h/α_e) are needed.

14.1.6   Spatial Uniformity over the Diode Area

In order to investigate the spatial uniformity of CM over the diode area, an x-y scan was performed over the illumination window in the front metallisation of the diode (ST75-1E16) with a focused 660 nm laser (spot size $\sigma_{spot}{=}20$ μm) and a step width of 200 μm at 480, 580, 650 and 800 V corresponding to mean CCE values of 1.0, 1.5, 2.2 and 4.0. Fig. 14.8 (*left*) shows for the example of 800 V that the CCE is very uniform over the whole area (note the zoom in the CCE scale). The normalised standard deviation $\sigma/\overline{CCE}$ is around 0.5% for 480, 580 and 650 V and 1% for 800 V. However, a closer look reveals that there seems to be a systematic, almost linear slope in x-direction as demonstrated by an x-scan with a much finer step width of 10 μm (Fig. 14.8, *right*). But the normalised slope is rather small with only 0.5% difference over 1 mm in the middle of the window for 480 V, increasing up to 1.7% difference over 1 mm for 800 V. A reason for this behaviour might be a slightly nonuniform irradiation.
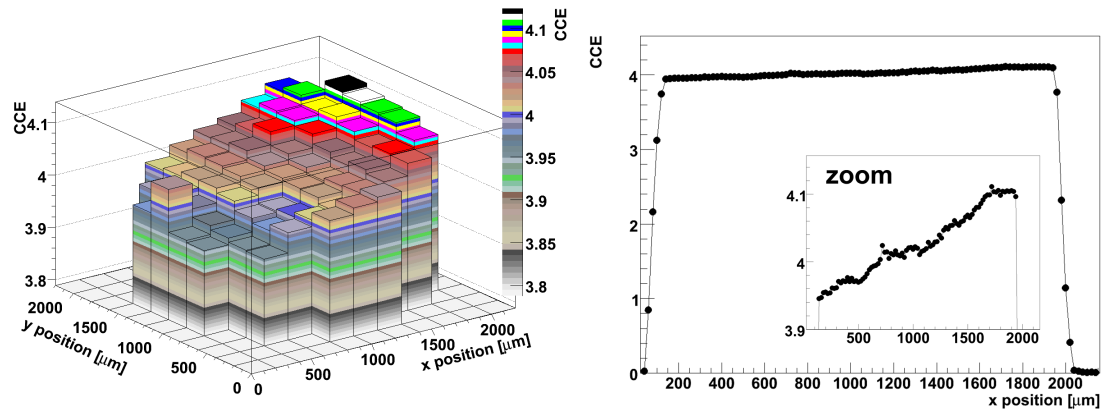
Figure 14.8: Uniformity of CM. *Left:* x-y scan over the illumination window with a focused laser spot of 660 nm wavelength at 800 V in ST75-1E16 (note the zoom in the CCE scale). *Right:* x-scan over the middle of the window at the same voltage in the same diode.

14.1.7 Long-Term Stability
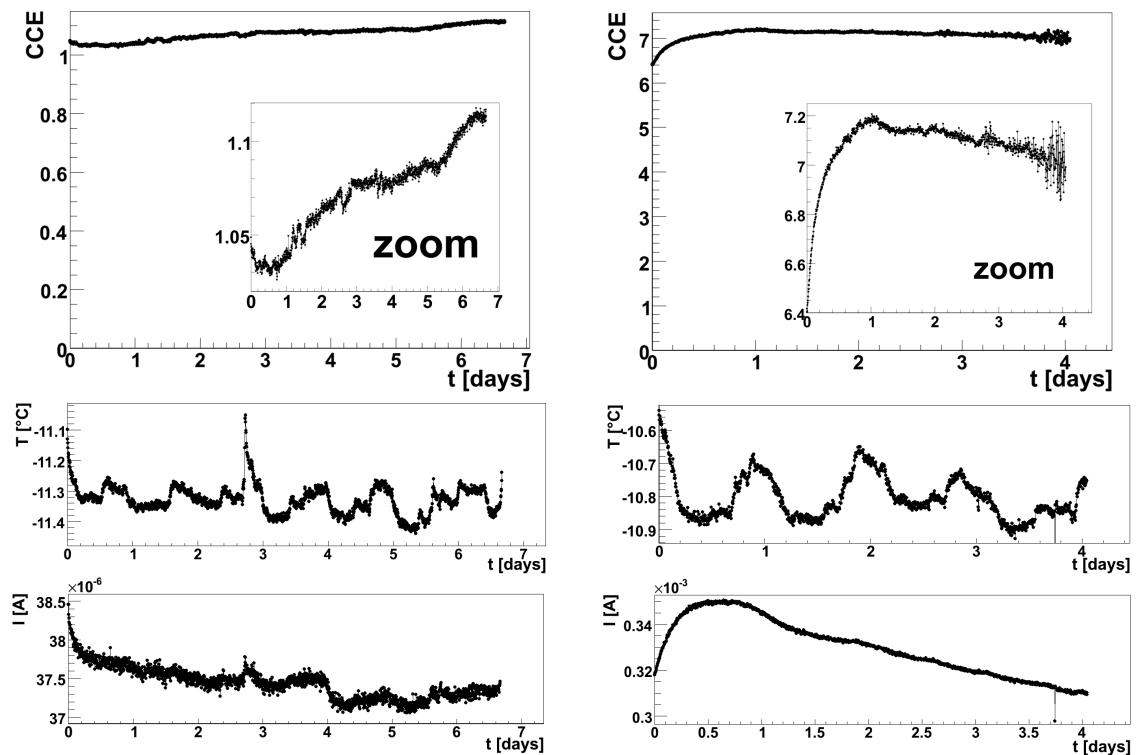
Figure 14.9: The stability of CCE (*top*, including a zoom), temperature (*middle*) and reverse current (*bottom*) measured with 670 nm laser light over several days in ST75-1E16 at 480 V (*left*) and 900 V (*right*).

For an application of the CM effect in a real detector, it is important that it remains

reliably stable over a long period of time. Fig. 14.9 shows a long-term measurement of CCE over several days in ST75-1E16 with 670 nm laser light. Every 5 min, a measurement was taken. The diode was kept at a constant bias voltage of 480 V, which corresponds to CCE≈1 (Fig. 14.9, *left*) or 900 V corresponding to CCE≈7 (Fig. 14.9, *right*). The corresponding temperature and reverse current is also shown. It can be seen that the temperature around -11°C was stable within 0.3°C and the leakage current within 3% (480 V) or 10% (900 V).

At 480 V, the CCE drops during the first half day from 1.05 to 1.03 and then increases more or less monotonically about 8% up to 1.11. However, over such a long period of time, the laser intensity might change. Reference measurements before and after this stability test were performed with an unirradiated diode. Also the charge collected by this reference diode was about 7% higher after the long-term measurement with the irradiated sample than before. Thus, the operation in the CM regime at 480 V can be regarded as stable.

At 900 V, there is a rise of about 12% from a CCE of 6.4 to 7.2 during the first day, before it decreases to 7.0 after 4 days. The reverse current shows a similar behaviour, although the shape of the curve is not completely identical. At such a high voltage, microdischarges occurred as already mentioned in Sec. 13.5. At the beginning, their rate was low enough not to be visible in the externally triggered measurements. But after about 2.5 days, their rate became so high that they often coincided with a TCT pulse. As 512 externally triggered pulses have been averaged, this becomes manifest only as moderate, but clearly visible fluctuations of the CCE curve. However, in the case of self-triggering or high-frequency readout like at the (HL-)LHC, it would be impossible to detect the signal of an impinging particle reliably. Moreover, it poses potential dangers for the readout electronics. For operation at such high voltages, microdischarges would have to be avoided.

14.1.8 Charge Spectrum and Noise

So far, only the signal averaged over 512 pulses was discussed. However, in a real experiment, a detector signal needs to be separated from noise event-by-event (see Sec. 11.4.5 and 11.4.6). Therefore, 301 single TCT pulses were taken, and the baseline noise and charge spectrum was investigated with special emphasis on the CM regime.

Noise and Signal-to-Noise Ratio

With a TCT setup, the transient current pulse is recorded directly. Thus, the equivalent noise charge (ENC) was determined in a similar way as the charge signal by integrating over the TCT baseline well before the pulse in a time window of about 10 ns. Fig. 14.10 (*left*) shows the RMS noise as a function of bias voltage for measurements with 670 and 1060 nm laser light. The difference is probably due to random fluctuations. The noise of an unirradiated diode, which should be mostly dominated by other noise contributions σ'_{noise} than shot noise since the reverse current is low, was found to be within 20–26 ke.
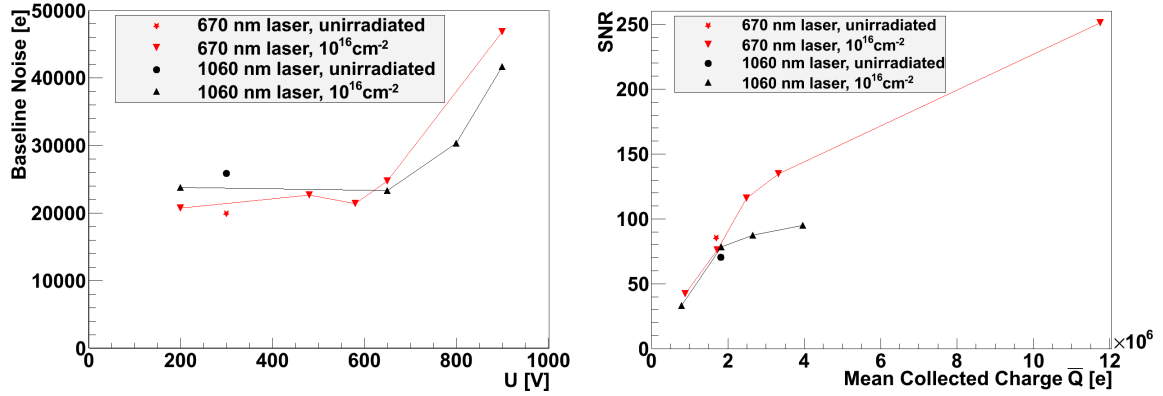
Figure 14.10: *Left:* The RMS noise of the TCT baseline in n-EPI-ST 75 μm (unirradiated and ST75-1E16) as a function of voltage. *Right:* The corresponding signal-to-noise ratio (SNR) as a function of the mean collected charge for about $1.8 \cdot 10^6$ e-h pairs deposited.

This shows that the noise of a TCT setup is significantly higher than in the case of a charge-sensitive readout with optimised shaper (see Sec. 11.4.5 and 14.2.3).

As explained in Sec. 11.4.6, the shot noise σ_{sh} is expected to increase in the CM regime due to the multiplication of the reverse current (see Fig. 14.1) and possible fluctuations in the CM process described by the excess noise factor F'. However, up to 650 V, the noise of ST75-1E16 is similar to the one of the unirradiated diode. Subsequently, it increases to about 45 ke at 900 V. This behaviour can be explained by the high value of σ'_{noise} of the TCT setup, which is exceeded by an increasing shot noise only above 650 V.

From this, the signal-to-noise ratio (SNR) was calculated. It is shown in Fig. 14.10 (*right*) as a function of the mean collected charge $\bar{Q}$. As for both 670 and 1060 nm laser light similar values of $Q_0 \approx 1.8 \cdot 10^6$ e-h pairs were deposited, the SNR for the unirradiated diodes are also similar (70–85). Even for ST75-1E16, similar SNR values were found at the same collected charge of Q_0 because at the voltages needed for CCE values of 1 (480 V for 670 nm and 650 V for 1060 nm), the noise has not increased as seen from Fig. 14.10 (*left*). For higher voltages respectively mean collected charge, the SNR is still improving, but slower than before because also the noise is increasing. For the same collected charge, the SNR of 670 nm is seen to be higher than the SNR of 1060 nm because in the case of 670 nm, lower voltages are needed for the same CCE (cf. Fig. 14.1), which implies lower noise. But also in the case of 1060 nm laser light, which has similar penetration as MIPs, higher SNR values are obtained in highly-irradiated sensors at high voltages than before irradiation due to CM. However, for the TCT setup with laser, both the noise and the signal were much higher than in a realistic (HL-)LHC detector. The noise and SNR measured with MIP-like particles and a low-noise charge readout is presented in Sec. 14.2.3.

Charge Spectra
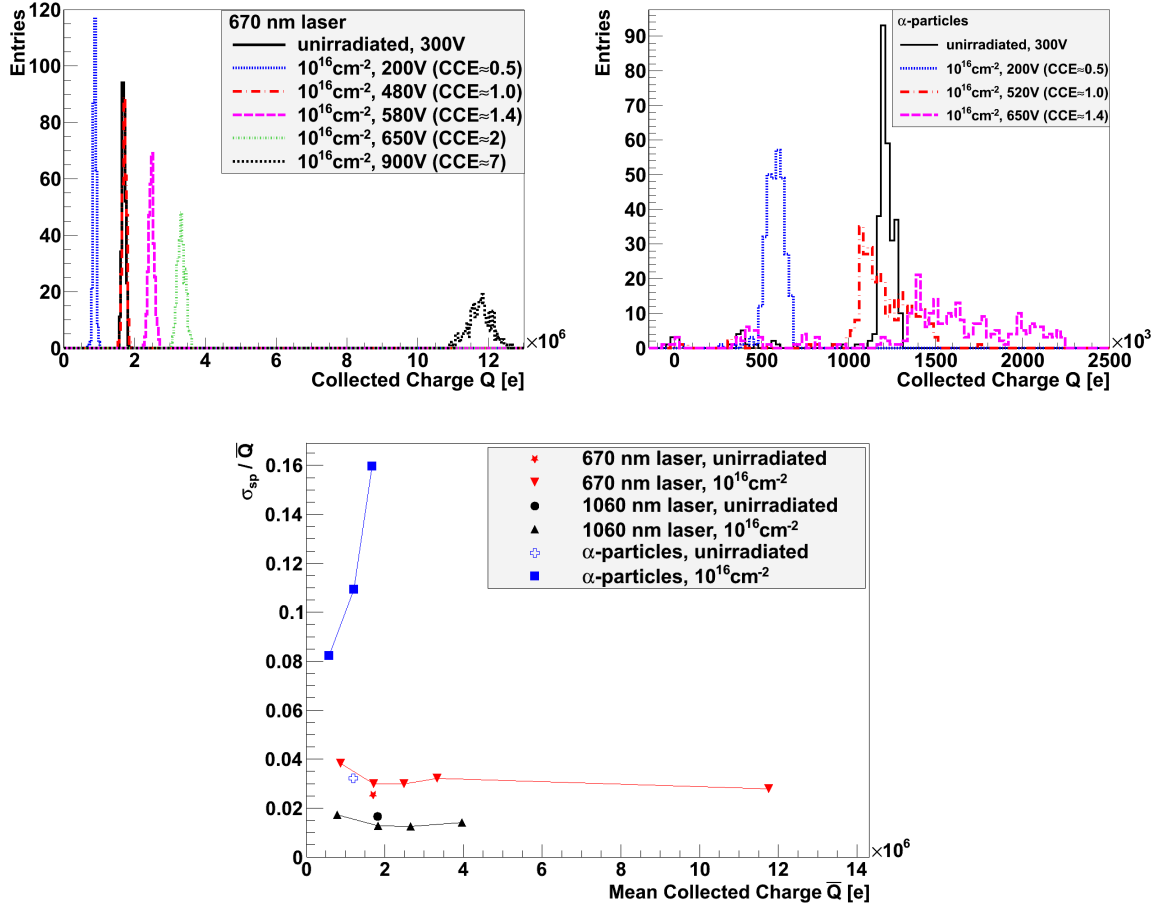
Figure 14.11: *Top:* The charge spectra measured with 670 nm laser light (*left*) and α particles (*right*) in ST75-1E16 at different voltages and in an unirradiated 75 μm diode at 300 V. For laser light, the unirradiated spectrum almost entirely overlaps with the one of ST75-1E16 at 480 V. *Bottom:* The relative width $\sigma_{sp}/\bar{Q}$ (corrected for noise) of the charge spectra as a function of the mean collected charge $\bar{Q}$ for 670 and 1060 nm laser light and α particles. In the case of α particles, single events with lower charge than in the central peak were excluded.

CM does not only affect the electronic noise of the baseline, but also the charge spectrum of the signal. The width of the spectrum is expected to increase due to multiplication and associated statistical fluctuations in a similar way as the shot noise as discussed in Sec. 11.4.6 (but note the different M and F): $\sigma_{sp} = \sigma_{sp,M=1} M \sqrt{F}$. Furthermore, when performing a measurement, the charge spectrum is convoluted with the baseline noise, so that the measured width is given by $\sigma_{sp,meas} = \sqrt{\sigma_{sp}^2 + \sigma_{noise}^2}$.

Fig. 14.11 (*top*) shows the charge spectra measured with 670 nm laser light (*left*) and α particles (*right*) for an unirradiated diode at 300 V and for ST75-1E16 at different voltages. A charge spectrum measured for 1060 nm laser light looks similar to the one

of 670 nm. The charge-spectrum width (standard deviation) for the unirradiated diode is 48 ke and 38 ke for 670 nm and α particles, respectively. The broadening due to CM is easily visible when comparing the spectra of ST75-1E16 at low and high voltages. The entries for α particles below the central peak are caused by low-energy particles, microdischarges and pickup noise. They are excluded in the following.

To investigate whether the broadening is enhanced by fluctuations, the relative width $\sigma_{sp}/\bar{Q}$ was calculated (after correcting for baseline noise) because both σ_{sp} and $\bar{Q}$ are proportional to M, so that M cancels. The relative width is shown in Fig. 14.11 (*bottom*) as a function of mean collected charge for 670 and 1060 nm laser light and α particles. For laser light, it can be seen that at $Q_0 \approx 1.8 \cdot 10^6$ e (CCE=1), the relative width of ST75-1E16 is not much higher than before irradiation (670 nm) or even slightly lower (1060 nm). The differences might be due to measurement uncertainties. Moreover, the relative width of ST75-1E16 stays constant even for higher $\bar{Q}$ (i.e. higher voltages and multiplication), which shows that in the range considered here CM fluctuations are not dominant, probably due to low values of M and k at not too high field values.

In contrast, the relative width of the spectrum measured with α particles significantly increases in the CM regime. Statistical fluctuations in the CM process were ruled out by the measurements with laser light. Thus, the large broadening is probably caused by fluctuations in the amount of charge deposited in the thin CM region. These might be caused by the divergence of the beam, which leads to varying penetration of the α particles (see Sec. 13.5.1). For instance, the Bragg-peak depth is reduced from 26 μm at perpendicular incidence to 18 μm at 45°, which makes a significant difference as the CM region is assumed to be in a similar thickness range and becomes increasingly stronger for decreasing depth.

A measurement of the charge spectrum for MIP-like particles with the β setup is presented in Sec. 14.2.4.

14.2   Measurements with the ^{90}Sr β Setup

Parts of the results obtained with the ^{90}Sr β setup are published in [235]. The following sections include material from there with some adaptations and extensions.

An overview on the measured charge as a function of applied bias voltage in EPI diodes of all studied materials and thicknesses for different fluences is given in Figs. 14.12 and 14.13. The first figure shows the mean value, the latter the most probable value (MPV) of the Landau distribution from a Landau-Gauss fit (see Sec. 13.5.3). The shown uncertainties are statistical. Unfortunately, for many of the irradiated diodes, the Landau-Gauss fit failed at high voltages due to high noise, rendering the determination of the MPV impossible. As the high-voltage regime is the main focus of this work, however, most of the following discussion regarding the measured charge in irradiated diodes is based on the mean value. The mean was found to be reasonably well defined even without truncations, which are usually preferred in the case of MIPs to exclude fluctuations in the high-energy Landau tails [19]. This is probably due to
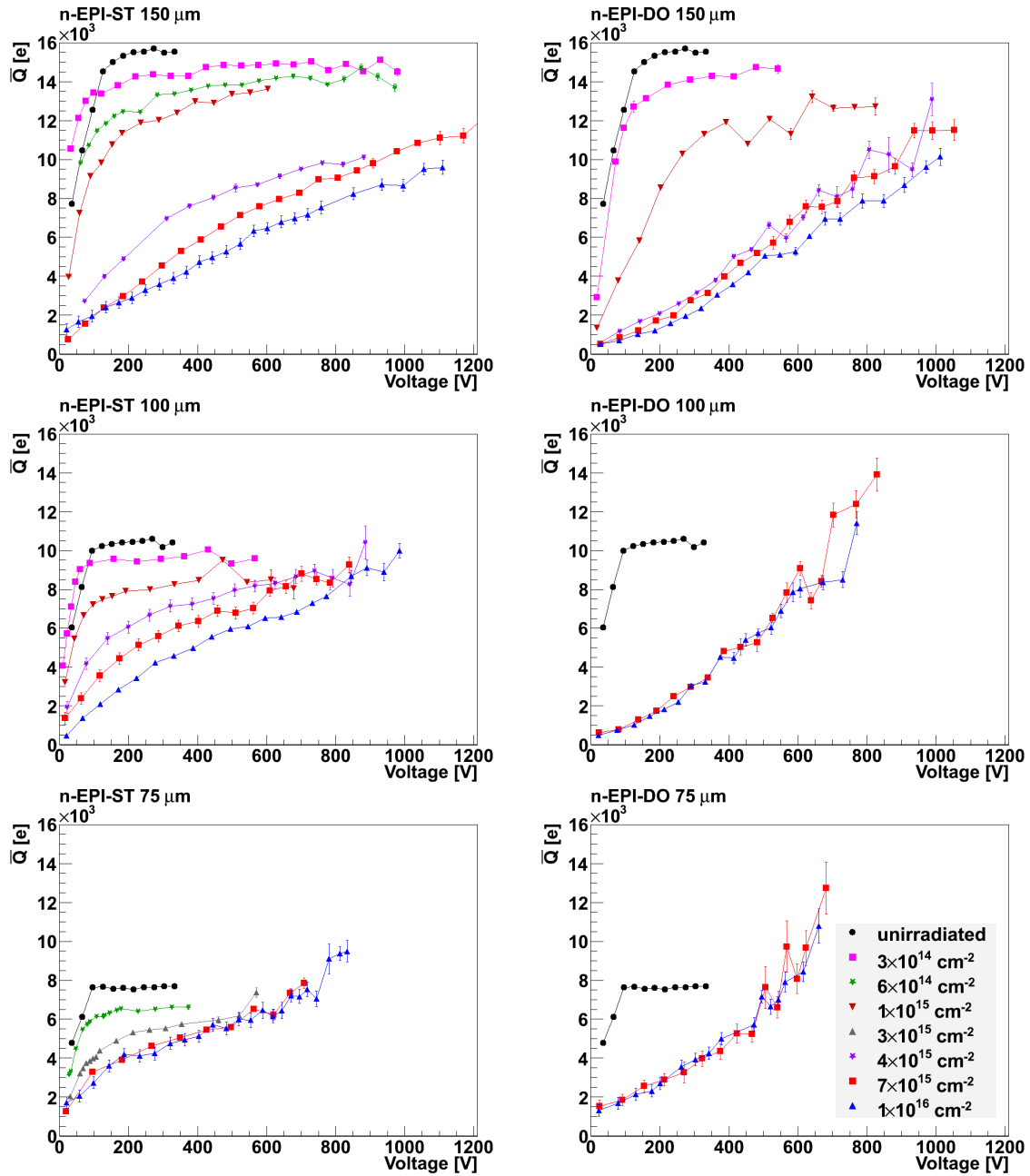
Figure 14.12: Mean collected charge $\bar{Q}$ for β particles as a function of voltage for different fluences in all available materials (ST *left*, DO *right*) and thicknesses (150 μm *top*, 100 μm *middle*, 75 μm *bottom*). Not for all fluences in the legend, a measurement was done in diodes of all materials and thicknesses. The unirradiated diodes are only measured for one material at each thickness, but plotted for both.
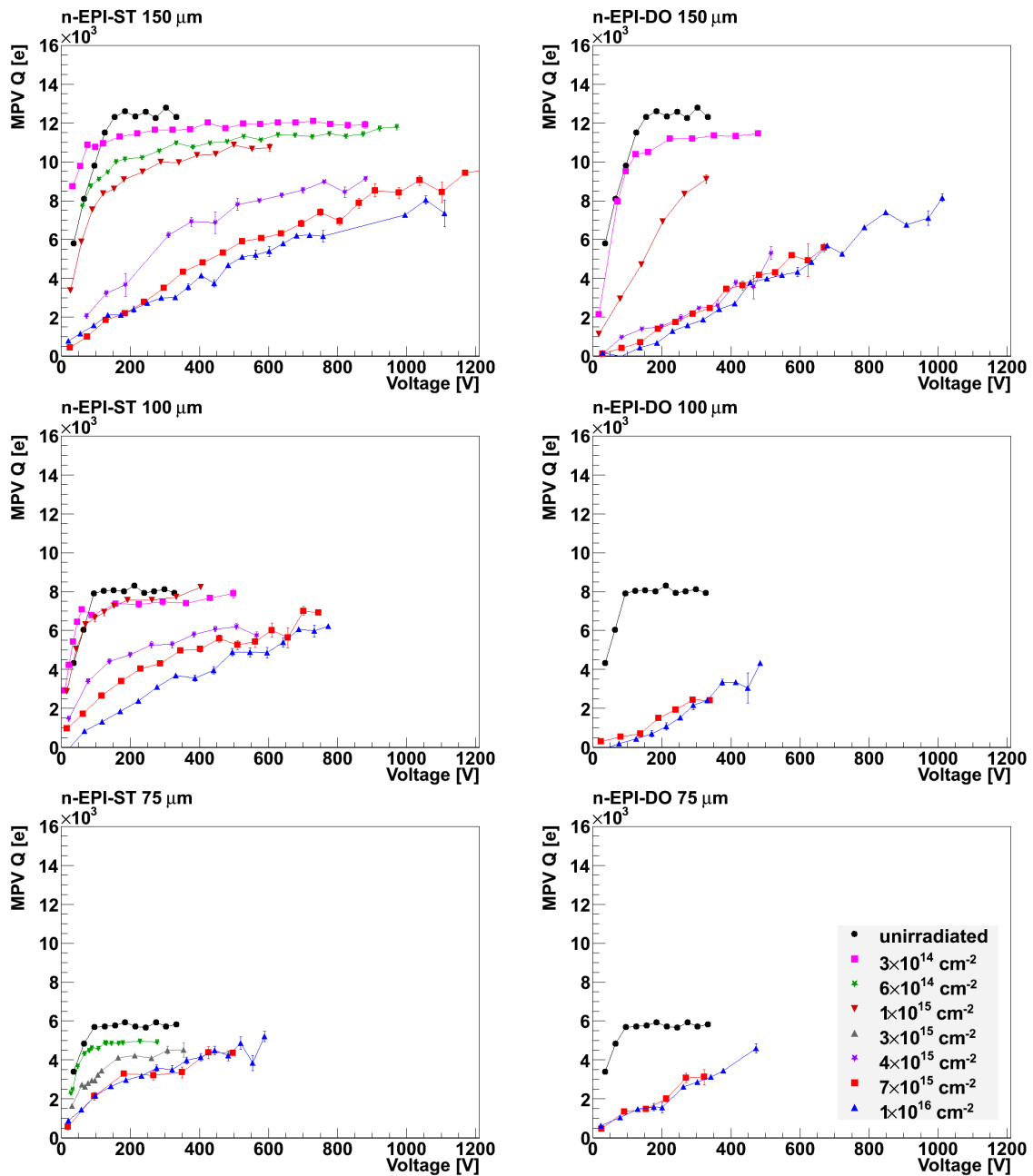
Figure 14.13: Most probable collected charge for β particles as a function of voltage for different fluences in all available materials (ST *left*, DO *right*) and thicknesses (150 μm *top*, 100 μm *middle*, 75 μm *bottom*). Not for all fluences in the legend, a measurement was done in diodes of all materials and thicknesses. The unirradiated diodes are only measured for one material at each thickness, but plotted for both. Measurements at high voltages with high noise, where the determination of the MPV was impossible, are excluded.

the relatively low energy limit of the β-source spectrum ($E_{max} \approx 2\,\text{MeV}$), avoiding too long tails. The good definition of the measured mean is e.g. demonstrated by the smoothness of the $\bar{Q}(V)$ curve of the unirradiated diodes above depletion in Fig. 14.12 and the corresponding variation of the MPV-to-mean ratio of only about 5%. Also for medium voltages of irradiated sensors, where both MPV and mean could be determined, the MPV-to-mean ratio was found to lie typically between 0.75 to 0.85 for 150 μm diodes and between 0.7 to 0.8 for 75 and 100 μm diodes.

14.2.1   Collected Charge before Irradiation
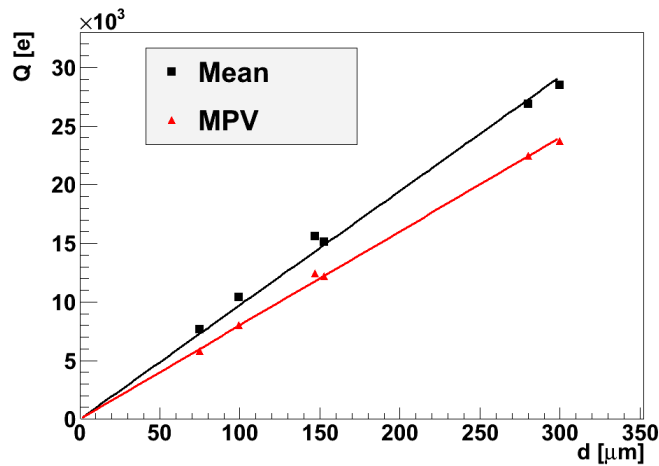
Figure 14.14: Mean and most probable value (MPV) of the collected charge for β particles as a function of detector thickness before irradiation. FZ material was used for the 280 and 300 μm thick diodes. For 150 μm, two diodes (small and large) are compared.

For unirradiated EPI diodes, only one material was measured for each thickness (ST 150 μm, DO 100 μm, ST 75 μm), but the collected charge in unirradiated diodes is expected to be independent of the material and therefore plotted for both. As can be seen from Figs. 14.12 and 14.13, the collected charge in unirradiated diodes reaches a plateau around 100–150 V, as expected from the depletion voltage. Fig. 14.14 shows the MPV and mean after full depletion (obtained as average over the highest four measured voltages) as a function of diode thickness. The thickness was obtained from CV measurements. Unirradiated diodes of 280 and 300 μm thick FZ material are also measured and shown for reference. As β particles deposit charge along their path through the sensor, the measured charge increases with thickness. A proportional dependence is observed both for the MPV and the mean collected charge. The slope was determined by a linear fit as 80 e-h pairs/μm (MPV) and 97 e-h pairs/μm (mean), respectively. This is in excellent agreement with previous measurements of 25 to 75 μm thick epitaxial diodes with the same setup [228]. Thus, the ratio between MPV/d and mean/d is about 0.8. The values found here differ slightly from the standard values for MIPS (MPV/d≈73 e-h pairs/μm in 300 μm sensors [19]), probably due to residual

differences between the β particles used in this analysis with about 1–2 MeV energy and an ideal MIP (e.g. higher stopping power or enhanced multiple scattering).

14.2.2   Collected Charge after Irradiation

The collected charge in irradiated diodes was measured for fluences between $3 \cdot 10^{14}$ cm^{-2} and 10^{16} cm^{-2} (see Figs 14.12 and 14.13). At low and medium voltages, one can clearly see the charge loss due to trapping, which increases for increasing fluence. However, at high voltages[4] in 100 and 75 μm thick diodes, the collected charge for the highest fluences ($4 \cdot 10^{15}$, $7 \cdot 10^{15}$ and 10^{16} cm^{-2}) reaches or even exceeds the one in unirradiated diodes, indicating CM. In 150 μm thick diodes, the collected charge for these fluences remains below the one in unirradiated diodes at the highest measured voltages. However, from the measurement with red laser light in Sec. 14.1.2, it is expected that CM also takes place in these diodes. It is only not explicitly visible at these voltages because in contrast to laser light, only a fraction of the charge deposited by β particles is multiplied in the thin CM region, and this effect is overcompensated by trapping.

In order to study the properties of charge collection in the CM regime, the following discussion focuses on the highest measured fluence of 10^{16} cm^{-2}. Fig. 14.15 shows the mean collected charge and the corresponding CCE for this fluence as a function of voltage. For all investigated materials and thicknesses, a mean of more than 9 ke was measured at high voltages (which can be tentatively converted to an MPV of 6.8 ke using a conservative factor of 0.75 found for irradiated diodes at moderate voltages as explained above). Even at 600 V, which is considered the voltage limit for the LHC detectors using the currently deployed infrastructure, mean signals between 5 and 8 ke could be achieved (approximately scalable to MPVs between 3.8 and 6 ke).

From the comparison of different thicknesses, it can be seen that the CCE is larger in thinner diodes compared to thicker ones, as already observed for red laser light presented in Sec. 14.1.2. Moreover, it is interesting to note that even the absolute amount of collected charge is higher in thinner diodes, although less charge is deposited in case of β particles. However, this is apparently (over)compensated by the higher values of both electric field (average value U/d) and weighting field ($1/d$) in thinner diodes. As already explained in Sec. 14.1.2, higher electric fields lead to stronger CM at high voltages and to a faster drift at low voltages (below the saturation-velocity regime), which increases the traversed distance of charge carriers before being trapped. Moreover, even for the same travelled distance, the measured charge per carrier is higher in thinner diodes due to the higher weighting field.

Comparing different materials, it can be seen that at low voltages (below the CM regime), the collected charge (and efficiency) is lower for DO diodes than for ST material, whereas it is the other way round at high voltages (in the CM regime). Also this behaviour is the same as observed for red laser light (see Sec. 14.1.2). Both effects can be explained by a higher donor-introduction rate in DO material (see Sec. 13.4), resulting in a higher space-charge density. For DO diodes, this leads to a smaller depleted

---

[4]As discussed above, only the mean collected charge could be extracted at high voltages.
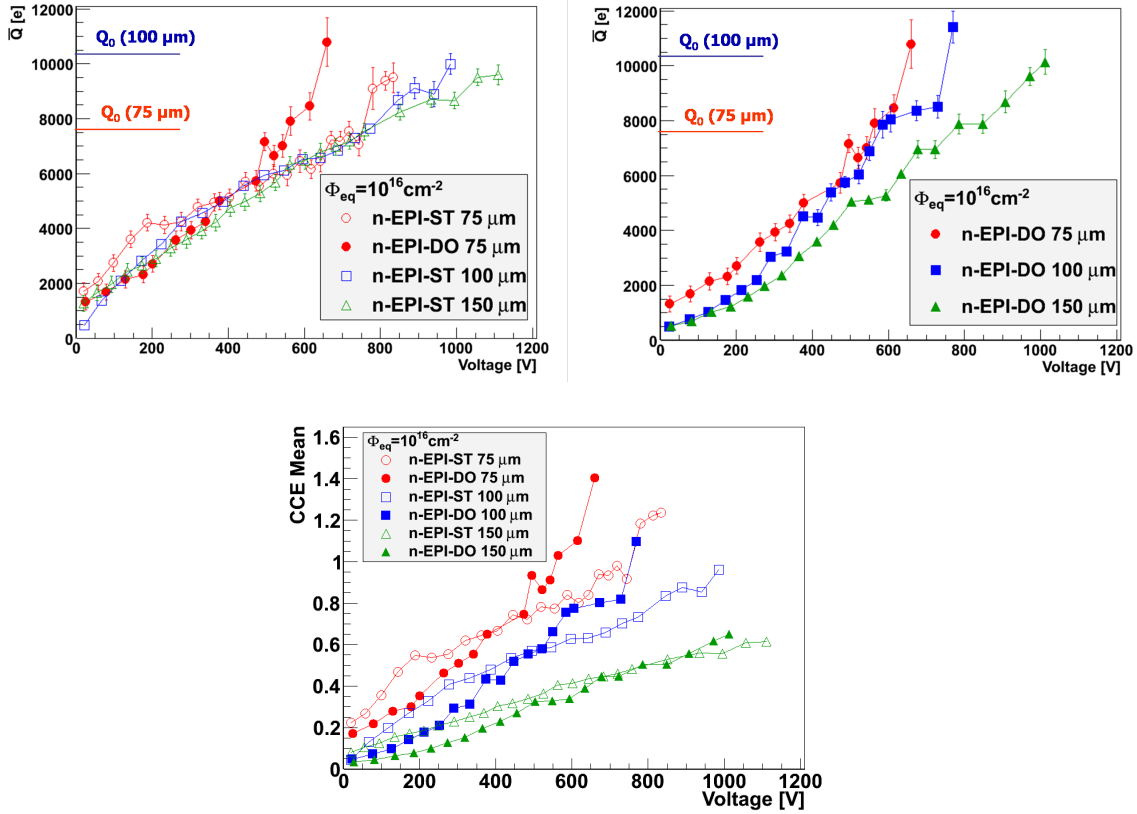
Figure 14.15: *Top:* Mean collected charge for β particles as a function of voltage for diodes irradiated to 10^{16} cm^{-2} for ST (*left*) and DO (*right*) material. For easier comparison of ST and DO diodes, the curve for EPI-DO 75 μm was also included *left*. The horizontal lines indicate the collected charge before irradiation, Q_0. *Bottom:* The corresponding charge-collection efficiency for all thicknesses and materials.

(i.e. sensitive) region at low voltages, whereas at high voltages, the larger maximum field value at the p-n junction causes a stronger CM.

14.2.3   Noise and Signal-to-Noise Ratio

The equivalent noise charge is obtained from the baseline spectrum (see Sec. 13.5.3). Due to pickup noise, there is also a small fraction of non-Gaussian components during some measurements, including those of unirradiated diodes. This shows that this probably originates from the setup. In other measurements, also microdischarges contribute to the tails. However, the rate of microdischarges was observed to be highest at medium fluences around $3 \cdot 10^{14}$–10^{15} cm^{-2}, but it depended on the exact diode used and no systematic behaviour could be found. During measurements of the diodes irradiated to the highest fluences presented in the following, they were negligible (for 75 μm) or even completely absent (all others). In fact, at high voltages, the noise spectrum of highly-irradiated diodes was observed to be almost perfectly Gaussian. Thus, in the following the noise refers to the standard deviation of a Gauss fit to the baseline
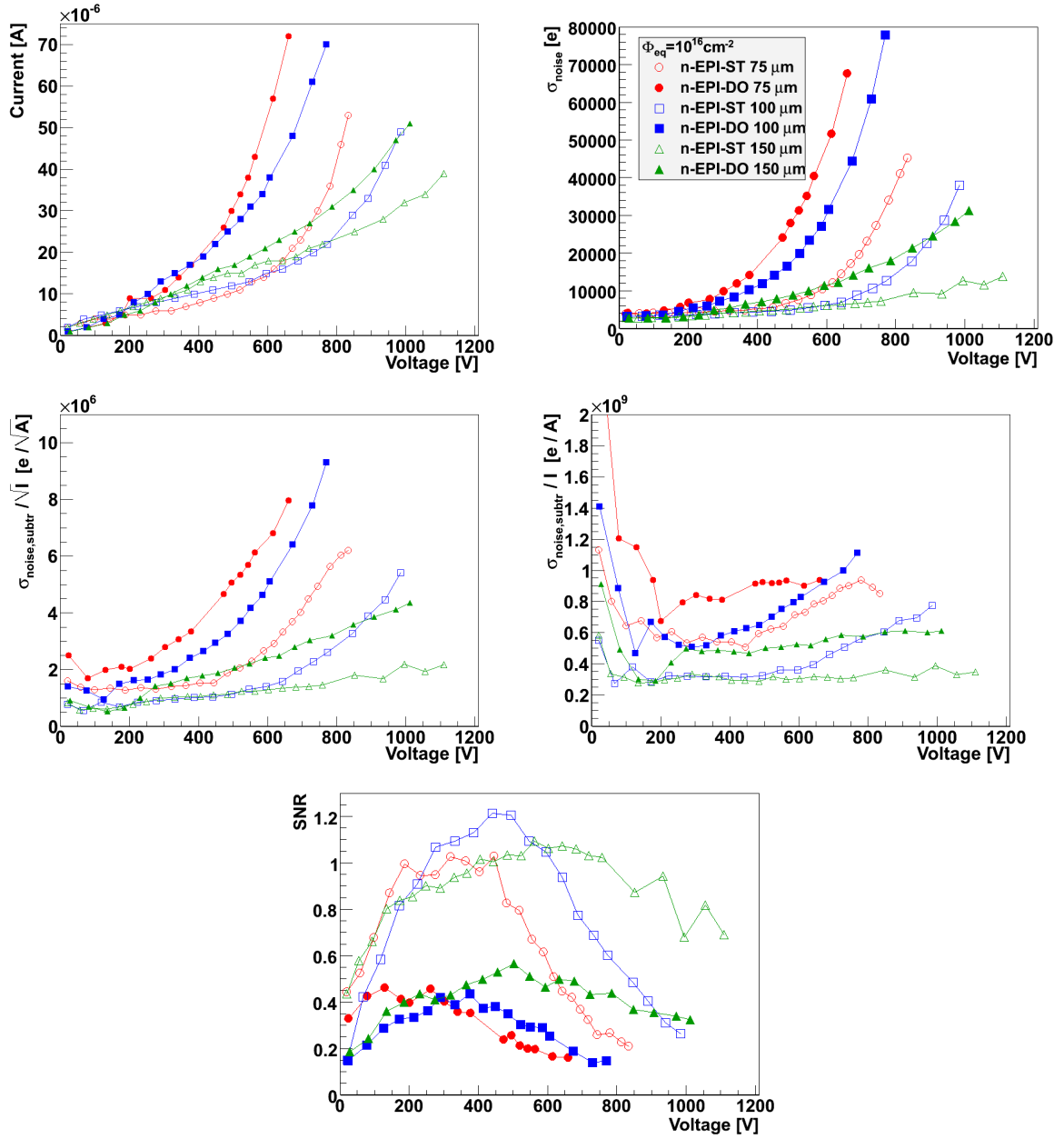
Figure 14.16: *Top:* Reverse current (*left*) and noise (*right*). *Middle:* $\sigma_{noise,subtr}/\sqrt{I_{rev}}$ (*left*) and $\sigma_{noise,subtr}/I_{rev}$ (*right*). *Bottom:* Mean signal-to-noise ratio ($SNR = \bar{Q}/\sigma_{noise}$). All quantities are shown as a function of applied voltage at a fluence of 10^{16} cm^{-2} for all investigated thicknesses and materials.

spectrum.

The measured noise in unirradiated diodes was between 2 and 3.3 ke with the β setup, depending on diode size and thickness. This is about an order of magnitude lower than the corresponding noise of 20–26 ke measured with the TCT setup (see Sec. 14.1.8).

The noise in irradiated diodes is expected to increase due to the increase of the reverse current, which is enhanced by multiplication and possible related fluctuations in the CM regime (see Sec. 11.4.6). For a fluence of 10^{16} cm^{-2}, the reverse current during the charge-collection measurement (i.e. with floating guard ring) and the measured noise are shown as a function of voltage in Fig. 14.16 (*top*). Both follow the same trend, namely a strong increase at high voltages.

They also show the same thickness and material dependence as the collected charge with β particles (see Sec. 14.2.2) and the charge-collection efficiency with laser light (see Sec. 14.1.2): the current and noise are higher for DO than for ST material at the same thickness and increase with decreasing thickness for the same material. At 600 V, the noise ranges from 6 ke for EPI-ST 100 and 150 μm to about 50 ke for EPI-DO 75 μm. It can be seen that the noise increase with respect to the pre-irradiated values (or the one at low voltages) is much faster for the β setup than for the TCT setup (see Sec. 14.1.8). This can be explained by the much lower intrinsic noise of the β setup of only 2 and 3.3 ke, so that the CM-dependent noise dominates the total noise already at low voltages.

To investigate the nature of the measured noise and its relation to the current in more detail, in a first step, an estimate of the shot noise is obtained. This is performed by subtracting the noise of the respective unirradiated diode, which is dominated by other noise sources inherent to the setup, from the measured noise in the irradiated sensor: $\sigma_{noise,subtr} = \sqrt{\sigma_{noise}^2 - \sigma_{noise,unirr}^2}$. If $\sigma_{noise,subtr}$ is dominated by shot noise in the absence of CM, one would expect $\sigma_{noise,subtr}/\sqrt{I_{rev}} = const$ (see Sec. 11.4.5). However, from Fig. 14.16 (*middle left*), one can see that this ratio increases faster with voltage than a constant, indicating CM. Taking CM effects into account, one would expect $\sigma_{noise,subtr} \propto \sqrt{I_{rev,M'=1}}M'\sqrt{F'}$ according to Eq. 11.27, where $I_{rev,M'=1}$ is the generated current without multiplication, M' the current multiplication factor and F' the corresponding excess noise factor. Dividing this by the current $I_{rev} = I_{rev,M'=1}M'$, M' cancels and only a dependence on F' and the current $I_{rev,M'=1}$ without multiplication remains: $\sigma_{noise,subtr}/I_{rev} \propto \sqrt{F'}/\sqrt{I_{rev,M'=1}}$. This ratio is shown in Fig. 14.16 (*middle right*). In general, the $\sigma_{noise,subtr}/I_{rev}$ curves are much flatter than $\sigma_{noise,subtr}/\sqrt{I_{rev}}$, excluding the region below 100–200 V, where CM does not play a role. However, for some of the curves, there is an increase at high voltages. As $I_{rev,M'=1}$ is not expected to decrease with voltage, this could either be explained with an increasing excess noise factor F' or with completely different noise sources not considered here.

The mean signal-to-noise ratio SNR= $\bar{Q}/\sigma_{noise}$ is shown in Fig. 14.16 (*bottom*). It can be seen that it is qualitatively very different to the SNR behaviour of the TCT setup (see Fig. 14.10, *right*) due to the different level of intrinsic noise. For the TCT setup with a large intrinsic noise, the SNR was observed to increase due to CM up to the highest measured voltage of 900 V, even for 1060 nm laser light with comparable penetration as β particles. In contrast, the SNR for the β setup rises only up to a maximum at voltages between 200 and 600 V, before decreasing again. This shows that in the CM regime at high voltages, the noise increase of the β setup for pad diodes is faster than the signal increase for β particles (see also Eq. 11.28 and related discussion in Sec. 11.4.6). In this respect, it is also interesting to note that the SNR for

DO material, which showed enhanced CM and thus a higher signal, exhibits a lower maximum (0.4–0.6) than the SNR for ST material (1–1.2). Furthermore, although the maximum values for different thicknesses of the same material are similar to each other, the maximum is reached at lower voltages for smaller diode thicknesses.

These observations indicate that it is beneficial for the SNR of the β setup for pad diodes not to operate in the high-CM regime, but rather at moderate voltages with lower multiplication, in contrast to the TCT setup. Comparing the measurements with different setups and diodes demonstrates that every setup and device has to be considered individually, as is also clear theoretically from Eq. 11.28.

Thus, the question arises how the situation looks like for realistic (HL-)LHC pixel detectors. It is clear that noise values of several 10 ke and corresponding SNRs less than 1 as measured here for pad diodes are not an option. The signal is expected to stay similar to the one measured in pad diodes, but the exact amount might also change due to the different weighting field, different electric field, especially at the edges of implantations, and charge sharing between neighbouring cells. However, the noise is expected to be very different: the area A of a current CMS pixel ($100 \times 150~\mu\mathrm{m}^2$) is about 1700 times smaller than for the large pad diodes studied here, and for the HL-LHC, even smaller cell sizes are envisaged. Thus, the reverse current for a readout element, which scales with the area, is much lower in pixel sensors than in pad diodes. This reduces the shot noise with and without CM (naively by a factor of $\sqrt{A_{pad}/A_{pixel}} \approx 40$). Operating at lower temperatures might be another option to reduce the noise further (however, the effect on the signal needs to be taken into account as well as demonstrated in Sec. 14.1.4). Moreover, for the operation of pixel detectors, the signal threshold is usually set much higher than necessary for an acceptable noise occupancy due to reasons not related to the sensor noise (e.g. cross talk on readout chips, see Sec. 11.4.5). Therefore, increase of noise due to CM might be tolerable up to a certain point, so that operation of pixel detectors in the CM regime might be applicable within wider limits than suggested here by the measurements in pad sensors. To clarify this, studies with realistic pixel sensors and readout are needed.

14.2.4 Charge Spectrum

For an efficient separation of signal and noise, not only the mean SNR, but the whole charge spectrum needs to be considered. It must not broaden too much due to multiplication and associated statistical fluctuations as discussed in Sec. 11.4.6. As shown in Sec. 14.1.8, the relative width of the spectrum in the CM regime remains constant in the case of laser light, but significantly broadens for α particles due to varying deposited charge in the CM region. Also in the case of β particles, Landau fluctuations of the amount of charge deposited in the thin CM region might additionally broaden the charge spectrum.

However, the charge spectrum can only be measured convoluted with the baseline noise. The noise and charge spectrum of EPI-ST 100 μm, 10^{16} cm^{-2}, at 985 V are shown in Fig. 14.17 (*top*). This diode was chosen because it is the one with least noise and maximum SNR among the samples with clear charge multiplication when
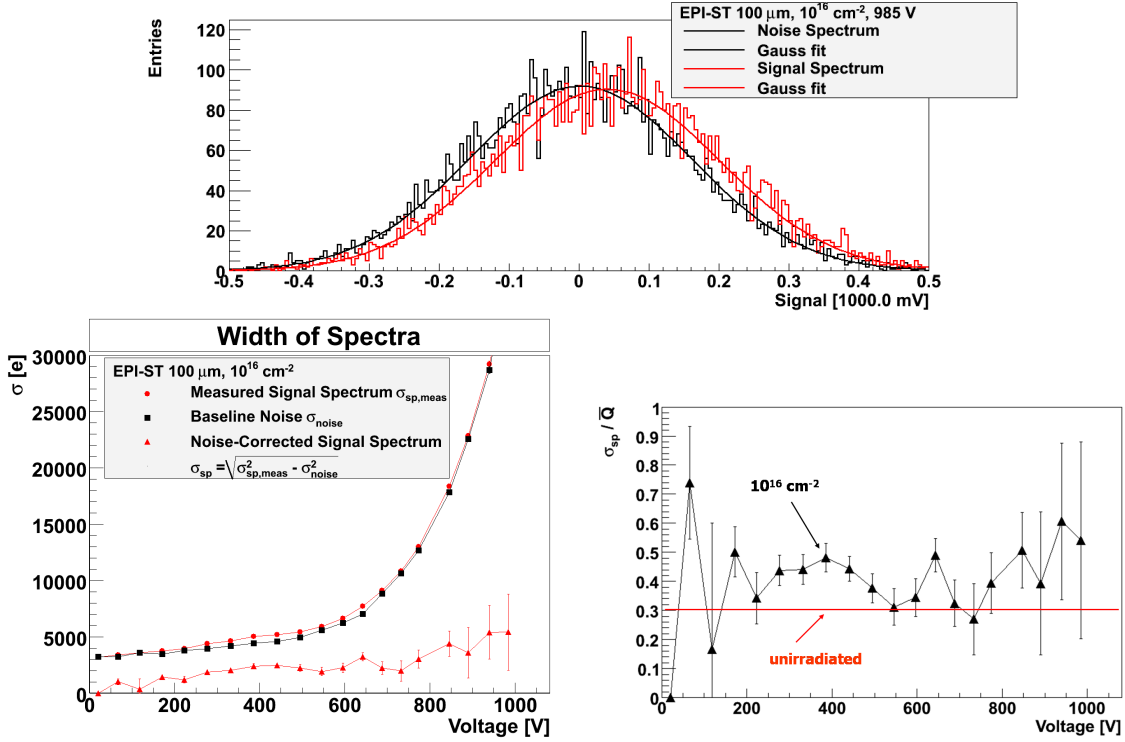
Figure 14.17: Effects of CM on the signal spectrum. *Top:* Noise and signal spectrum in EPI-ST 100 μm irradiated to 10^{16} cm^{-2} at 985 V. *Bottom left:* The Gaussian width σ of the noise and measured signal spectrum and the noise-corrected signal spectrum as a function of voltage. *Right:* The noise-corrected relative width of the signal spectrum $\sigma_{sp}/\bar{Q}$ as a function of voltage. The line indicates the level before irradiation.

measured with the β setup (CCE≈ 1 at 985 V), i.e. excluding the 150 μm thick diodes. However, it can be seen that also in this case, the noise clearly dominates the charge spectrum, so that the Landau distribution is completely smeared. Thus, both noise and signal spectrum are fitted with a Gaussian. Fig. 14.17 (*bottom left*) shows that the measured spectrum width $\sigma_{sp,meas}$ is only slightly higher than the noise width σ_{noise}. Thus, the noise-corrected spectrum width $\sigma_{sp} = \sqrt{\sigma_{sp,meas}^2 - \sigma_{noise}^2}$ has large uncertainties, especially at high voltages.

Nevertheless, it can be seen from Fig. 14.17 (*bottom right*) that the relative width[5] $\sigma_{sp}/\bar{Q}$ does not increase significantly at high voltages in the CM regime. For a tentative comparison, the red line indicates the relative width of an unirradiated 100 μm diode, which is for consistency also obtained from a Gauss fit to the signal spectrum and noise-corrected. It is only slightly lower than the relative width of the irradiated diode. Thus, at this level of precision, no significant impact of fluctuations in the CM process or in the deposited charge in the CM region on the spectrum is observed, similarly to measurements with laser light from Sec. 14.1.8. However, measurements with devices with less noise such as pixel detectors are desirable to improve the precision.

---

[5]As explained in Sec. 14.1.8, by normalising σ_{sp} to $\bar{Q}$, the dependence on M cancels, so that the relative width is only sensitive to fluctuations.

Chapter 15

Summary and Outlook

The work performed in this thesis covers two different aspects of modern particle-physics experiments: on the one hand a particle-physics analysis of differential $t\bar{t}$ cross sections; and on the other hand detector research and development towards radiation-hard silicon sensors for the high-luminosity upgrade of the LHC.

15.1   Differential Top-Quark-Pair Cross Section

A measurement was presented of normalised differential $t\bar{t}$ cross sections as a function of kinematic quantities of the $t\bar{t}$ system, the top quarks and their final decay products (b jets and electron or muon). The measurement was based on data recorded by CMS in 2011 corresponding to an integrated luminosity of 5 fb^{-1} and was performed in the lepton+jets decay channel. Such distributions represent a test of the standard model (SM), in particular of perturbative QCD, and allow to constrain QCD parameters such as parton-distribution functions (PDF). Furthermore, they are relevant in searches for physics beyond the SM, on the one hand because $t\bar{t}$ events often constitute a major background, and on the other hand because such distributions are sensitive to potential new physics effects themselves. For many of the presented quantities, this analysis represents the first such measurement in pp collisions, or even at all. The results were published in [6], together with a similar analysis in the dilepton channel.

The data taken is based on a single-muon and an electron-trijet trigger. A high-purity event selection with a signal fraction of 92% based on the identification of at least 2 b jets was used. The lepton-selection efficiencies and the lepton parts of the trigger efficiencies were determined in data with the tag-and-probe method using dileptonic Z-boson decays. Data-to-simulation scale factors close to unity were found and applied to the simulation as event weights (parametrised as a function of η^{μ} in the muon channel). The jet part of the electron-trijet trigger was determined in a factorisation approach using a single-lepton reference trigger. This technical work of the analysis contributed to the joint effort of the CMS top-quark group to determine efficiencies and helped to commission the triggers developed for recording top-quark events. The resulting scale factors were also used in other CMS analyses such as the most precise top-quark-mass

measurement to date [22].

The reconstruction of the $t\bar{t}$-event topology was performed with a kinematic fit constraining the reconstructed W-boson masses to $m_W = 80.4$ GeV and requiring equal reconstructed top- and antitop-quark masses. In at least 28% of the cases, the correct permutation was found, whereas the jets were misassigned in about 21% of the events, mostly due to interchanged b jets. For about 50% of the cases, the jet-parton matching was not successful, which can either arise from correctly reconstructed events with ambiguous jet-parton matching or from misreconstructed $t\bar{t}$ events (e.g. due to jets out of acceptance).

The reconstructed distributions were corrected for detector effects using a regularised unfolding technique that minimises the average global correlations between the bins. It was checked that no measurable bias was introduced in case of shape distortions and that the results were stable with respect to unfolding iterations.

The differential cross sections were normalised using the in-situ determined inclusive cross section, thereby reducing correlated systematic uncertainties. Thus, particular effort was made to determine shape uncertainties. The dominant uncertainties turned out to derive from model variations such as the Q^2 scale and the MadGraph matching threshold. The level of total systematic uncertainties was typically in the order of 3–10% and dominated over the statistical uncertainties of 2–5%.

The results were compared to different model predictions from Monte-Carlo event generators (MadGraph + pythia, powheg + pythia, mc@nlo + herwig) and fixed-order calculations (approximate NNLO or NLO+NNLL). Generally, a good agreement between data and SM predictions was observed. For the top-quark p_T distribution, the data was observed to be significantly softer than the predictions by the event generators, but the higher-order approximate NNLO calculation was seen to describe the data well. This means that top-quark-pair physics is well understood within the SM and no signs of new physics were observed at the current level of precision. The results were found to be consistent with those in the dilepton channel [6, 7] and by the ATLAS experiment [155], with this analysis being the most precise one.

Work performed in this thesis also contributed to the application of the analysis to data at $\sqrt{s} = 8$ TeV recorded by CMS in 2012 corresponding to 12.1 fb^{-1}, presented in [236]. This time, single-isolated-lepton triggers could be used in both channels. Small adaptations in the selection were done, especially to cope with the higher level of pile-up. Lepton-selection and trigger efficiencies and corresponding scale factors were again determined with the tag-and-probe method, but this time they were parametrised in two dimensions as a function of p_T and η of the lepton. The agreement of the normalised differential cross sections between data and SM predictions was observed to be very similar to the one in the 7 TeV analysis, especially also with respect to a better description of the top-quark-p_T distribution by an approx. NNLO calculation. Similar observations were made in the dilepton channel measured at 8 TeV [237]. It will be interesting to perform a measurement of the ratio of cross-section distributions at 7 and 8 TeV. In this way, further systematic uncertainties cancel [238].

For the future, different improvements of the analysis are envisaged. The measure-

ment is already now dominated by systematic uncertainties. Experimental systematic uncertainties are expected to reduce further with a larger dataset and improved understanding of the detector, although they are already now at a low level. To reduce the dominant model uncertainties related to the Q^2-scale and matching-threshold variations, the size of the corresponding simulated samples with a small number of events (especially for W/Z+jets) needs to be increased to reduce statistical fluctuations. The use of higher-order event generators might also reduce these uncertainties. Another option is the improvement of resolution and hence the decrease of bin-to-bin migration in order to reduce the dependence on uncertainties in the response matrix. The resolution of the variables obtained from the kinematic fit can be e.g. improved by discarding events with a low χ^2 fit probability, which includes a large fraction of badly-reconstructed events. Another option is to constrain the top-quark masses to a fixed, nominal value, which was found to reduce especially the permutations with swapped b jets. Further ideas include a correction for final-state radiation in the kinematic fit or inclusion of soft jets and correlations between jets and E_T^{miss} in the fit. The reduced level of migration can be either used to reduce systematic uncertainties or to increase the numbers of measurement intervals. A completely different approach without a kinematic fit is the attempt to define top quarks at hadron level (pseudo tops) to avoid hadronisation corrections [239, 240]. At large values of p_T^t and $m^{t\bar{t}}$, the efficiency and resolution is limited by jet-merging effects, which could be improved using dedicated reconstruction techniques such as top tagging with fat jets [153].

Results of this analysis can be used in fits to extract PDFs or α_s [241]. The analysis can be also extended to measure two-dimensional differential cross sections such as $\frac{d^2\sigma}{dy^{t\bar{t}} \cdot dm^{t\bar{t}}}$, which might be even more sensitive to PDFs. It can be also extended to measure further variables: e.g. $\Delta y^{t\bar{t}}$ or the top-quark polar angle in the $t\bar{t}$ rest frame, θ^*, to better separate the parton dynamics from the PDFs; the p_T and invariant mass of the $b\bar{b}$ system or the invariant mass of lepton and b jet $m^{\ell b}$, which are sensitive to narrow-width approximation and spin-correlation effects [242]; angles between top quarks or their decay products, which are sensitive to spin-correlations, decay properties, new physics or additional radiation [243, 244]; or the invariant mass of the top quarks and an additional jet $m^{t\bar{t}j}$, which might provide a novel method to measure the top-quark mass [245].

15.2 Charge Multiplication in Silicon Sensors

A comprehensive study was presented of the novel effect of radiation-induced charge multiplication (CM) in silicon sensors. This effect was studied as a possible solution to overcome the signal-to-noise degradation in silicon tracking sensors due to radiation damage, in particular charge-carrier trapping, at 1-MeV-neutron-equivalent fluences of about 10^{16} cm^{-2}, which are relevant for the innermost pixel layers at the high-luminosity upgrade of the LHC. The results were published in [230, 231, 235].

To investigate the CM effect, charge-collection measurements for different radiation (670, 830 and 1060 nm laser light, α and β particles) were performed with a TCT and

a ^{90}Sr β setup. The studies were done in n-type 75–150 μm thick epitaxial pad diodes irradiated with 24 GeV protons up to a neutron-equivalent fluence of 10^{16} cm^{-2}.

Exploiting the different penetration properties of the above-mentioned radiation, the CM region could be localised near the p$^+$ implant at the front side because the charge-collection efficiency (CCE) at high voltages was observed to increase for decreasing distance of charge deposition to the p$^+$ implant. CM was observed to set in unambiguously (indicated by CCE>1 for voltages below 1000 V) in highly irradiated sensors, starting from fluences of $4 \cdot 10^{15}$ cm^{-2}. It was observed to be higher for thinner sensors, which are expected to have a higher electric field above full depletion than thicker ones, and for oxygen-enriched material with a higher donor-introduction rate compared to standard material. The CCE annealing curve in the CM regime exhibited a similar behaviour as the one of U_{dep}. All this confirms the assumption of CM as a combined effect of thin sensors and large radiation-induced space-charge densities, leading to high electric fields. These aspects could be reproduced by a simple model with a linear electric field and donor introduction rates extrapolated from measurements at lower fluences. However, this model could not explain all details of the observations. For instance, against expectation, the CCE in the CM regime in sensors irradiated to $7 \cdot 10^{15}$ cm^{-2} was higher than for 10^{16} cm^{-2}. Also, the CCE was observed to decrease for decreasing temperature despite an increase of the ionisation rates. Thus, for a deeper understanding, an inclusion of trapping effects and in particular a better knowledge of the electric field is required. For this, effects arising from the high level of reverse current need to be taken into account, such as double junctions and possibly altered trapping times due to a non-uniform change of defect occupation. First simulations for n-in-p strip sensors can qualitatively describe observational data [232]. Experimentally, the recently developed method of Edge-TCT [233] allows further insights into the electric-field distribution and position-dependent charge-collection mechanisms in sensors in the CM regime.

Further properties of CM were measured. The collected charge in the CM regime was found to be proportional to the deposited charge, uniform over the sensor area at the percent level and stable over many days except for an increased rate of microdischarges setting in at high voltages.

The absolute amount of collected charge in response to MIP-like β particles at a fluence of 10^{16} cm^{-2} was found to exceed a mean of 9 ke (tentatively convertible to a most probable value (MPV) of 6.8 ke) for all thicknesses and materials at the highest measured voltage. Even at 600 V, the voltage limit for current LHC detectors, mean signals between 5 and 8 ke could be achieved (tentatively convertible to MPVs between 3.8 and 6 ke). These values are significantly higher than the readout threshold of 2.5–3 ke in current pixel detectors, and readout chips with a lower threshold are under development. This demonstrates that large enough signals are achievable in thin epitaxial silicon detectors at HL-LHC fluences.

However, to keep the threshold level (given a maximum tolerated noise occupancy), the noise must not increase too much in the CM regime. Two different scenarios were observed. For the TCT setup, only a moderate noise increase above the high pre-irradiated level ($\approx$ 25 ke) was observed in the CM regime, leading to a steady increase

of the signal-to-noise ratio (SNR) up to 900 V for 670 and 1060 nm laser light. In contrast, for the β setup with low intrinsic noise (2–3 ke), a strong noise increase was observed already starting from low voltages up to several 10 ke, along with a strong reverse-current increase. The dependence on material and thickness was the same as for the signal, indicating that the same mechanism is responsible for both. The SNR was observed to attain a maximum around 200–600 V and decreased for large voltages, which shows that the noise increased faster than the signal. To conclude, it depends on the readout and individual sensor type whether CM is beneficial for the SNR or not. The relative width of charge spectra in the CM regime remained constant in the case of laser light and β particles (within large uncertainties), which shows that statistical fluctuations in the CM process are small for the used setup. Microdischarges, which are especially detrimental for detector stability, readout electronics and discrimination between signal and noise, occasionally occurred at high voltages, but not in all sensors at 10^{16} cm^{-2}, and the rate was even observed to be higher at lower fluences. Thus, this is probably not a specific problem of operation in the CM regime and might be improved by device technology.

Pad diodes are a useful tool to study fundamental material and sensor properties. However, a transfer of the results to realistic segmented devices is difficult. The signal magnitude is expected to be similar, although a bending of the electric field lines near the implants and a non-constant weighting field can lead to different results (and in particular to non-uniform charge collection over the sensor area). The noise in segmented sensors is expected to be much lower (naively by a factor of the square root of the area ratio of ≈ 40, if shot noise dominates), so that it might be possible to keep the same readout threshold even in the CM regime. Measurements in highly-irradiated epitaxial pixel sensors are needed to find this out. Also, the influence of CM on the position resolution should be studied in segmented devices.

The observation of CM in highly-irradiated silicon sensors triggered a boost of research activities related to this topic. In addition to the study of CM in classical silicon sensors, a new field of *multiplication engineering* opened, which aims at developing completely new device structures with enhanced CM. Examples include: a change of processing parameters (implantation ion energy and diffusion time), implant geometry (width/pitch of strips) and sensor thickness [246,247]; completely new junction geometries by adding deep trenches to the n$^+$ electrode or adding a highly-doped p$^+$ layer between n$^+$ implant and low-doped p-type bulk (similar to APDs) [248–250]; the development of ultrafast thin epitaxial silicon detectors for timing applications [251]; or low-resistivity 3D detectors [250,252].

To conclude, this study has shown that high signals in silicon sensors at HL-LHC fluences are possible exploiting CM, and a better understanding of its formation and properties has been gained. For the application in real pixel detectors, the observed associated noise increase needs to be controlled, but due to the much smaller cell sizes compared to pad diodes and with the help of optimisation of device structure, readout and operation point, it seems achievable. CM in silicon tracking sensors has opened up a new exciting and dynamic research field with promising prospects to find radiation-hard detectors for high-luminosity colliders.

Appendix A

Result Tables and Correlation Matrices for $\frac{1}{\sigma} \cdot \frac{d\sigma}{dX}$

In Tabs. A.1 to A.3, the analysis results for all normalised differential distributions are summarised for the $t\bar{t}$ and top-quark quantities in the visible and full phase space at parton level and for the lepton and b-jet quantities in the visible phase space at particle level. For each bin, the central normalised cross-section value for the MAD-GRAPH prediction (MC) and the experimental result (exp) are quoted, as well as the corresponding statistical, systematic and total uncertainties.

In Tabs. A.4 to A.6, the statistical correlation matrices for the final results after normalisation are presented. The values are given in %.

The statistical covariance matrices **cov** can be obtained from these correlation matrices by rearranging Eq. 8.11 to:

$$\text{cov}_{\text{ij}} = \rho_{\text{ij}} \cdot \delta_{\text{i}} \cdot \delta_{\text{j}}. \tag{A.1}$$

Here, the correlation coefficients ρ_{ij} from Tabs. A.4 to A.6 are multiplied with the absolute statistical uncertainties δ_i, δ_j of the corresponding bins, which can be deduced from the relative statistical uncertainties and central values from Tabs. A.1 to A.3.

bin [GeV]	$\left(\frac{1}{\sigma}\frac{d\sigma}{dm^{t\bar{t}}}\right)_{MC}$ [GeV^{-1}]	$\left(\frac{1}{\sigma}\frac{d\sigma}{dm^{t\bar{t}}}\right)_{exp}$ [GeV^{-1}]	stat. [%]	sys. [%]	total [%]
345 to 400	0.004387	0.004302	5.4	10.3	11.6
400 to 470	0.004316	0.004430	4.9	8.0	9.4
470 to 550	0.002572	0.002513	5.2	10.0	11.2
550 to 650	0.001288	0.001252	5.6	10.6	11.9
650 to 800	0.000519	0.000515	6.1	7.6	9.8
800 to 1100	0.000123	0.000129	7.1	19.9	21.2
1100 to 1600	0.000014	0.000021	13.5	21.3	25.2

bin [GeV]	$\left(\frac{1}{\sigma}\frac{d\sigma}{dp_T^{t\bar{t}}}\right)_{MC}$ [GeV^{-1}]	$\left(\frac{1}{\sigma}\frac{d\sigma}{dp_T^{t\bar{t}}}\right)_{exp}$ [GeV^{-1}]	stat. [%]	sys. [%]	total [%]
0 to 20	0.014303	0.014180	4.2	12.0	12.7
20 to 45	0.011082	0.011775	3.5	7.1	7.9
45 to 75	0.005759	0.005862	3.8	8.9	9.7
75 to 120	0.002817	0.002692	4.3	13.9	14.5
120 to 190	0.001181	0.001135	4.5	8.2	9.3
190 to 300	0.000359	0.000305	6.3	16.2	17.4

bin	$\left(\frac{1}{\sigma}\frac{d\sigma}{dy^{t\bar{t}}}\right)_{MC}$	$\left(\frac{1}{\sigma}\frac{d\sigma}{dy^{t\bar{t}}}\right)_{exp}$	stat. [%]	sys. [%]	total [%]
-2.5 to -1.3	0.024756	0.023314	6.6	12.0	13.8
-1.3 to -0.9	0.202895	0.193961	3.4	6.0	6.9
-0.9 to -0.6	0.345553	0.332338	3.5	4.3	5.6
-0.6 to -0.3	0.447358	0.455695	3.1	3.2	4.4
-0.3 to 0.0	0.499325	0.505785	3.1	4.7	5.6
0.0 to 0.3	0.505010	0.550340	2.8	3.8	4.7
0.3 to 0.6	0.450145	0.450755	3.1	5.4	6.2
0.6 to 0.9	0.345083	0.336392	3.3	4.3	5.4
0.9 to 1.3	0.204939	0.199892	3.3	5.7	6.6
1.3 to 2.5	0.024514	0.020908	7.0	11.9	13.8

bin [GeV]	$\left(\frac{1}{\sigma}\frac{d\sigma}{dp_T^{t}}\right)_{MC}$ [GeV^{-1}]	$\left(\frac{1}{\sigma}\frac{d\sigma}{dp_T^{t}}\right)_{exp}$ [GeV^{-1}]	stat. [%]	sys. [%]	total [%]
0 to 60	0.003012	0.003669	2.6	4.1	4.9
60 to 100	0.005857	0.006062	2.4	5.2	5.7
100 to 150	0.005066	0.004834	2.3	2.7	3.6
150 to 200	0.003061	0.002846	2.6	4.8	5.5
200 to 260	0.001605	0.001430	2.9	5.0	5.8
260 to 320	0.000741	0.000631	3.7	8.7	9.4
320 to 400	0.000295	0.000235	5.7	10.1	11.6

bin	$\left(\frac{1}{\sigma}\frac{d\sigma}{dy^{t}}\right)_{MC}$	$\left(\frac{1}{\sigma}\frac{d\sigma}{dy^{t}}\right)_{exp}$	stat. [%]	sys. [%]	total [%]
-2.5 to -1.6	0.027730	0.029043	5.3	11.5	12.7
-1.6 to -1.2	0.157891	0.159814	2.9	6.1	6.8
-1.2 to -0.8	0.267341	0.278922	2.8	3.7	4.6
-0.8 to -0.4	0.355913	0.352371	2.6	3.8	4.6
-0.4 to 0.0	0.403630	0.377670	2.6	4.7	5.4
0.0 to 0.4	0.406499	0.406168	2.4	3.5	4.3
0.4 to 0.8	0.356712	0.365411	2.5	4.6	5.2
0.8 to 1.2	0.270889	0.275212	2.7	5.5	6.1
1.2 to 1.6	0.156691	0.154626	3.0	6.2	6.9
1.6 to 2.5	0.027543	0.028616	5.2	8.9	10.3

Table A.1: Normalised differential cross sections and uncertainties for the ℓ + jets channel in the visible phase space at parton level as a function of $t\bar{t}$ and top-quark quantities: $m^{t\bar{t}}$, $p_T^{t\bar{t}}$, $y^{t\bar{t}}$, p_T^{t} and y^{t}. The MC value refers to MADGRAPH.

bin [GeV]	$\left(\frac{1}{\sigma}\frac{d\sigma}{dm^{t\bar{t}}}\right)_{MC}$ [GeV^{-1}]	$\left(\frac{1}{\sigma}\frac{d\sigma}{dm^{t\bar{t}}}\right)_{exp}$ [GeV^{-1}]	stat. [%]	sys. [%]	total [%]
345 to 400	0.004899	0.004812	5.2	9.7	11.1
400 to 470	0.004477	0.004603	5.0	8.4	9.8
470 to 550	0.002516	0.002462	5.2	10.2	11.4
550 to 650	0.001175	0.001144	5.6	10.6	12.0
650 to 800	0.000435	0.000432	6.2	8.3	10.3
800 to 1100	0.000095	0.000099	7.1	20.0	21.2
1100 to 1600	0.000009	0.000014	13.5	19.4	23.7

bin [GeV]	$\left(\frac{1}{\sigma}\frac{d\sigma}{dp_T^{t\bar{t}}}\right)_{MC}$ [GeV^{-1}]	$\left(\frac{1}{\sigma}\frac{d\sigma}{dp_T^{t\bar{t}}}\right)_{exp}$ [GeV^{-1}]	stat. [%]	sys. [%]	total [%]
0 to 20	0.015187	0.015011	4.1	11.8	12.5
20 to 45	0.011405	0.012083	3.5	7.0	7.8
45 to 75	0.005723	0.005808	3.8	9.2	10.0
75 to 120	0.002706	0.002578	4.3	14.0	14.6
120 to 190	0.001077	0.001032	4.5	7.8	8.9
190 to 300	0.000291	0.000247	6.3	18.0	19.1

bin	$\left(\frac{1}{\sigma}\frac{d\sigma}{dy^{t\bar{t}}}\right)_{MC}$	$\left(\frac{1}{\sigma}\frac{d\sigma}{dy^{t\bar{t}}}\right)_{exp}$	stat. [%]	sys. [%]	total [%]
-2.5 to -1.3	0.058060	0.055296	6.4	10.8	12.5
-1.3 to -0.9	0.224558	0.217093	3.4	5.8	6.7
-0.9 to -0.6	0.321032	0.312239	3.6	4.4	5.7
-0.6 to -0.3	0.388325	0.400025	3.1	3.3	4.5
-0.3 to 0.0	0.424172	0.434507	3.1	4.1	5.1
0.0 to 0.3	0.425370	0.468782	2.8	3.8	4.8
0.3 to 0.6	0.388678	0.393596	3.1	5.9	6.7
0.6 to 0.9	0.321439	0.316880	3.4	4.7	5.8
0.9 to 1.3	0.225316	0.222247	3.3	5.8	6.6
1.3 to 2.5	0.057744	0.049806	6.8	9.7	11.9

bin [GeV]	$\left(\frac{1}{\sigma}\frac{d\sigma}{dp_T^t}\right)_{MC}$ [GeV^{-1}]	$\left(\frac{1}{\sigma}\frac{d\sigma}{dp_T^t}\right)_{exp}$ [GeV^{-1}]	stat. [%]	sys. [%]	total [%]
0 to 60	0.003806	0.004536	2.5	3.6	4.4
60 to 100	0.006574	0.006658	2.4	4.9	5.5
100 to 150	0.005077	0.004740	2.4	3.2	4.0
150 to 200	0.002748	0.002501	2.6	5.1	5.8
200 to 260	0.001195	0.001042	2.9	5.5	6.2
260 to 320	0.000454	0.000378	3.7	8.2	9.0
320 to 400	0.000154	0.000120	5.8	9.5	11.1

bin	$\left(\frac{1}{\sigma}\frac{d\sigma}{dy^t}\right)_{MC}$	$\left(\frac{1}{\sigma}\frac{d\sigma}{dy^t}\right)_{exp}$	stat. [%]	sys. [%]	total [%]
-2.5 to -1.6	0.062394	0.065109	5.1	10.3	11.5
-1.6 to -1.2	0.171139	0.172594	2.9	5.9	6.6
-1.2 to -0.8	0.252392	0.262370	2.8	4.1	5.0
-0.8 to -0.4	0.320539	0.316197	2.6	3.8	4.6
-0.4 to 0.0	0.358094	0.333846	2.7	4.8	5.5
0.0 to 0.4	0.359286	0.357691	2.5	2.6	3.6
0.4 to 0.8	0.320713	0.327341	2.5	5.2	5.8
0.8 to 1.2	0.252567	0.255667	2.7	5.0	5.7
1.2 to 1.6	0.170898	0.168034	3.0	5.7	6.4
1.6 to 2.5	0.062206	0.064393	5.0	7.1	8.7

Table A.2: Normalised differential cross sections and uncertainties for the ℓ+jets channel in the full phase space at parton level as a function of $t\bar{t}$ and top-quark quantities: $m^{t\bar{t}}$, $p_T^{t\bar{t}}$, $y^{t\bar{t}}$, p_T^t and y^t. The MC value refers to MADGRAPH.

bin [GeV]	$\left(\frac{1}{\sigma}\frac{d\sigma}{dp_T^\ell}\right)_{MC}$ [GeV^{-1}]	$\left(\frac{1}{\sigma}\frac{d\sigma}{dp_T^\ell}\right)_{exp}$ [GeV^{-1}]	stat. [%]	sys. [%]	total [%]
30 to 35	0.023135	0.022467	2.4	6.1	6.6
35 to 40	0.021859	0.022432	2.5	3.8	4.5
40 to 45	0.019937	0.021218	2.5	6.0	6.5
45 to 50	0.017849	0.018795	2.6	3.7	4.5
50 to 60	0.015048	0.014960	2.1	2.2	3.0
60 to 70	0.011546	0.011378	2.3	3.6	4.3
70 to 80	0.008683	0.008993	2.5	4.3	5.0
80 to 100	0.005456	0.005349	2.4	3.7	4.4
100 to 120	0.002857	0.002738	3.3	5.6	6.5
120 to 150	0.001300	0.001211	3.9	5.5	6.7
150 to 200	0.000414	0.000358	5.8	8.5	10.3

bin	$\left(\frac{1}{\sigma}\frac{d\sigma}{d\eta^\ell}\right)_{MC}$	$\left(\frac{1}{\sigma}\frac{d\sigma}{d\eta^\ell}\right)_{exp}$	stat. [%]	sys. [%]	total [%]
-2.1 to -1.8	0.078139	0.082910	5.4	10.0	11.4
-1.8 to -1.5	0.123611	0.134900	4.1	6.1	7.4
-1.5 to -1.2	0.182927	0.173754	3.3	8.3	8.9
-1.2 to -0.9	0.244145	0.253799	2.8	4.2	5.1
-0.9 to -0.6	0.306812	0.302701	2.4	4.2	4.8
-0.6 to -0.3	0.353602	0.349279	2.2	2.9	3.6
-0.3 to 0.0	0.373260	0.352434	2.3	3.8	4.4
0.0 to 0.3	0.375999	0.368476	2.3	3.2	3.9
0.3 to 0.6	0.348645	0.356583	2.2	3.4	4.0
0.6 to 0.9	0.307721	0.310965	2.3	2.2	3.2
0.9 to 1.2	0.247001	0.234381	2.7	4.3	5.1
1.2 to 1.5	0.184545	0.194789	3.2	6.8	7.5
1.5 to 1.8	0.128012	0.141218	4.1	5.1	6.5
1.8 to 2.1	0.078914	0.077145	5.4	12.8	13.9

bin [GeV]	$\left(\frac{1}{\sigma}\frac{d\sigma}{dp_T^b}\right)_{MC}$ [GeV^{-1}]	$\left(\frac{1}{\sigma}\frac{d\sigma}{dp_T^b}\right)_{exp}$ [GeV^{-1}]	stat. [%]	sys. [%]	total [%]
30 to 60	0.012561	0.013534	1.0	4.5	4.6
60 to 95	0.009467	0.009594	1.3	2.6	2.9
95 to 140	0.004236	0.003824	1.8	3.6	4.0
140 to 200	0.001252	0.001073	2.6	9.7	10.0
200 to 400	0.000125	0.000104	5.3	16.3	17.1

bin	$\left(\frac{1}{\sigma}\frac{d\sigma}{d\eta^b}\right)_{MC}$	$\left(\frac{1}{\sigma}\frac{d\sigma}{d\eta^b}\right)_{exp}$	stat. [%]	sys. [%]	total [%]
-2.4 to -1.5	0.086963	0.101215	2.1	4.2	4.7
-1.5 to -1.0	0.202040	0.201326	1.7	2.8	3.3
-1.0 to -0.5	0.292136	0.286412	1.4	2.2	2.6
-0.5 to 0.0	0.345742	0.339115	1.3	2.5	2.8
0.0 to 0.5	0.347446	0.329709	1.3	3.2	3.5
0.5 to 1.0	0.293696	0.284156	1.5	3.0	3.3
1.0 to 1.5	0.203470	0.205945	1.8	2.6	3.1
1.5 to 2.4	0.088298	0.095083	2.1	6.1	6.5

Table A.3: Normalised differential cross sections and uncertainties for the ℓ + jets channel in the visible phase space at particle level as a function of the lepton and b-jet quantities: p_T^ℓ, η^ℓ, p_T^b and η^b. The MC value refers to MADGRAPH.

Bins $m^{t\bar{t}}$[GeV]	345 − 400	400 − 470	470 − 550	550 − 650	650 − 800	800 − 1100	1100 − 1600
345 − 400	*100.0*	-82.7	4.8	6.4	-15.2	-5.5	-4.4
400 − 470	-82.7	*100.0*	-48.5	-4.9	12.7	-3.5	1.2
470 − 550	4.8	-48.5	*100.0*	-46.1	-7.5	4.9	-7.2
550 − 650	6.4	-4.9	-46.1	*100.0*	-40.0	-17.2	5.1
650 − 800	-15.2	12.7	-7.5	-40.0	*100.0*	-25.4	-31.4
800 − 1100	-5.5	-3.5	4.9	-17.2	-25.4	*100.0*	26.2
1100 − 1600	-4.4	1.2	-7.2	5.1	-31.4	26.2	*100.0*

Bins $p_T^{t\bar{t}}$[GeV]	0 − 20	20 − 45	45 − 75	75 − 120	120 − 190	190 − 300
0 − 20	*100.0*	-77.8	-66.0	19.1	4.3	-16.8
20 − 45	-77.8	*100.0*	26.0	-59.2	-5.0	12.8
45 − 75	-66.0	26.0	*100.0*	-4.5	-43.5	2.3
75 − 120	19.1	-59.2	-4.5	*100.0*	11.8	-42.4
120 − 190	4.3	-5.0	-43.5	11.8	*100.0*	-23.3
190 − 300	-16.8	12.8	2.3	-42.4	-23.3	*100.0*

Bins $y^{t\bar{t}}$	-2.5 − -1.3	-1.3 − -0.9	-0.9 − -0.6	-0.6 − -0.3	-0.3 − 0.0	0.0 − 0.3	0.3 − 0.6	0.6 − 0.9	0.9 − 1.3	1.3 − 2.5
-2.5 − -1.3	*100.0*	-5.3	-26.2	1.1	-3.8	-7.5	-0.8	-4.0	-6.2	0.2
-1.3 − -0.9	-5.3	*100.0*	-0.3	-37.3	-2.9	0.7	-8.5	-9.3	-6.3	-0.9
-0.9 − -0.6	-26.2	-0.3	*100.0*	-17.0	-34.7	-3.7	-5.3	-5.8	-4.3	-1.4
-0.6 − -0.3	1.1	-37.3	-17.0	*100.0*	-17.9	-34.0	1.3	-2.6	-7.1	-2.8
-0.3 − 0.0	-3.8	-2.9	-34.7	-17.9	*100.0*	-23.1	-34.2	3.7	-3.5	-4.4
0.0 − 0.3	-7.5	0.7	-3.7	-34.0	-23.1	*100.0*	-15.1	-32.1	-3.4	-1.6
0.3 − 0.6	-0.8	-8.5	-5.3	1.3	-34.2	-15.1	*100.0*	-18.8	-32.3	-2.1
0.6 − 0.9	-4.0	-9.3	-5.8	-2.6	3.7	-32.1	-18.8	*100.0*	-3.0	-30.3
0.9 − 1.3	-6.2	-6.3	-4.3	-7.1	-3.5	-3.4	-32.3	-3.0	*100.0*	-7.9
1.3 − 2.5	0.2	-0.9	-1.4	-2.8	-4.4	-1.6	-2.1	-30.3	-7.9	*100.0*

Bins p_T^{t}[GeV]	0 − 60	60 − 100	100 − 150	150 − 200	200 − 260	260 − 320	320 − 400
0 − 60	*100.0*	-53.4	-45.1	3.7	-3.9	-2.7	-4.3
60 − 100	-53.4	*100.0*	-25.9	-33.7	0.1	-3.7	-4.3
100 − 150	-45.1	-25.9	*100.0*	-19.6	-20.1	-1.2	-11.8
150 − 200	3.7	-33.7	-19.6	*100.0*	-16.5	-26.2	-4.4
200 − 260	-3.9	0.1	-20.1	-16.5	*100.0*	11.7	-31.4
260 − 320	-2.7	-3.7	-1.2	-26.2	11.7	*100.0*	-0.6
320 − 400	-4.3	-4.3	-11.8	-4.4	-31.4	-0.6	*100.0*

Bins y^{t}	-2.5 − -1.6	-1.6 − -1.2	-1.2 − -0.8	-0.8 − -0.4	-0.4 − 0.0	0.0 − 0.4	0.4 − 0.8	0.8 − 1.2	1.2 − 1.6	1.6 − 2.5
-2.5 − -1.6	*100.0*	3.7	-34.2	-3.1	-0.6	-3.6	0.6	-3.3	-4.2	1.4
-1.6 − -1.2	3.7	*100.0*	3.2	-37.9	-4.7	2.2	-6.1	-8.6	-4.6	0.6
-1.2 − -0.8	-34.2	3.2	*100.0*	-21.0	-31.3	-5.5	-6.2	-4.9	-2.9	-0.9
-0.8 − -0.4	-3.1	-37.9	-21.0	*100.0*	-21.9	-29.2	-0.1	-3.2	-4.5	-1.8
-0.4 − 0.0	-0.6	-4.7	-31.3	-21.9	*100.0*	-27.2	-29.3	1.8	-2.0	-1.6
0.0 − 0.4	-3.6	2.2	-5.5	-29.2	-27.2	*100.0*	-19.6	-29.5	-4.9	1.9
0.4 − 0.8	0.6	-6.1	-6.2	-0.1	-29.3	-19.6	*100.0*	-23.3	-31.7	-6.0
0.8 − 1.2	-3.3	-8.6	-4.9	-3.2	1.8	-29.5	-23.3	*100.0*	-0.9	-36.8
1.2 − 1.6	-4.2	-4.6	-2.9	-4.5	-2.0	-4.9	-31.7	-0.9	*100.0*	-0.5
1.6 − 2.5	1.4	0.6	-0.9	-1.8	-1.6	1.9	-6.0	-36.8	-0.5	*100.0*

Table A.4: Correlation matrices (statistical, in %) for the ℓ+jets channel in the visible phase space at parton level for $t\bar{t}$ and top-quark quantities.

Bins $m^{t\bar{t}}$[GeV]	345 – 400	400 – 470	470 – 550	550 – 650	650 – 800	800 – 1100	1100 – 1600
345 − 400	*100.0*	-84.6	2.9	4.7	-16.6	-6.0	-4.3
400 − 470	-84.6	*100.0*	-46.4	-3.6	14.1	-1.4	2.7
470 − 550	2.9	-46.4	*100.0*	-45.6	-6.6	6.2	-6.0
550 − 650	4.7	-3.6	-45.6	*100.0*	-39.0	-15.9	6.1
650 − 800	-16.6	14.1	-6.6	-39.0	*100.0*	-23.6	-29.9
800 − 1100	-6.0	-1.4	6.2	-15.9	-23.6	*100.0*	27.1
1100 − 1600	-4.3	2.7	-6.0	6.1	-29.9	27.1	*100.0*

Bins $p_T^{t\bar{t}}$[GeV]	0 – 20	20 – 45	45 – 75	75 – 120	120 – 190	190 – 300
0 − 20	*100.0*	-79.5	-66.9	17.9	3.0	-15.9
20 − 45	-79.5	*100.0*	27.3	-58.5	-4.5	15.1
45 − 75	-66.9	27.3	*100.0*	-3.7	-42.3	5.0
75 − 120	17.9	-58.5	-3.7	*100.0*	11.6	-40.2
120 − 190	3.0	-4.5	-42.3	11.6	*100.0*	-21.3
190 − 300	-15.9	15.1	5.0	-40.2	-21.3	*100.0*

Bins $y^{t\bar{t}}$	-2.5 – -1.3	-1.3 – -0.9	-0.9 – -0.6	-0.6 – -0.3	-0.3 – 0.0	0.0 – 0.3	0.3 – 0.6	0.6 – 0.9	0.9 – 1.3	1.3 – 2.5
-2.5 − -1.3	*100.0*	-13.8	-32.9	-6.6	-11.4	-15.9	-8.4	-10.4	-14.5	-7.8
-1.3 − -0.9	-13.8	*100.0*	1.5	-35.9	-1.6	2.1	-7.2	-6.8	-6.7	-8.8
-0.9 − -0.6	-32.9	1.5	*100.0*	-12.5	-29.2	1.0	-1.1	-0.6	-1.9	-7.4
-0.6 − -0.3	-6.6	-35.9	-12.5	*100.0*	-13.6	-28.6	4.9	2.1	-5.2	-10.2
-0.3 − 0.0	-11.4	-1.6	-29.2	-13.6	*100.0*	-17.7	-29.1	8.4	-1.5	-11.7
0.0 − 0.3	-15.9	2.1	1.0	-28.6	-17.7	*100.0*	-10.3	-25.0	-1.0	-9.6
0.3 − 0.6	-8.4	-7.2	-1.1	4.9	-29.1	-10.3	*100.0*	-13.2	-29.8	-9.5
0.6 − 0.9	-10.4	-6.8	-0.6	2.1	8.4	-25.0	-13.2	*100.0*	0.1	-36.7
0.9 − 1.3	-14.5	-6.7	-1.9	-5.2	-1.5	-1.0	-29.8	0.1	*100.0*	-15.9
1.3 − 2.5	-7.8	-8.8	-7.4	-10.2	-11.7	-9.6	-9.5	-36.7	-15.9	*100.0*

Bins p_T^{t}[GeV]	0 – 60	60 – 100	100 – 150	150 – 200	200 – 260	260 – 320	320 – 400
0 − 60	*100.0*	-60.7	-48.6	0.9	-6.4	-4.0	-2.5
60 − 100	-60.7	*100.0*	-23.1	-31.9	1.5	-1.9	-0.3
100 − 150	-48.6	-23.1	*100.0*	-15.2	-15.8	2.3	-6.2
150 − 200	0.9	-31.9	-15.2	*100.0*	-13.4	-22.8	0.1
200 − 260	-6.4	1.5	-15.8	-13.4	*100.0*	13.9	-26.5
260 − 320	-4.0	-1.9	2.3	-22.8	13.9	*100.0*	2.8
320 − 400	-2.5	-0.3	-6.2	0.1	-26.5	2.8	*100.0*

Bins y^{t}	-2.5 – -1.6	-1.6 – -1.2	-1.2 – -0.8	-0.8 – -0.4	-0.4 – 0.0	0.0 – 0.4	0.4 – 0.8	0.8 – 1.2	1.2 – 1.6	1.6 – 2.5
-2.5 − -1.6	*100.0*	-3.8	-40.6	-10.4	-7.8	-11.6	-6.9	-9.2	-11.5	-6.7
-1.6 − -1.2	-3.8	*100.0*	4.8	-37.1	-4.6	2.3	-5.6	-6.2	-5.6	-6.9
-1.2 − -0.8	-40.6	4.8	*100.0*	-16.0	-26.4	-1.3	-1.6	1.1	-0.6	-6.6
-0.8 − -0.4	-10.4	-37.1	-16.0	*100.0*	-18.7	-25.7	3.0	1.7	-3.4	-8.8
-0.4 − 0.0	-7.8	-4.6	-26.4	-18.7	*100.0*	-24.2	-25.8	6.1	-1.2	-8.7
0.0 − 0.4	-11.6	2.3	-1.3	-25.7	-24.2	*100.0*	-16.2	-23.6	-4.0	-5.7
0.4 − 0.8	-6.9	-5.6	-1.6	3.0	-25.8	-16.2	*100.0*	-17.2	-30.1	-13.5
0.8 − 1.2	-9.2	-6.2	1.1	1.7	6.1	-23.6	-17.2	*100.0*	1.9	-42.7
1.2 − 1.6	-11.5	-5.6	-0.6	-3.4	-1.2	-4.0	-30.1	1.9	*100.0*	-7.4
1.6 − 2.5	-6.7	-6.9	-6.6	-8.8	-8.7	-5.7	-13.5	-42.7	-7.4	*100.0*

Table A.5: Correlation matrices (statistical, in %) for the ℓ + jets channel in the full phase space at parton level for $t\bar{t}$ and top-quark quantities

Bins $p_{\mathrm{T}}^{\ell}[\mathrm{GeV}]$	30 − 35	35 − 40	40 − 45	45 − 50	50 − 60	60 − 70	70 − 80	80 − 100	100 − 120	120 − 150	150 − 200
30 − 35	100.0	-15.0	-18.4	-17.4	-13.0	-10.6	-6.6	-11.2	-3.7	-4.1	-10.6
35 − 40	-15.0	100.0	-10.4	-12.2	-17.2	-10.5	-14.7	-11.2	-9.1	-10.2	-5.4
40 − 45	-18.4	-10.4	100.0	-12.8	-15.3	-10.9	-6.1	-7.5	-5.7	-10.9	-12.7
45 − 50	-17.4	-12.2	-12.8	100.0	-18.2	-11.8	-3.4	-6.4	-7.5	-2.4	-2.2
50 − 60	-13.0	-17.2	-15.3	-18.2	100.0	-15.9	-16.0	-13.0	-10.7	-0.4	-3.9
60 − 70	-10.6	-10.5	-10.9	-11.8	-15.9	100.0	-9.3	-19.0	-5.1	-7.2	-7.6
70 − 80	-6.6	-14.7	-6.1	-3.4	-16.0	-9.3	100.0	-13.5	-3.4	-9.1	-11.7
80 − 100	-11.2	-11.2	-7.5	-6.4	-13.0	-19.0	-13.5	100.0	-13.4	-6.6	-2.6
100 − 120	-3.7	-9.1	-5.7	-7.5	-10.7	-5.1	-3.4	-13.4	100.0	-2.9	-11.4
120 − 150	-4.1	-10.2	-10.9	-2.4	-0.4	-7.2	-9.1	-6.6	-2.9	100.0	6.1
150 − 200	-10.6	-5.4	-12.7	-2.2	-3.9	-7.6	-11.7	-2.6	-11.4	6.1	100.0

Bins η^{ℓ}	-2.1 − -1.8	-1.8 − -1.5	-1.5 − -1.2	-1.2 − -0.9	-0.9 − -0.6	-0.6 − -0.3	-0.3 − 0.0	0.0 − 0.3	0.3 − 0.6	0.6 − 0.9	0.9 − 1.2	1.2 − 1.5	1.5 − 1.8	1.8 − 2.1
-2.1 − -1.8	100	-2.2	-5.8	-5.7	-5.9	-6.8	-10.3	-7.9	-10.6	-2.8	2.0	-7.5	3.5	-1.1
-1.8 − -1.5	-2.2	100	-6.0	-4.4	-2.1	-10.5	-10.7	-11.9	-5.1	-7.7	-3.3	-7.6	-2.5	-5.0
-1.5 − -1.2	-5.8	-6.0	100	-8.6	-5.2	-7.2	-5.8	-4.5	-1.1	-13.7	-9.6	-7.4	-10.6	-1.4
-1.2 − -0.9	-5.7	-4.4	-8.6	100	-6.2	-8.0	-11.0	-12.7	-10.8	-4.8	-6.7	-14.6	-4.1	-8.4
-0.9 − -0.6	-5.9	-2.1	-5.2	-6.2	100	-17.0	-4.6	-5.6	-16.8	-9.2	-7.9	-7.9	-9.7	-10.4
-0.6 − -0.3	-6.8	-10.5	-7.2	-8.0	-17.0	100	-5.7	-12.2	-14.0	-3.1	-11.9	-2.8	-13.6	-1.5
-0.3 − 0.0	-10.3	-10.7	-5.8	-11.0	-4.6	-5.7	100	-12.7	-12.5	-14.7	-11.0	-13.8	-7.7	-4.7
0.0 − 0.3	-7.9	-11.9	-4.5	-12.7	-5.6	-12.2	-12.7	100	-10.3	-15.3	-12.6	-4.6	-8.6	-6.1
0.3 − 0.6	-10.6	-5.1	-1.1	-10.8	-16.8	-14.0	-12.5	-10.3	100	-10.4	-5.4	-4.4	-8.3	-3.9
0.6 − 0.9	-2.8	-7.7	-13.7	-4.8	-9.2	-3.1	-14.7	-15.3	-10.4	100	-1.4	-7.0	-9.6	-2.5
0.9 − 1.2	2.0	-3.3	-9.6	-6.7	-7.9	-11.9	-11.0	-12.6	-5.4	-1.4	100	-11.1	-5.2	-6.7
1.2 − 1.5	-7.5	-7.6	-7.4	-14.6	-7.9	-2.8	-13.8	-4.6	-4.4	-7.0	-11.1	100	-0.2	-3.7
1.5 − 1.8	3.5	-2.5	-10.6	-4.1	-9.7	-13.6	-7.7	-8.6	-8.3	-9.6	-5.2	-0.2	100	-4.8
1.8 − 2.1	-1.1	-5.0	-1.4	-8.4	-10.4	-1.5	-4.7	-6.1	-3.9	-2.5	-6.7	-3.7	-4.8	100

Bins $p_{T}^{b}[\mathrm{GeV}]$	30 − 60	60 − 95	95 − 140	140 − 200	200 − 400
30 − 60	100.0	-71.4	-19.7	-13.7	-19.9
60 − 95	-71.4	100.0	-39.3	-14.6	3.9
95 − 140	-19.7	-39.3	100.0	-16.1	-19.7
140 − 200	-13.7	-14.6	-16.1	100.0	5.1
200 − 400	-19.9	3.9	-19.7	5.1	100.0

Bins η^{b}	-2.4 − -1.5	-1.5 − -1.0	-1.0 − -0.5	-0.5 − 0.0	0.0 − 0.5	0.5 − 1.0	1.0 − 1.5	1.5 − 2.4
-2.4 − -1.5	100.0	-10.6	-12.2	-18.6	-15.4	-13.9	-12.6	-10.2
-1.5 − -1.0	-10.6	100.0	-6.3	-23.2	-18.5	-12.1	-5.4	-7.6
-1.0 − -0.5	-12.2	-6.3	100.0	-18.0	-20.9	-19.2	-14.0	-9.2
-0.5 − 0.0	-18.6	-23.2	-18.0	100.0	-12.9	-13.1	-13.8	-16.3
0.0 − 0.5	-15.4	-18.5	-20.9	-12.9	100.0	-18.7	-19.8	-7.3
0.5 − 1.0	-13.9	-12.1	-19.2	-13.1	-18.7	100.0	-9.7	-20.3
1.0 − 1.5	-12.6	-5.4	-14.0	-13.8	-19.8	-9.7	100.0	-16.4
1.5 − 2.4	-10.2	-7.6	-9.2	-16.3	-7.3	-20.3	-16.4	100.0

Table A.6: Correlation matrices (statistical, in %) for the ℓ+jets channel in the visible phase space at particle level for the lepton and b-jet quantities.

Appendix B

Individual Components of the Lepton-Selection Efficiencies

As introduced in Sec. 6, the muon- and electron-selection efficiency is factorised into its individual components (see Eq 6.6 and 6.7): identification (ID) and relative-isolation efficiency for the muon channel and impact-parameter (d_0), CiC-identification ($\mathrm{ID}_{\mathrm{CiC}}$), relative-isolation and conversion-rejection efficiency for the electron channel. These individual contributions are shown separately in the following as a function of p_{T} and η of the lepton, the number of reconstructed primary vertices in the event and the distance ΔR between the lepton and the closest jet.
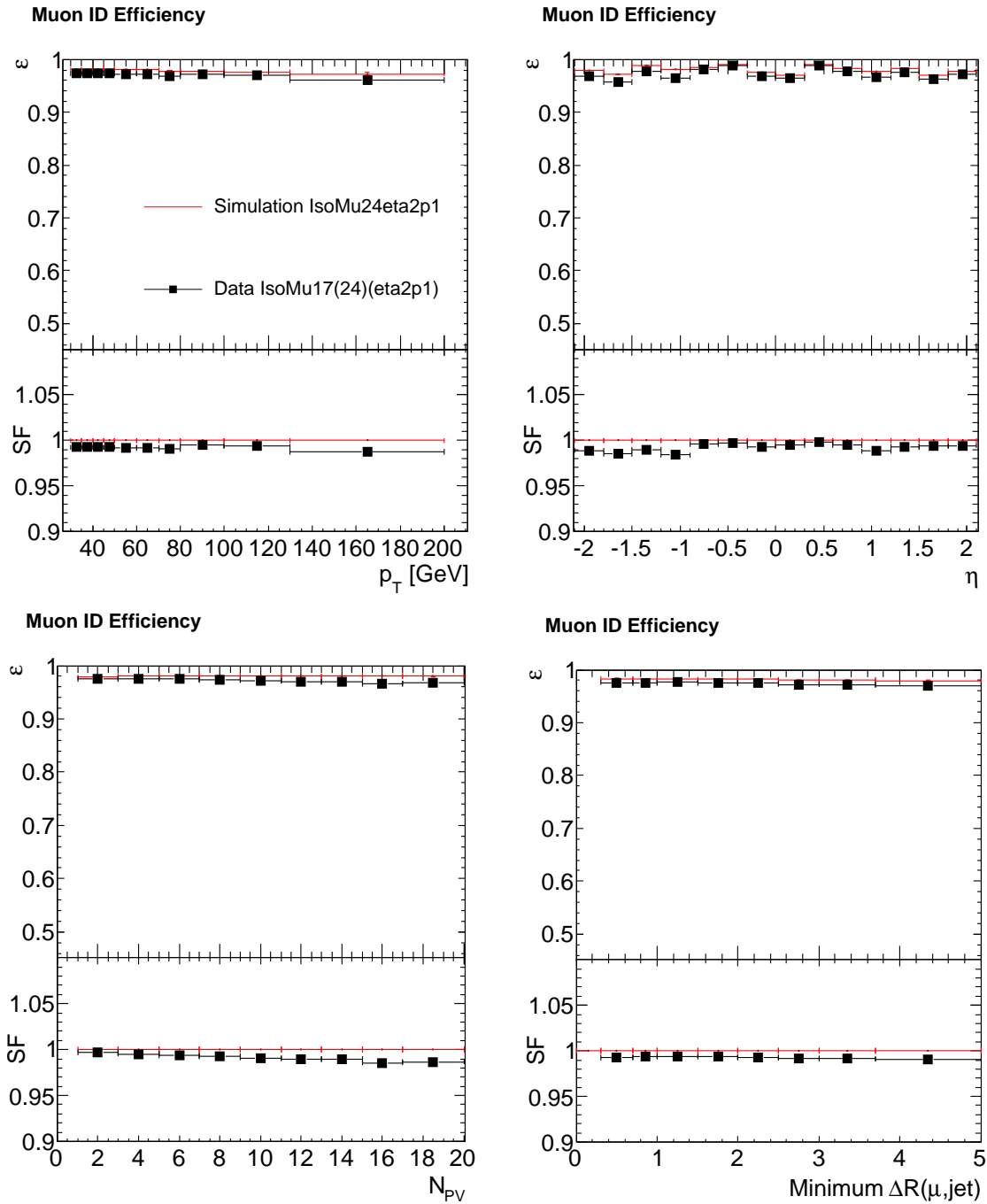
Figure B.1: The muon-ID efficiency for simulation and data with corresponding SF as a function of p_T and η of the muon (*first row*) and the number of primary vertices in the event and the distance between the muon and the closest jet ΔR (*second row*). A preselection of $I_{rel} < 0.2$ is applied to the ΔR distribution.
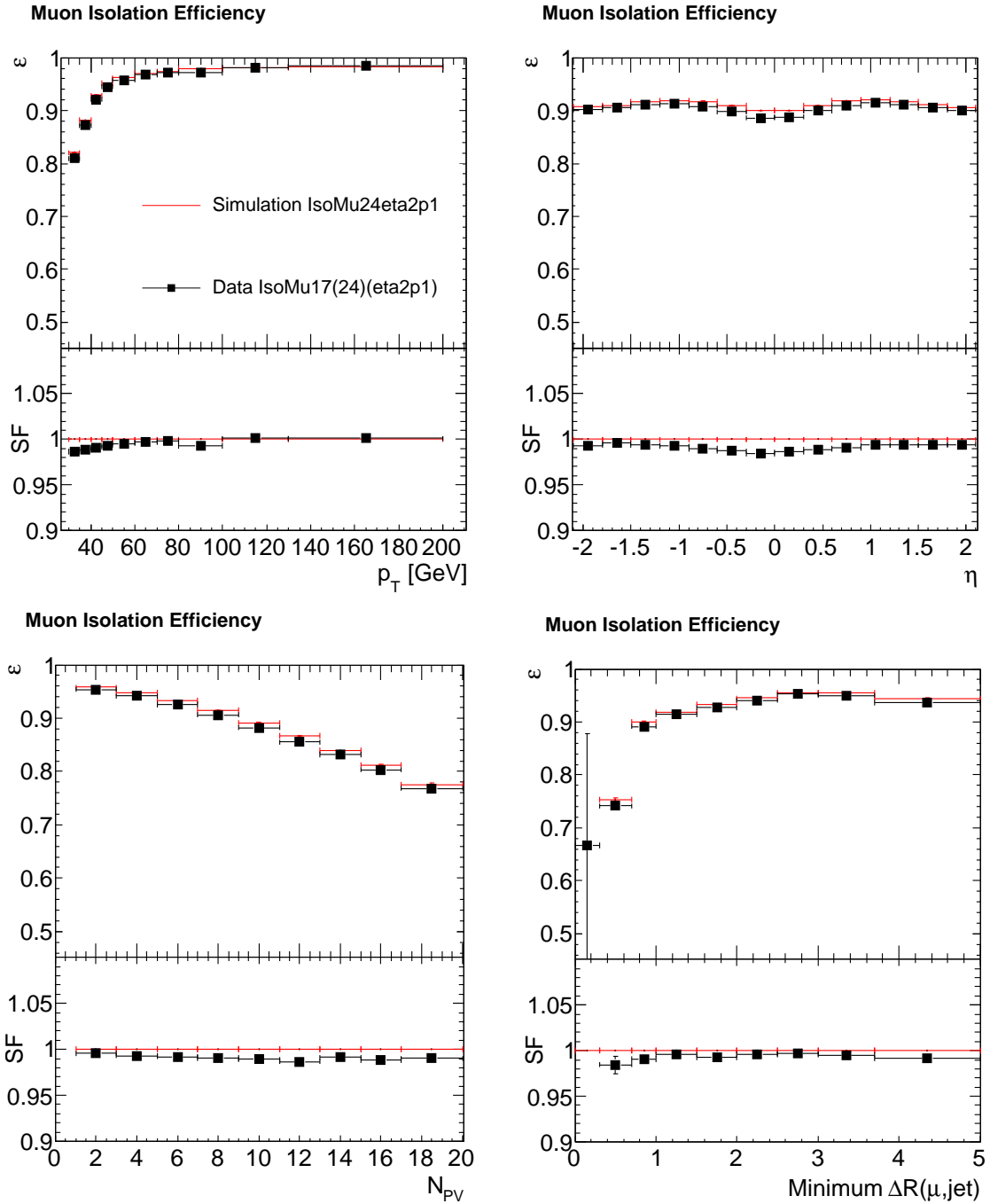
Figure B.2: The muon-relative-isolation efficiency for simulation and data with corresponding SF as a function of p_T and η of the muon (*first row*) and the number of primary vertices in the event and the distance between the muon and the closest jet ΔR (*second row*). A preselection of $I_{rel} < 0.2$ is applied to the ΔR distribution.
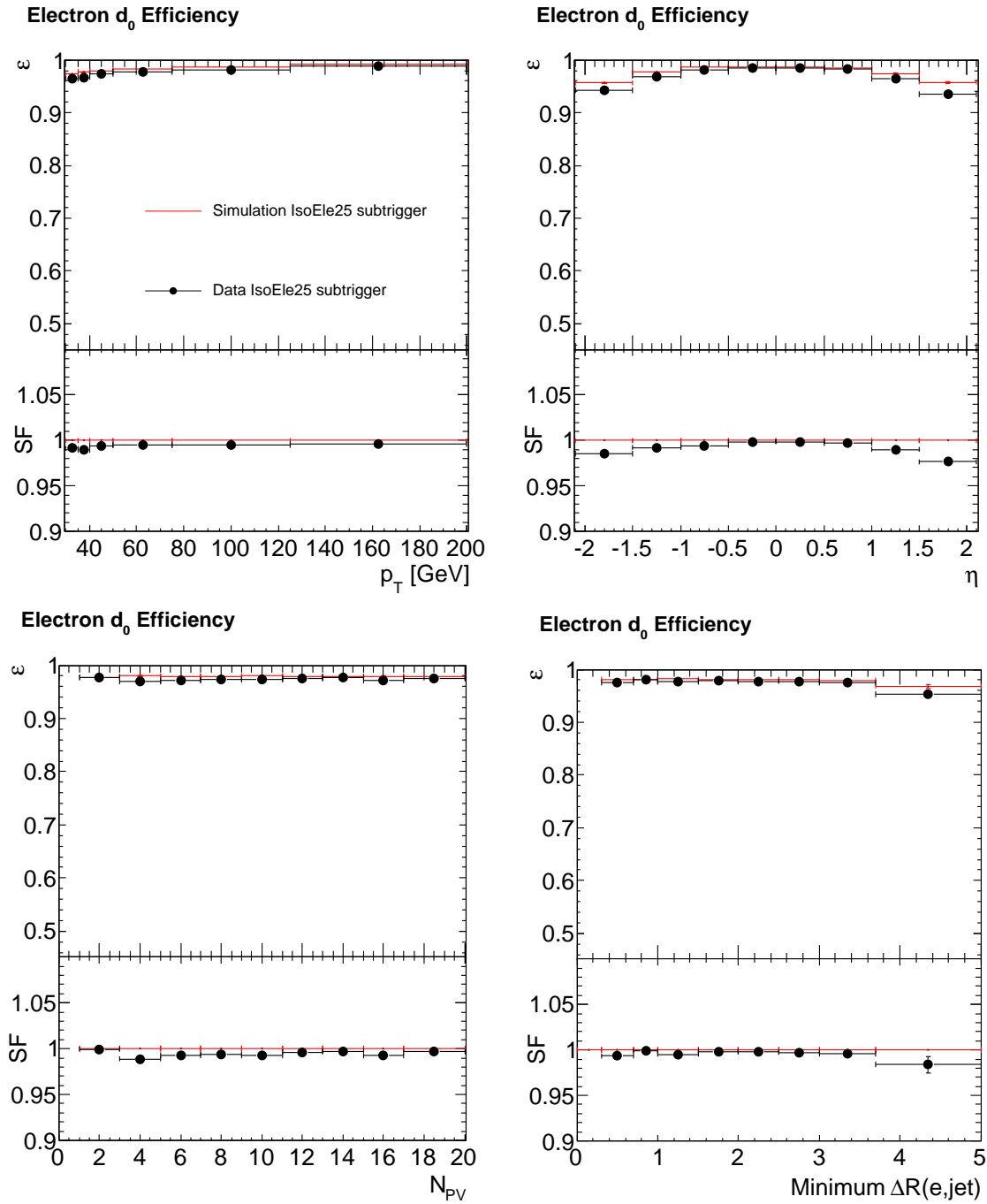
Figure B.3: The electron-d_0 efficiency obtained with the IsoEle25TriJet cross trigger for simulation and data with corresponding SF as a function of p_T and η of the electron (*first row*) and the number of primary vertices in the event and the distance between the electron and the closest jet ΔR (*second row*). A preselection of $I_{rel} < 0.2$ is applied to the ΔR distribution.
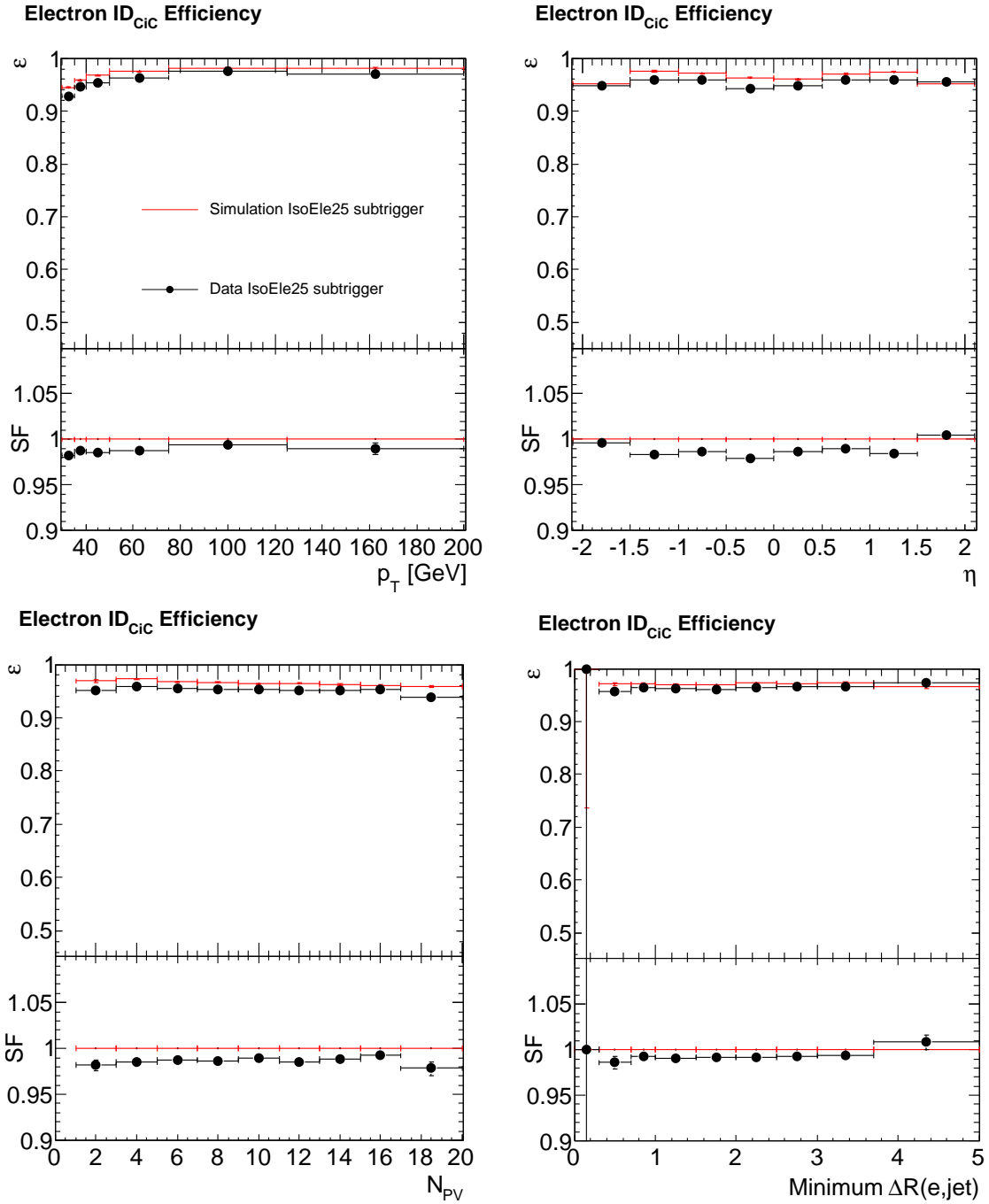
Figure B.4: The electron-ID$_{\text{CiC}}$ efficiency obtained with the IsoEle25TriJet cross trigger for simulation and data with corresponding SF as a function of p_{T} and η of the electron (*first row*) and the number of primary vertices in the event and the distance between the electron and the closest jet ΔR (*second row*). A preselection of $I_{rel} < 0.2$ is applied to the ΔR distribution.
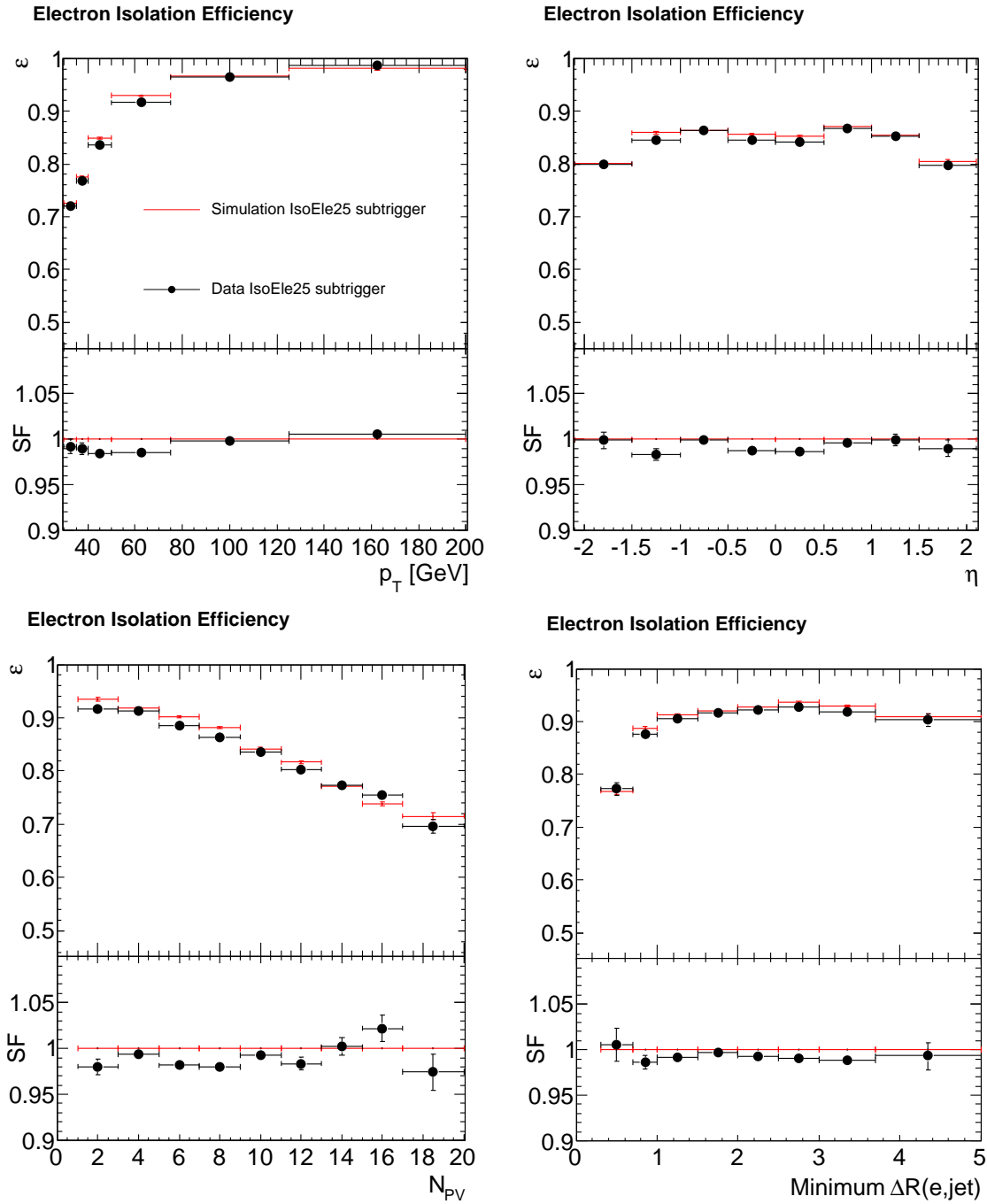
Figure B.5: The electron-relative-isolation efficiency obtained with the IsoEle25TriJet cross trigger for simulation and data with corresponding SF as a function of p_T and η of the electron (*first row*) and the number of primary vertices in the event and the distance between the electron and the closest jet ΔR (*second row*). A preselection of $I_{rel} < 0.2$ is applied to the ΔR distribution.
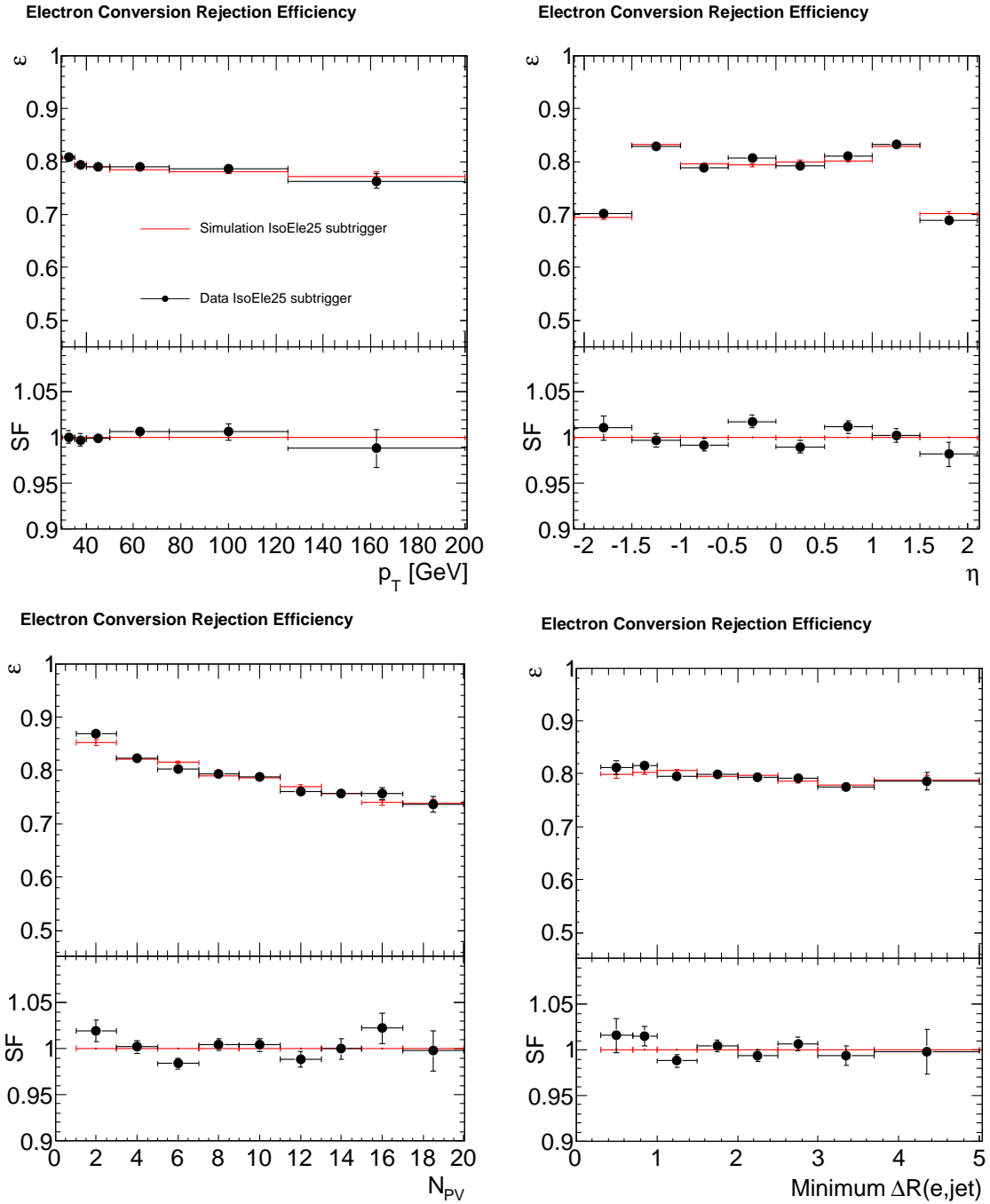
Figure B.6: The electron-conversion-rejection efficiency obtained with the IsoEle25TriJet cross trigger for simulation and data with corresponding SF as a function of p_T and η of the electron (*first row*) and the number of primary vertices in the event and the distance between the electron and the closest jet ΔR (*second row*). A preselection of $I_{rel} < 0.2$ to the ΔR distribution is not necessary as it is evaluated after the tight I_{rel} cut anyway.

Appendix C

Kinematic Event Reconstruction for the Individual Channels
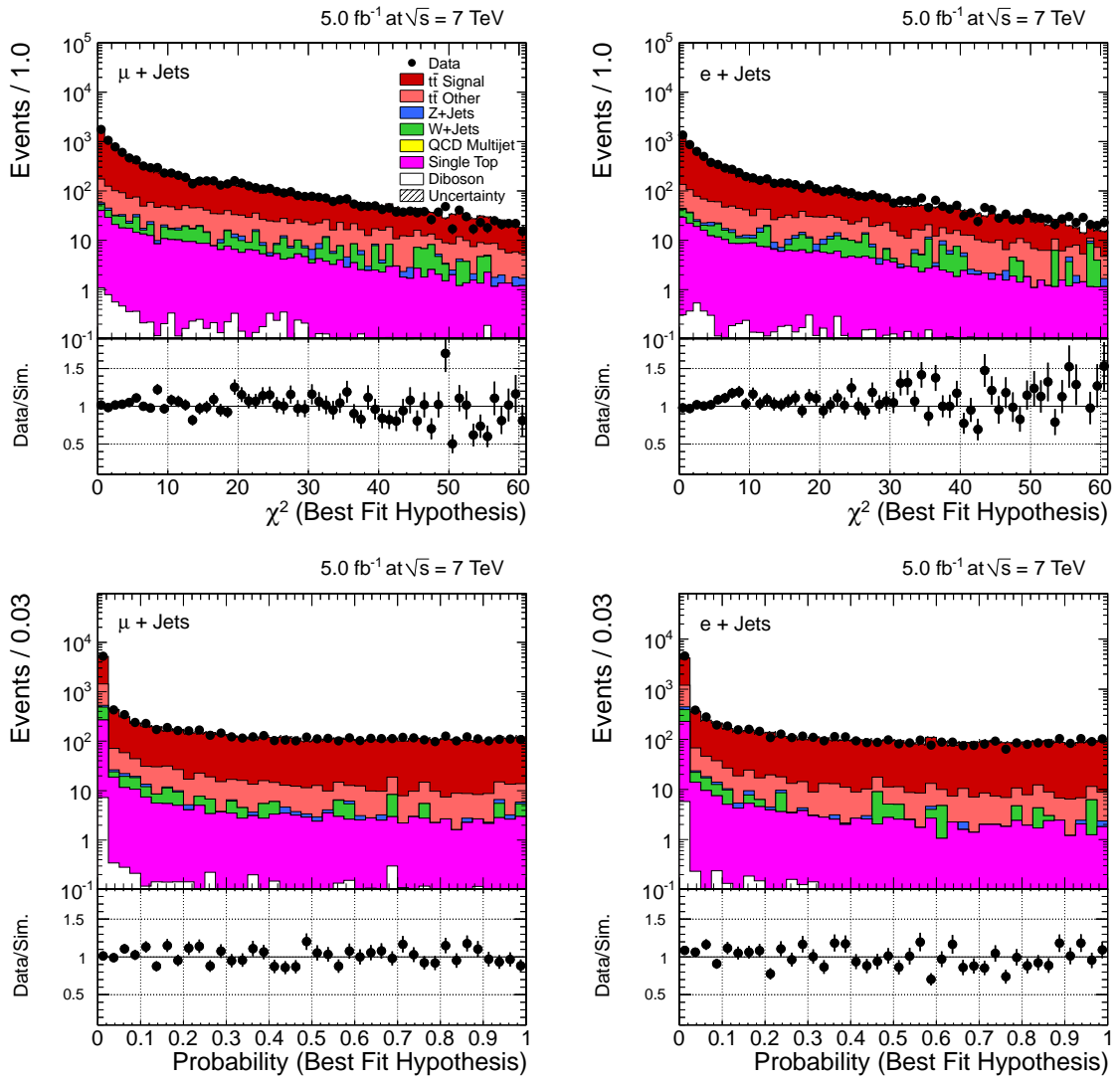
Figure C.1: χ^2 (*top row*) and corresponding probability (*bottom row*) for the muon (*left*) and electron (*right*) channel. Shown uncertainties and applied corrections are the same as detailed in Sec. 5.2.6.
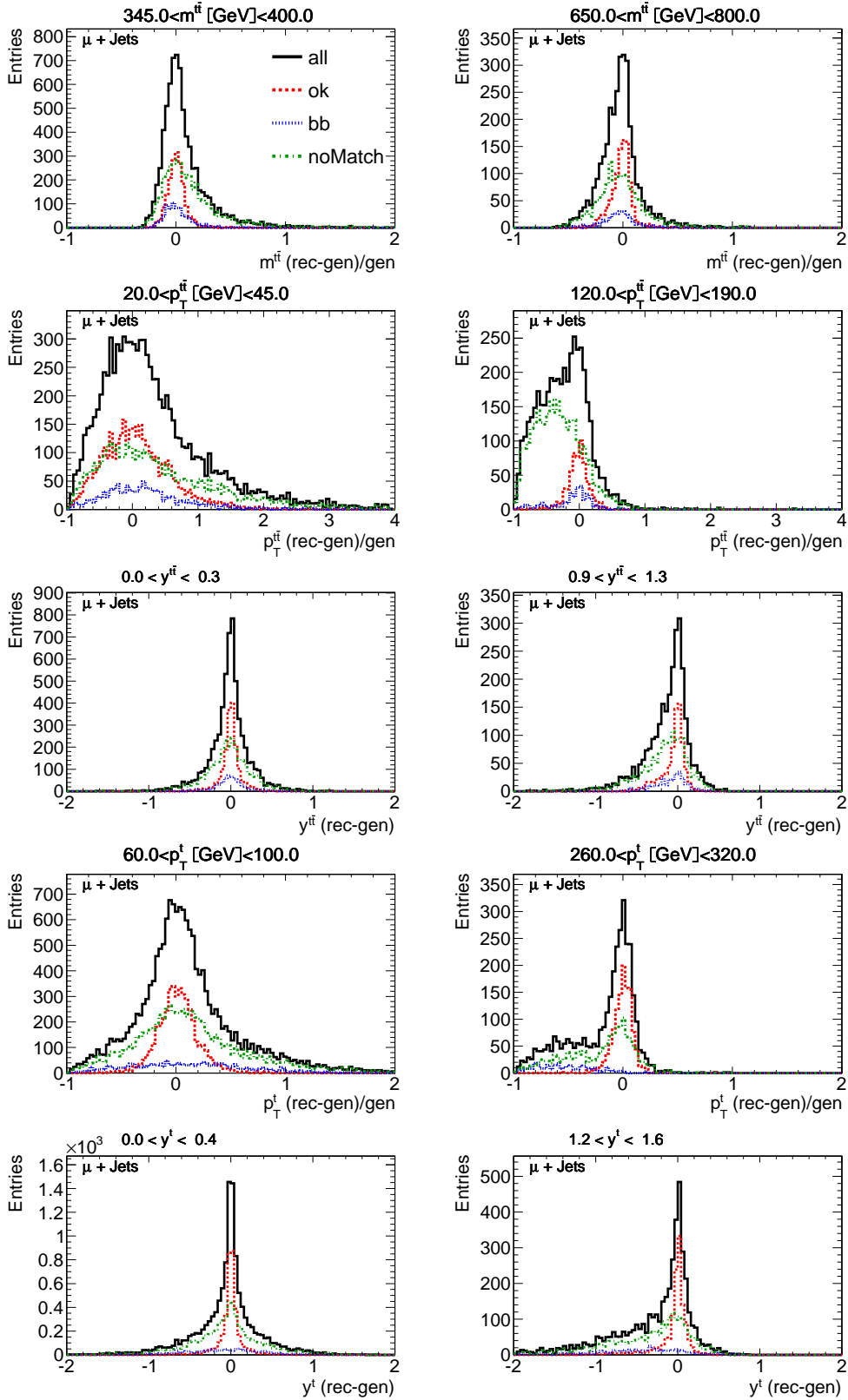
Figure C.2: The residuum distributions (relative to the generated value in case of p_T and mass quantities) in the muon channel for the $t\bar{t}$ and top-quark quantities at parton level for the dominating permutations. This is shown for two selected bins of the generated quantity according to the final binning.
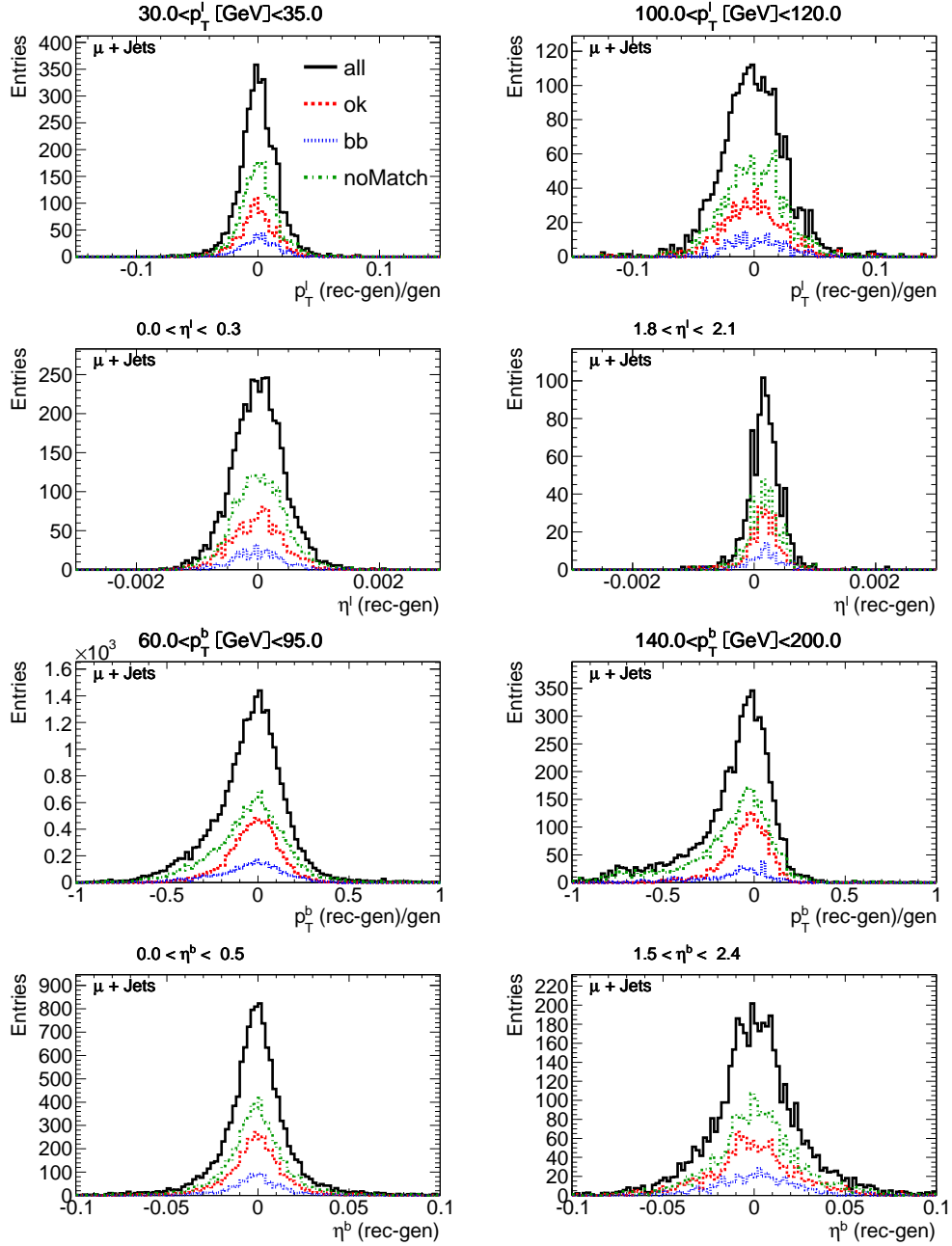
Figure C.3: The residuum distributions (relative to the generated value in case of p_T quantities) in the muon channel for the lepton and b-jet kinematic quantities at particle level for the dominating permutations. This is shown for two selected bins of the generated quantity according to the final binning.
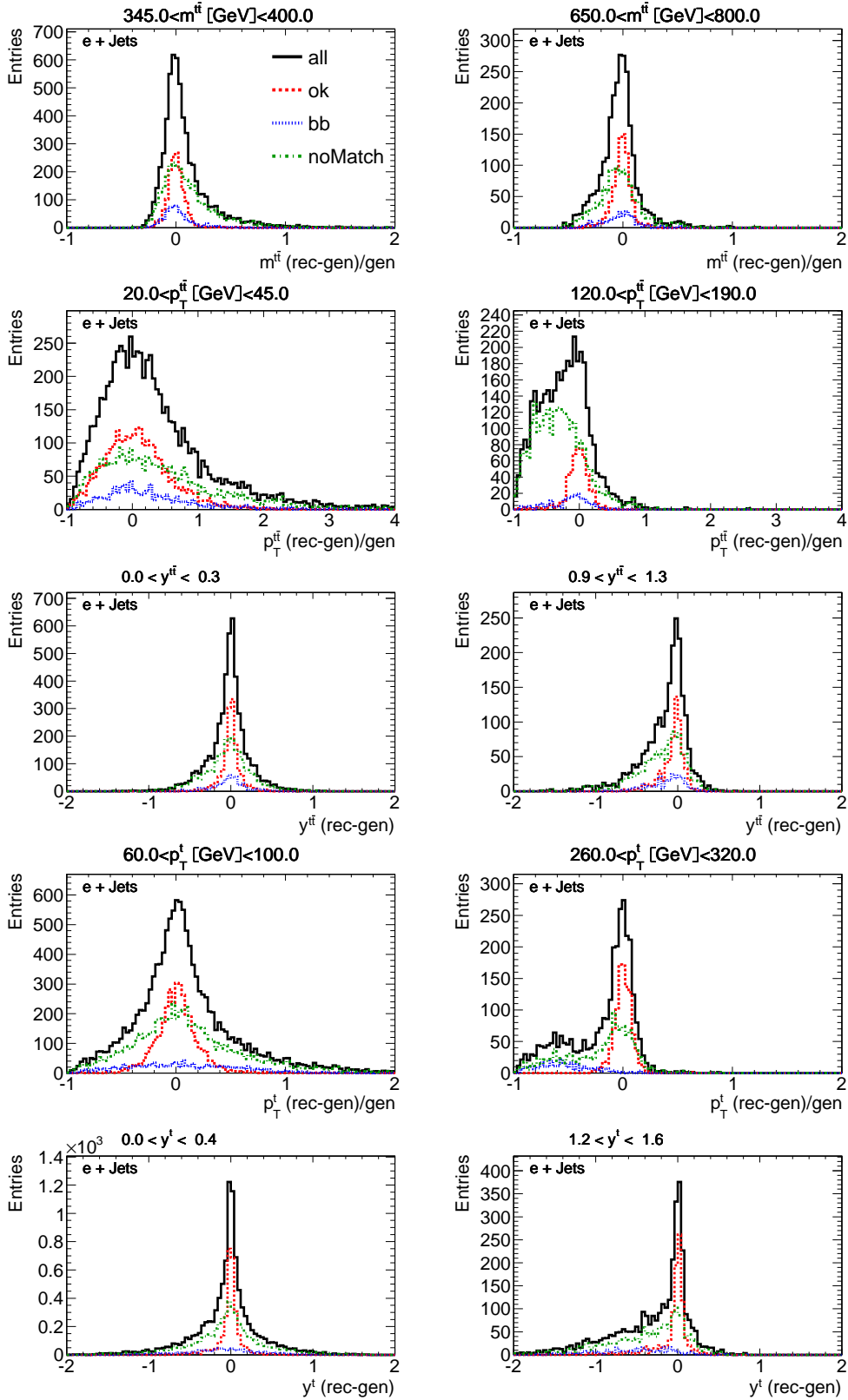
Figure C.4: The residuum distributions (relative to the generated value in case of p_T quantities) in the electron channel for the $t\bar{t}$ and top-quark quantities at parton level for the dominating permutations. This is shown for two selected bins of the generated quantity according to the final binning.
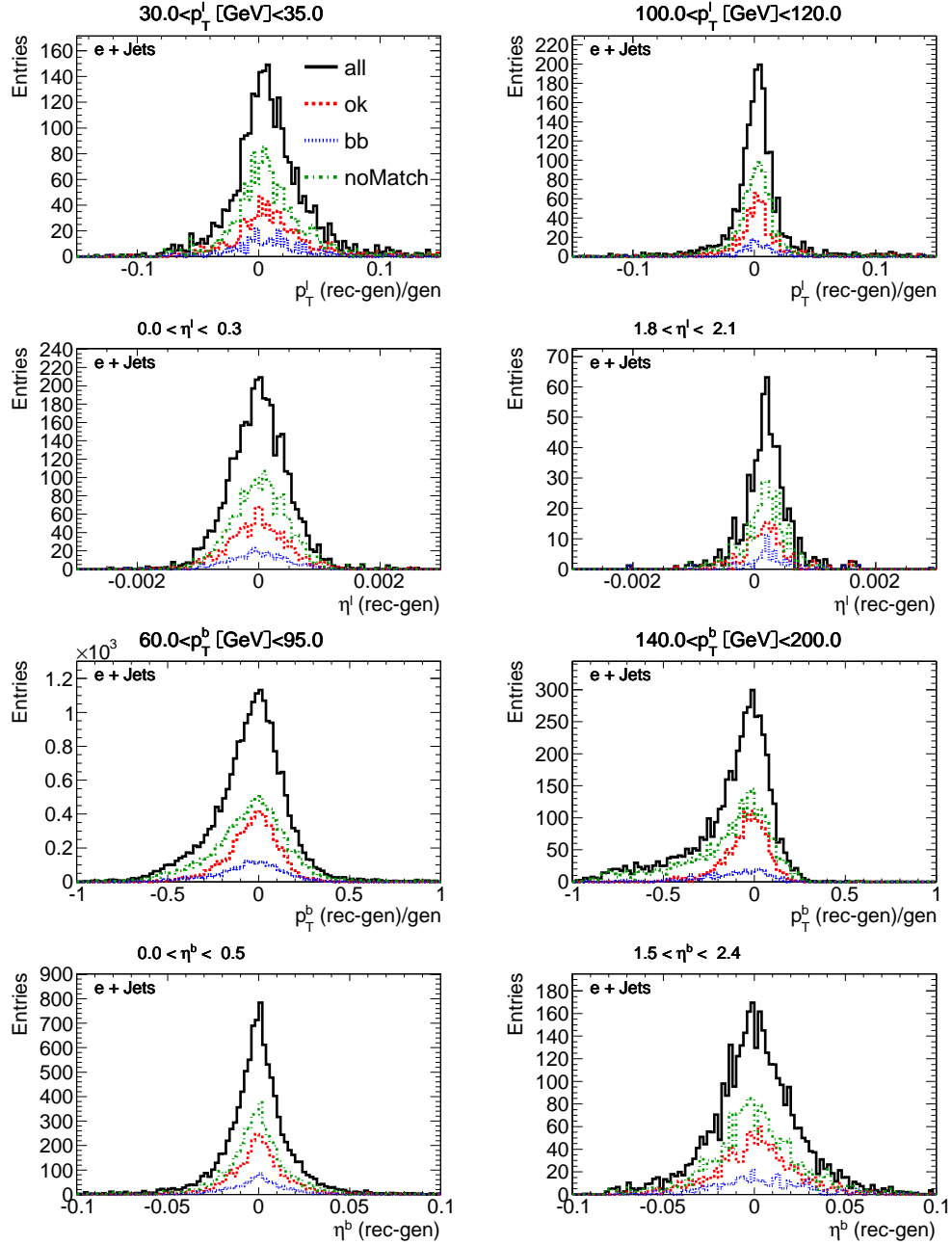
Figure C.5: The residuum distributions (relative to the generated value in case of p_T and mass quantities) in the electron channel for the lepton and b-jet kinematic quantities at particle level for the dominating permutations. This is shown for two selected bins of the generated quantity according to the final binning.
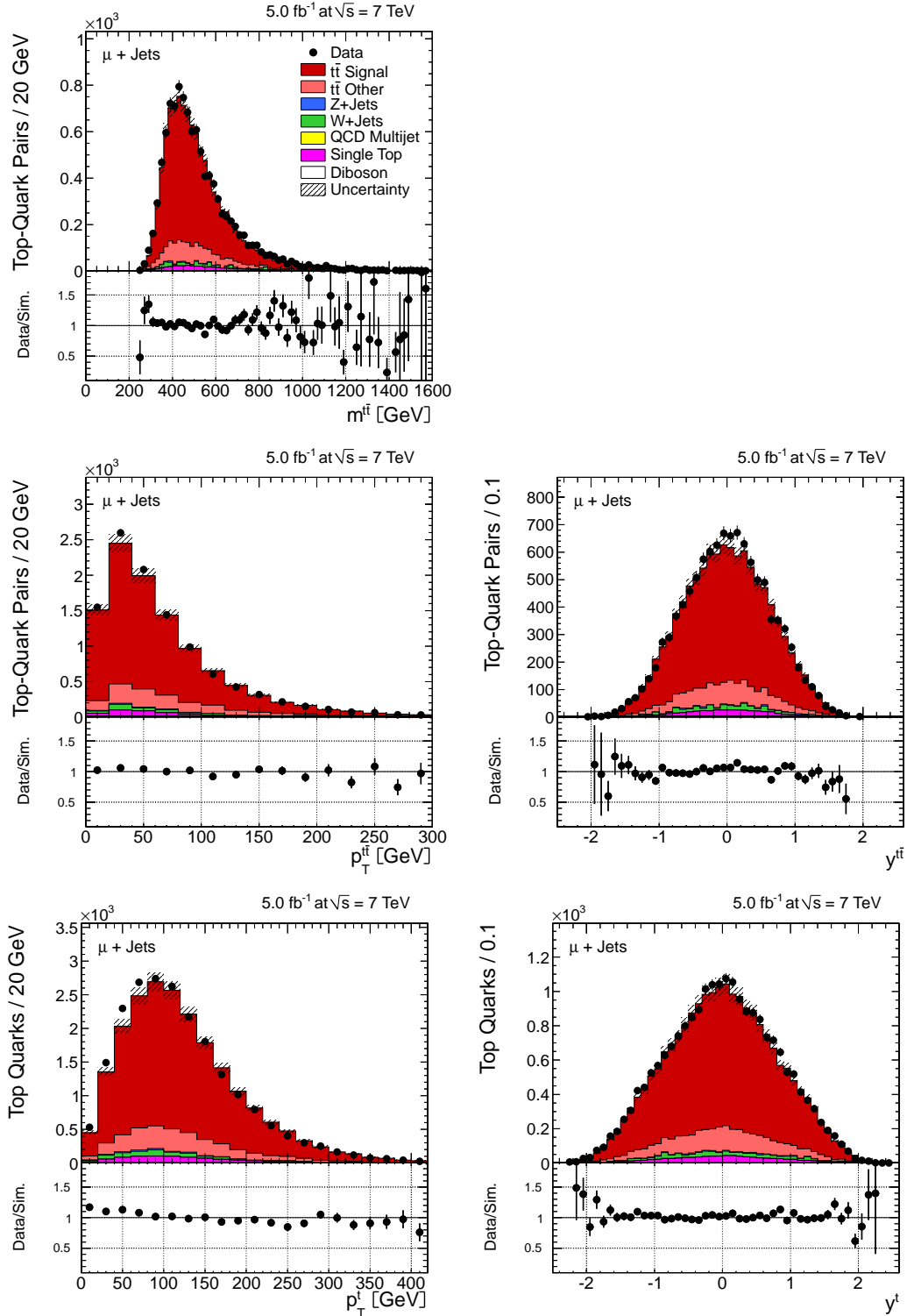
Figure C.6: Event yields as a function of reconstructed quantities of the $t\bar{t}$ system and top quarks in data and simulation for the muon channel. Shown uncertainties and applied corrections are the same as detailed in Sec. 5.2.6.
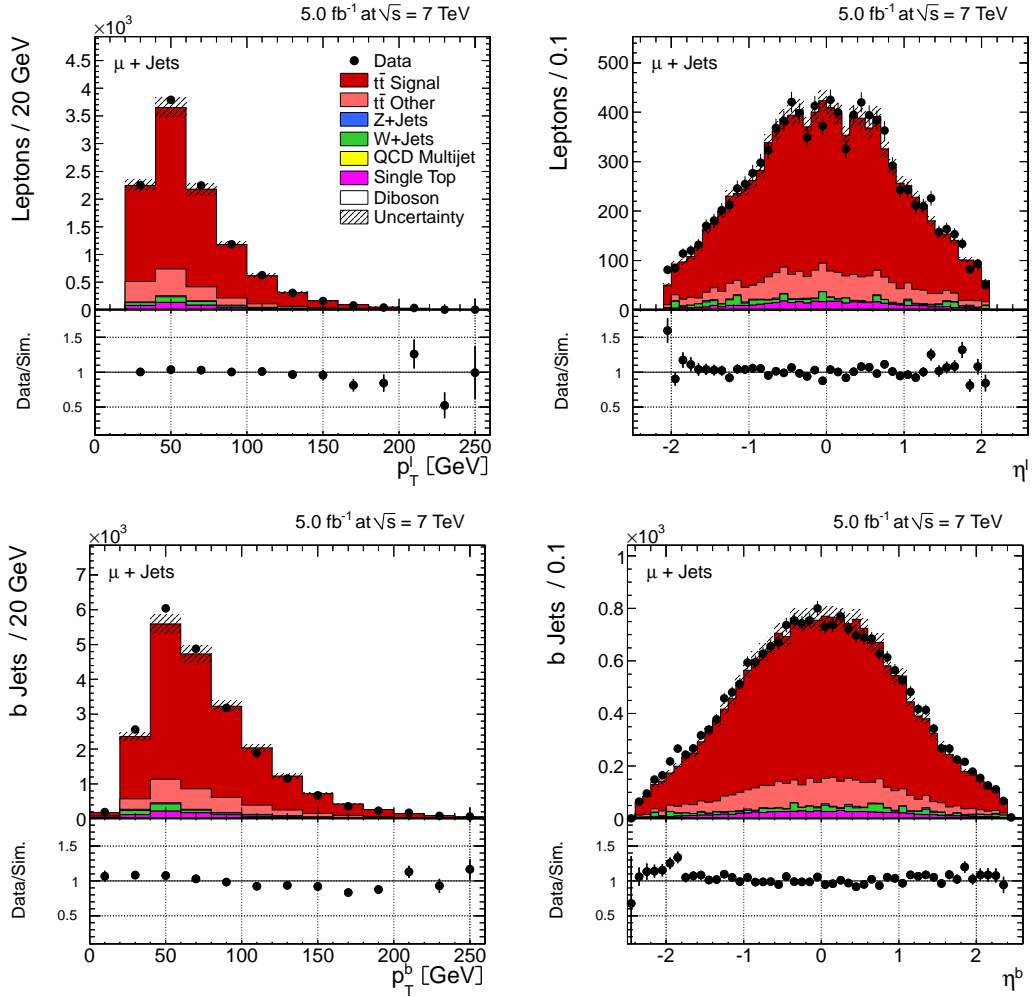
Figure C.7: Event yields as a function of reconstructed lepton (*first row*: p_{T}^{ℓ}, η^{ℓ}) and b-jet (*second row*: p_{T}^{b}, η^{b}) quantities in data and simulation for the muon channel. Shown uncertainties and applied corrections are the same as detailed in Sec. 5.2.6.
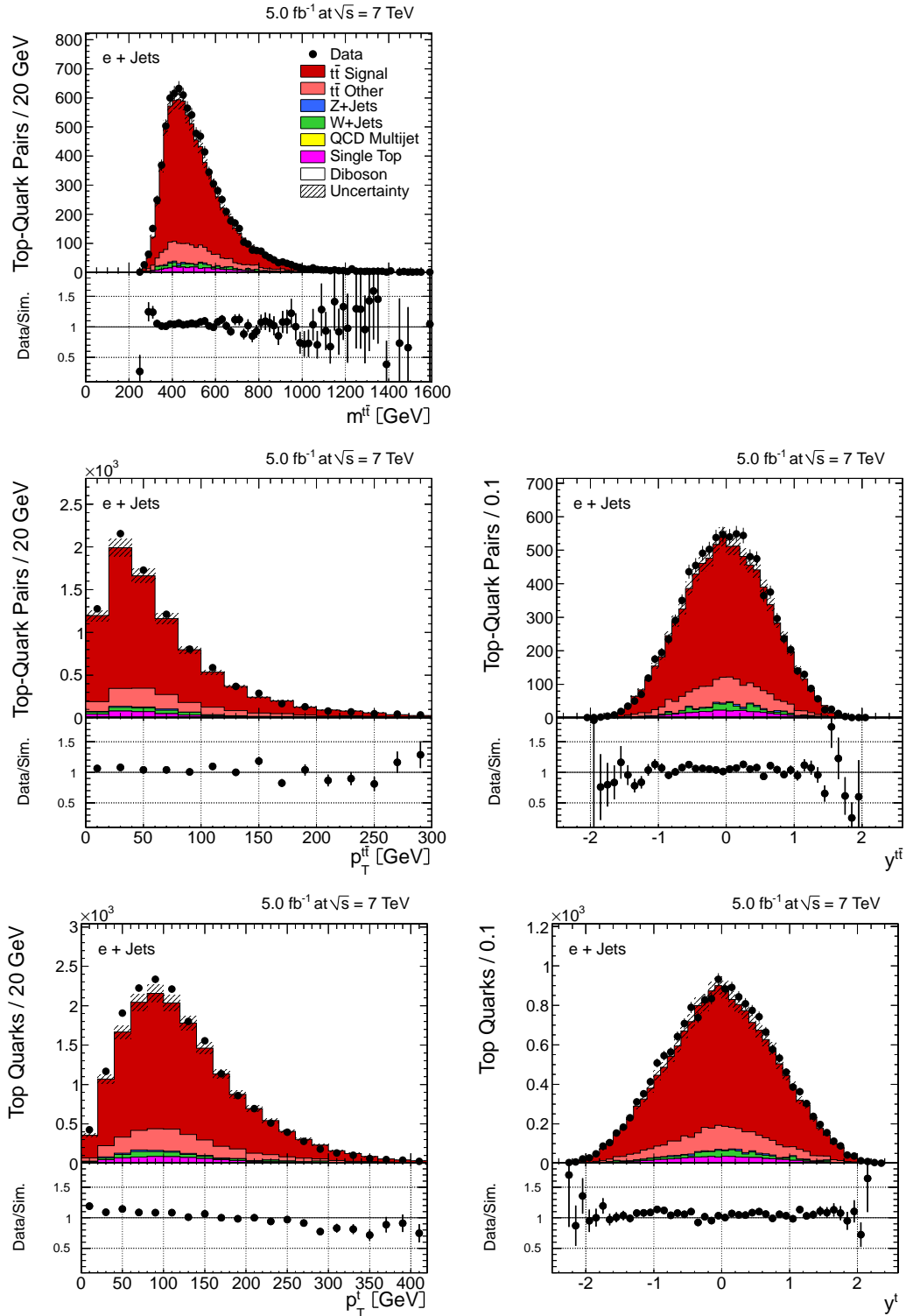
Figure C.8: Event yields as a function of reconstructed quantities of the $t\bar{t}$ system and top quarks in data and simulation for the electron channel. Shown uncertainties and applied corrections are the same as detailed in Sec. 5.2.6.
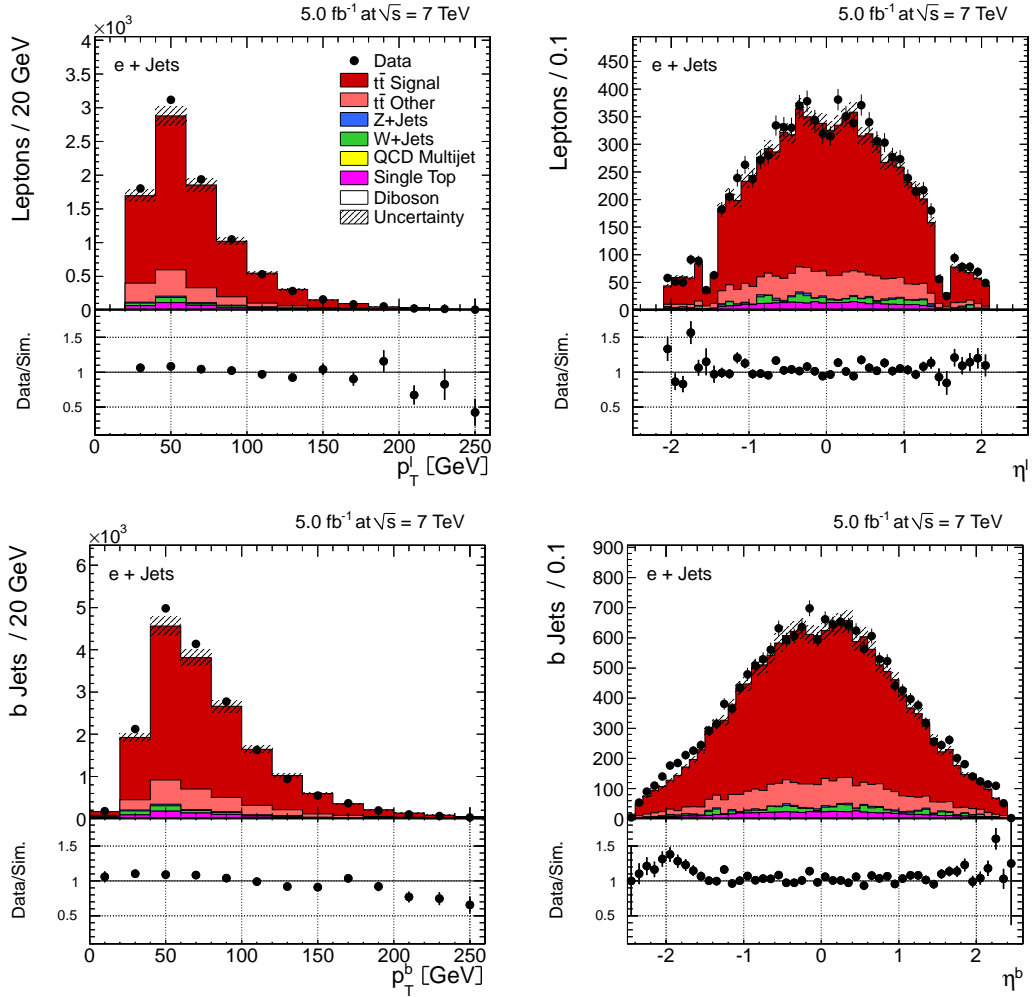
Figure C.9: Event yields as a function of reconstructed lepton (*first row*: p_{T}^{ℓ}, η^{ℓ}) and b-jet (*second row*: p_{T}^{b}, η^{b}) quantities in data and simulation for the electron channel. Shown uncertainties and applied corrections are the same as detailed in Sec. 5.2.6.

Appendix D

Migration and Efficiencies for the Individual Channels
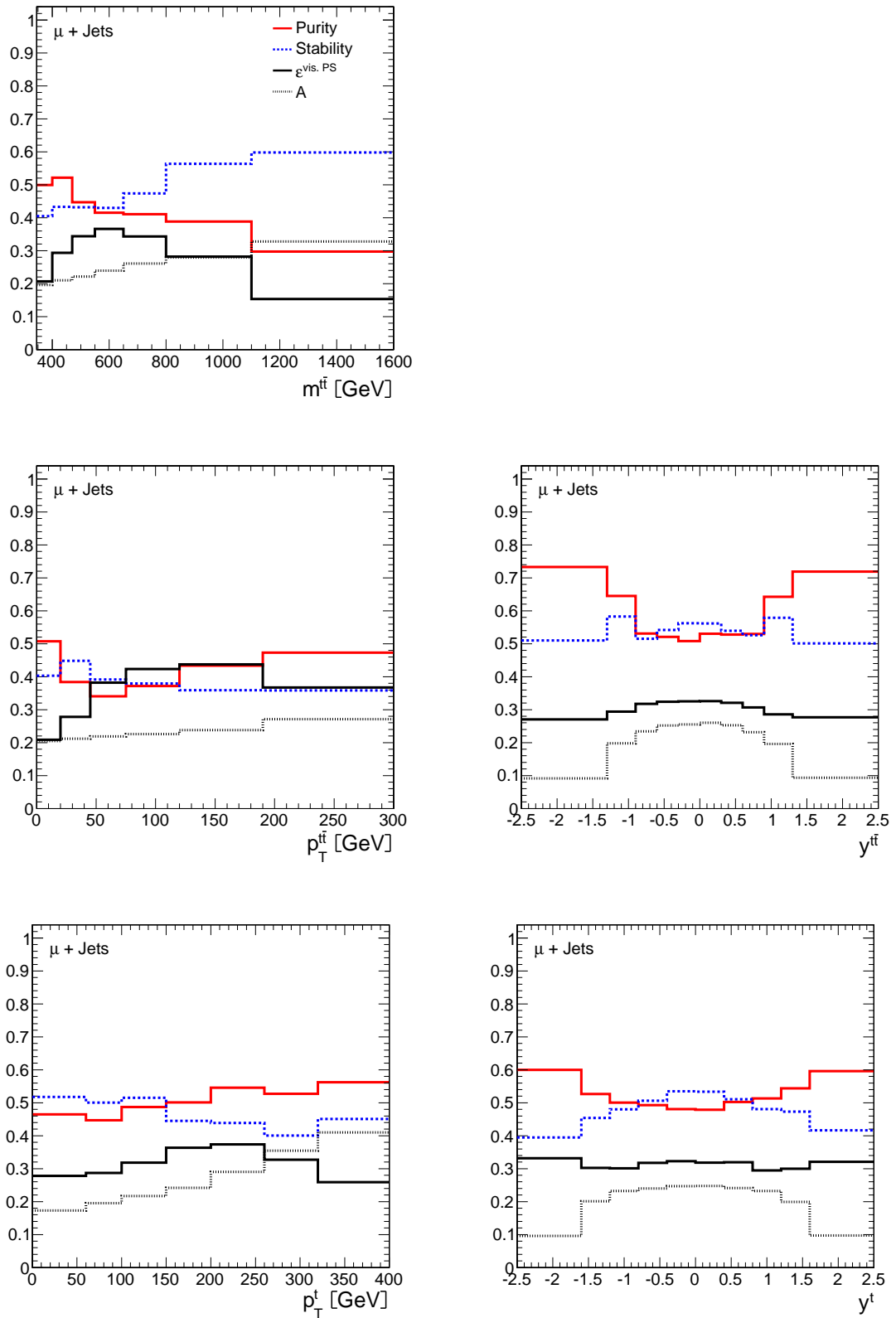
Figure D.1: Purity, stability, efficiency $\epsilon^{\text{vis. PS}}$ and acceptance A for $t\bar{t}$ and top-quark quantities for the muon channel. Generated quantities at parton level.
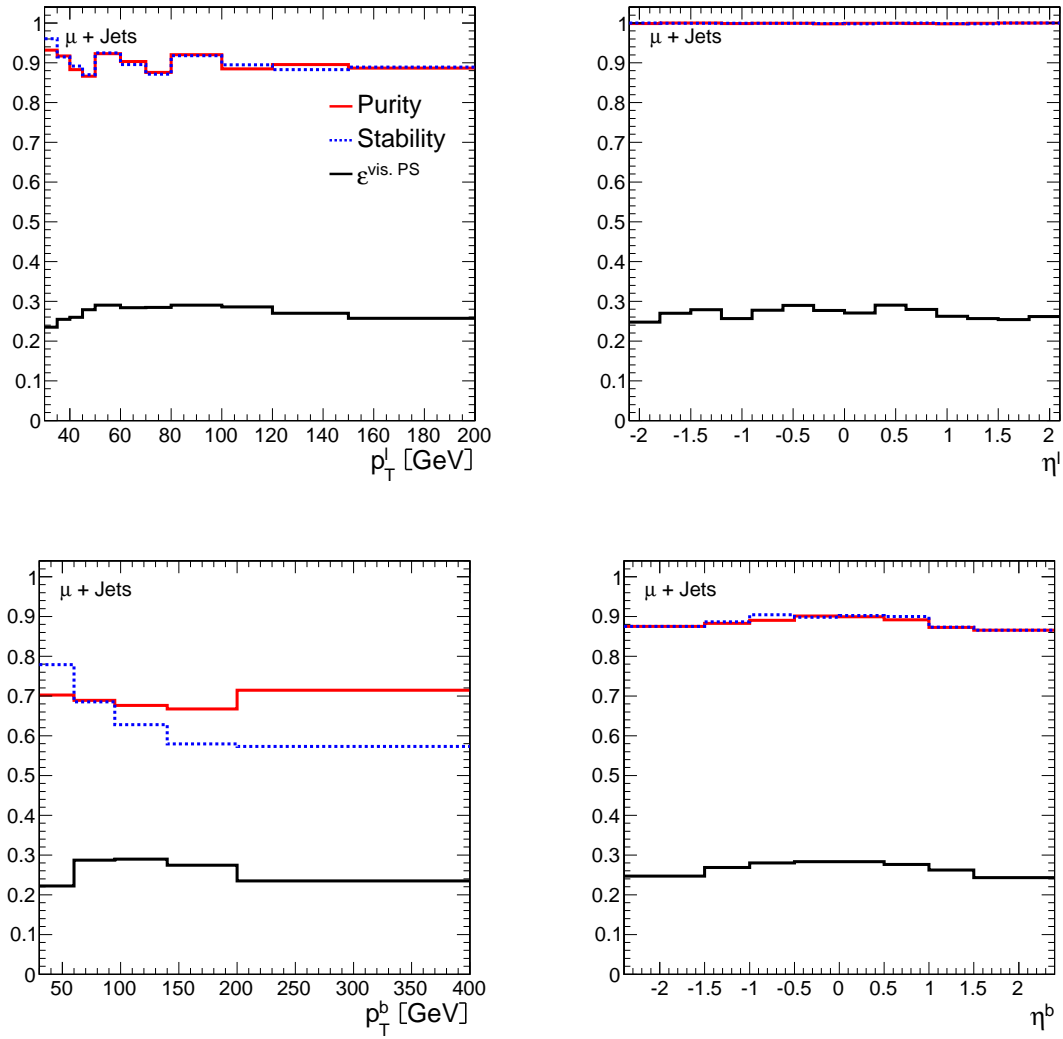
Figure D.2: Purity, stability and efficiency $\epsilon^{\mathrm{vis.\,PS}}$ for lepton (*first row*: p_{T}^{ℓ}, η^{ℓ}) and b-jet (*second row*: p_{T}^{b}, η^{b}) quantities for the muon channel. Generated quantities at particle level.

Figure D.3: Migration matrix $\mathbf{M}$ for $t\bar{t}$ and top-quark quantities for the muon channel. Generated quantities at parton level.

Figure D.4: Migration matrix **M** for lepton (*first row*: p_T^ℓ, η^ℓ) and b-jet (*second row*: p_T^b, η^b) quantities for the muon channel. Generated quantities at particle level.
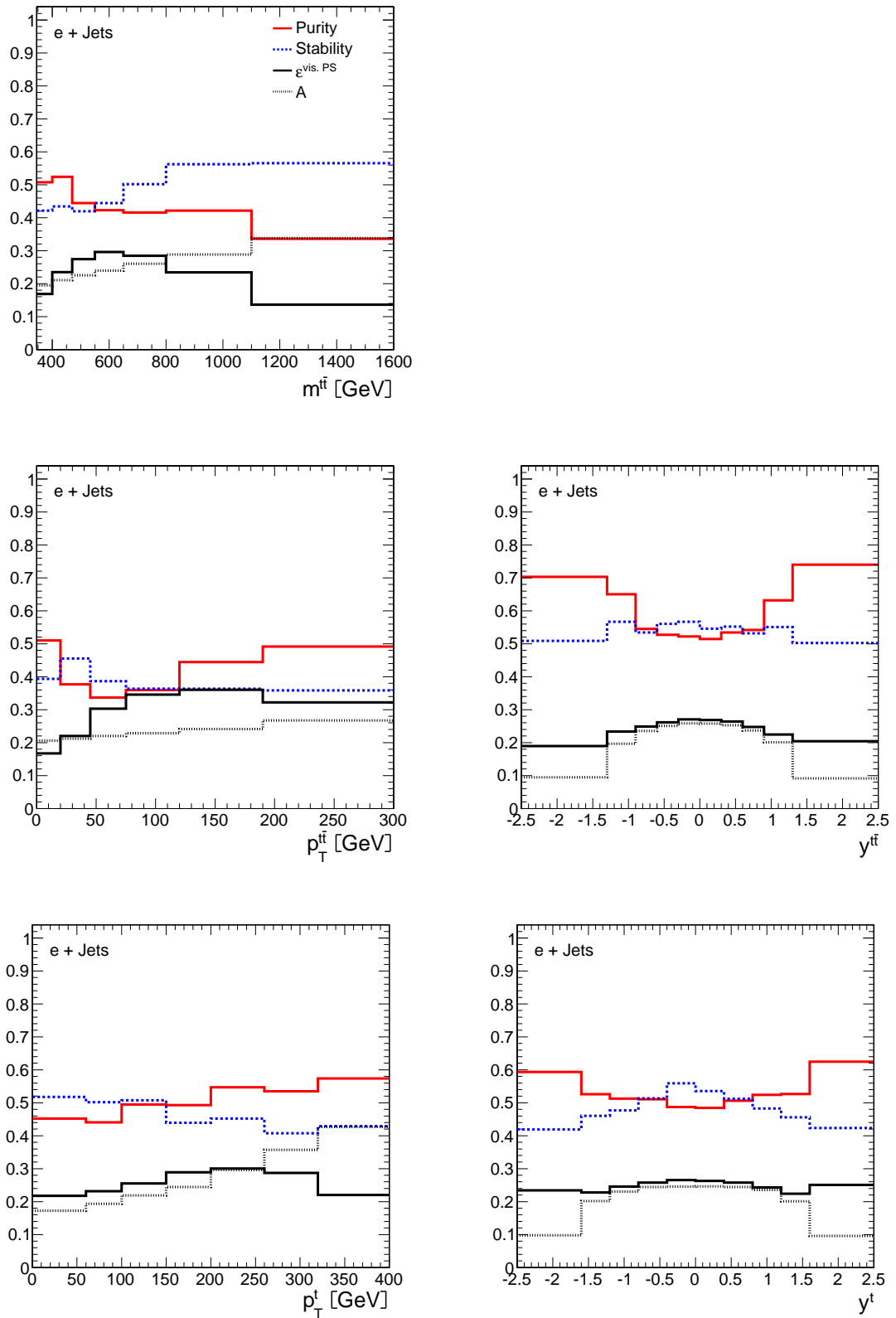
Figure D.5: Purity, stability, efficiency $\epsilon^{\text{vis. PS}}$ and acceptance A for $t\bar{t}$ and top-quark quantities for the electron channel. Generated quantities at parton level.
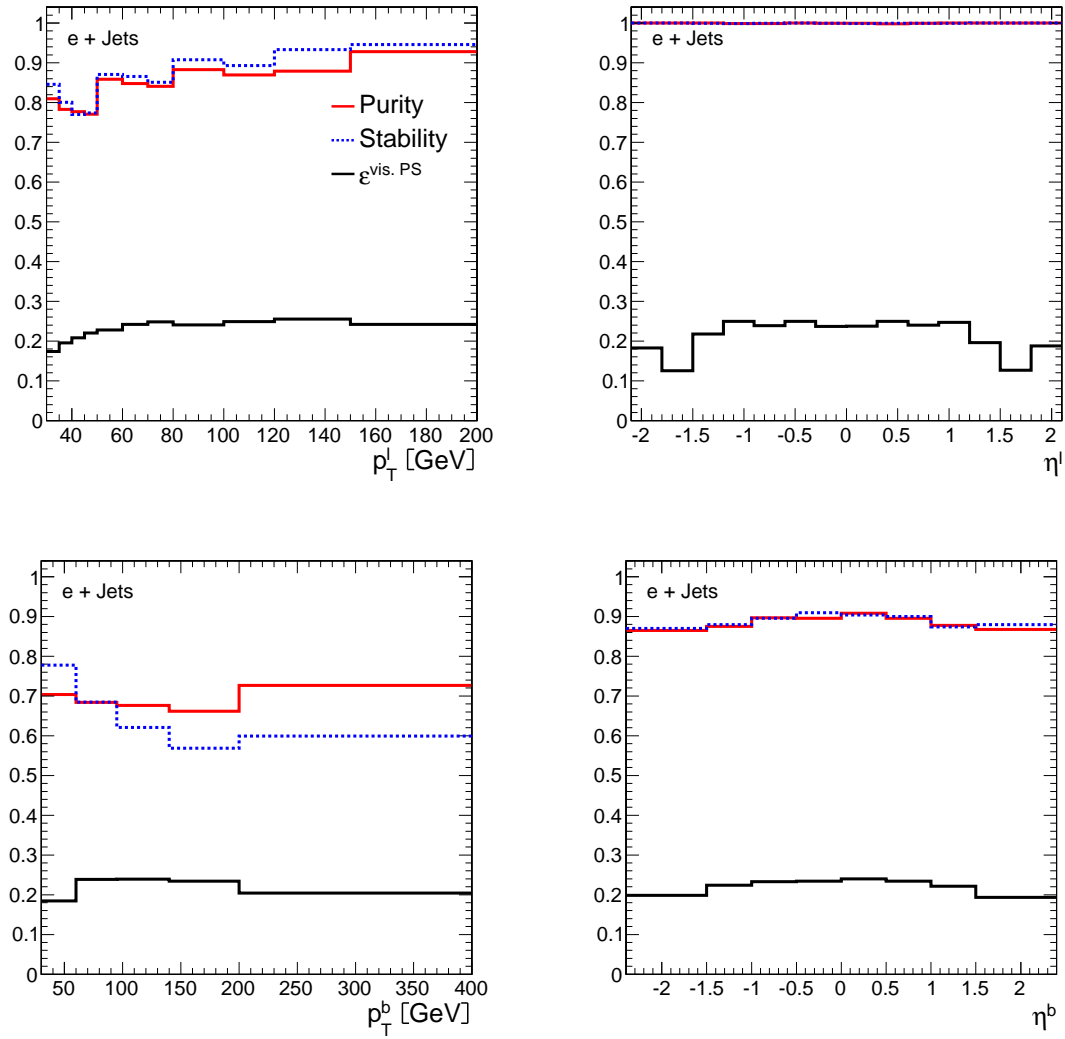
Figure D.6: Purity, stability and efficiency $\epsilon^{\text{vis. PS}}$ for lepton (*first row*: p_T^ℓ, η^ℓ) and b-jet (*second row*: p_T^b, η^b) quantities for the electron channel. Generated quantities at particle level.
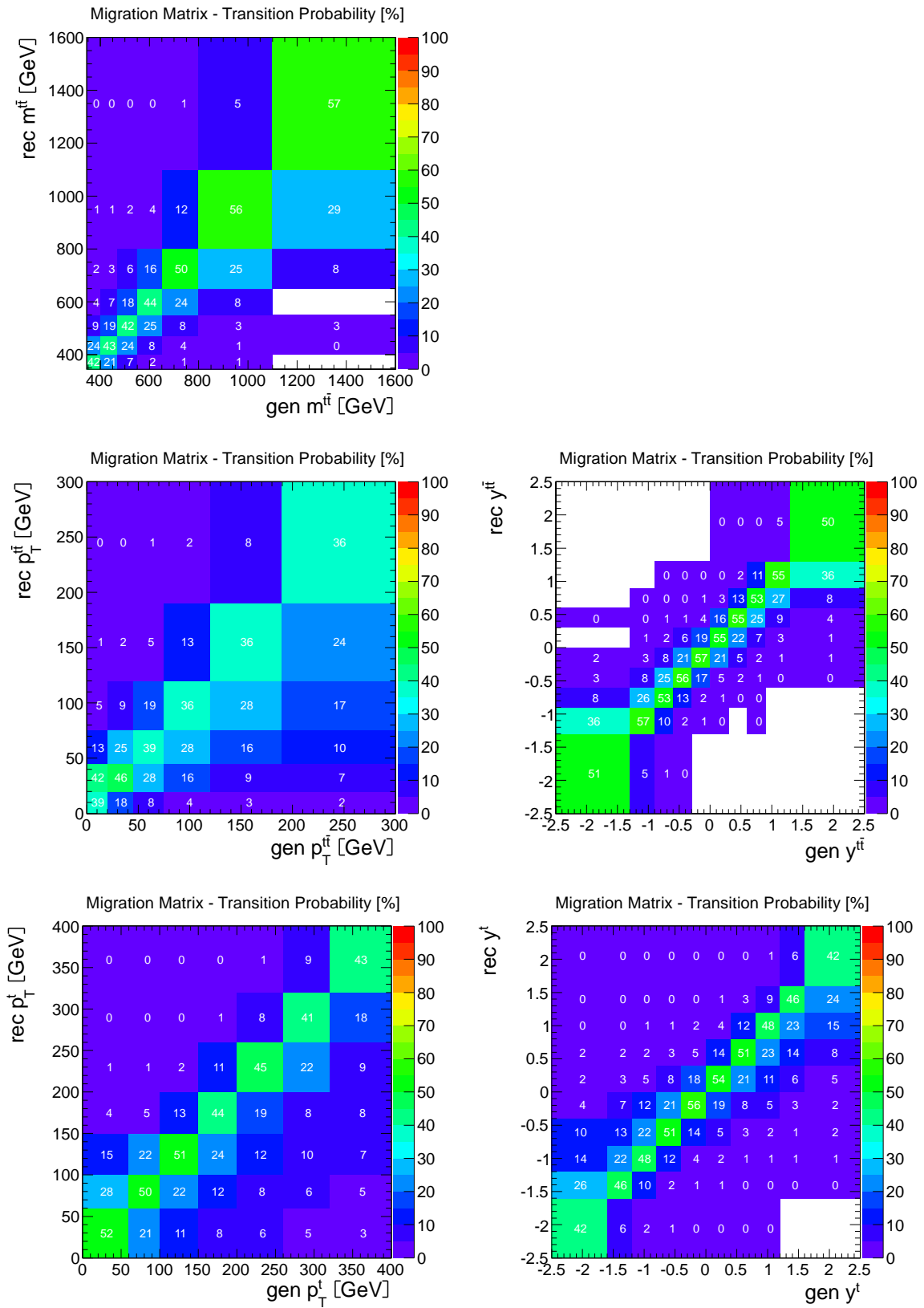
Figure D.7: Migration matrix **M** for tt̄ and top-quark quantities for the electron channel. Generated quantities at parton level.
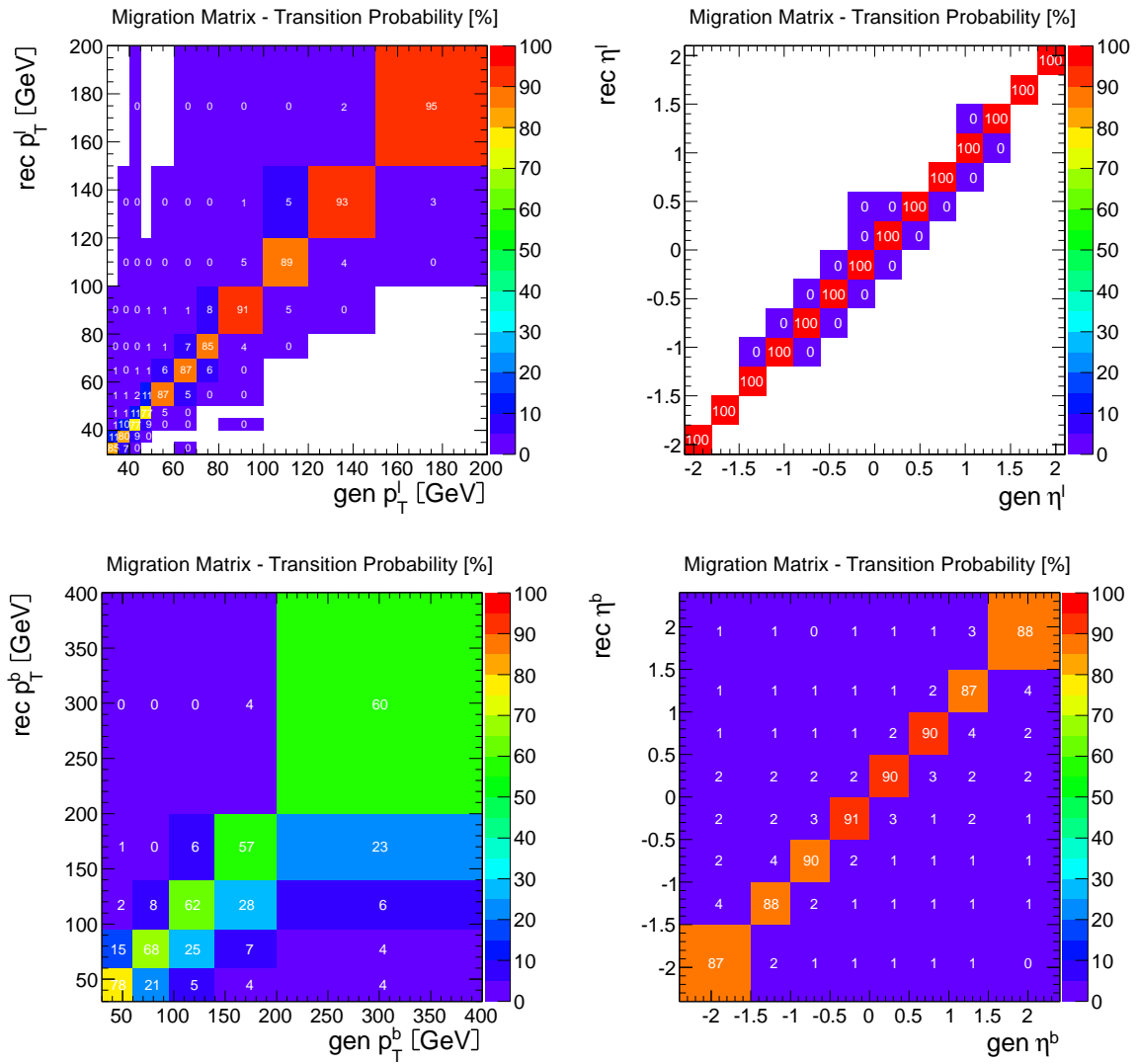
Figure D.8: Migration matrix $\mathbf{M}$ for lepton (*first row*: p_T^ℓ, η^ℓ) and b-jet (*second row*: p_T^b, η^b) quantities for the electron channel. Generated quantities at particle level.

Appendix E

Results: Comparison of $\frac{1}{\sigma} \cdot \frac{d\sigma}{dX}$ for the Different Channels
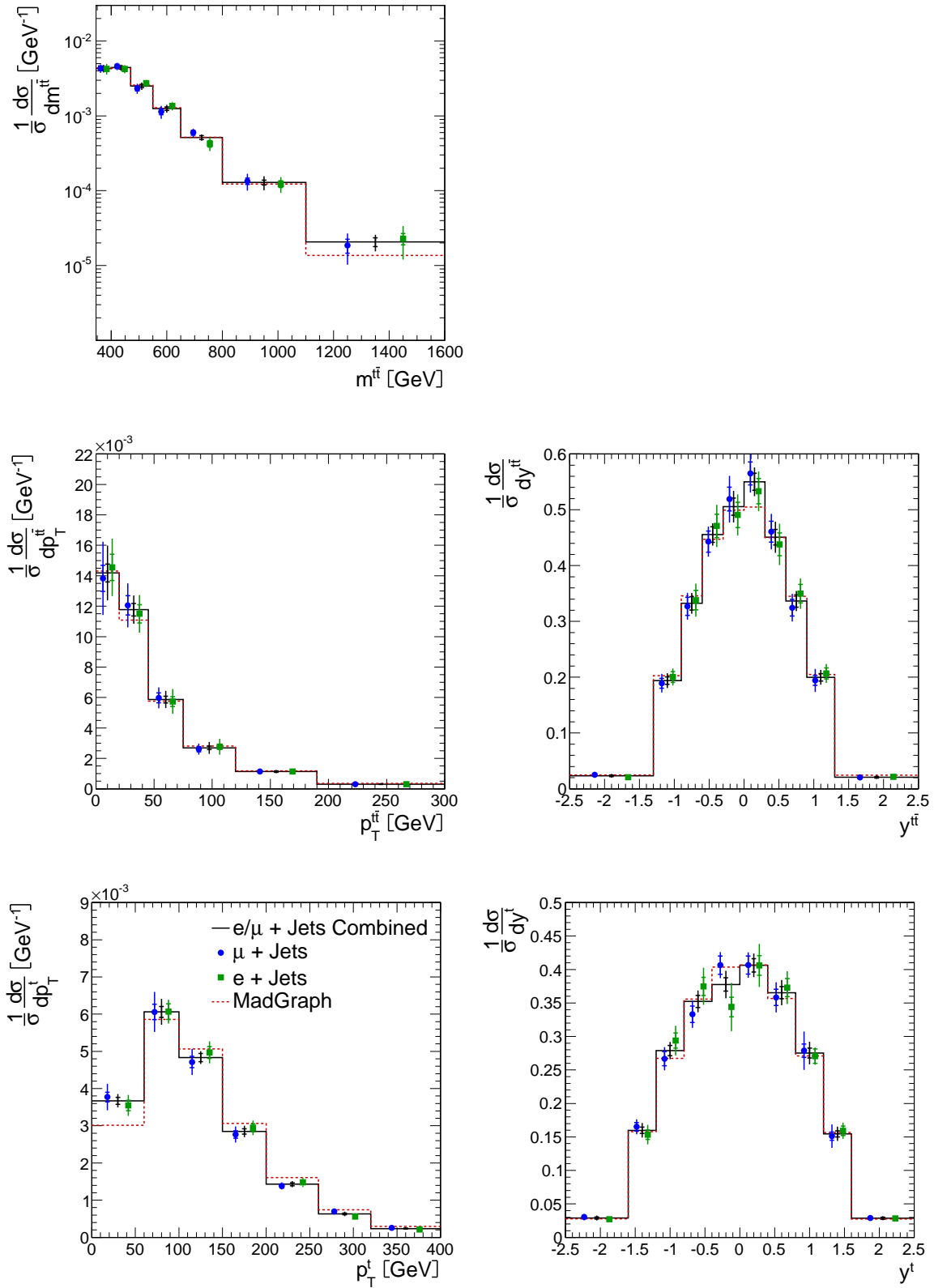
Figure E.1: Comparison of different decay channels for the normalised differential cross sections for the **$t\bar{t}$** and **top-quark** quantities in the **visible phase space at parton level**.
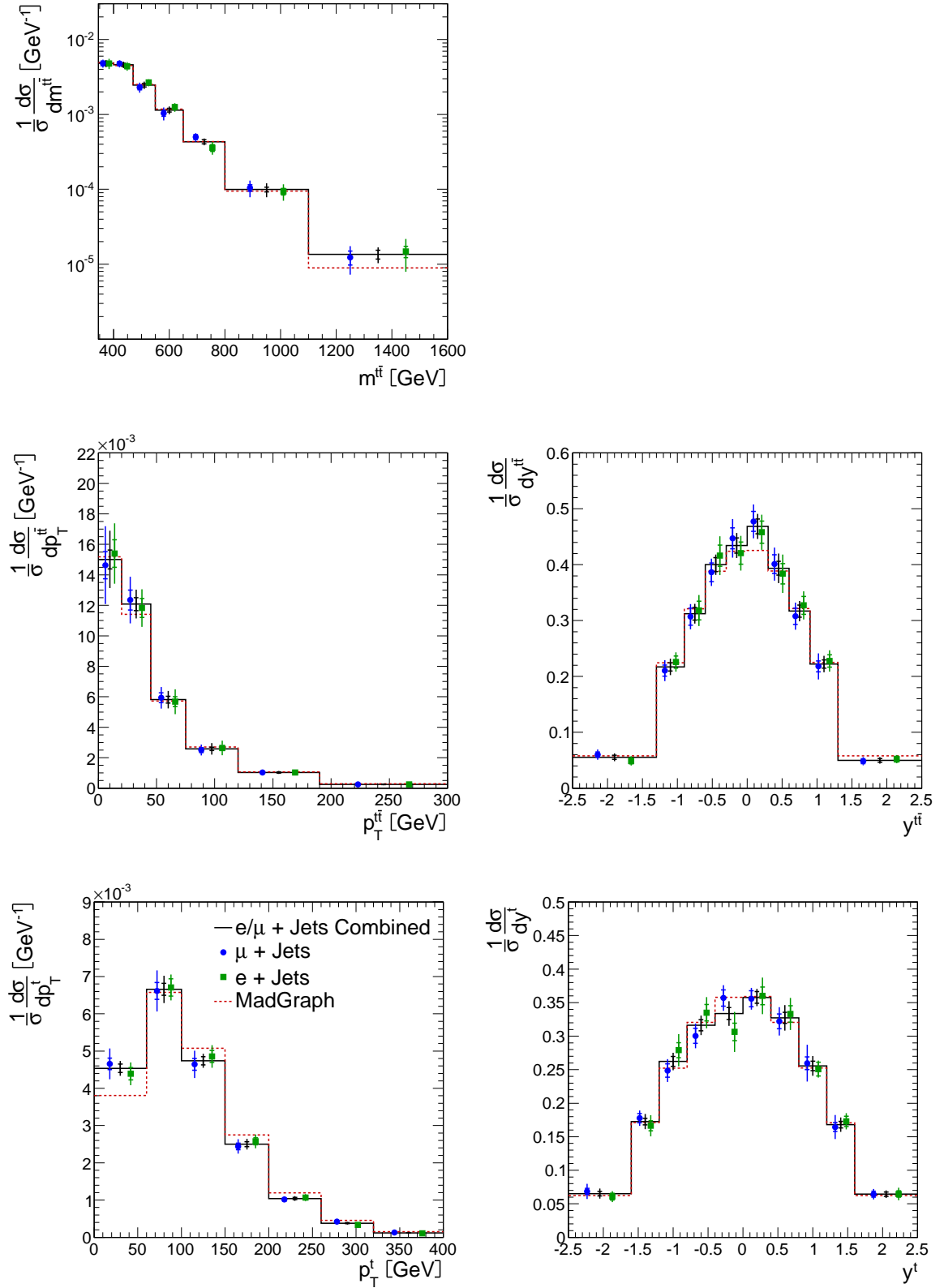
Figure E.2: Comparison of different decay channels for the normalised differential cross sections for the $t\bar{t}$ and **top-quark** quantities in the **full phase space at parton level**.
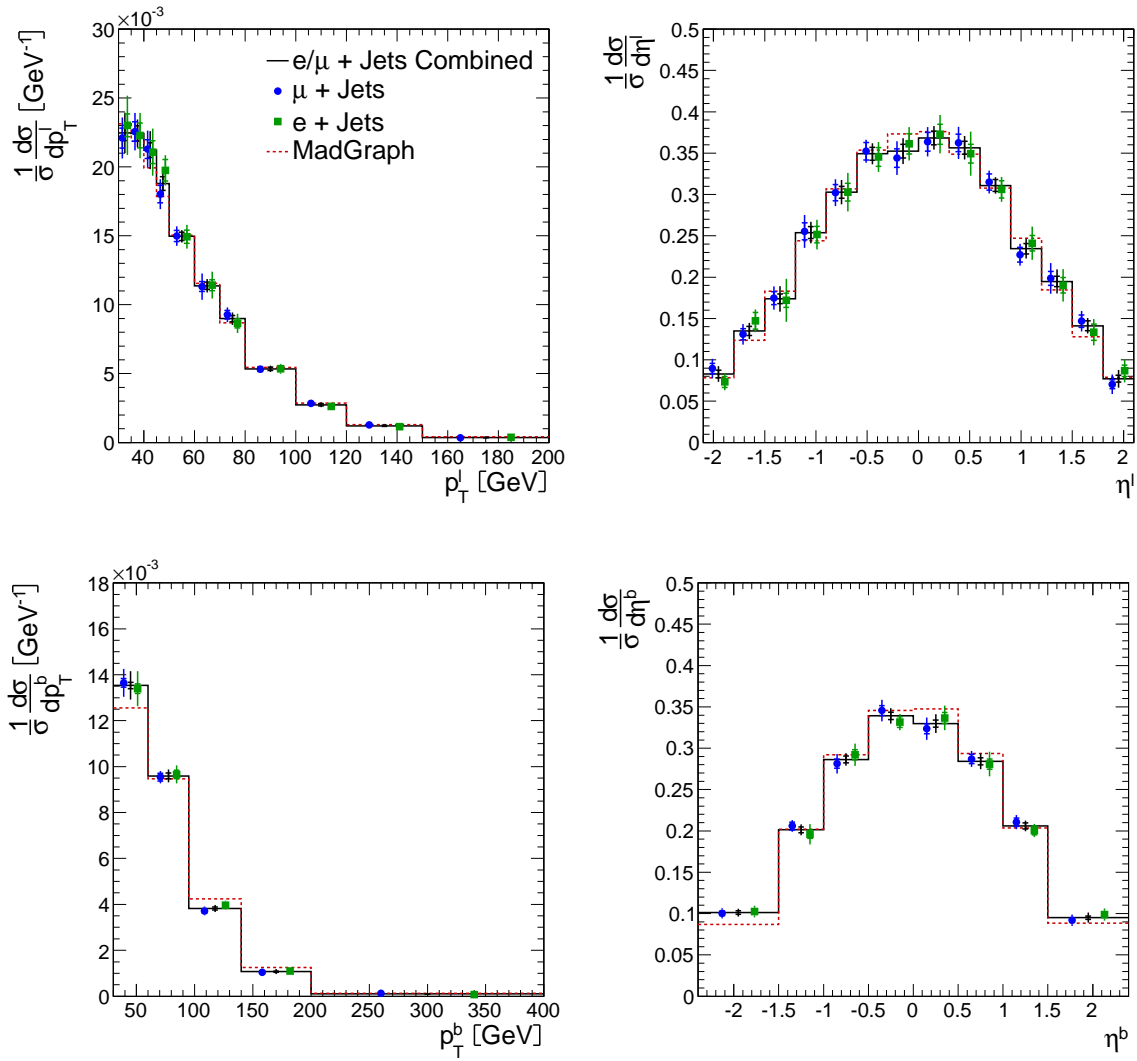
Figure E.3: Comparison of different decay channels for the normalised differential cross sections for the **lepton** (*top row*) and **b-jet** (*bottom row*) quantities (*left*: p_{T}, *right*: η) in the **visible phase space at particle level**.

List of Figures

List of Tables

Bibliography

[1] CDF Collaboration, "Measurement of the Top Quark p_T Distribution", *Phys. Rev. Lett.* **87** (2001) 102001.

[2] D0 Collaboration, "Dependence of the $t\bar{t}$ production cross section on the transverse momentum of the top quark", *Phys. Lett. B* **693** (2010) 515, `arXiv:1001.1900`. `doi:10.1016/j.physletb.2010.09.011`.

[3] CDF Collaboration, "First Measurement of the $t\bar{t}$ Differential Cross Section $d\sigma/dM_{t\bar{t}}$ in $p\bar{p}$ Collisions at $\sqrt{s} = 1.96$ TeV", *Phys. Rev. Lett.* **102** (2009) 222003, `arXiv:0903.2850`. `doi:10.1103/PhysRevLett.102.222003`.

[4] M. Görner, "Messung von Myonen, Jets und Top-Quarks mit dem CMS-Detektor am LHC", Diploma thesis, University of Hamburg, Germany, 2010. CERN-THESIS-2010-176.

[5] H. Enderle, "Momentum Bias Determination in the Tracker Alignment and First Differential $t\bar{t}$ Cross Section Measurement at CMS". PhD thesis, University of Hamburg, Germany, 2012. DESY-THESIS-2012-001.

[6] CMS Collaboration, "Measurement of differential top-quark pair production cross sections in pp collisions at $\sqrt{s} = 7$ TeV", *Eur. Phys. J. C* **73** (2013) 2339, `arXiv:1211.2220`. `doi:10.1140/epjc/s10052-013-2339-4`.

[7] W. Behrenhoff, "Measurement of Differential $t\bar{t}$ Cross Sections in the Dilepton Decay Channels with the CMS Detector at 7 TeV Centre-of-Mass-Energy". PhD thesis, University of Hamburg, Germany, 2012. DESY-THESIS-2012-037.

[8] F. Gianotti, M. Mangano, T. Virdee et al., "Physics potential and experimental challenges of the LHC luminosity upgrade", *Eur. Phys. J. C* **39** (2005) 293–333, `arXiv:hep-ph/0204087`. `doi:10.1140/epjc/s2004-02061-6`.

[9] J. Lange, "Radiation Damage in Proton-Irradiated Epitaxial Silicon Detectors", Diploma thesis, University of Hamburg, Germany, 2008. DESY-THESIS-2009-022.

[10] I. Mandic, V. Cindro, G. Kramberger et al., "Measurement of anomalously high charge collection efficiency in n+ p strip detectors irradiated by up to $10^{16} \, n_{eq}/cm^2$", *Nucl. Instrum. Meth. A* **603** (2009) 263–267. `doi:10.1016/j.nima.2009.01.207`.

[11] I. Mandic, V. Cindro, A. Gorisek et al., "Observation of full charge collection efficiency in heavily irradiated n+p strip detectors irradiated up to 3 x $10^{15} \, n_{eq}/cm^2$", *Nucl. Instrum. Meth. A* **612** (2010) 474–477. `doi:10.1016/j.nima.2009.08.004`.

[12] G. Casse, A. Affolder, P. Allport et al., "Enhanced efficiency of segmented silicon detectors of different thicknesses after proton irradiations up to 1×10^{16} n_{eq}cm^{-2}", *Nucl. Instrum. Meth. A* **624** (2010) 401–404. `doi:10.1016/j.nima.2010.02.134`.

[13] G. Casse, A. Affolder, P. Allport et al., "Evidence of enhanced signal response at high bias voltages in planar silicon detectors irradiated up to 2.2×10^{16} n_{eq}cm^{-2}", *Nucl. Instrum. Meth. A* **636** (2011), no. 1, Supplement, S56 – S61. `doi:10.1016/j.nima.2010.04.085`.

[14] M. Köhler, L. Wiik, R. Bates et al., "Beam Test Measurements With Planar and 3D Silicon Strip Detectors Irradiated to sLHC Fluences", *IEEE Trans. Nucl. Sci.* **58** (June), no. 3, 1308–1314. `doi:10.1109/TNS.2011.2126598`.

[15] M. Köhler, R. Bates, C. Fleta et al., "Comparative measurements of highly irradiated n-in-p and p-in-n 3D silicon strip detectors", *Nucl. Instrum. Meth. A* **659** (2011), no. 1, 272 – 281. `doi:10.1016/j.nima.2011.08.041`.

[16] D. Griffiths, "Introduction to Elementary Particles". John Wiley & Sons, 1987.

[17] C. Berger, "Elementarteilchenphysik". Springer-Verlag Berlin Heidelberg, 2006.

[18] M. E. Peskin and D. V. Schroeder, "An Introduction to Quantum Field Theory". Westview Press, 1995.

[19] Particle Data Group Collaboration, "Review of Particle Physics", *Phys. Rev. D* **86** (2012) 010001. `doi:10.1103/PhysRevD.86.010001`.

[20] M. Schröder, "Quality of Jet Measurements and Impact on a Search for New Physics at CMS". PhD thesis, University of Hamburg, Germany, 2012. DESY-THESIS-2012-042.

[21] CDF and D0 Collaboration, "Combination of the top-quark mass measurements from the Tevatron collider", *Phys. Rev. D* **86** (2012) 092003, `arXiv:1207.1069`. `doi:10.1103/PhysRevD.86.092003`.

[22] CMS Collaboration, "Measurement of the top-quark mass in $t\bar{t}$ events with lepton+jets final states in pp collisions at $\sqrt{s}$=7 TeV", *JHEP* **2012** (2012) 1–37, `arXiv:hep-ex/1209.2319`. `doi:10.1007/JHEP12(2012)105`.

[23] Planck Collaboration, "Planck 2013 results. XVI. Cosmological parameters", `arXiv:1303.5076`.

[24] ATLAS Collaboration, "Observation of a new particle in the search for the Standard Model Higgs boson with the ATLAS detector at the LHC", *Physics Letters B* **716** (2012), no. 1, 1–29, `arXiv:hep-ph/1207.7214`. `doi:10.1016/j.physletb.2012.08.020`.

[25] CMS Collaboration, "Observation of a new boson at a mass of 125 GeV with the CMS experiment at the LHC", *Physics Letters B* **716** (2012), no. 1, 30–61, `arXiv:hep-ph/1207.7235`. `doi:10.1016/j.physletb.2012.08.021`.

[26] F. Englert and R. Brout, "Broken Symmetry and the Mass of Gauge Vector Mesons", *Phys. Rev. Lett.* **13** (1964) 321 – 323. `doi:10.1103/PhysRevLett.13.321`.

[27] P. W. Higgs, "Broken symmetries, massless particles and gauge fields", *Phys. Lett.* **12** (1964) 132–133. `doi:10.1016/0031-9163(64)91136-9`.

[28] G. S. Guralnik, C. R. Hagen, and T. W. B. Kibble, "Global Conservation Laws and Massless Particles", *Phys. Rev. Lett.* **13** (1964) 585 – 587. `doi:10.1103/PhysRevLett.13.585`.

[29] W. Bernreuther, "Top quark physics at the LHC", *J. Phys.* **G35** (2008) 083001, `arXiv:0805.1333`. `doi:10.1088/0954-3899/35/8/083001`.

[30] J. R. Incandela, A. Quadt, W. Wagner et al., "Status and prospects of top-quark physics", *Progress in Particle and Nuclear Physics* **63** (2009), no. 2, 239 – 292. `doi:10.1016/j.ppnp.2009.08.001`.

[31] F.-P. Schilling, "Top Quark Physics at the LHC: A Review of the First Two Years", *Int. J. Mod. Phys. A* **27** (2012) 1230016, `arXiv:1206.4484`. `doi:10.1142/S0217751X12300165`.

[32] M. Kobayashi and T. Maskawa, "CP-Violation in the Renormalizable Theory of Weak Interaction", *Progress of Theoretical Physics* **49** (1973), no. 2, 652–657. `doi:10.1143/PTP.49.652`.

[33] CDF Collaboration, "Observation of top quark production in $\bar{p}p$ collisions", *Phys. Rev. Lett.* **74** (1995) 2626–2631, `arXiv:hep-ex/9503002`. `doi:10.1103/PhysRevLett.74.2626`.

[34] D0 Collaboration, "Observation of the top quark", *Phys. Rev. Lett.* **74** (1995) 2632–2637, `arXiv:hep-ex/9503003`. `doi:10.1103/PhysRevLett.74.2632`.

[35] H1 and ZEUS Collaboration, "PDF fits including HERA-II high Q^2 data (HERAPDF1.5)", *H1 and ZEUS reports* **H1prelim-10-142, ZEUS-prel-10-018**. [Online, accessed 17 Oct. 2012].

[36] H1 and ZEUS Collaboration, "Combined Measurement and QCD Analysis of the Inclusive e+- p Scattering Cross Sections at HERA", *JHEP* **1001** (2010) 109, `arXiv:0911.0884`. `doi:10.1007/JHEP01(2010)109`.

[37] W. Stirling, "7 TeV LHC x,Q^2 parton kinematics (Private Communication)". `http://www.hep.phy.cam.ac.uk/~wjs/plots/plots.html`. [Online, accessed 17 Oct. 2012].

[38] CMS Collaboration, "Measurement of the $t\bar{t}$ production cross section in the dilepton channel in pp collisions at $\sqrt{s} = 8\,\mathrm{TeV}$", *CMS Physics Analysis Summary* **CMS-PAS-TOP-12-007** (2012).

[39] P. Baernreuther, M. Czakon, and A. Mitov, "Percent Level Precision Physics at the Tevatron: First Genuine NNLO QCD Corrections to $q\bar{q} \to t\bar{t} + X$", *Phys. Rev. Lett.* **109** (2012) 132001, `arXiv:1204.5201`. `doi:10.1103/PhysRevLett.109.132001`.

[40] M. Czakon and A. Mitov, "NNLO corrections to top pair production at hadron colliders: the quark-gluon reaction", *JHEP* **1301** (2013) 080, `arXiv:1210.6832`. `doi:10.1007/JHEP01(2013)080`.

[41] M. Czakon, P. Fiedler, and A. Mitov, "Total Top-Quark Pair-Production Cross Section at Hadron Colliders Through $\mathcal{O}(\alpha_S^4)$", *Phys. Rev. Lett.* **110** (2013) 252004, `arXiv:1303.6254`. `doi:10.1103/PhysRevLett.110.252004`.

[42] V. Ahrens et al., "Renormalization-group improved predictions for top-quark pair production at hadron colliders", *JHEP* **09** (2010) 097, `arXiv:1003.5827`.

[43] N. Kidonakis, "Next-to-next-to-leading soft-gluon corrections for the top quark cross section and transverse momentum distribution", *Phys. Rev. D* **82** (2010) 114030, `arXiv:1009.4935`. `doi:10.1103/PhysRevD.82.114030`.

[44] N. Kidonakis, "The top quark rapidity distribution and forward-backward asymmetry", *Phys. Rev. D* **84** (2011) 011504(R), `arXiv:1105.5167`.

[45] J. M. Campbell and R. K. Ellis, "MCFM for the Tevatron and the LHC", *Nucl. Phys. Proc. Suppl.* **205-206** (2010) 10–15, `arXiv:1007.3492`. `doi:10.1016/j.nuclphysbps.2010.08.011`.

[46] A. Martin, W. Stirling, R. Thorne et al., "Parton distributions for the LHC", *Eur. Phys. J. C* **63** (2009) 189–285, `arXiv:hep-ph/0901.0002`. `doi:10.1140/epjc/s10052-009-1072-5`.

[47] N. Kidonakis, "Next-to-next-to-leading-order collinear and soft gluon corrections for t-channel single top quark production", *Phys. Rev. D* **83** (2011) 091503. `doi:10.1103/PhysRevD.83.091503`.

[48] N. Kidonakis, "NNLL resummation for s-channel single top quark production", *Phys. Rev. D* **81** (2010) 054028, `arXiv:1001.5034`. `doi:10.1103/PhysRevD.81.054028`.

[49] N. Kidonakis, "Two-loop soft anomalous dimensions for single top quark associated production with a W^- or H^-", *Phys. Rev. D* **82** (2010) 054018. `doi:10.1103/PhysRevD.82.054018`.

[50] ATLAS Collaboration, "Measurement of the charge asymmetry in top quark pair production in pp collisions at $\sqrt{s} = 7$ TeV using the ATLAS detector", *Eur. Phys. J C72* (2012) 1–27, `arXiv:hep-ex/1203.4211`. `doi:10.1140/epjc/s10052-012-2039-5`.

[51] CMS Collaboration Collaboration, "Inclusive and differential measurements of the $t\bar{t}$ charge asymmetry in proton-proton collisions at 7 TeV", *Phys. Lett. B* **717** (2012) 129–150, `arXiv:1207.0065`. `doi:10.1016/j.physletb.2012.09.028`.

[52] CDF Collaboration, "Measurement of the top quark forward-backward production asymmetry and its dependence on event kinematic properties", *Phys. Rev. D* **87** (2012) 092002, `arXiv:hep-ex/1211.1003`. `doi:10.1103/PhysRevD.87.092002`.

[53] The D0 Collaboration Collaboration, "Forward-backward asymmetry in top quark-antiquark production", *Phys. Rev. D* **84** (2011) 112005, `arXiv:hep-ex/1107.4995`. `doi:10.1103/PhysRevD.84.112005`.

[54] M. Baak, M. Goebel, J. Haller et al., "The Electroweak Fit of the Standard Model after the Discovery of a New Boson at the LHC", *Eur. Phys. J. C* **72** (2012) 2205, `arXiv:1209.2716`. `doi:10.1140/epjc/s10052-012-2205-9`.

[55] C. T. Hill, "Topcolor: top quark condensation in a gauge extension of the standard model", *Physics Letters B* **266** (1991), no. 3–4, 419–424.
doi:10.1016/0370-2693(91)91061-Y.

[56] C. T. Hill, "Topcolor assisted technicolor", *Physics Letters B* **345** (1995) 483–489,
arXiv:hep-ph/9411426. doi:10.1016/0370-2693(94)01660-5.

[57] M. Schmaltz and D. Tucker-Smith, "Little Higgs Theories", *Annual Review of Nuclear and Particle Science* **55** (2005), no. 1, 229–270, arXiv:hep-ph/0502182.
doi:10.1146/annurev.nucl.55.090704.151502.

[58] G. Altarelli, B. Mele, and M. Ruiz-Altaba, "Searching for new heavy vector bosons in $p\bar{p}$ colliders", *Z. Phys. C* **45** (1989) 109. doi:10.1007/BF01556677.

[59] R. M. Harris, C. T. Hill, and S. J. Parke, "Cross Section for Topcolor Z' decaying to top-antitop", arXiv:hep-ph/9911288. Fermilab-FN-687.

[60] R. M. Harris and S. Jain, "Cross Sections for Leptophobic Topcolor Z' decaying to top-antitop", *Eur. Phys. J. C* **72** (2012) 2072, arXiv:hep-ph/1112.4928.
doi:10.1140/epjc/s10052-012-2072-4.

[61] D. Choudhury, R. M. Godbole, R. K. Singh et al., "Top production at the Tevatron/LHC and nonstandard, strongly interacting spin one particles", *Physics Letters B* **657** (2007), no. 1–3, 69–76, arXiv:hep-ph/07051499.
doi:10.1016/j.physletb.2007.09.057.

[62] H. Davoudiasl, J. L. Hewett, and T. G. Rizzo, "Phenomenology of the Randall-Sundrum Gauge Hierarchy Model", *Phys. Rev. Lett.* **84** (2000) 2080–2083,
arXiv:hep-ph/9909255. doi:10.1103/PhysRevLett.84.2080.

[63] K. Agashe, H. Davoudiasl, S. Gopalakrishna et al., "CERN LHC signals for warped electroweak neutral gauge bosons", *Phys. Rev. D* **76** (2007) 115015,
arXiv:hep-ph/0709.0007. doi:10.1103/PhysRevD.76.115015.

[64] K. Agashe, A. Belyaev, T. Krupovnickas et al., "CERN LHC signals from warped extra dimensions", *Phys. Rev. D* **77** (2008) 015003, arXiv:hep-ph/0612015.
doi:10.1103/PhysRevD.77.015003.

[65] N. Arkani-Hamed, S. Dimopoulos, and G. Dvali, "The hierarchy problem and new dimensions at a millimeter", *Physics Letters B* **429** (1998), no. 3–4, 263 – 272,
arXiv:hep-ph/9803315. doi:10.1016/S0370-2693(98)00466-3.

[66] L. Randall and R. Sundrum, "Large Mass Hierarchy from a Small Extra Dimension",
Phys. Rev. Lett. **83** (1999) 3370–3373, arXiv:hep-ph/9905221.
doi:10.1103/PhysRevLett.83.3370.

[67] C. Delaunay, O. Gedalia, Y. Hochberg et al., "Implications of the CDF $t\bar{t}$ forward-backward asymmetry for hard top physics", *JHEP* **2011** (2011) 1–15,
arXiv:hep-ph/1103.2297. doi:10.1007/JHEP08(2011)031.

[68] S. Jung, H. Murayama, A. Pierce et al., "Top quark forward-backward asymmetry from new t-channel physics", *Phys. Rev. D* **81** (2010) 015004,
arXiv:hep-ph/09074112. doi:10.1103/PhysRevD.81.015004.

[69] J. Shelton and K. M. Zurek, "Maximal flavor violation from new right-handed gauge bosons", *Phys. Rev. D* **83** (2011) 091701, `arXiv:hep-ph/11015392`. `doi:10.1103/PhysRevD.83.091701`.

[70] I. Aitchison, "Supersymmetry in Particle Physics – An Elementary Introduction". Cambridge University Press, 2007. ISBN 978-0-521-88023-7.

[71] Z. Han, A. Katz, D. Krohn et al., "(Light) Stop Signs", *JHEP* **1208** (2012) 083, `arXiv:1205.5808`. `doi:10.1007/JHEP08(2012)083`.

[72] CMS Collaboration, "CMS physics: Technical design report", Technical Report CERN-LHCC-2006-001, (2006).

[73] CMS Collaboration, "The CMS experiment at the CERN LHC", *JINST* **3** (2008) S08004. `doi:10.1088/1748-0221/3/08/S08004`.

[74] L. Evans, (ed.) and P. Bryant, (ed.), "LHC Machine", *JINST* **3** (2008) S08001. `doi:10.1088/1748-0221/3/08/S08001`.

[75] C. Lefèvre, "The CERN accelerator complex". `http://cdsweb.cern.ch/record/1260465`, 2008. CERN-DI-0812015. [Online, accessed 17 Oct. 2012].

[76] ATLAS Collaboration, "The ATLAS Experiment at the CERN Large Hadron Collider", *JINST* **3** (2008) S08003. `doi:10.1088/1748-0221/3/08/S08003`.

[77] LHCb Collaboration, "The LHCb Detector at the LHC", *JINST* **3** (2008) S08005. `doi:10.1088/1748-0221/3/08/S08005`.

[78] ALICE Collaboration, "The ALICE experiment at the CERN LHC", *JINST* **3** (2008) S08002. `doi:10.1088/1748-0221/3/08/S08002`.

[79] LHCf Collaboration, "The LHCf detector at the CERN Large Hadron Collider", *JINST* **3** (2008) S08006.

[80] TOTEM Collaboration, "The TOTEM Experiment at the CERN Large Hadron Collider", *JINST* **3** (2008) S08007.

[81] M. Lamont, "Input from Evian 2011", 2012. Proceedings of Chamonix 2012 workshop on LHC Performance, Chamonix, France, 6 - 10 Feb 2012, pp.54-59.

[82] CMS Collaboration, "CMS Luminosity - Public Results". `https://twiki.cern.ch/twiki/bin/view/CMSPublic/LumiPublicResults`, 2012. [Online, accessed 19 Dec. 2012].

[83] R. L. Gluckstern, "Uncertainties in track momentum and direction, due to multiple scattering and measurement errors", *Nucl. Instrum. Meth.* **24** (1963) 381.

[84] CMS Collaboration. `https://twiki.cern.ch/twiki/bin/view/CMSPublic/DPGResultsTRK`. CMS Tracker Detector Performance Results - Public Twiki. [Online, accessed 17 Nov. 2012].

[85] CMS Collaboration, "Description and performance of the CMS track and primary vertex reconstruction", *CMS internal, to be published* **CMS-TRK-11-001**.

[86] CMS Collaboration, "Tracking and Primary Vertex Results in First 7 TeV Collisions", *CMS Physics Analysis Summary* **CMS-PAS-TRK-10-005** (2010).

[87] CMS Collaboration Collaboration, "Performance of CMS muon reconstruction in pp collision events at $\sqrt{s} = 7\,\mathrm{TeV}$", *JINST* **7** (2012) P10002, `arXiv:1206.4071`. `doi:10.1088/1748-0221/7/10/P10002`.

[88] CMS Collaboration, "Measurement of CMS luminosity", *CMS Physics Analysis Summary* **CMS-PAS-EWK-10-004** (2010).

[89] CMS Collaboration, "Absolute Calibration of the Luminosity Measurement at CMS: Winter 2012 Update", *CMS Physics Analysis Summary* **CMS-PAS-SMP-12-008** (2012).

[90] S. van der Meer, "Calibration of the effective beam height in the ISR", Technical Report CERN-ISR-PO-68-31, CERN, Geneva, (1968).

[91] M. Dobbs and J. Hansen, "HepMC 2 — a C++ Event Record for Monte Carlo Generators: User Manual Version 2.06", *Comput. Phys. Commun.* **134** (2001) 41.

[92] CMS Collaboration, "Interactive Slice of the CMS detector". `https://cms-docdb.cern.ch/cgi-bin/PublicDocDB/RetrieveFile?docid=4172&version=2&filename=CMS_Slice.gif`. CMS-doc-4172-v2. [Online, accessed 27 Nov. 2012].

[93] T. Sjostrand, S. Mrenna, and P. Z. Skands, "PYTHIA 6.4 Physics and Manual", *JHEP* **05** (2006) 026, `arXiv:hep-ph/0603175`.

[94] G. Corcella et al., "HERWIG 6.5: an event generator for Hadron Emission Reactions With Interfering Gluons (including supersymmetric processes)", *JHEP* **01** (2001) 010, `arXiv:hep-ph/0011363`.

[95] S. Frixione and B. R. Webber, "The MC@NLO 3.4 Event Generator", `arXiv:0812.0770`.

[96] P. Nason, "A new method for combining NLO QCD with shower Monte Carlo algorithms", *JHEP* **11** (2004) 040, `arXiv:hep-ph/0409146`. `doi:10.1088/1126-6708/2004/11/040`.

[97] S. Frixione, P. Nason, and C. Oleari, "Matching NLO QCD computations with Parton Shower simulations: the POWHEG method", *JHEP* **11** (2007) 070, `arXiv:0709.2092`. `doi:10.1088/1126-6708/2007/11/070`.

[98] F. Maltoni and T. Stelzer, "MadEvent: Automatic event generation with MadGraph", *JHEP* **02** (2003) 027, `arXiv:hep-ph/0208156`.

[99] J. Alwall, M. Herquet, F. Maltoni et al., "MadGraph v5: Going Beyond", *JHEP* **06** (2011) 128, `arXiv:1106.0522`. `doi:10.1007/JHEP06(2011)128`.

[100] V. N. Gribov and L. N. Lipatov, "Deep inelastic ep scattering in perturbation theory", *Sov. J. Nucl. Phys.* **15** (1972) 438–450.

[101] G. Altarelli and G. Parisi, "Asymptotic Freedom in Parton Language", *Nucl. Phys. B* **126** (1977) 298. `doi:10.1016/0550-3213(77)90384-4`.

[102] Y. L. Dokshitzer, "Calculation of the Structure Functions for Deep Inelastic Scattering and e^+e^- Annihilation by Perturbation Theory in Quantum Chromodynamics", *Sov. Phys. JETP* **46** (1977) 641–653.

[103] M. L. Mangano, M. Moretti, F. Piccinini et al., "Matching matrix elements and shower evolution for top- quark production in hadronic collisions", *JHEP* **01** (2007) 013, `arXiv:hep-ph/0611129`. `doi:10.1088/1126-6708/2007/01/013`.

[104] R. Field, "Min-bias and the underlying event at the LHC", *Acta Physica Polonica B* **42** (2011) 2631. `doi:10.5506/APhysPolB.42.2631`.

[105] S. Agostinelli, J. Allison, K. Amako et al., "Geant4 – a simulation toolkit", *Nucl. Instrum. Meth. A* **506** (2003), no. 3, 250 – 303. `doi:10.1016/S0168-9002(03)01368-8`.

[106] J. Allison, K. Amako, J. Apostolakis et al., "Geant4 developments and applications", *IEEE Trans. Nucl. Sci.* **53** (2006), no. 1, 270 –278. `doi:10.1109/TNS.2006.869826`.

[107] M. Gosselink, "Top quark signal modeling uncertainties at CMS". `http://indico.cern.ch/contributionDisplay.py?contribId=17&confId=180665`. Presentation at the TOP 2012 - 5th International Workshop on Top Quark Physics, Winchester. Sep. 2012. [Online, accessed 12 Feb. 2013].

[108] J. Pumplin et al., "New generation of parton distributions with uncertainties from global QCD analysis", *JHEP* **07** (2002) 012, `arXiv:hep-ph/0201195`.

[109] K. Melnikov and F. Petriello, "Electroweak gauge boson production at hadron colliders through $\mathcal{O}(\alpha_s^2)$", *Phys. Rev. D* **74** (2006) 114017, `arXiv:hep-ph/0609070`. `doi:10.1103/PhysRevD.74.114017`.

[110] TOTEM Collaboration, "First measurement of the total proton-proton cross-section at the LHC energy of $\sqrt{s} = 7$ TeV", *EPL (Europhys. Lett.)* **96** (2011), no. 2, 21002.

[111] T. Hermanns. Private Communication.

[112] CMS Physics Validation Group, "Pileup Reweighting Utilities". `https://twiki.cern.ch/twiki/bin/view/CMS/PileupMCReweightingUtilities`. [CMS internal. Online, accessed 14 Jan. 2012].

[113] A. Venturi. `http://venturia.home.cern.ch/venturia/TrackingStudies/largepileup.htm#pvreco`. Relation between pile-Up and primary-vertex multiplicity. Private Homepage [Online, accessed 17 Nov. 2012].

[114] CMS Collaboration, "Measurement of the $t\bar{t}$ Production Cross Section in pp Collisions at $\sqrt{s} = 7$ TeV using the Kinematic Properties of Events with Leptons and Jets", *Eur. Phys. J. C* **71** (2011) 1721, `arXiv:1106.0902`. `doi:10.1140/epjc/s10052-011-1721-3`.

[115] CMS Collaboration, "Particle-Flow Event Reconstruction in CMS and Performance for Jets, Taus, and MET", *CMS Physics Analysis Summary* **CMS-PAS-PFT-09-001** (2009).

[116] P. Lenzi, C. Genta, and B. Mangano, "Track reconstruction of real cosmic muon events with CMS tracker detector", *J. Phys. Conf. Ser.* **119** (2008) 032030. `doi:10.1088/1742-6596/119/3/032030`.

[117] R. Fruhwirth, "Application of Kalman filtering to track and vertex fitting", *Nucl. Instrum. Meth. A* **262** (1987) 444–450. `doi:10.1016/0168-9002(87)90887-4`.

[118] R. Fruhwirth, W. Waltenberger, and P. Vanlaer, "Adaptive vertex fitting", *J. Phys. G34* (2007) N343. `doi:10.1088/0954-3899/34/12/N01`.

[119] CMS Collaboration, "Commisioning of the particle-flow event reconstruction with leptons from J/Psi and W decays at 7 TeV", *CMS Physics Analysis Summary* **CMS-PAS-PFT-10-003** (2010).

[120] W. Adam, R. Fruhwirth, A. Strandlie et al., "Reconstruction of Electrons with the Gaussian-Sum Filter in the CMS Tracker at the LHC", *J. Phys. G: Nucl. Part. Phys.* **31** (2005) N9. `doi:10.1088/0954-3899/31/9/N01`.

[121] CMS Collaboration, "Electron reconstruction and identification at $\sqrt{s}$=7 TeV", *CMS Physics Analysis Summary* **CMS-PAS-EGM-10-004** (2010).

[122] CMS Egamma Group, "Cuts in Categories (CiC) Electron Identification". `https://twiki.cern.ch/twiki/bin/view/CMSPublic/SWGuideCategoryBasedElectronID`. [Online, accessed 17 Oct. 2012].

[123] M. Cacciari, G. P. Salam, and G. Soyez, "The anti-k_t jet clustering algorithm", *JHEP* **04** (2008) 063, `arXiv:0802.1189`. `doi:10.1088/1126-6708/2008/04/063`.

[124] CMS Collaboration, "Determination of Jet Energy Calibration and Transverse Momentum Resolution in CMS", *JINST* **6** (2011) P11002, `arXiv:1107.4277`. `doi:10.1088/1748-0221/6/11/P11002`.

[125] M. Cacciari and G. P. Salam, "Pileup subtraction using jet areas", *Phys. Lett. B* **659** (2007) 119–126. `doi:10.1016/j.physletb.2007.09.077`.

[126] M. Cacciari, G. P. Salam, and G. Soyez, "The Catchment Area of Jets", *JHEP* **0804:005** (2007). `doi:10.1088/1126-6708/2008/04/005`.

[127] CMS Collaboration, "Identification of b-quark jets with the CMS experiment", *JINST* **8** (2013), no. 04, P04013, `arXiv:1211.4462`.

[128] A. B. Galtieri, F. Margaroli, and I. Volobouev, "Precision measurements of the top quark mass from the Tevatron in the pre-LHC era", *Reports on Progress in Physics* **75** (2012), no. 5, 056201.

[129] CMS Collaboration, "Missing transverse energy performance of the CMS detector", *JINST* **6** (2011) P09001, `arXiv:1106.5048`. `doi:10.1088/1748-0221/6/09/P09001`.

[130] L. Tuura, A. Meyer, I. Segoni et al., "CMS data quality monitoring: Systems and experiences", *Journal of Physics: Conference Series* **219** (2010), no. 7, 072020.

[131] R. D. Cousins, K. E. Hymes, and J. Tucker, "Frequentist evaluation of intervals estimated for a binomial parameter and for the ratio of Poisson means", *Nucl. Instrum. Meth. A* **612** (2010), no. 2, 388. `doi:10.1016/j.nima.2009.10.156`.

[132] C. Clopper and E. Pearson, "The Use of Confidence or Fiducial Limits Illustrated in the Case of the Binomial", *Biometrika* **26** (1934) 404.

[133] CMS Collaboration, "Measurements of Inclusive W and Z Cross Sections in pp Collisions at $\sqrt{s}$=7 TeV", *JHEP* **01** (2011) 080, `arXiv:hep-ph/1012.2466`. `doi:10.1007/JHEP01(2011)080`.

[134] T. Michael, "Determination of muon reconstruction efficiencies in the ATLAS detector using a tag & probe approach in $Z \to \mu\mu$ events", Diploma thesis, University of Dresden, Germany, 2011.

[135] M. Görner. Private Communication.

[136] CMS Collaboration, "Fitting of Event Topologies with External Kinematic Constraints in CMS", *Public CMS Note* **CMS NOTE-2006/023** (2006).

[137] CMS Top-Quark Group, "Top-Quark-Analysis Framework (TQAF)". `https://twiki.cern.ch/twiki/bin/view/CMSPublic/SWGuideTQAF`. [Online, accessed 17 Oct. 2012].

[138] H. Enderle, "Resolutions for the Kinematic Fit in the Top-Quark-Analysis Framework". `http://cmssw.cvs.cern.ch/cgi-bin/cmssw.cgi/CMSSW/TopQuarkAnalysis/TopObjectResolutions/python/stringResolutions_etEtaPhi_Fall11_cff.py`. [Online, accessed 17 Oct. 2012].

[139] CMS Collaboration, "Absolute Calibration of the Luminosity Measurement at CMS:Winter 2012 Update", *CMS Physics Analysis Summary* **CMS PAS-SMP-12-008** (2012).

[140] V. Blobel, "A survey of unfolding methods for particle physics". `https://www.wiki.terascale.de/images/a/a8/Blobel_Unfold_Note_20100524.pdf`, 2002. Prepared for Alliance Workshop on Unfolding and Data Correction, DESY, Hamburg, Germany, 27-28 May 2002. [Online; accessed 17 Oct. 2012].

[141] G. Cowan, "Statistical Data Analysis". Clarendon Press, Oxford, 1998.

[142] A. Hoecker and V. Kartvelishvili, "SVD Approach to Data Unfolding", *Nucl. Instrum. Meth. A* **372** (1996) 469, `arXiv:hep-ph/9509307v2`. `doi:10.1016/0168-9002(95)01478-0`.

[143] F. James, "Statistical Methods in Experimental Physics". World Scientific, 2nd edition, 2006.

[144] K. Tackmann, A. Hoecker, and H. Lacker, "TSVDUnfold Software Package". `http://root.cern.ch/root/html/TSVDUnfold.html`. [Online; accessed 17 Oct. 2012].

[145] D. Fischer, "Private Communication".

[146] CMS Collaboration Collaboration, "Search for resonant $t\bar{t}$ production in lepton+jets events in pp collisions at $\sqrt{s} = 7$ TeV", *JHEP* **1212** (2012) 015, `arXiv:1209.4397`. `doi:10.1007/JHEP12(2012)015`.

[147] CMS Physics Validation Group, "Estimating Systematic Errors Due to Pileup Modeling (revision 5)". `https://twiki.cern.ch/twiki/bin/view/CMS/PileupSystematicErrors?rev=5`. [CMS internal. Online, accessed 14 Jan. 2012].

[148] M. Botje et al., "The PDF4LHC Working Group Interim Recommendations", `arXiv:1101.0538`.

[149] L. Hung-Liang et al., "New parton distributions for collider physics", *Phys. Rev. D* **82** (2010) 074024, `arXiv:hep-ph/1007.2241`. `doi:10.1103/PhysRevD.82.074024`.

[150] NNPDF Collaboration, "Unbiased global determination of parton distributions and their uncertainties at NNLO and LO", *Nucl. Phys. B* **855** (2012) 153, `arXiv:1107.2652`. `doi:10.1016/j.nuclphysb.2011.09.024`.

[151] M. Gosselink. Private Communication.

[152] G. D. Lafferty and T. R. Wyatt, "Where to stick your data points: The treatment of measurements within wide bins", *Nucl. Instrum. Meth. A* **355** (1995) 541–547. `doi:10.1016/0168-9002(94)01112-5`.

[153] D. E. Kaplan, K. Rehermann, M. D. Schwartz et al., "Top Tagging: A Method for Identifying Boosted Hadronically Decaying Top Quarks", *Phys. Rev. Lett.* **101** (2008) 142001, `arXiv:hep-ph/0806.0848`. `doi:10.1103/PhysRevLett.101.142001`.

[154] CMS Collaboration, "Measurement of the rapidity and transverse momentum distributions of Z bosons in pp collisions at $\sqrt{(}s)$=7 TeV", *Phys. Rev. D* **85** (2012) 032002, `arXiv:hep-ph/1110.4973`. `doi:10.1103/PhysRevD.85.032002`.

[155] ATLAS Collaboration, "Measurements of top quark pair relative differential cross-sections with ATLAS in pp collisions at $\sqrt{s} = 7$ TeV", *Eur. Phys. J. C* **73** (2013) 2261, `arXiv:1207.5644`. `doi:10.1140/epjc/s10052-012-2261-1`.

[156] CMS Collaboration, "Measurement of the $t\bar{t}$ production cross section in pp collisions at $\sqrt{s}$=7 TeV with lepton+jets final states", *Physics Letters B* **720** (2013), no. 1–3, 83–104. `doi:10.1016/j.physletb.2013.02.021`.

[157] ATLAS Collaboration, "Measurement of the $t\bar{t}$ production cross-section in pp collisions at $\sqrt{s}$=7 TeV using kinematic information of lepton+jets events", *ATLAS Conference Note* **ATLAS-CONF-2011-121** (2011).

[158] S. M. Sze and K. K. Ng, "Physics of Semiconductor Devices". Wiley-Interscience, 3rd edition, 2006.

[159] G. Lutz, "Semiconductor Radiation Detectors: Device Physic". Accelerator Physics Series. Springer-Verlag, 1999.

[160] H. Spieler, "Semiconductor Detector Systems (Semiconductor Science and Technology)". Oxford University Press, USA, 2005.

[161] L. Rossi, P. Fischer, T. Rohe et al., "Pixel Detectors: From Fundamentals to Applications". Particle Acceleration and Detection. Springer, 2006.

[162] F. Hartmann, "Evolution of silicon sensor technology in particle physics". Springer, 2009.

[163] M. Moll, "Radiation Damage in Silicon Particle Detectors". PhD thesis, University of Hamburg, Germany, 1999. DESY-THESIS-1999-040.

[164] S. Müller, "The Beam Condition Monitor 2 and the Radiation Environment of the CMS Detector at the LHC". PhD thesis, University of Karlsruhe, Germany, 2011. IEKP-KA/2011-01.

[165] E. Belau, R. Klanner, G. Lutz et al., "Charge collection in silicon strip detectors", *Nucl. Instrum. Meth.* **214** (1983) 253–260.

[166] R. Turchetta, "Spatial resolution of silicon microstrip detectors", *Nucl. Instrum. Meth. A* **335** (1993) 44–58.

[167] F. Hönniger, "Strahlentoleranz von Cz-Silizium-Detektoren", Diploma thesis, University of Hamburg, Germany, 2003.

[168] A. Junkes, "Investigation of electrically active defects induced in silicon diodes after low doses of electron and neutron irradiation", Diploma thesis, University of Hamburg, Germany, 2007.

[169] A. Chilingarov, "Generation current temperature scaling", Technical Report RD50-2011-01, PH-EP-Tech-Note-2013-001, CERN, Geneva, (2013).

[170] W. Shockley, "Currents to Conductors Induced by a Moving Point Charge", *Journal of Applied Physics* **9** (1938), no. 10, 635–636. `doi:10.1063/1.1710367`.

[171] S. Ramo, "Currents Induced by Electron Motion", *Proceedings of the IRE* **27** (1939), no. 9, 584–585. `doi:10.1109/JRPROC.1939.228757`.

[172] J. Becker, "Signal Development in Silicon Sensors Used for Radiation Detection". PhD thesis, University of Hamburg, Germany, 2010. DESY-THESIS-2010-033.

[173] C. Jacoboni, C. Canali, G. Ottaviani et al., "A review of some charge transport properties of silicon", *Solid-State Electronics* **20** (1977), no. 2, 77–89. `doi:10.1016/0038-1101(77)90054-5`.

[174] P. P. Webb, R. J. McIntyre, and J. Conradi, "Properties of Avalanche Photodiodes", *RCA Review* **35** (1974) 234.

[175] W. Grant, "Electron and hole ionization rates in epitaxial silicon at high electric fields", *Solid-State Electronics* **16** (1973), no. 10, 1189–1203. `doi:10.1016/0038-1101(73)90147-0`.

[176] A. G. Chynoweth, "Ionization Rates for Electrons and Holes in Silicon", *Phys. Rev.* **109** (1958) 1537–1540. `doi:10.1103/PhysRev.109.1537`.

[177] R. V. Overstraeten and H. D. Man, "Measurement of the ionization rates in diffused silicon p-n junctions", *Solid-State Electronics* **13** (1970), no. 5, 583–608. `doi:10.1016/0038-1101(70)90139-5`.

[178] T. Lackner, "Avalanche multiplication in semiconductors: A modification of Chynoweth's law", *Solid-State Electronics* **34** (1991), no. 1, 33 – 42. `doi:10.1016/0038-1101(91)90197-7`.

[179] Y. Okuto and C. R. Crowell, "Ionization coefficients in semiconductors: A nonlocalized property", *Phys. Rev. B* **10** (1974) 4284–4296. `doi:10.1103/PhysRevB.10.4284`.

[180] A. Cristofoli, P. Palestri, M. Giordani et al., "Experimental Determination of the Impact Ionization Coefficients in Irradiated Silicon", *IEEE Trans. Nucl. Sci.* **58** (Aug.), no. 4, 2091–2096.

[181] D. Kotliński, "Status of the CMS Pixel detector", *JINST* **4** (2009), no. 03, P03019.

[182] R. McIntyre, "Multiplication noise in uniform avalanche diodes", *IEEE Trans. Electron Devices* **13** (1966), no. 1, 164 – 168. `doi:10.1109/T-ED.1966.15651`.

[183] R. McIntyre, "The distribution of gains in uniformly multiplying avalanche photodiodes: Theory", *IEEE Trans. Electron Devices* **19** (1972), no. 6, 703 – 713. `doi:10.1109/T-ED.1972.17485`.

[184] Institute of Electronic Materials Technology (ITME), Warsaw, Poland. `http://www.ITME.edu.pl`.

[185] V. van Lint, T. Flanagan, R. Leadon et al., "Mechanisms of radiation effects in electronic materials". Number Bd. 1 in Mechanisms of Radiation Effects in Electronic Materials. Wiley, 1980.

[186] M. Lazo, D. Woodall, and P. McDaniel, "Silicon and silicon dioxide neutron damage functions", pp. 85–103. 1987. In. Proc. Fast Burt React. Workshop, 1986, Sandia National Laboratories, 1987. [Tech.Rep.] SAND, SAND87-0098 Vol.1.

[187] A. Vasilescu and G. Lindström, "Displacement Damage in Silicon". `http://sesam.desy.de/members/gunnar/Si-dfuncs.html`. Online compilation [accessed 1 June 2011].

[188] Y. Shi, D. X. Shen, F. M. Wu et al., "A numerical study of cluster center formation in neutron-irradiated silicon", *Journal of Applied Physics* **67** (1990), no. 2, 1116–1118. `doi:10.1063/1.345799`.

[189] B. R. Gossick, "Disordered Regions in Semiconductors Bombarded by Fast Neutrons", *Journal of Applied Physics* **30** (1959), no. 8, 1214–1218. `doi:10.1063/1.1735295`.

[190] A. Junkes, "Influence of Radiation Induced Defect Clusters on Silicon Particle Detectors". PhD thesis, University of Hamburg, Germany, 2011. DESY-THESIS-2011-031.

[191] G. Lindström for the RD48 (ROSE) collaboration, "Radiation hard silicon detectors—developments by the RD48 (ROSE) collaboration", *Nucl. Instrum. Meth. A* **466** (2001), no. 2, 308 – 326. `doi:10.1016/S0168-9002(01)00560-5`.

[192] G. Kramberger, D. Contarato, E. Fretwurst et al., "Superior radiation tolerance of thin epitaxial silicon detectors", *Nucl. Instrum. Meth. A* **515** (2003), no. 3, 665 – 670. `doi:10.1016/j.nima.2003.07.021`.

[193] G. Lindström, I. Dolenc, E. Fretwurst et al., "Epitaxial silicon detectors for particle tracking—Radiation tolerance at extreme hadron fluences", *Nucl. Instrum. Meth. A* **568** (2006), no. 1, 66 – 71. `doi:10.1016/j.nima.2006.05.203`.

[194] I. Pintilie, G. Lindstroem, A. Junkes et al., "Radiation-induced point- and cluster-related defects with strong impact on damage properties of silicon detectors", *Nucl. Instrum. Meth. A* **611** (2009), no. 1, 52 – 68. `doi:10.1016/j.nima.2009.09.065`.

[195] R. Wunstorf, "Systematische Untersuchung zur Strahlenresistenz von Silizium-Detektoren für die Verwendung in Hochenergiephysik-Experimenten". PhD thesis, University of Hamburg, Germany, 1992.

[196] V. Eremin, E. Verbitskaya, and Z. Li, "The origin of double peak electric field distribution in heavily irradiated silicon detectors", *Nucl. Instrum. Meth. A* **476** (2002), no. 3, 556 – 564. `doi:10.1016/S0168-9002(01)01642-4`.

[197] E. Verbitskaya and V. Eremin, "Simulation of electric field profile in Si irradiated detectors with a consideration of carrier generation parameters". `https://indico.cern.ch/contributionDisplay.py?contribId=21&sessionId=0&confId=200290`. Presentation at the 21st RD50 Workshop, CERN. Nov 2012. [Online, accessed 21 Feb. 2013].

[198] E. Verbitskaya, V. Eremin, I. Ilyashenko et al., "Operation of heavily irradiated silicon detectors in non-depletion mode", *Nucl. Instrum. Meth. A* **557** (2006), no. 2, 528 – 536. `doi:10.1016/j.nima.2005.10.126`.

[199] G. Kramberger, "Signal Development in Irradiated Silicon Detectors". PhD thesis, University of Ljubljana, Slovenia, 2001.

[200] G. Kramberger, V. Cindro, I. Mandić et al., "Effective trapping time of electrons and holes in different silicon materials irradiated with neutrons, protons and pions", *Nucl. Instrum. Meth. A* **481** (2002), no. 1–3, 297 – 305. `doi:10.1016/S0168-9002(01)01263-3`.

[201] G. Kramberger, V. Cindro, I. Mandić et al., "Impact of annealing of trapping times on charge collection in irradiated silicon detectors", *Nucl. Instrum. Meth. A* **579** (2007), no. 2, 762 – 765. `doi:10.1016/j.nima.2007.05.294`.

[202] T. Pöhlsen, "Charge Collection and Space Charge Distribution in Neutron-Irradiated Epitaxial Silicon Detectors", Diploma thesis, University of Hamburg, Germany, 2010. DESY-THESIS-2010-013.

[203] G. Casse, "Charge multiplication in highly irradiated planar silicon sensors", *PoS* **VERTEX2010** (2010) 020.

[204] T. Pöhlsen et al., "Life time determination of free charge carriers in irradiated silicon sensors". `https://indico.cern.ch/contributionDisplay.py?contribId=20&sessionId=1&confId=175330`. Presentation at the 20th RD50 Workshop, Bari. May 2012. [Online, accessed 12 Feb. 2013].

[205] L. Beattie, T. Brodbeck, A. Chilingarov et al., "Carrier lifetimes in heavily irradiated silicon diodes", *Nucl. Instrum. Meth. A* **421** (1999), no. 3, 502 – 511. `doi:10.1016/S0168-9002(98)01229-7`.

[206] G. Vincent, A. Chantre, et al., "Electric field effect on the thermal emission of traps in semiconductor junctions", *Journal of Applied Physics* **50** (1979), no. 8, 5484. `doi:10.1063/1.326601`.

[207] G. A. M. Hurkx, D. B. M. Klaassen, and M. P. G. Knuvers, "A new recombination model for device simulation including tunneling", *IEEE Trans. Electron Devices* **39** (1992) 331–338.

[208] J. Frenkel, "On pre-breakdown phenomena in insulators and electronic semi-conductors", *Phys. Rev.* **54** (1938) 647–648.

[209] CERN RD50 Collaboration, "Develoment of Radiation Hard Semiconductor Devices for Very High Luminosity Colliders", *R&D Proposal* **CERN-LHCC 2002-003/P6** (2002).

[210] CERN RD50 Collaboration, "Radiation Hard Semiconductor Devices for Very High Luminosity Colliders", *RD50 Status Report 2009/2010* **CERN-LHCC-2012-010 / LHCC-SR-004** (2012).

[211] S. Mersi, "CMS Silicon Tracker upgrade for HL-LHC", *CMS Conference Report* **CMS-CR-2012-137** (2012).

[212] M. Capeans, G. Darbo, K. Einsweiller et al., "ATLAS Insertable B-Layer Technical Design Report", Technical Report CERN-LHCC-2010-013. ATLAS-TDR-19, CERN, Geneva, (2010).

[213] A. Chilingarov and T. Sloan, "Operation of heavily irradiated silicon detectors under forward bias", *Nucl. Instrum. Meth. A* **399** (1997) 35–37.

[214] E. Tuominen et al., "Recent Progress in CERN RD39: radiation hard cryogenic silicon detectors for applications in LHC experiments and their future upgrades", *IEEE Trans. Nucl. Sci.* **56** (2009) 2119–2123.

[215] W. Adam et al., "Radiation hard diamond sensors for future tracking applications", *Nucl. Instrum. Meth. A* **565** (2006) 278–283.

[216] G. Kramberger, V. Cindro, I. Mandic et al., "Influence of trapping on silicon microstrip detector design and performance", *IEEE Trans. Nucl. Sci.* **49** (2002), no. 4, 1717 – 1723.

[217] G. Casse, "Radiation hardness of p-type silicon detectors", *Nucl. Instrum. Meth. A* **612** (2010), no. 3, 464 – 469. `doi:10.1016/j.nima.2009.08.050`.

[218] Y. Unno et al., "Development of n-on-p silicon sensors for very high radiation environments", *Nucl. Instrum. Meth. A* **636** (2011), no. 1, Supplement, S24 – S30. `doi:10.1016/j.nima.2010.04.080`.

[219] S. Parker, C. Kenney, and J. Segal, "3D - A proposed new architecture for solid-state radiation detectors", *Nucl. Instrum. Meth. A* **395** (1997) 328–343.

[220] M. Köhler, "Double-Sided 3D Silicon Detectors for the High-Luminosity LHC". PhD thesis, University of Freiburg, Germany, 2011.

[221] SIMS laboratory. Physics Institute of the Polish Academy of Science, Warsaw, Poland.

[222] CERN RD50 Collaboration, "Radiation Hard Semiconductor Devices for Very High Luminosity Colliders", *RD50 Status Report 2007* **CERN-LHCC-2008-001** / **LHCC-RD-015** (2008).

[223] CiS Institut für Mikrosensorik GmbH, Erfurt, Germany.

[224] M. Glaser, L. Durieu, F. Lemeilleur et al., "New irradiation zones at the CERN-PS", *Nucl. Instrum. Meth. A* **426** (1999), no. 1, 72 – 77. `doi:10.1016/S0168-9002(98)01472-7`.

[225] M. Glaser. `https://irradiation.web.cern.ch/irradiation/irrad1.htm`. CERN PS Irradiation Facility Webpage. [Online, accessed 8 Jan. 2012].

[226] K. Rajkanan, R. Singh, and J. Shewchun, "Absorption coefficient of silicon for solar cell calculations", *Solid State Electronics* **22** (1979) 793–795. `doi:10.1016/0038-1101(79)90128-X`.

[227] J. Ziegler, "The Stopping and Range of Ions in Matter". `www.srim.org`. SRIM 2008 [Online, accessed 1 Jul. 2008].

[228] G. Kramberger, V. Cindro, I. Dolenc et al., "Charge collection properties of heavily irradiated epitaxial silicon detectors", *Nucl. Instrum. Meth. A* **554** (2005), no. 1–3, 212 – 219. `doi:10.1016/j.nima.2005.08.066`.

[229] R. Brun and F. Rademakers, "ROOT - An Object Oriented Data Analysis Framework", *Nucl. Instr. Meth. A* **389** (1997) 81–86. Proceedings AIHENP'96 Workshop, Lausanne. See also `http://root.cern.ch/`.

[230] J. Lange, J. Becker, D. Eckstein et al., "Charge collection studies of proton-irradiated n- and p-type epitaxial silicon detectors", *Nucl. Instrum. Meth. A* **624** (2010), no. 2, 405 – 409. `doi:10.1016/j.nima.2009.11.082`.

[231] J. Lange, J. Becker, E. Fretwurst et al., "Properties of a radiation-induced charge multiplication region in epitaxial silicon diodes", *Nucl. Instrum. Meth. A* **622** (2010), no. 1, 49–58. `doi:10.1016/j.nima.2010.07.036`.

[232] V. Eremin, E. Verbitskaya, A. Zabrodskii et al., "Avalanche effect in Si heavily irradiated detectors: Physical model and perspectives for application", *Nucl. Instrum. Meth. A* **658** (2011), no. 1, 145 – 151. `doi:10.1016/j.nima.2011.05.002`.

[233] G. Kramberger, V. Cindro, I. Mandić et al., "Investigation of Irradiated Silicon Detectors by Edge-TCT", *IEEE Trans. Nucl. Sci.* **57** (2010), no. 4, 2294 –2302. `doi:10.1109/TNS.2010.2051957`.

[234] E. Verbitskaya, V. Eremin, and A. Zabrodskii, "Operational voltage of silicon heavily irradiated strip detectors utilizing avalanche multiplication effect", *JINST* **7** (2012), no. 02, C02061.

[235] J. Lange, J. Becker, E. Fretwurst et al., "Charge multiplication properties in highly irradiated epitaxial silicon detectors", *PoS* **VERTEX2010** (2010) 025.

[236] CMS Collaboration, "Measurement of differential top-quark pair production cross sections in the lepton+jets channel in pp collisions at 8 TeV", *CMS Physics Analysis Summary* **CMS-PAS-TOP-12-027** (2013).

[237] CMS Collaboration, "Measurement of the differential ttbar cross section in the dilepton channel at 8 TeV", *CMS Physics Analysis Summary* **CMS-PAS-TOP-12-028** (2013).

[238] M. L. Mangano and J. Rojo, "Cross Section Ratios between different CM energies at the LHC: opportunities for precision measurements and BSM sensitivity", *JHEP* **1208** (2012) 010, `arXiv:1206.3557`. `doi:10.1007/JHEP08(2012)010`.

[239] R. Chierici et al., "Particle level objects and pseudo top definitions". `https://twiki.cern.ch/twiki/bin/view/LHCPhysics/ParticleLevelTopDefinitions`. [Online, accessed 14 Mar. 2013].

[240] W. H. Bell, "Common top (pair) acceptance: definitions". `https://indico.cern.ch/getFile.py/access?contribId=9&resId=0&materialId=slides&confId=189617`. [Online, accessed 14 Mar. 2013].

[241] J. Rojo, "Top quark production at the LHC as a gluon luminometer". `https://indico.cern.ch/getFile.py/access?contribId=12&sessionId=1&resId=0&materialId=slides&confId=217721`. Presentation at the TOP LHC WG meeting, CERN. Nov. 2012. [Online, accessed 12 Feb. 2013].

[242] A. Denner, S. Dittmaier, S. Kallweit et al., "Finite-width effects in top-quark pair production and decay at the LHC", `arXiv:1203.6803`. In: "The SM and NLO multileg and SM MC Working Groups: Summary Report" (J. A. Maestre, S. Alioli, J. Andersen, R. Ball, A. Buckley, et al., eds.).

[243] M. Baumgart and B. Tweedie, "A New Twist on Top Quark Spin Correlations", `arXiv:1212.4888`.

[244] S. Choi and H. S. Lee, "Azimuthal decorrelation in $t\bar{t}$ production at hadron colliders", *Phys. Rev. D* **87** (2013) 034012, `arXiv:1207.1484`. `doi:10.1103/PhysRevD.87.034012`.

[245] S. Alioli, P. Fernandez, J. Fuster et al., "A new observable to measure the top-quark mass at hadron colliders", `arXiv:1303.6415`.

[246] G. Kramberger, "Charge collection studies on heavily irradiated diodes from the RD50 multiplication run". `https://indico.cern.ch/contributionDisplay.py?contribId=15&sessionId=4&confId=175330`. Presentation at the 20th RD50 Workshop, Bari. May 2012. [Online, accessed 12 Feb. 2013].

[247] C. Betancourt, "A Charge Collection Study with Dedicated RD50 Charge Multiplication Sensors". `https://indico.cern.ch/contributionDisplay.py?contribId=19&sessionId=3&confId=200290`. Presentation at the 21st RD50 Workshop, CERN. Nov. 2012. [Online, accessed 12 Feb. 2013].

[248] P. Fernandez-Martinez, G. Pellegrini, J. Balbuena et al., "Simulation of new p-type strip detectors with trench to enhance the charge multiplication effect in the n-type electrodes", *Nucl. Instrum. Meth. A* **658** (2011), no. 1, 98 − 102. `doi:10.1016/j.nima.2011.04.056`.

[249] G. Casse, D. Forshaw, T. Huse et al., "Charge multiplication in irradiated segmented silicon detectors with special strip processing", *Nucl. Instrum. Meth. A* **699** (2013) 9–13. `doi:10.1016/j.nima.2012.04.033`.

[250] G. Pellegrini, "Status of the RD50 funding request for detectors with enhanced multiplication". `https://indico.cern.ch/getFile.py/access?contribId=14&sessionId=3&resId=2&materialId=slides&confId=200290`. Presentation at the 21st RD50 Workshop, CERN. Nov. 2012. [Online, accessed 12 Feb. 2013].

[251] H. Sadrozinski, "Ultra-Fast Silicon Sensors". `https://indico.cern.ch/contributionDisplay.py?contribId=3&confId=226647`. Presentation at the 8th Trento Workshop on Advanced Radiation Detectors. Trento 2013. [Online, accessed 12 March 2013].

[252] J.-P. Balbuena, "Simulation of 3D detectors". `http://indico.cern.ch/contributionDisplay.py?contribId=27&sessionId=6&confId=114255`. Presentation at the 6th Trento Workshop on Advanced Radiation Detectors. Trento 2011. [Online, accessed 12 Feb. 2013].

DANKE!